Alma Mater Studiorum - Università di Bologna

DOTTORATO DI RICERCA IN
ASTROFISICA

Ciclo 36

Settore Concorsuale: 02/C1 - ASTRONOMIA, ASTROFISICA, FISICA DELLA TERRA E DEI PIANETI

Settore Scientifico Disciplinare: FIS/05 - ASTRONOMIA E ASTROFISICA

IMPACT OF ACTIVE GALACTIC NUCLEI ON THE MOLECULAR GAS: A RADIATIVE AND KINEMATICAL PERSPECTIVE

Presentata da: Federico Esposito

Coordinatore Dottorato

Prof. Andrea Miglio

Supervisori

Prof. Francesca Pozzi

Dr. Livia Vallini

Dr. Viviana Casasola

Esame finale anno 2024

Abstract

The molecular phase of the interstellar medium (ISM), essential for star formation (SF) and central to galaxy evolution, undergoes significant changes in its properties due to feedback processes from SF and active galactic nuclei (AGNs). Both newly formed stars and AGNs emit high-energy radiation, particularly far-UV and X-rays, creating photodissociation regions (PDRs) and X-ray dominated regions (XDRs) in the ISM, influencing its heating/cooling rates and chemistry. Furthermore, they both inject turbulence and induce molecular outflows, considered crucial factors in shaping galaxy evolution. In this Thesis, we utilize both observational and theoretical approaches to quantify the impact of AGNs on molecular gas from both radiative and kinematical perspectives. To trace and examine its excitation conditions, we employ carbon monoxide (CO) emission, its spectral line energy distribution (SLED), and its spatially resolved kinematics. We first deliver a study on the relative contribution of SF and AGN in a new sample of X-ray selected local active galaxies, utilizing a comprehensive collection of multiwavelength observational data. We then present a new physically-motivated model for estimating CO excitation and line emission in active galaxies, leveraging the previously collected observations. The model, named `galaxySLED` and publicly released, takes into account the internal density structure of giant molecular clouds (GMCs), the heating and cooling in PDRs and XDRs, and the GMC mass distribution. Finally, we provide a detailed kinematical analysis on the multiphase ISM in NGC 5506, a nearby Seyfert galaxy with outflow signatures. We did not detect evidence for AGN influence on the cold and low-density gas on kpc-scales. This is also reflected by our model's indications for a Galactic CO-to-H_2 conversion factor in AGNs. Nevertheless, we find the AGN dominating CO excitation and influencing its spatial distribution and kinematics within the central kpc. On the one hand, this may become apparent only by taking into account the actual distribution of molecular gas density and the effect of X-ray irradiation on it. On the other hand, a detailed modelling of the gas kinematics is necessary to interpret non-circular motions in the AGN vicinity. In conclusion, this Thesis demonstrates that AGNs impact both the excitation and kinematics of molecular gas. This influence is observable primarily in the central regions and requires careful comparisons of models and observations. Considering that the central regions of star-forming galaxies typically host the bulk of molecular gas and SF, this impact may constrain SF efficiency, ultimately contributing to its quenching.

Contents

Acronyms and abbreviations

ADAF Advection dominated accretion flow. 32, 33

AGN Active Galactic Nucleus. 10, 30

ALMA Atacama Large Millimeter/submillimeter Array. 10, 14, 50, 96, 97, 127, 134, 159

BAL Broad absorption line. 37, 93

BAT Burst Alert Telescope. 31, 47, 54, 94

BCG Brightest cluster galaxy. 34

BHAR Black hole accretion history. 34

BLR Broad-line region. 13, 32

CGM Circumgalactic medium. 36

CND Circumnuclear disc. 43

CT Compton-thick. 32

ETG Early-type galaxy. 8

EUV Extreme ultraviolet. 5, 19

FUV Far ultraviolet. 5, 20, 44, 57, 61, 66, 73, 159

GATOS Galaxy Activity, Torus, and Outflow Survey. 43, 94, 135

GMC Giant molecular cloud. 4, 25, 67–69, 71, 72

HST Hubble Space Telescope. 6, 50, 95, 168

ICM Intraclump medium. 71

IMF Initial mass function. 7, 9

INTEGRAL International Gamma-Ray Astrophysics Laboratory. 31

IR Infrared. 14, 57

IRAC Infrared Array Camera (of the *Spitzer Space Telescope*). 10

ISM Interstellar medium. 2, 20, 93

ISRF Interstellar radiation field. 20

To the people who feel lost
on this pale blue dot

1

Introduction

Away from city lights, on a moonless summer night, it is easy to see the Milky Way. Within some constellations, such as Cygnus, Cassiopeia, and Perseus in the north, and the Southern Cross and Centaurus in the southern hemisphere, diffuse light seems to link the luminous stars: this is the combined glow of millions of stars situated tens of thousands of light-years away (or parsecs, where 1 pc = 3.26 light years). The bright stars of Cassiopeia and Centaurus, on the other hand, are between 10 and 100 pc from us. It is as if we live in the countryside of the Galaxy[1], with sparse lights around us — corresponding to nearby houses — while the city lights in the distance are packed and aligned. Upon closer inspection, beneath an exceptionally dark sky, we start to recognize interesting areas along the Milky Way line: clumps of diffuse light, and mysteriously dark patches, as if someone painted them with a black marker (e.g. Figure 1.1). The former are called star clusters (see the reviews by Lada & Lada, 2003; Portegies Zwart et al., 2010; Krumholz et al., 2019), and predominantly host very young stars, still close together because they did not have enough time, during their trip around the centre of the Galaxy, to lose track of their sibling stars. We know their age thanks to their colour and to our solid understanding of stellar evolution (Iben, 1967, 1974; Renzini, 1977; Iben & Renzini, 1983). The latter have been initially called dark clouds, since they cover what is beyond (and within) them. We now know they are dark thanks to their high density and cold temperature, and due to their chemical mix of dust and molecular gas. For this reason, we now usually refer to them as molecular clouds: these are the gas clouds from which stars are born, and they are one of the main actors of this Thesis.

---

[1]We use the names Milky Way and Galaxy interchangeably to indicate our galaxy

Figure 1.1: Overexposed photo of a portion of the Milky Way, showing isolated stars, star clusters and dark clouds. Credits: A. Fujii/NASA

1.1 Historical overview

1.1.1 The molecular clouds

The first to observe the molecular clouds with a telescope was probably William Herschel, who notably called them "Holes in the heavens" (Herschel, 1785). A bit more than a century ago, Barnard (1919), with the "invaluable aid" of his niece Mary Ross Calvert, published the first catalogue of the "Dark markings of the sky". Bok & Reilly (1947) and Bok (1948) recognized the association of these dark clouds with star formation. The direct detection of the molecular interstellar medium (ISM) started slightly before, with the first optical observation of methylidyne (CH, at $\lambda = 4300$ Å, by Dunham, 1937; Swings & Rosenfeld, 1937; McKellar, 1940), but it was only with the development of radio telescopes that we really started to "see" the molecular clouds (Figure 1.2), with the emission of neutral hydrogen (at $\nu = 1.42$ GHz, see Ewen & Purcell, 1951; Muller & Oort, 1951), followed by the first molecular radio detection (the hydroxyl radical OH, at $\nu = 1.67$ GHz, by Weinreb et al., 1963). Finally, the emission of the lowest-energy rotational line of carbon monoxide (CO), the $CO(1-0)$ at 115 GHz, was detected by Wilson et al. (1970). Since then, many molecules have been observed in space: the most

E.E. Barnard: Nebulous Region in Taurus (January 1907)
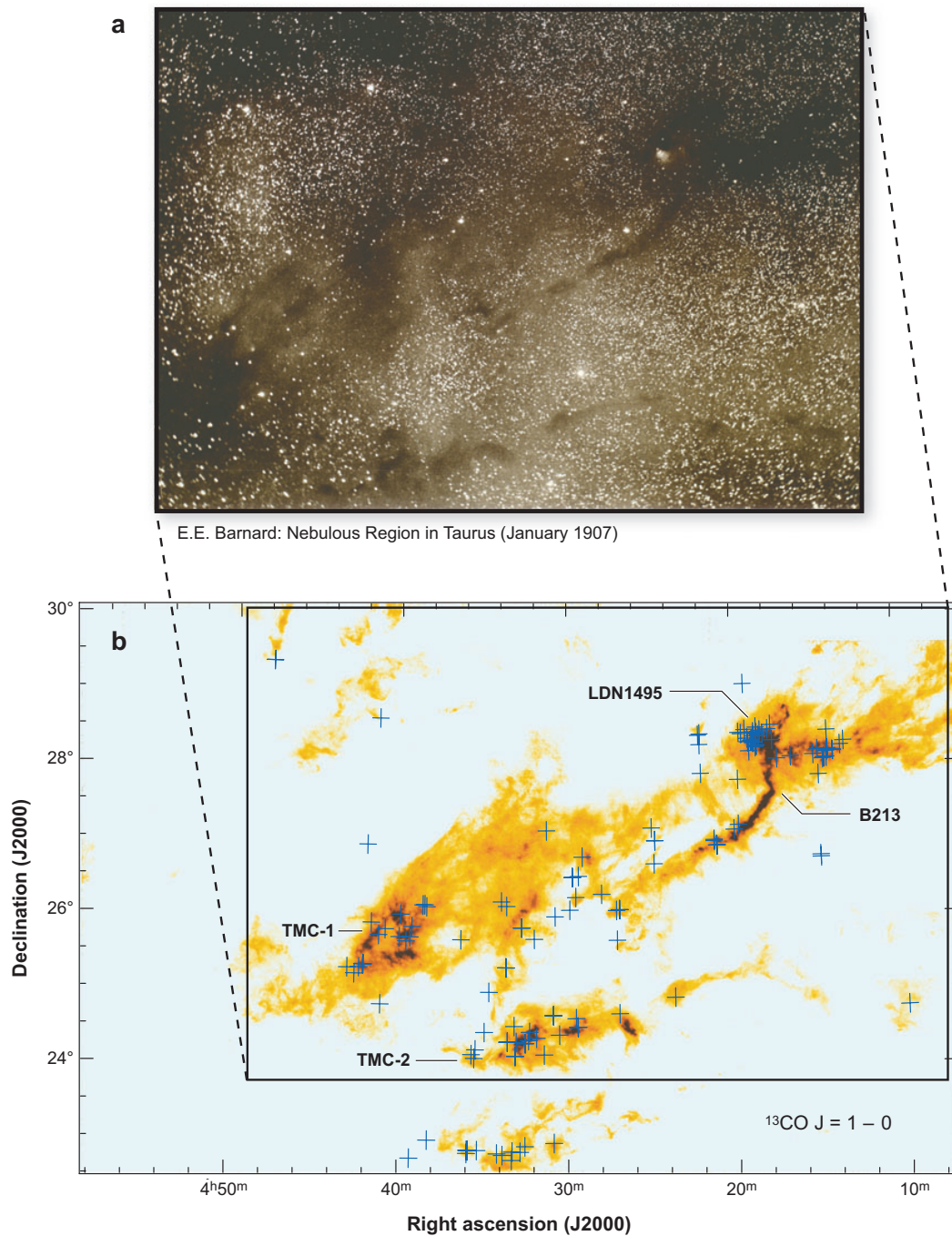
Figure 1.2: (*a*) Photographic image of the Taurus molecular cloud taken by E.E. Barnard (Barnard 1919). (*b*) ^{13}CO $(1 - 0)$ integrated emission map of the same region obtained using the Five College Radio Astronomy Observatory. Blue crosses mark the location of known stellar and protostellar objects and the emission colour scale ranges from 0.5 to 10 K km s^{-1}. Image from Bergin & Tafalla (2007).

3

recent catalogue (McGuire, 2022) lists 241 individual molecular species, composed by a number of atoms between 2 and 70.

Molecules can survive only in cold climates. On the Earth we have plenty of molecules thanks to our stable cold temperature, while in the Galaxy the diffuse gas surrounding stars is at thousands of degrees: molecules are destroyed in such regions, and most electrons even leave the atoms. Molecular clouds remain cold (down to ~ 10 K) thanks to a combination of mechanisms, mainly the self-shielding of molecular hydrogen (H$_2$) at column densities $N_H > 10^{14}$ cm^{-2}, and the efficient cooling through molecular lines (mostly CO). These mechanisms will be reviewed in Section 1.2.

Thanks to its cold temperature, the molecular gas can form large aggregates, called Giant Molecular Clouds (GMCs), with typical masses $M_{GMC} \sim 10^5$ M$_\odot$, and typical sizes of $\sim 30-50$ pc (see e.g. Omont, 2007; Chevance et al., 2020a, 2023a). Such clouds are massive enough to feel their own gravity, but can remain stable thanks to the balance of magnetic and turbulent pressure acting against the gravitational collapse. Within them it exists a complex hierarchical structure of so-called clumps ($50-500$ M$_\odot$) and cores ($0.5-5$ M$_\odot$, e.g. the review by Bergin & Tafalla, 2007), which can be also described with fractal dimensions (e.g. Elmegreen & Falgarone, 1996; Stutzki et al., 1998; Elia et al., 2018). We will discuss in more detail on GMCs and their internal structure in Section 1.2.5.

The theory of gravitational collapse was firstly outlined by Jeans (1902). It says that, in an isothermal and uniform medium of mean density ρ, there is a maximum size for gravitational stability, called the Jeans length:

$$\lambda_J = \sqrt{\frac{\pi c_s^2}{G\rho}} \quad , \tag{1.1}$$

where c_s is the sound speed, and $G = 6.67 \times 10^{-8}$ cm^3 g^{-1} s is the gravitational constant. We can calculate the corresponding Jeans mass as $M_J = (4\pi/3)(\lambda_J/2)^3 \rho$ (see also Binney & Tremaine, 1987). If we put reasonable values for a GMC ($\rho = 6 \times 10^{-22}$ g cm^{-3}, $c_s = 3$ km s^{-1}), we obtain $M_J = 130$ M$_\odot$, which is orders of magnitude below typical GMC masses. According to Jeans theory, then, such massive clouds should collapse in a free-fall time, i.e. in $t_{ff} = \sqrt{3\pi/(32G\rho)} \sim 3$ Myr. Given that the total mass of molecular gas in the Milky Way is $M_{H_2} \sim 10^9$ M$_\odot$ (see Heyer & Dame, 2015, and references therein), and that most of it is in GMCs, we can calculate the star formation rate (SFR) of the Milky Way as

$$\text{SFR} = \epsilon_{ff} \frac{M_{H_2}}{t_{ff}} \sim 300 \epsilon_{ff} \text{ M}_\odot \text{ yr}^{-1} \quad , \tag{1.2}$$

where $\epsilon_{\rm ff}$ is the (unknown) efficiency per free-fall time of the star formation process (Krumholz & McKee, 2005). Given that the observed Galactic SFR is $\sim 1 - 3$ M$_\odot$ yr^{-1} (Robitaille & Whitney, 2010; Chomiuk & Povich, 2011; Licquia & Newman, 2015), this would mean that the GMCs form stars with a very low efficiency of $\epsilon_{\rm ff} \sim 10^{-2}$ (see the discussion in Krumholz et al., 2019; Chevance et al., 2023a, and references therein).

Turbulence is widely observed in GMCs (Larson, 1981; Evans, 1999; Heyer & Brunt, 2004; Merello et al., 2019) and it is typically invoked as a mechanism to counteract gravitational collapse (see reviews by Mac Low & Klessen, 2004; Ballesteros-Paredes et al., 2007; McKee & Ostriker, 2007; Hennebelle & Falgarone, 2012), thereby maintaining a low $\epsilon_{\rm ff}$. Another physical mechanism that could support the gravitational inward collapse of a GMC is magnetic pressure (a theory first developed by Mouschovias & Spitzer, 1976; Nakano, 1976; Shu, 1977). The presence of magnetic fields in molecular gas is known primarily through the observation of polarized radiation from dust grains (see review by Andersson et al., 2015). Although constituting less than 1% of the gaseous mass in a star-forming galaxy (Casasola et al., 2020), dust is a crucial component of the ISM, particularly in molecular gas, as H$_2$ mainly forms on the surfaces of dust grains (Hollenbach & Salpeter, 1971; Tielens, 2005). The influence of dust on molecular gas will be further discussed in Section 1.2, and dust emission will be addressed in Section 2.3.5.

At some point, the dense cores within a GMC undergo collapse, and this can also accrete more mass from the surrounding gas, leading to the formation of a rotating disc. Many questions are still open regarding the physical processes from which dense cores form a star (see McKee & Ostriker, 2007, for a review). We know that the youngest stellar clusters in the Galaxy are closely associated with massive molecular cores (e.g. NGC 2024, NGC 1333, Ophiuchi, MonR2, and Serpens, see the review by Lada & Lada, 2003). A spectacular example is given by the Orion Nebula, the nearest active site of massive star formation (Figure 1.3, Robberto et al., 2013; McCaughrean & Pearson, 2023). Massive young stars (spectral types O and B, OB from now on) are the strongest stellar emitters of extreme-ultraviolet (EUV, $h\nu = 13.6 - 150$ eV) and far-ultraviolet (FUV, $h\nu = 6 - 13.6$ eV) photons. The EUV photons are able to dissociate molecules and ionise the gas, so that the regions immediately surrounding these stars are called HII regions (i.e. where most of H is ionised). Once the EUV photons are completely extinguished by the ISM, it begins a gaseous region called photo-dissociation region (PDR, Tielens & Hollenbach, 1985), where the FUV photons dominate the gas heating processes. We will discuss in detail about PDRs in Section 1.2.

Most of the stars in the Galaxy (and probably in the other galaxies as well) are born in clusters comprising 100 or more members (as observed in the Orion Nebula Cluster,

Figure 1.3: The Orion Nebula imaged by the HST (top right panel, from Robberto et al., 2013) and the JWST (bottom panel, from McCaughrean & Pearson, 2023). The position of the nebula is indicated by a white arrow in the Orion constellation (top left panel, image from Encyclopedia Britannica). The black square in the HST image shows the JWST image field of view, and it measures 10.95×7.45 arcmin^2, or 1.24×0.85 pc assuming a distance of 390 pc (McCaughrean & Pearson, 2023).

see Figure 1.3, and also Da Rio et al., 2009; Kroupa et al., 2018). Since we cannot observe the star formation process in real-time, one of the primary indirect methods of investigating the conversion of gas to stars is the study of the initial mass function (IMF, see fundamental works by Salpeter, 1955; Miller & Scalo, 1979; Kroupa, 2001; Chabrier, 2003) in entire galaxies or individual clusters. The IMF is a particularly powerful tool, since the evolution and observable properties of single stars are almost entirely determined by their birth mass (although being part of a binary system also plays a role). In any version of the IMF (see recent reviews by Hopkins, 2018; Smith, 2020), low-mass stars are numerous, redder in colour, and dominate the stellar mass budget of a galaxy. Conversely, the less numerous high-mass stars are bluer and dominate the galaxy luminosity (and drive the PDRs chemistry and physics, see Section 1.2.2).

The initial mass of a star also determines its lifespan. Typically, stellar clusters have a lifetime of 100 Myr[2], after which the stars disperse in the Galaxy and lose memory of their birth site (Lada & Lada, 2003). The bright bluish OB stars have a lifespan of $\sim 10 - 100$ Myr, spending most of their lives within the cluster. The other stars can live longer (e.g. the Sun's lifespan is $\sim 10^4$ Myr), with the reddest ones outliving the the current age of the Milky Way (estimated at 13.6 ± 0.8 Gyr, Pasquini et al., 2004). Stars more massive than ≈ 8 M$_\odot$ explode as core-collapse supernovae (SNe, Smartt, 2009), enriching the ISM with metals[3] (see reviews by Nomoto et al., 2013; Maiolino & Mannucci, 2019).

1.1.2 External galaxies

Up to now we have focused on clouds and stars in the Milky Way. Until the 1920s, it was still debated if this was the only galaxy (containing the whole Universe), or if the distant spiral nebulae visible with a telescope were external galaxies (this was called "The Great Debate", see Hoskin, 1976, for an historical discussion). Now we know that there are billions or trillions of other galaxies in the observable Universe. Some of them are isolated (also called *field* galaxies), while many live in groups and clusters (see e.g Yang et al., 2007; Feretti et al., 2012; Wetzel et al., 2013). Hubble (1926) was the first (but some ideas were already in Reynolds, 1920) to classify what he called "Extragalactic nebulae" into morphological types: ellipticals, spirals (normal and barred),

---

[2]To provide a comparison of these Galactic timescales, at the Sun's position (~ 8 kpc from the Galactic centre), it takes 230 Myr for a star (or a cluster) to orbit around the centre of the Galaxy (one Galactic year ago, therefore, the Earth was in the Triassic period, and dinosaurs were starting to dominate the Pangaea supercontinent).

[3]With metals we intend all the elements heavier than helium. The mass of metals divided by the total mass of an astrophysical obect is called the metallicity (Z). For reference, the metallicity of the Sun is $Z_\odot = 0.0134$ (Grevesse et al., 2010).

and irregulars. Interestingly, he noticed that three galaxies of the analysed sample, NGC 1068, NGC 4051, and NGC 4151, had nuclear emission lines in the spectra, similarly to planetary nebulae (something already observed by Fath, 1909; Slipher, 1917, for NGC 1068). He also started to use the terms "early" and "late" to define the different types of spirals, since he wanted to "express a progression from simple to complex forms". It was then assumed that galaxies evolve along the Hubble sequence from ellipticals (early-type) to spirals (late-type), which we now know it is completely not true. The morphological classification of galaxies has since then been revised to accomodate many more details in the galaxy structure (see de Vaucouleurs, 1959; de Vaucouleurs et al., 1976, 1991; Sandage, 1961, 2005; Paturel et al., 2003), but this main division still remains.

Early-type galaxies (ETGs) are characterized by lack of spiral arms, old stellar populations, red colours, and small amounts of cold gas and dust (see Cappellari, 2016, for a review). It has been found that ETGs follow several scaling relations: the intrinsic luminosity (L) of a ETG is correlated to its stellar velocity dispersion ($L \propto \sigma^4$ Faber & Jackson, 1976), and an anti-correlation exists between the surface brightness and the effective radius R_e (Kormendy, 1977). It was then discovered that these two relations are just special projections of the so-called fundamental plane of ETGs (Djorgovski & Davis, 1987; Dressler et al., 1987; Kormendy & Djorgovski, 1989). A main division (morphological and kinematical) among ETGs comes from the analysis of the different elliptical shapes of the isophotes: *disky* ellipticals appear to rotate faster than *boxy* ellipticals (Lauer, 1985; Bender, 1988; Kormendy & Bender, 1996). Also the environment in which they reside plays a role: slow rotators (i.e. the boxy ellipticals) are more often found near the centres of groups and clusters (Cappellari et al., 2011), while fast rotators (i.e. the disky ellipticals) and spiral galaxies are more likely to be found in the field or in groups (Blanton & Moustakas, 2009; Cappellari et al., 2011; Cappellari, 2013). This division is also reflected in the mass-size diagram (Figure 1.4).

Late-type galaxies (LTGs) are conversely characterized by the presence of spiral arms, young stellar populations, blue colours, and large amounts of cold gas and dust. Usually the nuclear region, called *bulge*, resembles a small ETG. A main division among spirals (already recognized by Hubble, 1926) is between barred and unbarred ones. Spiral arms are thought to be density waves of stars and gas (Lindblad, 1948, 1960; Lin & Shu, 1964). Within the arms the piling-up gas can then reach the conditions for star formation: this is why the arms shine in cold molecular emission (mostly traced by CO lines) and young stellar clusters (mostly traced by Hα), as shown in Figure 1.5. Also LTGs follow several scaling relations, the most famous being the ones between the intrinsic luminosity and the rotational velocity (the Tully-Fisher relation, see Tully & Fisher, 1977; McGaugh et al., 2000), between stellar mass and SFR (the star-forming main sequence Brinchmann et al.,
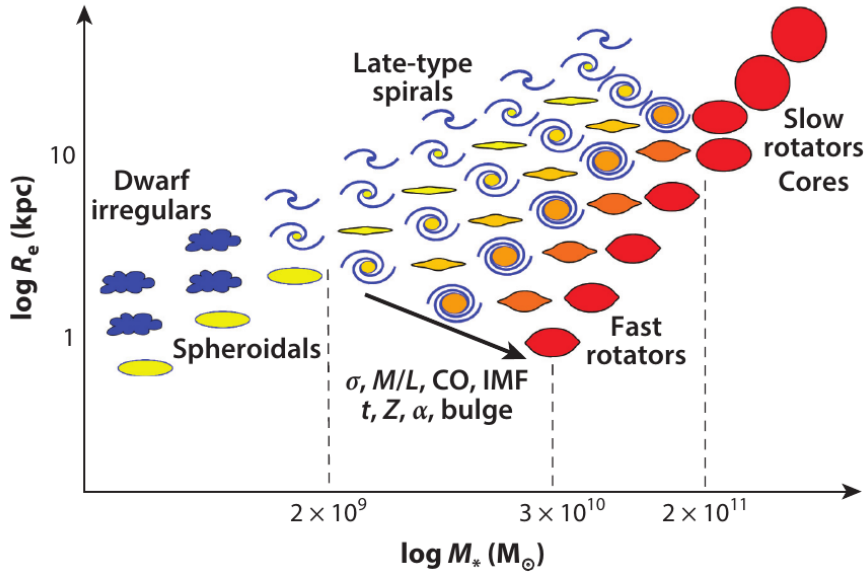
Figure 1.4: Mass-size diagram (where M_* is the stellar mass, and R_e the half-light radius). The stellar velocity dispersion σ, mass-to-light ratio M/L, CO poorness, heaviness of the IMF, age of stellar populations t, metallicity Z, fraction of α-elements, and bulge mass fraction, all increase following the black arrow. Three characteristic masses are marked with vertical black dashed lines: below $M_* \sim 2 \times 10^9$ $M_\odot$ there are no regular ETGs, $M_* \sim 3 \times 10^{10}$ $M_\odot$ there is a slope change in the ETGs mass-size relation, and above $M_* \sim 2 \times 10^{11}$ $M_\odot$ there are no spirals and the population is dominated by slow rotators with a flat core. Image from Cappellari (2016).

2004; Schiminovich et al., 2007), and between molecular mass and SFR (or their surface and volume densities, collectively known as Schmidt-Kennicutt laws, from Schmidt, 1959, 1963a; Kennicutt, 1998a,b).

From the beginning of this century, enormous amounts of high-quality data about galaxies started being collected with several surveys, as the 2dF Galaxy Redshift Survey (2dFGRS Colless et al., 2001), the Sloan Digital Sky Survey (SDSS Strauss et al., 2002), the Cosmic Evolution Survey (COSMOS Scoville et al., 2007) the Wide-Field Infrared Survey Explorer (WISE Wright et al., 2010), the Galaxy and Mass Assembly (GAMA Driver et al., 2011). One of the main results of these surveys was the discovery of a clear bimodality in the galaxy population (see Figure 1.6): one population consists of blue galaxies, with low stellar masses (M_*) and surface mass densities (μ_*), and with significant ongoing star formation; the other one consists of red galaxies, with high M_* and μ_*, and with little ongoing star formation (Strateva et al., 2001; Kauffmann et al., 2003; Baldry et al., 2004). Following the shapes on the colour-mass diagram of Figure 1.6, the two populations have been named "blue cloud" and "red sequence", respectively, with the area between them being called the "green valley" (Salim, 2014). Interestingly, both the Milky Way and M31 (the Andromeda galaxy) are in the green
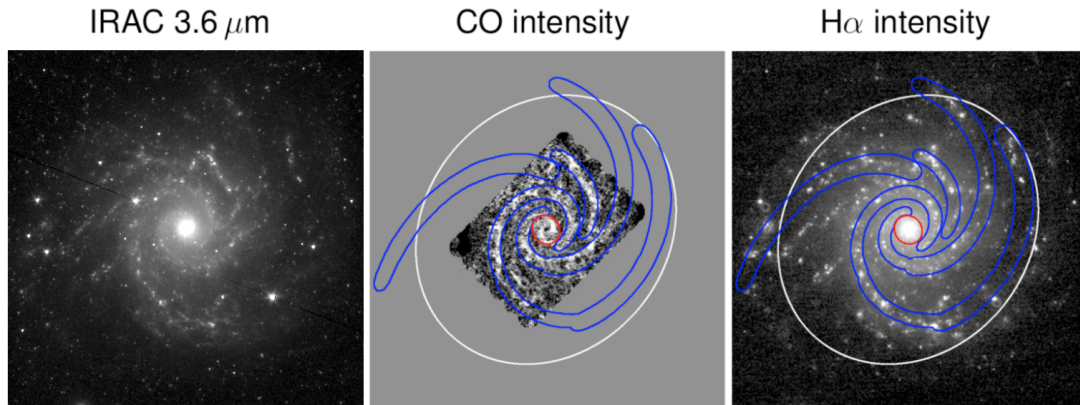
Figure 1.5: A typical spiral galaxy (NGC 628, or M74) at three different wavelengths. From left to right: 3.6 μm emission, tracing stellar mass, from the Infrared Array Camera (IRAC) onboard of the *Spitzer Space Telescope*; CO(2 − 1) emission (λ = 1.3 mm), tracing the cold molecular gas, from ALMA; Hα emission (λ = 656.3 nm), tracing ionised gas around young OB stars, from the Wide Field Imager (WFI) at the MPG 2.2-metre telescope in La Silla. Image from Querejeta et al. (2021).

valley (Bland-Hawthorn & Gerhard, 2016).

Since a stellar population passively evolves from blue to red colours, it is immediate to interpret the galaxy bimodality as an evolutionary track, where blue LTGs quickly transition to red ETGs (so inverting the original meanings of early-type and late-type). However, the real picture is more complicated than this, and it seems that ETGs and LTGs follow different evolutions: the first rapidly (∼ hundreds of Myr) quench their star formation (more rapidly for the most massive systems), probably during and after a major merger, while the latter slowly (several Gyr) transition from the blue cloud to the green valley by exhausting the cold gas reservoir (e.g. Thomas et al., 2010; Schawinski et al., 2014; Peng et al., 2015; Powell et al., 2017; Nelson et al., 2018). The exact processes that quench the galaxies are still unclear. In general, the large topic of formation and evolution of galaxies is a very complex one which is still not completely understood (as pointed by recent books and reviews, as Stark, 2016; Naab & Ostriker, 2017; Cimatti et al., 2020; Robertson, 2022).

1.1.3 Active galaxies

Among galaxies, we are particularly interested in this Thesis on a specific class known as active galaxies, or galaxies hosting an Active Galactic Nucleus (AGN). Seyfert (1943) was the first to systematically study those galaxies with high-excitation emission lines coming from their nucleus, which are now called Seyfert (Sy) galaxies (see Shields, 1999, for a more detailed history on AGN discoveries). As shown in Figure 1.7, a normal (i.e. not active) galaxy has an optical spectrum characterized by a stellar continuum and
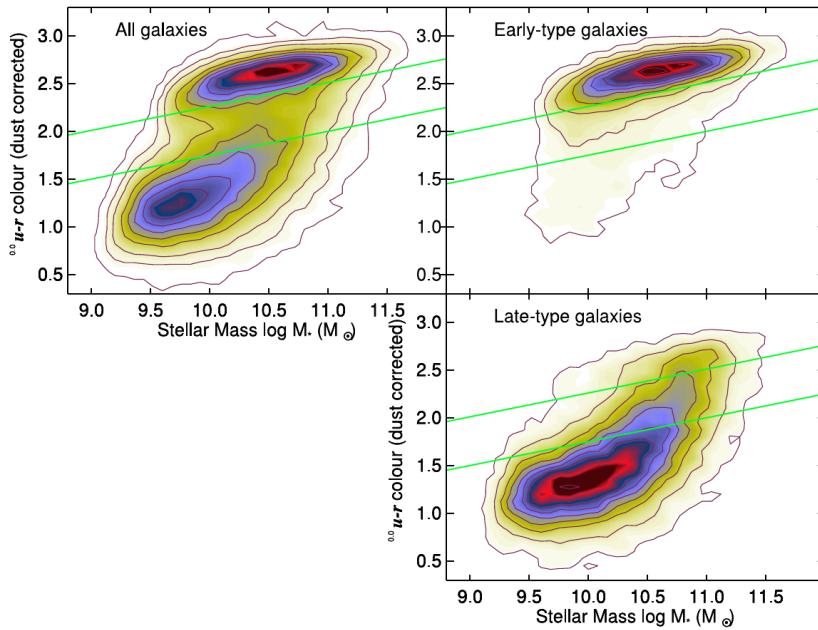
Figure 1.6: The reddening-corrected $u - r$ colour–mass diagram for the SDSS Galaxy Zoo sample (http://data.galaxyzoo.org/). The top-left panel shows all the galaxies, while the right panels show the ETGs (top) and LTGs (bottom). The green lines delimit the *green valley* defined by the all-galaxy panel. The contours are linear and scaled to the highest value in each panel. Figure from Schawinski et al. (2014).

absorption lines. If star formation is ongoing, they also present some low-excitation emission lines, as Hα ($\lambda = 6563$ Å) and Hβ ($\lambda = 4861$ Å). Seyfert galaxies show instead very bright high-excitation lines, as the [OIII] doublet ($\lambda\lambda = 4959, 5007$ Å). Seyfert (1943) also noted exceptional broadening of these lines, which he converted into velocities of the emitting gas: NGC 4151 (also shown in Figure 1.7), for example, was found to have hydrogen moving up to 7500 km s^{-1}, while [OIII] is relatively narrow (< 1800 km s^{-1}). We will discuss in Section 1.4 how to interpret these velocities.

In those same years, the development of radio telescopes by Karl Jansky (e.g. Jansky, 1933) inspired Grote Reber, an engineer and amateur radio operator, to build his own radio telescope in his backyard, with which he was the first to detect Cygnus A (at 160 MHz, see Reber, 1944, with a picture of the telescope). Cygnus A (also in Figure 1.7) was then recognized, in the optical band, as "an extragalactic affair, two galaxies in collision" by Baade & Minkowski (1954). Sources like Cygnus A were then named radio galaxies. Optical counterparts of many radio sources were still thought to be very special stars due to their point-like appearance (e.g. Matthews & Sandage, 1963). Then, thanks to a lunar occultation, 3C 273 was discovered to be a "star-like" object with the very large (for the time) redshift of $z = 0.16$ (Hazard et al., 1963; Schmidt, 1963b; Oke, 1963; Greenstein, 1963, the findings were published in *Nature* in adjoining papers by). Such
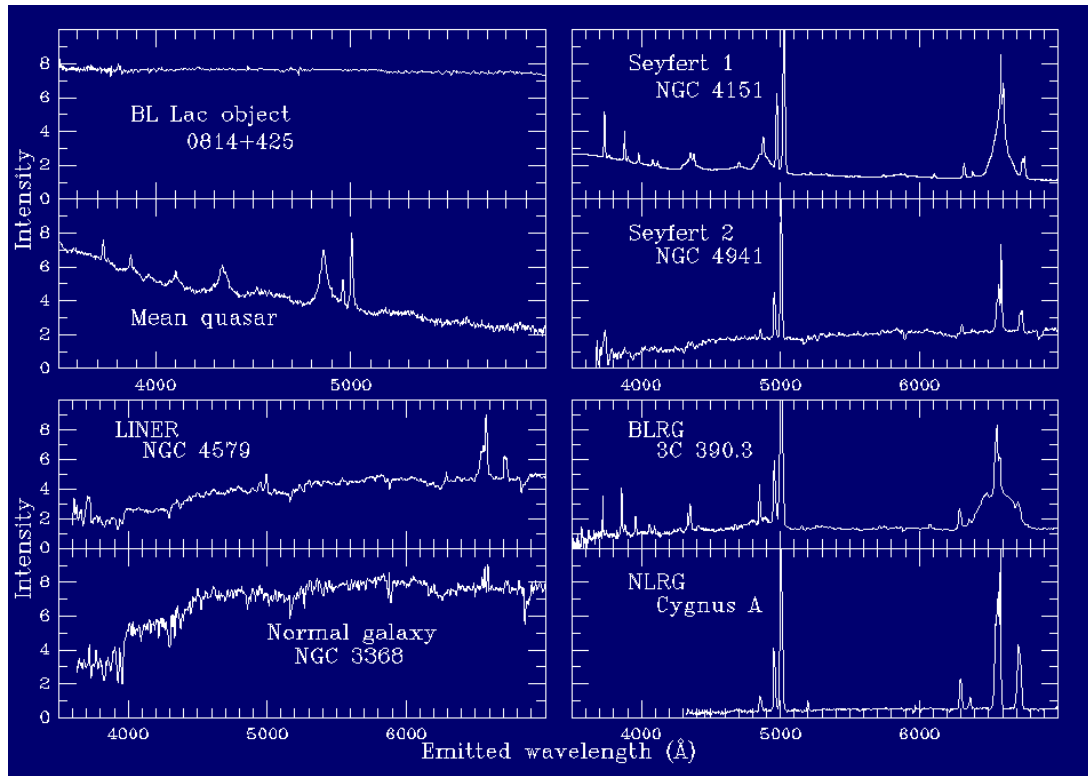
Figure 1.7: Optical spectra of various kinds of AGN. Image from `https://pages.astronomy.ua.edu/keel/agn/`.

sources became known as quasi-stellar objects (QSO), or quasars.

One year later, following the pioneering experiments of Giacconi et al. (1962), 3C 273 and M87 were the first external galaxies to be detected in X-rays (in the 1-10 keV band, by Friedman & Byram, 1967). Seyfert galaxies NGC 1275 and NGC 4151 were then detected by the first X-ray satellite, *Uhuru* (at 2-6 keV, by Gursky et al., 1971). Tucker et al. (1973) modelled the emission of NGC 5128 (the galaxy at the centre of the radio source Centaurus A), combining the $1 - 10$ keV X-ray spectrum with radio and infrared emission, deriving an obscuring column density of $N_{\mathrm{H}} = 9 \times 10^{22}$ cm^{-2}, and associating the X-ray emitter with the galaxy nucleus. Winkler & White (1975) detected a sudden increase in the X-ray flux of NGC 5128 over a six-day period, from which they calculated an emitting size of 10^{16} cm (i.e. ~ 700 AU). The quest for the power source of active galaxies was narrowing down.

From the first pioneering studies of Tonry (1984, 1987) (see also the reviews by Genzel et al., 1994; Kormendy & Richstone, 1995), to the recent achievements of Event Horizon Telescope Collaboration et al. (2019, 2022), we are all now convinced about the existence of supermassive black holes (SMBH) at the centre of galaxies. The first to speculate about their existence, and their source for AGN energy, were Hoyle & Fowler

(1963), Salpeter (1964), and Zel'dovich (1964). Lynden-Bell (1969) supported the idea, and also calculated that, given a mass accretion rate of 1 $M_\odot$ yr^{-1} and a 10% efficiency of converting mass to light, a galactic nucleus could outshine the stellar luminosity of the whole galaxy ("Can this be the explanation of the Seyfert galaxies?"). He then modelled an accretion disc around the SMBH, predicting a disc temperature of $\sim 10^5$ K. Notably, he also suggested that the centre of the Milky Way would host a SMBH of $\sim 3 \times 10^7$ $M_\odot$.

The fact that black holes can power some of the most luminous sources in the Universe may sound counter-intuitive, and it needs some explanation. Detailed calculations can be found in, e.g., Netzer (2006); we refer also to Netzer (2015) for a recent review on the AGN models. The concentration of such a high mass ($10^6 - 10^{10}$ $M_\odot$) in a small radius ($0.02 - 200$ AU), causes the surrounding gas, as it falls in, to lose a tremendous amount of gravitational potential energy and angular momentum. The falling gas can efficiently transfer angular momentum out by forming an accretion disc (Shakura & Sunyaev, 1973; Abramowicz & Fragile, 2013), or can be accreted less efficiently in an advection-dominated flow (Ichimaru, 1977; Yuan & Narayan, 2014). The disc/flow releases then the energy by radiating it, mostly as blackbody radiation peaking in the UV band (as predicted by Lynden-Bell, 1969). Based on the physics of the solar corona, Liang & Price (1977) proposed the existence of an X-ray emitting corona for the Galactic X-ray binary Cygnus X-1, and then Liang & Thompson (1979) applied it to AGN. The corona is made of very hot (10^8 K) gas layers sandwiching the accretion disk, where electrons up-scatter the disk photons to X-ray wavelengths through the inverse Compton process. This X-ray emission (first observed by Friedman & Byram, 1967) seems to be ubiquitous in AGN (except in heavily obscured sources, see e.g. Comastri et al., 2015).

At larger distances ($\sim 0.01 - 1$ pc), dense ($\sim 10^{10}$ cm^{-3}) fast-moving clouds (firstly postulated by Woltjer, 1959) produce the broad hydrogen emission lines observed by Seyfert (1943): this region is called the broad-line region (BLR), to distinguish it from the larger ($\sim 10^2 - 10^3$ pc) and sparser ($\sim 10^3 - 10^4$ cm^{-3}) narrow-line region (NLR, firstly defined by Shields, 1974). The fact that some sources (e.g. NGC 1566, NGC 4151, NGC 5548) displayed broad lines, and some others (e.g. NGC 1068, NGC 1667, NGC 4941) did not, was puzzling. Khachikian & Weedman (1974) collected a sample of 71 Seyfert galaxies, and classified them into class 1 (where the Balmer lines are broader than the forbidden lines) and class 2 (where the two have the same width). Rowan-Robinson (1977) postulated about the BLR being obscured by dust. Antonucci & Miller (1985), using a spectropolarimeter at the Lick Observatory, discovered that the polarized optical spectrum of NGC 1068 (a Seyfert-2 galaxy) showed broad (~ 7500 km s^{-1}) Balmer lines ("They look like the spectra of a Seyfert Type 1 object!"). The polarized emission was immediately interpreted as light scattered by electrons above

13
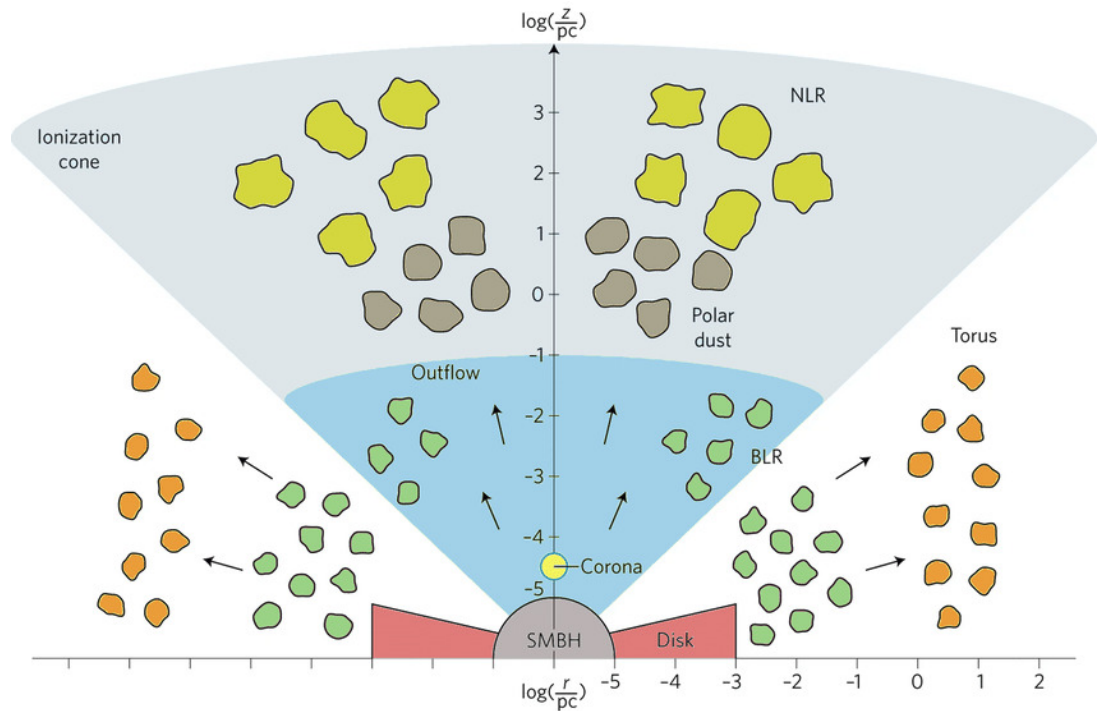
Figure 1.8: Schematic view of the main AGN structures seen along the equatorial (*x*-axis) and polar (*y*-axis) directions in logarithmic scale. Image from Ramos Almeida & Ricci (2017).

some obscuring disc, optically and geometrically thick, that should contain the BLR when seen at high inclinations. This was soon pictured as a torus of gas and dust (e.g. MacAlpine, 1985), also supported by the first discovery of ionisation cones (Pogge, 1988). A sketch, in logarithmic scale, of most of the AGN structures so far described, is shown in Figure 1.8.

The discovery of the torus, and so of the dependance of the relative inclination of it with the observer's line of sight, led to the so-called Unified Model for AGNs (Antonucci, 1993; Urry & Padovani, 1995; Netzer, 2015). Due to its small size ($\sim 0.1 - 10$ pc), direct observations of the torus had to wait until the advent of mid-infrared (mid-IR, $7 - 26\,\mu$m) interferometry: these showed the presence of an unresolved compact ($\sim 1 - 10$ pc) source (e.g. Burtscher et al., 2013) plus an extended polar component, which ultimately accounts for most of the mid-IR emission (Hönig et al., 2013; Tristram et al., 2014; López-Gonzaga et al., 2014). More recently, sub-mm interferometric observations made with the Atacama Large Millimeter/submillimeter Array (ALMA) made possible to resolve the cold dust emission of the torus, together with its molecular emission (García-Burillo et al., 2016; Imanishi et al., 2016). The molecular gas of the torus is then usually connected to the central reservoirs of molecular gas of the host galaxy (Izumi et al., 2018; Alonso-Herrero et al., 2019, 2021; Combes et al., 2019), and there is evidence of molecular tori not only rotating but also outflowing (García-Burillo et al., 2014a; Gallimore et al., 2016;

Alonso-Herrero et al., 2018, 2023). In Chapter 4, we will present a similar case.

In ∼ 10% of the AGN population, for reasons that are not yet completely understood, very fast and collimated streams of plasma, called "relativistic jets", originate from the vicinity of the SMBH, and travel up to several Mpc (way beyond the host galaxy), releasing over 10^{40} erg s^{-1} in the radio band (see reviews by Tadhunter et al., 2014; Blandford et al., 2019). These objects are called radio-loud AGN, and are mostly hosted in ETGs. In this Thesis we will primarily focus on radio-quiet AGNs. However, we want to highlight that the historical distinction between radio-loud and radio-quiet may not describe correctly the existence of two separate AGN populations, as pointed out by recent works (see e.g. Barvainis et al., 2005; Broderick & Fender, 2011; Nyland et al., 2020).

Numerous questions regarding AGNs remain open and constitute active fields of research today. The detection of massive quasars at $z \gtrsim 7$ (Mortlock et al., 2011; Bañados et al., 2018; Yang et al., 2020; Wang et al., 2021; Bogdán et al., 2023), raises a fundamental mystery: the rapid growth of black holes from stellar masses (Chandrasekhar, 1931; Oppenheimer & Volkoff, 1939) to the supermassive stage (∼ $10^6 - 10^{10}$ M$_\odot$) in less than a Gyr. This enigma is commonly referred to as black hole *seeding* (see Shapiro, 2005; Volonteri et al., 2008; Lupi et al., 2014; Latif & Ferrara, 2016, and references therein). Just outside the black hole, the intricate physics governing the production and maintenance of jets and winds, along with the respective roles of black hole spin, magnetic fields, and infalling gas properties, are still unknown (Tchekhovskoy & Bromberg, 2016; Blandford et al., 2019; Lister et al., 2021; Marcotulli et al., 2022). On a larger scale, the understanding of the torus has undergone several changes (e.g. Alonso-Herrero et al., 2021, and references therein). However, the precise influence of nuclear obscuration on observed AGN properties and its impact on quantifying the AGN population remains elusive (Vignali et al., 2010; Hickox & Alexander, 2018; Ricci et al., 2023; Sengupta et al., 2023). Further away from the SMBH, interactions between the AGN with the host galaxy further complicate the picture, as we will see in Sections 1.2.3, 1.3 and 1.4.

1.2 The molecular gas

Thanks to the efforts of the DustPedia project[4] (Davies et al., 2017), we know that in a typical nearby star-forming galaxy (SFG), approximately $10 - 40\%$ of the baryonic mass forms the ISM, while the rest is encapsulated in stars, planets, and black holes. The gas

---

[4]The DustPedia project is a multiwavelength study of cosmic dust in nearby galaxies
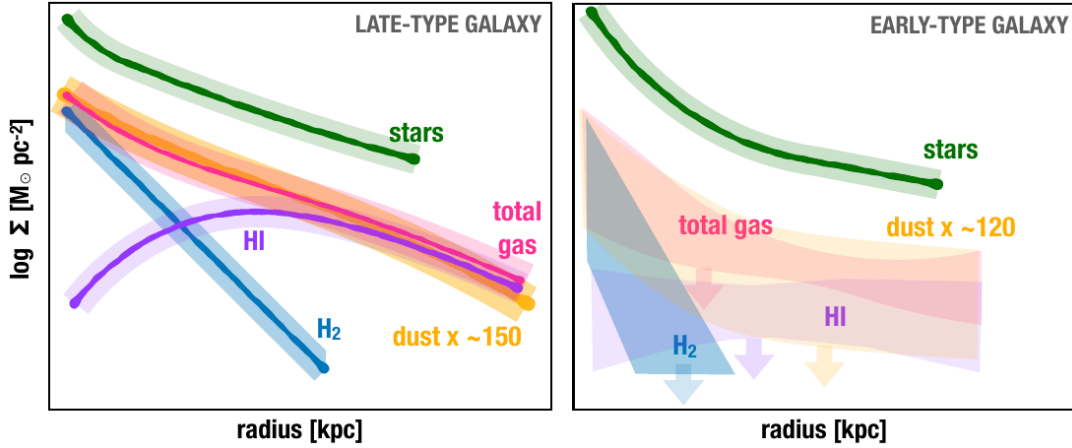
Figure 1.9: Radial distribution of stars, dust and total gas, further broken up into its atomic (HI) and molecular (H$_2$) components, for local LTGs and ETGs (left and right panels, respectively). Dust curves are scaled up by typical gas-to-dust ratios. Image from Saintonge & Catinella (2022).

is roughly 50% molecular and 50% atomic (Casasola et al., 2020). Despite ionised gas dominating the volume, its overall low density ($10^{-3} - 10^{-1}$ cm^{-3}) contributes minimally to the gas mass budget (e.g. Saintonge & Catinella, 2022): For instance, HII regions like the Orion Nebula (Figure 1.3) typically consist of ~ 50 M$_\odot$ pockets of hot gas surrounded by $10^3 - 10^5$ M$_\odot$ of cold, atomic and molecular, gas (Shields, 1990). Dust particles, mixed with the cold gas (as they sublimate above $1200 - 1900$ K Barvainis, 1987), constitute less than 1% of the mass budget (e.g. Casasola et al., 2020).

The molecular gas is predominantly cold and composed of $\sim 100\%$ H$_2$, the most abundant molecule in the Universe. Unfortunately, H$_2$ is a nonpolar molecule, i.e. it lacks an internal electric field due to the presence of two identical atoms. Consequently, it cannot undergo dipolar rotational transitions. H$_2$ can be observed through the emission of quadrupole rotational lines, with the lowest-energy transition being the $0 - 0$ S(0) at $\lambda = 28.22$ μm, or through vibrational lines, with the lowest-energy transition being the $1 - 0$ S(0) at $\lambda = 2.22$ μm. However, these transitions have long decay lifetimes and high excitation temperatures, typically occurring in gas where $T \gtrsim 100$ K (see Shull & Beckwith, 1982; Dabrowski, 1984). This high temperature is more characteristic of shock-heated regions (Ogle et al., 2010; Guillard et al., 2012; Pereira-Santaella et al., 2022). Cold H$_2$, on the other hand, is practically invisible in emission but it can be seen in absorption, albeit only in the Solar neighbourhood (Jura, 1975; Rachford et al., 2002) or in damped Ly-α systems (Ledoux et al., 2003; Wolfe et al., 2005; Noterdaeme et al., 2008).

After hydrogen and helium (which does not form molecules), carbon and oxygen are the most common atoms in the Universe (their abundances being 2.7×10^{-4} and

4.9×10^{-4}, respectively, see Grevesse et al., 2010). Unlike H_2, carbon monoxide (CO)[5] is a polar molecule with a very weak permanent dipole moment of 0.12 D (Scuseria et al., 1991). This characteristic allows it to undergo dipolar rotational transitions, and indeed, these CO lines are the primary source of information for the bulk of the molecular gas in the Universe. Due to its astronomical significance, the next subsection is dedicated to delving into the details of the excitation and emission of CO.

1.2.1 CO excitation and emission

Since it is a polar molecule, CO exhibits dipolar rotational transitions with the selection rule $\Delta J = \pm 1$, where J is the rotational quantum number. The energy of the rotational state J is usually approximated[6] as

$$E_{\mathrm{rot}} = \frac{J(J+1)\hbar^2}{2I} \quad , \tag{1.3}$$

where I is the moment of inertia of the molecule and $\hbar$ is the reduced Planck constant. The CO rotational lines are collectively called the CO *ladder* (due to their regularly spaced frequencies, see Table 1.1), and they are the main coolants of fully molecular gas. It is customary to break down the CO ladder into three different regions (see e.g. Vallini et al., 2019; Decarli et al., 2020). The low-J lines ($J_{\mathrm{upp}} \leq 3$) mainly trace the cold ($T \approx 20 - 50$ K), low-density ($n \leq 10^3$ cm^{-3}) gas; in normal ISM conditions, this is where the majority of the molecular mass resides, making these lines good tracers of the total molecular gas mass in galaxies (Bolatto et al., 2013). Both the mid-J ($4 \leq J_{\mathrm{upp}} \leq 7$, still observable from ground-based telescope for low-z sources) and the high-J ($J_{\mathrm{upp}} \geq 8$) lines originate from increasingly denser ($n \approx 10^4 - 10^6$ cm^{-3}) and warmer ($T \approx 100 - 500$ K) molecular gas (e.g. Greve et al., 2014). For this reason, the excitation of the CO ladder, especially in the mid/high-J region, can be exploited to disentangle different heating sources such as radiation from star formation, AGN accretion, and mechanical heating from shocks (see e.g. van der Werf et al., 2010; Mingozzi et al., 2018). CO($1 - 0$) is by far the most observed molecular line (from Wilson et al., 1970, observations with the NRAO 12 m antenna), and its emission has been systematically used to estimate the molecular mass in Galactic GMCs and in external galaxies (see reviews by Omont, 2007; Heyer & Dame, 2015; Tacconi et al., 2020; Saintonge & Catinella, 2022, and references therein).

---

[5]If not stated differently, with CO we always mean the most common isotopologue ^{12}C^{16}O.

[6]In reality, as centrifugal forces increase with J, the distance between the atoms also increases, thereby altering I, so that frequencies become slightly less spaced than 115.27 GHz. This phenomenon can be harnessed to accurately determine the redshift of a source based on two CO lines (e.g. Weiß et al., 2009).

Table 1.1: Fundamental parameters of the first 13 rotational CO lines

Line	ν [GHz]	λ [μm]	T_{ex} [K]	A [s^{-1}]	n_{crit} [cm^{-3}]
CO(1 − 0)	115.27	2600.8	5.5	7.20e-08	2.18e+03
CO(2 − 1)	230.54	1300.4	16.6	6.91e-07	2.29e+04
CO(3 − 2)	345.80	866.96	33.2	2.50e-06	3.50e+04
CO(4 − 3)	461.04	650.25	55.3	6.13e-06	1.19e+06
CO(5 − 4)	576.27	520.23	83.0	1.22e-05	2.43e+05
CO(6 − 5)	691.47	433.56	116.2	2.14e-05	2.69e+05
CO(7 − 6)	806.65	371.65	154.9	3.42e-05	1.10e+07
CO(8 − 7)	921.80	325.23	199.1	5.13e-05	5.37e+06
CO(9 − 8)	1036.9	289.12	248.9	7.33e-05	1.18e+06
CO(10 − 9)	1152.0	260.24	304.2	1.01e-04	1.24e+06
CO(11 − 10)	1267.0	236.61	365.0	1.34e-04	1.38e+08
CO(12 − 11)	1382.0	216.93	431.3	1.73e-04	2.78e+07
CO(13 − 12)	1496.9	200.27	503.1	2.20e-04	1.76e+07

Notes. Data from the Leiden Atomic and Molecular Database (Schöier et al., 2005), with n_{crit} calculated for collisions with H_2 at T_{gas} = 10 K.

The different rotational levels are populated based on collisions, typically with H_2 molecules, and interactions with the radiation field. Once excited to a certain $J > 0$ level, CO can return to the ground state through radiative or collisional de-excitation. The Einstein coefficients (listed in Table 1.1, see Einstein, 1916) provide the probability for radiative de-excitation. These coefficients do not depend on the state of the gas but solely on the quantum properties of the molecule. Their inverses can serve as a measure of the average time to wait for spontaneous emission. For example, once CO is excited to the level $J = 1$, it takes, on average, $\tau_{1-0} = 1/A_{1-0} \approx 161$ days before emitting a CO(1 − 0) photon and returning to the ground ($J = 0$) level. During this time, given the availability of collisional partners, CO can also transition back to the ground level through collisional de-excitation, which, conversely, depends on the state of the gas. A key quantity is the critical density n_{crit} (also in Table 1.1), i.e. the density at which collisional de-excitation (dependent on the kinetic temperature of the collisional partners) counterbalances spontaneous radiative de-excitation. For densities $n \ll n_{crit}$, the cooling rate is proportional to n^2, while for $n \gg n_{crit}$, the cooling rate becomes proportional to n and the rotational levels are thermalized. This means that they are populated according to the Boltzmann distribution, and the gas is in local thermodynamic equilibrium (LTE).

Another crucial quantity is the optical depth τ_ν, a measure of how much radiation (at frequency ν) is absorbed along its path (e.g. Condon & Ransom, 2016). It can be demonstrated that, for a given $J \rightarrow J - 1$ transition, $\tau_J \propto N_J/\Delta v$, where N_J is the column density of CO molecules in the J level, and Δv is the velocity width of the

line, encompassing both thermal and turbulent broadening (Bolatto et al., 2013; Wolfire et al., 2022). The emitted line is considered optically thick if $\tau_J \gg 1$ and optically thin if $\tau_J \ll 1$. In the optically thin case, we can directly determine N_J from the observed line intensity and then convert it to the more useful N_{H_2}, from which we calculate the molecular mass M_{mol}. However, under typical GMC conditions, the CO$(1-0)$ line rapidly becomes optically thick after CO becomes the primary carbon reservoir (Bolatto et al., 2013). This implies that CO$(1-0)$ photons are readily absorbed by other CO molecules before reaching the edge of the GMC, a phenomenon known as line trapping or radiative trapping. This, in turn, reduces the effective n_{crit}, making the CO$(1-0)$ emission bright already at $n \sim 10^2 - 10^3$ cm^{-3} (e.g. Shirley, 2015; den Brok et al., 2021).

Since the CO$(1-0)$ line is optically thick (and the same applies to the other low/mid-J lines, see Narayanan & Krumholz, 2014), estimating M_{mol} from its observed intensity is not straightforward. By applying the virial theorem, Dickman et al. (1986), Solomon et al. (1987) and Scoville et al. (1987) found a strong correlation between M_{mol} and the CO luminosity (L_{CO}). This correlation led to the introduction of a CO-to-H$_2$ conversion factor (see the extensive review by Bolatto et al., 2013). This conversion factor can be expressed as a mass-to-light ratio, defined as $\alpha_{CO} \equiv M_{mol}/L_{CO}$, in M$_\odot$ (K km s^{-1} pc^{-2})$^{-1}$ units. Alternatively, it can be expressed as the ratio between the observed intensity and the H$_2$ column density, i.e. $X_{CO} \equiv N_{H_2}/I_{CO}$, in cm^{-2} (K km s^{-1})$^{-1}$ units. Both are referred to as CO-to-H$_2$ conversion factors. The values typically adopted for the MW are $\alpha_{CO} = 4.3$ M$_\odot$ (K km s^{-1} pc^{-2})$^{-1}$, corresponding to $X_{CO} = 2 \times 10^{20}$ cm^{-2} (K km s^{-1})$^{-1}$ (Bolatto et al., 2013).

The intensity of the different CO lines can be plotted against their J numbers (or their frequencies), forming the CO spectral line energy distribution (SLED). Over the last 15 years, particularly following the launch of the *Herschel* Space Observatory (Pilbratt et al., 2010a), the CO SLED has been observed in numerous galaxies, and it has become a crucial tool for probing the physical state of molecular gas (e.g. Dannerbauer et al., 2009; Papadopoulos et al., 2010; Carilli & Walter, 2013; Kamenetzky et al., 2014; Rosenberg et al., 2015; Saito et al., 2017; Vallini et al., 2018; Valentino et al., 2020; Pensabene et al., 2021). One significant finding has been that the CO SLED does not appear to be thermalized, even in the extremely luminous starbursting systems known as submillimetre galaxies (SMGs, see Figure 1.10 and Narayanan & Krumholz, 2014).

The shape of the CO SLED can be estimated by computing the radiative transfer (RT) of external radiation onto the molecular gas. As illustrated in Figures 1.2-1.3, molecular clouds are often found in proximity to clusters of young OB stars, which emit a significant amount of UV radiation. The EUV photons are extinguished by the HII regions surrounding the stars (also known as Strömgren spheres, see Strömgren, 1939).
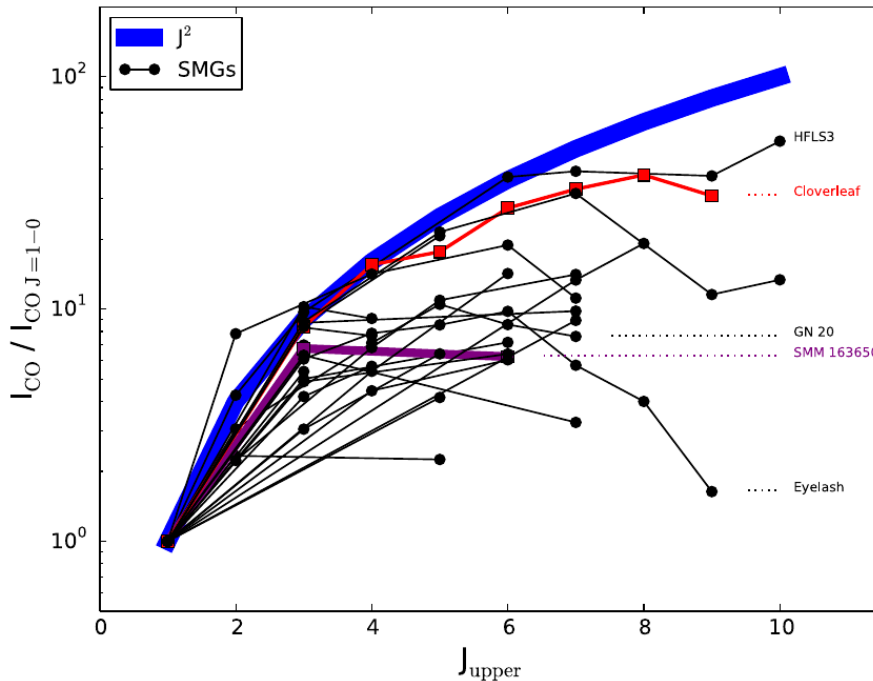
Figure 1.10: CO SLEDs of high-z submillimetre galaxies (SMGs). The intensities on the y-axis are normalized by the CO(1 − 0) intensity. The blue line denotes J^2, the scaling of intensities expected in the LTE case. Red and purple lines denote the Cloverleaf quasar and SMG SMM 163650, respectively. Image from Narayanan & Krumholz (2014).

Conversely, FUV photons impact the more distant atomic and molecular gas, creating a photo-dissociation region (PDR Tielens & Hollenbach, 1985). PDRs essentially encompass all the neutral and molecular phases of the ISM within a star-forming galaxy. Additionally, X-ray radiation from the AGN also impacts the molecular gas, creating an X-ray dominated region (XDR Maloney et al., 1996). In the next two sections we describe in detail these two regions, and eventually, we present the most commonly used PDR and XDR numerical codes.

1.2.2 Photo-dissociation regions (PDRs)

Photo-dissociation regions (PDR) are ISM regions in which FUV photons (6 eV $< h\nu <$ 13.6 eV), mostly emitted by OB stars, play a crucial role in influencing the structure, chemistry, thermal balance, and evolution of the gas. In PDR studies, it is customary to normalize the incident FUV radiation to that measured in the Solar neighbourhood, referred to as the interstellar radiation field (ISRF) or Habing field. This field has been measured as 1.6×10^{-3} erg cm^{-2} s^{-1} (Habing, 1968), and it is denoted as G_0, such that the ISRF is $G_0 = 1$. Another convention involves using visual extinction (A_V, in mag) or the hydrogen nucleus column density (N_H, in cm^{-2}, only column density from now
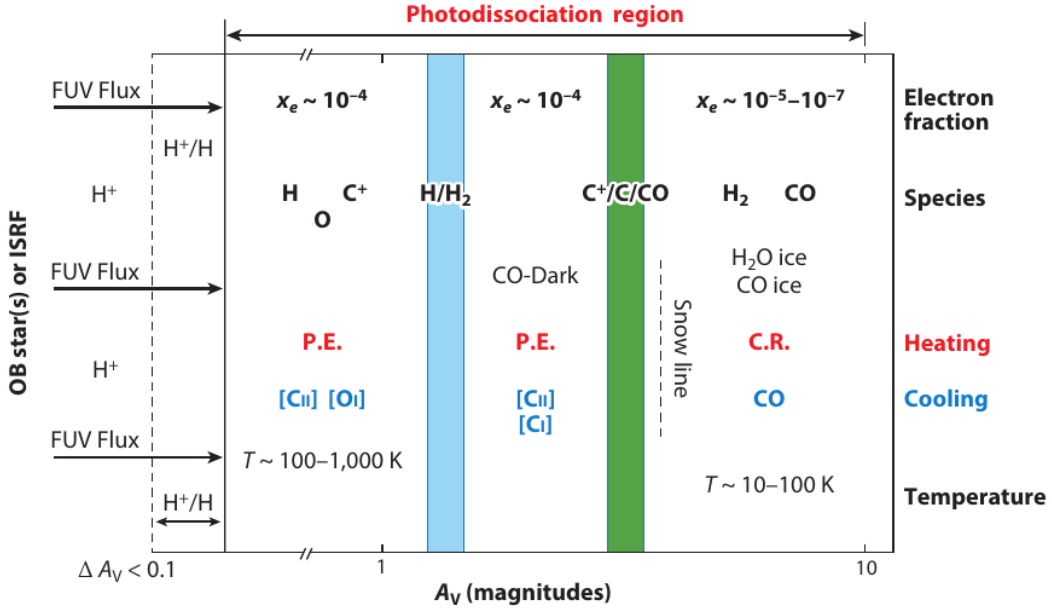
Figure 1.11: Schematic diagram of a PDR as a function of the visual extinction A_V (see Equation 1.4 for converting between A_V and N_H). The PDR is illuminated from the left. The high values of the electron fraction (x_e) are provided by photoionisation of C to C^+. Heating sources within the PDR are the photoelectric effect (P.E.) and cosmic rays (C.R.). Atoms and molecules freeze out on dust grains beyond the snow line. Lower/higher G_0/n values move the H/H_2 and C^+/C/CO transitions to lower/higher A_V. Figure from Wolfire et al. (2022).

on) to measure the penetration depth of FUV photons into a gas cloud. For a standard Galactic interstellar extinction curve with $R_V = A_V/E(B-V) = 3.1$, where $E(B-V)$ is the colour excess, we can easily convert between A_V and N_H:

$$N_H = N_{HI} + 2N_{H_2} \approx 1.9 \times 10^{21} A_V \ \text{cm}^{-2} \quad , \tag{1.4}$$

where we have explicitly accounted for the two gas phases within N_H. To convert N_H to cloud depth (d, in pc), the gas volume density n is needed, so that $d = N_H/n$.

The external layer of a PDR (see Figure 1.11) is typically devoid of molecules, as they are photodissociated by FUV photons. Specifically, H_2 dissociates $\sim 10\%$ of the time when exposed to Lyman-Werner photons ($912 < \lambda < 1108$ Å). Meanwhile, the remaining $\sim 90\%$ of the time, it emits back a UV photon and cascades through vibration and rotation levels, emitting IR lines (see Shaw et al., 2005, for the emitted spectrum). CO always dissociates when exposed to FUV photons, but it can be shielded by the most numerous H_2. Depending on whether their ionisation potential is above or below 13.6 eV, free atoms could be neutral (e.g. H, He, N, O) or singly ionised (e.g. C, Si, S). The largest molecules in the ISM are not easily photodissociated: among these the most famous are the polycyclic aromatic hydrocarbons (PAHs), a class of organic compounds (see

Tielens, 2008, for a review). PAHs and small dust grains absorb FUV photons and emit an electron through the photoelectric effect, and the kinetic energy of the photoelectron is the main source of gas and dust heating in PDRs (Draine, 1978; Tielens & Hollenbach, 1985). Dust cools by emitting continuum radiation (see Galliano et al., 2018, for a recent review), while gas cools by line radiation. In the most external layer, the main coolants are the fine structure lines of [CII] ($^2P_{3/2} -^2 P_{1/2}$) at 158 μm, and [OI] ($^3P_1 -^3 P_2$) at 63 μm and ($^3P_0 -^3 P_1$) at 146 μm.

Deeper into the PDR, dust opacity diminishes the FUV radiation, and at $A_V \sim 1 - 2$, there is the transition between HI and H_2. This is where the GMC begins. Here, H atoms meet and react on the surface of dust grains to form H_2 (via a process called adsorption Hollenbach & Salpeter, 1970; Cazaux & Tielens, 2004, 2010). Beyond this transition lies a CO-dark region, in which the main coolants are the fine structure lines of [CI] ($^3P_2 -^3 P_1$) at 370 μm and ($^3P_1 -^3 P_0$) at 609 μm, and the [CII]$_{158\mu m}$ line (Grenier et al., 2005; Wolfire et al., 2010).

The C^+/C/CO transition occurs further deep, at $A_V \sim 2 - 4$: there, CO can form mainly by reactions of CH or CH_2 with O, or of SiO with C^+ (Tielens & Hollenbach, 1985; Osterbrock & Ferland, 2006). External FUV radiation cannot penetrate there, and the gas is heated by collisions with dust grains, or, most importantly, by cosmic-ray ionisation. Cosmic rays are high-speed particles, probably accelerated in AGNs or supernovae (or even in protostars, see Padovani et al., 2015, 2016). Thanks to their high kinetic energy, they can penetrate deeper than photons into molecular clouds, ionising atoms and molecules and activating a rich chemical network (see reviews by Strong et al., 2007; Blasi, 2013). The gas in this fully molecular region is cooled by rotational transitions of CO (Table 1.1).

1.2.3 X-ray dominated regions (XDRs)

The ISM regions in which X-ray photons ($0.1 - 100$ keV) dominate the heating of the gas and influence the chemical composition are referred to as X-ray dominated regions (XDRs). As illustrated in Figure 1.9, molecular gas predominates in the inner regions of galaxies, typically up to $\sim 3 - 5$ kpc from the centre (Casasola et al., 2017). We, therefore, expect a central X-ray emitter such as the AGN, to impact the molecular gas excitation. X-ray photons can penetrate the molecular gas to larger column densities compared to FUVs, and they are capable of heating the gas to higher temperatures and enhancing the abundance of molecular ions (Wolfire et al., 2022, and references therein). For these reasons, the concept of XDR (firstly defined by Maloney et al., 1996), has been introduced. Seminal works on the effect of X-rays on molecular gas in GMCs and in
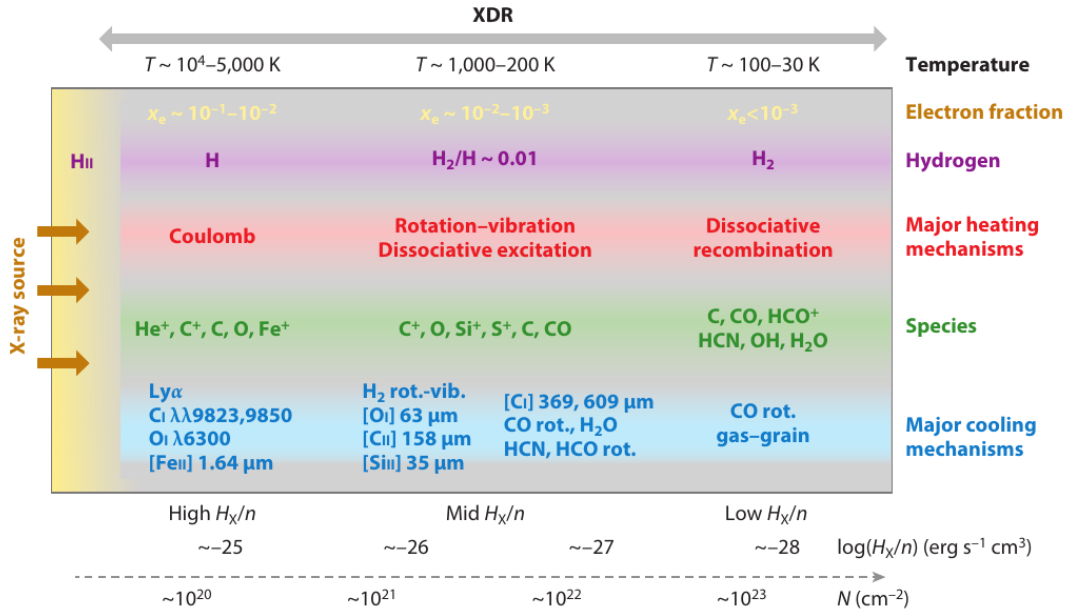
Figure 1.12: Schematic 1D structure of an XDR as a function of the column density N and of the ratio of the energy deposition rate per particle to the gas density H_X/n (calculated by assuming an incident $F_X \approx 100$ erg s^{-1} cm^{-2} and $n = 10^5$ cm^{-3}). The XDR is illuminated from the left. Major heating and cooling processes, and approximate temperatures, electron fractions, and chemical compositions are given in three representative regions at different depths. Image from Wolfire et al. (2022).

the torus of Seyfert galaxies include Krolik & Kallman (1983); Lepp & McCray (1983); Krolik & Begelman (1988); Krolik & Lepp (1989).

Figure 1.12 displays a schematic view of a typical XDR. The structure of an XDR can be parametrized in terms of the ratio between the energy deposition rate per particle (H_X, in units of erg s^{-1}) and the gas density n. This is because heating and molecular destruction rates induced by X-rays are proportional to nH_X, while cooling and molecular formation rates are proportional to n^2. Therefore, at equilibrium, the thermal and chemical conditions are governed by the ratio H_X/n (Maloney et al., 1996).

X-rays interact with matter differently depending on their energy. Photons with $h\nu \lesssim 10$ keV are absorbed; at higher energies, Compton scattering (Compton, 1923) dominates. Absorbed X-ray photons ionise heavy elements typically by removing a K-shell electron (the one closest to the atomic nucleus), which then initiates a cascade of radiative (fluorescent) and nonradiative transitions (Hardouin Duparc, 2009, Auger-Meitner electrons). The latter are called primary photoelectrons, as they are typically energetic enough (~ 1 keV) to induce secondary ionisations, resulting in the ejection of secondary photoelectrons. If the electron fraction is relatively high ($x_e > 0.1$, left side of Figure 1.12), almost all the X-ray energy goes into heating through Coulomb collisions between secondary photoelectrons and the ambient electrons. This heating could lead

to temperatures of $T \approx 10^4$ K (Swartz et al., 1971; Dalgarno et al., 1999; Wolfire et al., 2022).

Deeper in the XDR, where $x_e \lesssim 0.01$, if the gas is predominantly atomic ($x_{H_2} \ll 1$), $\approx 40\%$ of the energy deposited by X-rays goes into the production of FUV photons, nearly all of which are Lyα (Maloney et al., 1996). Since Lyα photons ($h\nu = 10.2$ eV) lack sufficient energy to ionise carbon, the C$^+$/C/CO transition is less abrupt than in PDRs, with CO dominating from $N_H \approx 10^{22} - 10^{23}$ cm^{-2}(Meijerink & Spaans, 2005). Most of this internally generated FUV field is absorbed by dust and emitted as IR continuum, similar to PDRs. However, gas in XDR typically receives higher heating than dust grains compared to PDRs, resulting in a larger ratio of cooling lines to IR continuum (Maloney et al., 1996). Once the gas becomes molecular ($x_{H_2} \approx 50\%$), the warm temperatures ($T \approx 10^3$ K) favour the excitation of H$_2$ rovibrational transitions, significantly contributing to the cooling (Neufeld & Kaufman, 1993; Spaans & Meijerink, 2008; Lique, 2015).

At lower temperatures ($T \lesssim 500$ K), the primary coolants become the [OI]$_{63\mu m}$, [SiII]$_{35\mu m}$, and [CII]$_{158\mu m}$ (Maloney et al., 1996; Meijerink et al., 2007). The [OI]$_{63\mu m}$ cooling is particularly efficient due to oxygen being neutral at warm temperatures. Consequently, XDRs are characterized by high [OI]/[CII] ratios ($\gtrsim 10$) with respect to $\lesssim 10$ in PDRs (Maloney et al., 1996; Hollenbach & Gorti, 2009). At the same depth, high-J CO lines provide significant cooling due to the higher $T \approx 200$ K (see Table 1.1), in contrast to PDRs where the molecular gas is typically at $T \approx 20$ K. Other molecular coolants of XDRs include H$_2$O, HCN, HCO$^+$, HNC, and OH. The HCN/HCO$^+$ and HNC/HCN ratios have been proposed as XDR diagnostics (Imanishi et al., 2007; Meijerink et al., 2007; Baan et al., 2008; Loenen et al., 2008; Krieger et al., 2020), but with many caveats (see discussions in Aalto et al., 2007; Costagliola et al., 2011; Cañameras et al., 2021).

1.2.4 PDR and XDR codes

Reproducing the shape of the CO SLED, i.e. the relative intensity of CO lines at different J levels, is a complex task when studying a specific galaxy, or a class of objects. The typical approach involves employing numerical codes capable of self-consistently solving the equations of radiative transfer, statistical equilibrium, charge conservation, and energy conservation. These codes utilize various approximations to handle extensive calculations (which can be taxing for a rich chemical network). Despite their differences, the fundamental philosophy is the same: users input certain physical parameters such as metallicity, relative abundances, and the cosmic ray ionisation rate. Subsequently, the

code runs a grid of models by varying the gas density n and the incident FUV radiation G_0. Prominent PDR and XDR codes include: `UCL-PDR` (Bell et al., 2006; Priestley et al., 2017), and its evolution `3D-PDR` (Bisbas et al., 2012; Gaches et al., 2019), `PDR Toolbox` (Pound & Wolfire, 2008, 2023), which contains `Kosma-τ` (Röllig et al., 2006, 2013) `Meudon PDR code` (Le Petit et al., 2006; Bron et al., 2014), `Leiden PDR-XDR code` (Meijerink & Spaans, 2005; Meijerink et al., 2007) and `Cloudy` (Ferland et al., 1998; Chatzikos et al., 2023). We refer to Röllig et al. (2007) for a comparison of different PDR codes. Other commonly used numerical codes for estimating molecular line emission employ different approaches, such as the Sobolev or large velocity gradient (LVG) approximation (Sobolev, 1960), as in `RADEX` (Schöier et al., 2005; van der Tak et al., 2007), and the escape probability method (Capriotti, 1965), as in `MOLPOP-CEP` (Elitzur & Asensio Ramos, 2006; Asensio Ramos & Elitzur, 2018).

1.2.5 Internal structure of molecular clouds

In Section 1.1.1, we introduced the concept of giant molecular clouds (GMCs). Although not isolated and discrete entities, the definition of GMCs proves to be very useful, as indicated by recent surveys within the Milky Way (MW, Umemoto et al., 2017; Benedettini et al., 2020) and in external galaxies (Schruba et al., 2017; Wong et al., 2019; Leroy et al., 2021; Miura et al., 2021). GMCs contain the majority of the H_2 mass in a normal SFG, and identifying them is more straightforward than identifying atomic clouds (see Heyer & Dame, 2015, for a review of different GMC identification techniques).

Observations of GMCs in several emission lines (CO being the most important one) return typical values for the line broadenings of $\sigma_{obs} \sim 1 - 10$ km s^{-1}. The gas thermal velocity can be estimated as

$$v_{th} \simeq \sqrt{\frac{k_B T}{\mu m_p}} \quad , \tag{1.5}$$

where k_B is the Boltzmann constant, T is the gas temperature, μ is the mean molecular weight, and m_p is the proton mass. For a typical GMC ($T = 10$ K, $\mu = 2.2$) this means $v_{th} \approx 0.2$ km s^{-1}, an order of magnitude lower than the observed values. This indicates that gas in GMCs has non-thermal chaotic (i.e. not ordered as rotation) motions, which we refer to as *turbulence*. Since molecular gas is also a magnetic fluid (see reviews by Crutcher, 2012; Han, 2017) we often refer to it as magnetohydrodynamic (MHD) turbulence. MHD turbulence induces a complex structure within GMCs, with clumps of dense gas ($\sim 10 - 100$ M$_\odot$, a few pc in size) connected by filaments ($\lesssim 10^4$ M$_\odot$, a few pc wide $\times 20 - 40$ pc long), and denser, rounder cores found within the filaments ($\lesssim 10$ M$_\odot$, $\lesssim 0.1$ pc, Molinari et al., 2010; Schisano et al., 2014; Heyer & Dame, 2015;
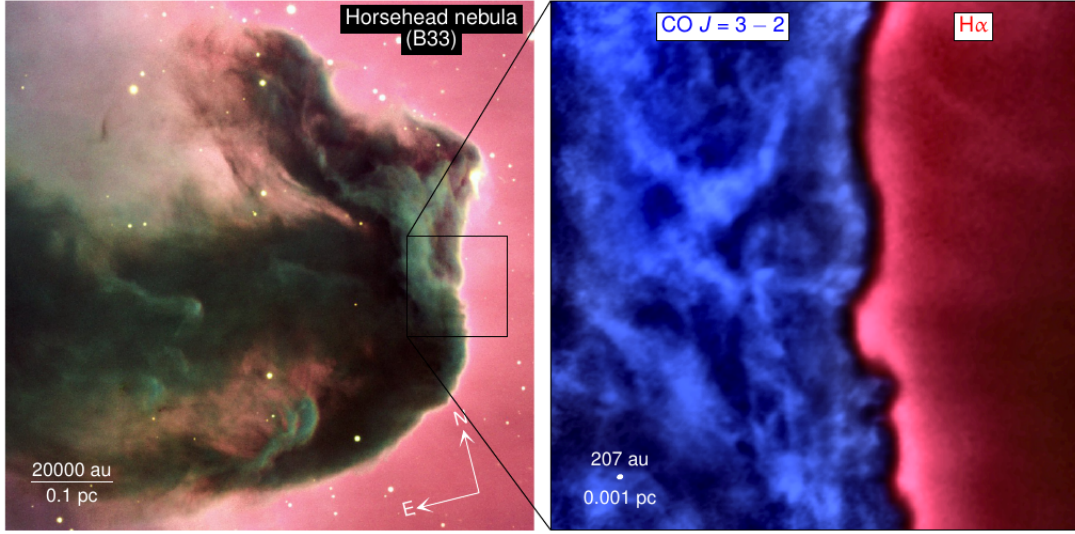
Figure 1.13: *Left panel*: Composite colour image of the Horsehead nebula (Barnard 33) observed with VLT. *Right panel*: Zoom of the edge of the molecular cloud and the adjacent HII region (IC 434), imaged by ALMA in the CO(3 − 2) emission (in blue) and the 0.9m KPNO telescope in the Hα emission (in red). The dark region between CO and Hα emission reveals a sharp transition between ionised and molecular gas (see also Section 1.2.2). Figure from Hernández-Vera et al. (2023).

Ballesteros-Paredes et al., 2020). A visual example of such complexity comes from the CO(3 − 2) emission in a very small region in the Horsehead nebula (left panel of Figure 1.13).

We showed in Section 1.1.1 (see also Equation 1.2) that GMCs should collapse in a free-fall time (∼ 3 Myr) due to their own gravity. However, the widespread existence of GMCs, coupled with the observation that the SFR is typically low compared to the available molecular mass in a galaxy, suggests the presence of a physical mechanism counterbalancing the gravitational inward pull. To assess whether turbulence could play this role, we can examine the ratio between turbulent kinetic energy (K_{turb}) and gravitational energy (W_{g}):

$$\frac{2K_{\text{turb}}}{|W_{\text{g}}|} \sim \frac{M 3\sigma_{\text{obs}}^2}{GM^2 R^{-1}} \sim \left(\frac{\sigma_{\text{obs}}}{2 \text{ km s}^{-1}}\right)^2 \left(\frac{M}{10^5 \text{ M}_\odot}\right)^{-1} \left(\frac{R}{50 \text{ pc}}\right) \quad , \qquad (1.6)$$

where G is the gravitational constant, the factor 2 comes from the virial theorem, and the factor 3 comes from the fact that σ_{obs} is projected along the line of sight. The fact that the ratio in Equation (1.6) is ∼ 1 given the typical GMC values tells us that turbulence can prevent gravitational collapse, hence influencing the star formation (SF) efficiency (e.g. Federrath & Klessen, 2012).

Equation (1.6) is often rewritten in terms of the virial parameter $\alpha_{\text{vir}} \equiv \sigma_{\text{obs}} \, v_{\text{vir}}$,

where $v_{\rm vir} = GM/R$. By collecting a sample of Galactic GMCs, Larson (1981) showed that $\alpha_{\rm vir} \sim 1$ over a 3-dex range of GMC sizes. This result, known as the second Larson's law, has been confirmed and extended in sizes range, both in Galactic (Solomon et al., 1987; Heyer et al., 2009) and extragalactic observations (Bolatto et al., 2008; Sun et al., 2018), and in simulations (Hopkins et al., 2018; Ganguly et al., 2022). The other two Larson's laws (also from Larson, 1981) are the line width-size relation ($\sigma_{\rm obs} \propto R^{0.38}$) and the density-size relation ($n \propto R^{-1.1}$), which implies a nearly constant $N_{\rm H} \sim nR \propto R^{-0.1}$ (or surface density Σ, in $M_\odot$ pc^{-2} units) in GMCs (Lombardi et al., 2010b). More recent studies have confirmed that these relations are still valid, but the exact coefficients depend on the galactic environments in which GMCs are embedded (see Section 2.3.2 in Chevance et al., 2023a, and references therein).

Turbulence in GMCs is supersonic, since $\sigma_{\rm obs}$ is larger than the speed of sound $c_{\rm s} = \sqrt{\gamma} v_{\rm th}$, where γ is the adiabatic index (typically between 7/5 and 5/3). We define the Mach number as $\mathcal{M} \equiv v/c_{\rm s}$, so that a fluid is supersonic if $\mathcal{M} > 1$. GMCs have typically $\mathcal{M} \gtrsim 10$ (Heyer & Dame, 2015; Chevance et al., 2023a). Supersonic turbulence (described by the seminal works of Burgers, 1939; Kolmogorov, 1941) has been shown to induce a log-normal probability distribution function (PDF) of gas densities (Vazquez-Semadeni, 1994; Federrath et al., 2008; Padoan & Nordlund, 2011):

$$p_s \, ds = \frac{1}{\sqrt{(2\pi\sigma_s^2)}} \exp\left[-\frac{1}{2}\left(\frac{s - s_0}{\sigma_s}\right)^2\right] ds \ , \qquad (1.7)$$

where $s = \ln(\rho/\rho_0)$ is the logarithmic density, with mean value $s_0 = -\sigma_s^2/2$. The standard deviation of the distribution, σ_s, depends on $\mathcal{M}$ and on the b factor, which parametrizes the kinetic energy injection mechanism (often referred to as forcing) driving the turbulence (Molina et al., 2012). Equation (1.7) contains the volumetric density ρ, which is not a straightforward quantity to measure. However, the observed column density (or visual extinction, see Equation 1.4) of non star-forming GMCs also exhibits a log-normal PDF (e.g. Kainulainen et al., 2009; Lombardi et al., 2010a; Burkhart et al., 2015; Schneider et al., 2016; Sharda et al., 2022). We refer to Brunt et al. (2010) for a conversion method between 2D and 3D distributions.

Supersonic motions due to turbulence are expected to dissipate rapidly within a few Myr, following a cascade from large to small (sub-pc) scales (Mac Low & Klessen, 2004; Hennebelle & Falgarone, 2012). Given their widespread observation, GMCs require a continuous injection of turbulent energy. The most probable sources, which are not mutually exclusive, include gas accretion into the cloud (Klessen & Hennebelle, 2010; Goldbaum et al., 2011) and stellar feedback in the form of protostellar outflows, stellar

winds, SNe, HII regions expansion, or UV radiation (Matzner, 2002; Nakamura & Li, 2007; Gritschneder et al., 2009; Hernández-Vera et al., 2023; Chevance et al., 2023a).

1.2.6 Molecular gas and star formation

The large-scale structure of molecular gas in a galaxy is presumed to be connected with the one of star formation. One expectation is that the IMF is linked to the mass distribution of GMCs. Observational findings in the MW and nearby galaxies consistently show that GMCs follow a power-law mass distribution:

$$\frac{dN}{dM} \propto M^{-\alpha_{\mathrm{GMC}}}. \tag{1.8}$$

where $1.5 < \alpha_{\mathrm{GMC}} < 2.5$ (Rosolowsky, 2005; Fukui & Kawamura, 2010; Roman-Duval et al., 2010; Miville-Deschênes et al., 2017). Notably, an $\alpha_{\mathrm{GMC}} < 2$ implies that, unlike stars, the majority of molecular mass would be concentrated in the largest clouds (Kennicutt & Evans, 2012).

Establishing a direct link between the IMF and the GMC mass distribution (Equation 1.8) may not be straightforward. One possibility is that star formation is not a uniform process everywhere but depends on the environment (as GMCs do, Chevance et al., 2023a). Bigiel et al. (2008) and Kennicutt & Evans (2012) identify three distinct SF regimes that depend on the local gas surface density. In the low-density regime ($\Sigma_{\mathrm{gas}} \gtrsim 10$ $M_\odot$ pc^{-2}, typical of outer discs, ETGs, Solar neighbourhood) star formation is highly dispersed and characterized by a high depletion time ($\tau_{\mathrm{dep}} \equiv \mathrm{SFR}/M_{\mathrm{gas}} \sim 3 - 5$ Gyr, Saintonge et al., 2011; Davis et al., 2014). The intermediate-density regime ($\Sigma_{\mathrm{gas}} > 10$ $M_\odot$ pc^{-2}) corresponds to normal LTGs and entire GMCs, characterized by $\tau_{\mathrm{dep}} \sim 1 - 2$ Gyr (see e.g. Leroy et al., 2008, 2013). The high-density regime ($\Sigma_{\mathrm{gas}} > 100 - 300$ $M_\odot$ pc^{-2}, $\tau_{\mathrm{dep}} \gtrsim 0.3$ Gyr) is typical of starbursts and molecular cores (see also the more recent works by de los Reyes & Kennicutt, 2019; Kennicutt & De Los Reyes, 2021a).

The empirical relationship between Σ_{gas} and the SFR surface density Σ_{SFR} is known as the Schmidt-Kennicutt (SK) law (from the seminal studies of Schmidt, 1959, 1963a; Kennicutt, 1989). Different forms of the SK law exist depending on how the two quantities are measured. Kennicutt (1998b) found a nonlinear $\Sigma_{\mathrm{SFR}} \propto \Sigma_{\mathrm{gas}}^{1.4}$ when averaging the total gas mass (HI + H$_2$) and the SFR over the main star-forming disc, with a turnover occurring at $\Sigma_{\mathrm{gas}} \approx 10$ $M_\odot$ pc^{-2}. A linear relation exists between the integrated SFR and the dense molecular gas mass, as derived from HCN(1 − 0) line emission[7] (Gao &

---

[7]The HCN molecule is characterized by a higher n_{crit} than CO but comparable T_{ex}, which make it a good tracer of the cold dense molecular gas. For example, the HCN(1 − 0) line has $T_{\mathrm{ex}} = 4$ K and $n_{\mathrm{crit}} = 2.6 \times 10^6$ cm^{-3} (Carilli & Walter, 2013).
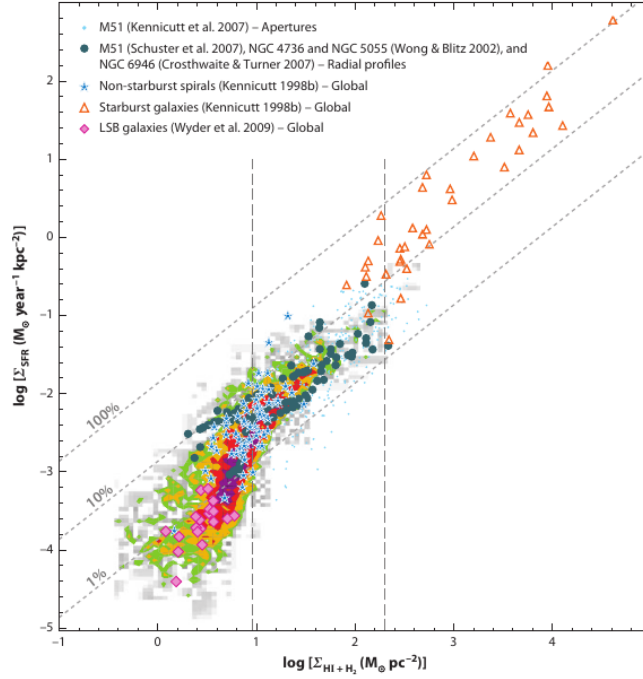
Figure 1.14: Schmidt-Kennicutt law (Σ_{SFR} vs. Σ_{gas}) for various sets of measurements (from Bigiel et al., 2008), listed in the figure legend. The gray diagonal lines reflect constant star formation efficiency (SFE). The two vertical lines denote the three distinct SF regimes discussed in Section 1.2.6. Figure from Kennicutt & Evans (2012).

Solomon, 2004). The relation becomes nonlinear if $CO(1-0)$ is used as the M_{mol} tracer (Solomon & Sage, 1988; Gao & Solomon, 2004), implying a strong coupling between dense gas (such as that within molecular clumps) and SF. Finally, the addition of spatially resolved data highlighted the presence of previously discussed different SF regimes (see Figure 1.14 and Bigiel et al., 2008; Casasola et al., 2015; Azeez et al., 2016; Audibert et al., 2021; Sánchez-García et al., 2022).

Both the SFR and M_{mol}, or their surface densities, exhibit strong correlations with stellar mass ($M_\star$) or its surface density ($\Sigma_\star$). The former is known as the star forming main sequence (SFMS Brinchmann et al., 2004; Schiminovich et al., 2007; Enia et al., 2020), and it is close to linear. The latter is the molecular gas main sequence (MGMS Lin et al., 2019; Morselli et al., 2020; Ellison et al., 2021a; Casasola et al., 2022). Clearly, the three scaling relations (SK, SFMS, and MGMS) are interconnected. Baker et al. (2022) found the SFMS to be a consequence of the other two more fundamental relations. Pessa et al. (2021) used data from the PHANGS survey (Leroy et al., 2021) to analyze the three relations at a spatial scale of 100 pc, finding their scatters to be $\sigma_{\text{SFMS}} > \sigma_{\text{SK}} > \sigma_{\text{MGMS}}$, consistent with expectations from an evolutionary scenario in which each tracer (Hα for Σ_{SFR}, CO for Σ_{mol}, and stars for $\Sigma_\star$) is visible for different timespans τ across the SF cycle ($\tau_{\text{H}\alpha} < \tau_{\text{CO}} < \tau_\star$, as described by Kruijssen et al., 2019; Chevance et al., 2020b).

1.3   The AGN-galaxy coevolution

The fact that only $\sim 1\%$ of the galaxies are hosting an AGN in the Local Universe led to think that nuclear activity is a phase during a galaxy lifetime. This would mean that galaxies not hosting an AGN should contain a SMBH in their centre. This is called the Soltan argument (Soltan, 1982). We now have evidence that the Milky Way was in an AGN phase just a few Myr ago (Bland-Hawthorn et al., 2019; Predehl et al., 2020; Pillepich et al., 2021; Yang et al., 2022, see Figure 1.18). We review our current view of the AGN structures and emission features in Section 1.3.1. In Section 1.3.2, then, we review the motivation for the idea that AGNs and their galaxy hosts coevolve.

1.3.1   AGN: structures and emission features

As depicted in Section 1.1.3, AGNs represent the observable outcome of gas accretion onto a SMBH. This process is highly efficient, with $\sim 10\%$ of the accreting mass converted into emission. The resulting radiation pressure can counteract gravitational accretion: by equating these two forces, we determine the maximum luminosity that an object of mass M can emit, known as the Eddington luminosity:

$$L_{\text{Edd}} = \frac{4\pi c G \mu m_{\text{p}}}{\sigma_{\text{T}}} M \simeq 1.5 \times 10^{38} \left(\frac{M}{M_{\odot}} \right) \text{ erg s}^{-1} \quad , \qquad (1.9)$$

where σ_{T} is the Thomson cross section and c is the speed of light. Given that the emitted L results from mass-to-energy conversion ($L = \eta \dot{m} c^2$, where $\dot{m}$ is the mass accretion rate and $\eta \sim 0.1$ is the efficiency of the process), we can calculate the accretion rate required to produce L_{Edd} as $\dot{m}_{\text{Edd}} \equiv L_{\text{Edd}}/(\eta c^2)$, termed the Eddington accretion rate. This value represents the maximum theoretical $\dot{m}$ (though super-Eddington accretion is possible, see e.g. Abramowicz et al., 1988; King, 2003; Strubbe & Quataert, 2009; Kaaret et al., 2017). Both L_{Edd} and $\dot{m}_{\text{Edd}}$ depend on the mass M of the central object, i.e. the SMBH. Another pertinent quantity is the Eddington ratio, expressed as $\lambda_{\text{Edd}} \equiv L_{\text{bol}}/L_{\text{Edd}}$, where L_{bol} is the AGN bolometric luminosity. Generally, AGNs are considered highly accreting if $\lambda_{\text{Edd}} \geq 0.01$ (Heckman & Best, 2014).

In Figure 1.8, we presented a schematic overview of the key physical structures comprising an AGN: the SMBH, the accretion disc, the hot corona, the BLR and NLR clouds, and the torus. Due to the wide range of temperatures, densities and environments within these structures, they give rise to distinct emission features in their spectral energy distribution (SED). The observed SED is also significantly influenced by the relative strength of the AGN in comparison to the host galaxy and to the level of nuclear
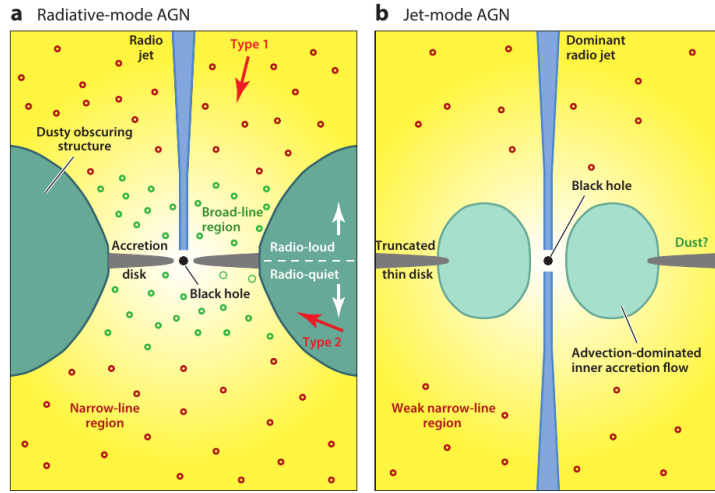
Figure 1.15: Spectral energy distributions (SED) of four AGN templates, broken up into the emitting physical processes (plotted with different colours): accretion disc and optical/UV emission lines (*dark blue*), AGN torus (*red*), AGN X-rays (*light blue*), host galaxy (*gray*), and combination of AGN and host galaxy (*black*). The templates differ for increasing AGN dominance (from left to right, traced by the AGN fraction at 1 μm f_{AGN}) and obscuration (from bottom to top, traced by the hydrogen column density N_H). For each template, the top panel indicate how the host galaxy would appear in the mid-IR, optical, and X-ray bands on the basis of the model SED. Figure from Hickox & Alexander (2018).

obscuration, parametrized by the AGN fraction f_{AGN} at 1 μm and the hydrogen column density N_H, respectively, as illustrated in Figure 1.15. Nuclear obscuration strongly affects the optical/UV emission from the accretion disc and the soft X-ray emission from the hot corona. The mid-IR emission coming from the torus remains unaffected, but in cases of low f_{AGN}, it might be submerged beneath the emission from the host galaxy's dust (left panels of Figure 1.15).

Of particular interest is the hard X-ray emission ($\geq$ 10 keV), which consistently appears in all AGN SEDs. For this reason, hard X-ray instruments such as the International Gamma-Ray Astrophysics Laboratory (INTEGRAL), the Nuclear Spectroscopic Telescopic Array (NuSTAR), and the Burst Alert Telescope (BAT, aboard the *Swift* observatory), are one of the most reliable tools for identifying obscured AGNs (Brandt & Alexander, 2015; Hickox & Alexander, 2018). Furthermore, X-ray emission from other astrophysical objects, such as X-ray binaries and hot gas, is either comparably weak or primarily falls within the soft X-ray band (Ranalli et al., 2003; Fabbiano, 2006; Mineo

31

Figure 1.16: Schematic drawings (not to scale) of the central engines of radiative-mode and jet-mode AGNs. (*a*) The difference between Type 1 and Type 2 depend on the presence of the dusty obscuring structure (i.e. the torus) along the line of sight, that prohibit a direct view of the broad-line region (BLR). The production of powerful radio jets (predominantly present toward the high end of the M_{BH} range) further divide these AGNs in radio-loud and radio-quiet. (*b*) The thin accretion disc is replaced in the inner regions by a geometrically thick advection-dominated accretion flow (ADAF). At larger radii a transition to an outer thin disk is expected. Radiative emission is less powerful, but can ionise weak, low-ionisation narrow-line regions (NLRs). Figure from Heckman & Best (2014).

et al., 2012; Faucher-Giguère & Oh, 2023).

X-ray obscuration in AGNs is commonly classified into three regimes: unabsorbed AGNs ($N_H \leq 10^{22}$ cm^{-2}), Compton-thin AGNs ($10^{22} < (N_H / \text{cm}^{-2}) \leq 1.5 \times 10^{24}$), and Compton-thick AGNs (CT-AGN, $N_H > \sigma_T^{-1} \simeq 1.5 \times 10^{24}$ cm^{-2}). It is intriguing that, despite the distinct source of X-ray obscuration (gas) compared to longer wavelengths (dust), there is a notable agreement between the optical extinction threshold for type 1/2 AGNs (typically $A_V = 5 - 10$ mag, see e.g. Schnorr-Müller et al., 2016) and the $N_H > 10^{22}$ cm^{-2} threshold (see e.g. Burtscher et al., 2016; Koss et al., 2017). The CT regime can be further divided into mild and heavy, with the boundary at $N_H \sim 10^{25}$ cm^{-2}: mildly CT-AGN are absorbed below 10 keV but visible above, while heavily CT-AGN have their entire X-ray spectrum depressed by Compton recoil (Comastri, 2004). The presence of a strong iron Kα line complex at $6.4 - 7$ keV (visible in every panel of Figure 1.15) and a characteristic reflection spectrum can be used to infer the presence of CT matter (Mushotzky et al., 1993; Levenson et al., 2006; Ricci et al., 2011).

The intensity of X-ray emission also depends on the relative importance of the accretion disc and the hot corona. We can identify two extreme regimes, called radiative-mode AGN and jet-mode AGN (Figure 1.16). In the radiative mode, the accretion disc efficiently accretes mass to the SMBH, reaching a maximum temperature of $\sim 10^5$ K

in the innermost radii (Netzer, 2006), thereby emitting the majority of its energy in the UV band. The emitted photons are then upscattered to X-rays by electrons in the hot corona throught the inverse Compton process (Mushotzky et al., 1993; Liu et al., 2003). Conversely, in the jet mode, lower accretion rates create a void at the centre of the accretion disc, which is then filled by hot coronal gas (Esin et al., 1997; Narayan, 2005). This plasma is well described by a two-temperature state, where ions are significantly hotter than electrons (Shapiro et al., 1976; Yuan & Narayan, 2014), resulting in the former being advected into the SMBH in an advection dominated accretion flow (ADAF, see Yuan & Narayan, 2014, for a review). Radiative-mode AGNs are radiatively efficient and exhibit a softer spectrum compared to the radiatively inefficient jet-mode AGNs (Heckman & Best, 2014).

Although radiatively inefficient, jet-mode AGNs release the majority of their energy through the bulk motion of relativistic particles transported in two-sided collimated jets (Heckman & Best, 2014). These jets are observable through synchrotron radio emission (see Blandford et al., 2019, for a recent review).

The cyclic process of mass accretion and injection of radiative and kinetic energy suggests that AGNs and their host galaxies are part of a shared ecosystem, coevolving over time. In the following section, we will explore the main pieces of evidence that underpin this coevolution.

1.3.2 Evidence of AGN-galaxy coevolution

By comparing the black hole masses (M_{BH}) in M31 and M32, Dressler & Richstone (1988) noted that they were proportional to the luminosity of the galaxy bulges (L_{bulge}). With more datapoints, it became clear that this was a fundamental scaling relation (Magorrian et al., 1998; Marconi & Hunt, 2003; McConnell & Ma, 2013), which can be also expressed in terms of the bulge mass: $M_{\mathrm{BH}} \approx 5 \times 10^{-3} M_{\mathrm{bulge}}$. A tighter correlation was then found to exist between M_{BH} and the stellar velocity dispersion σ (Ferrarese & Merritt, 2000; Gebhardt et al., 2000, see Figure 1.17, left panel). These correlations between the central SMBH mass, which can accrete mass only during AGN episodes, and kpc-scale properties of galaxies, kickstarted investigations on the so-called "AGN feedback".

In the following years, other pieces of evidence were collected (see the reviews by Cattaneo et al., 2009; Alexander & Hickox, 2012; Fabian, 2012; Kormendy & Ho, 2013; Heckman & Best, 2014; Morganti, 2017; Harrison et al., 2018). Firstly, considering a typical efficiency of converting mass to energy of ~ 0.1 (Soltan, 1982; Yu & Tremaine, 2002), an AGN emits $L_{\mathrm{AGN}} \sim \dot{m}_{\mathrm{BH}} c^2$, where $\dot{m}_{\mathrm{BH}}$ is the mass accretion rate and c is the
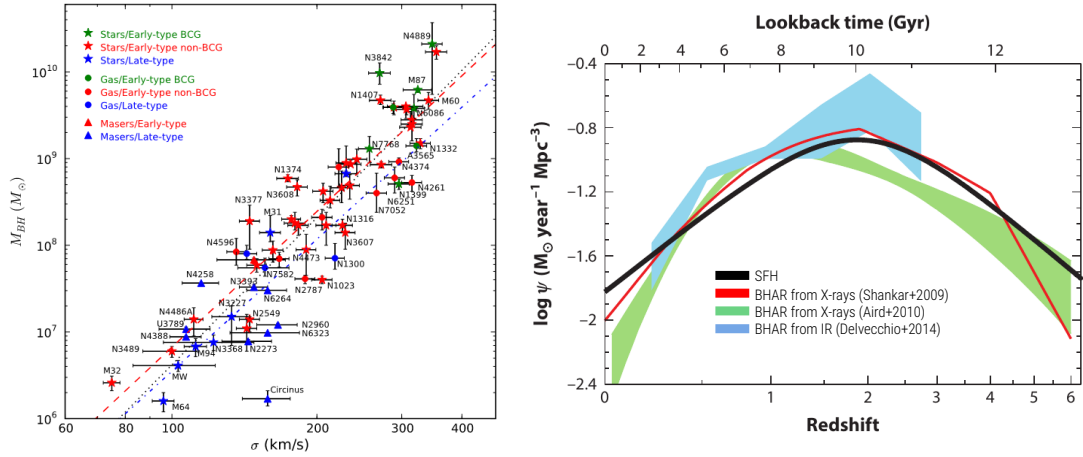
Figure 1.17: Indirect evidence for the impact of AGN feedback on properties of the host galaxy. (*Left*) $M_{BH} - \sigma$ relation for 72 galaxies, colour-coded on their morphological type, and if they are, or not, the brightest cluster galaxies (BCG) of their clusters. Different markers are used for different tracers: masers dynamics (triangles), stars (stars), and gas (circles). The diagonal lines are the best-fit relations for the entire sample (black), ETG only (red), and LTG only (blue). Figure from McConnell & Ma (2013) *Right panel.* Comparison between the comoving densities of star formation history (SFH, black curve) and black hole accretion history (BHAR), determined from X-ray (red curve from Shankar et al. 2009, green shading from Aird et al. 2010) and infrared (blue shading from Delvecchio et al., 2014) data. The shading indicates the $\pm 1\sigma$ uncertainty range on the total bolometric luminosity density. The radiative efficiency has been set to $\varepsilon = 0.1$. The BHAR values have been scaled up by a factor of 3,300 to facilitate visual comparison to the SFH ones. Figure adapted from Madau & Dickinson (2014).

speed of light. This means that, during a SMBH lifetime, the emitted energy is much larger than the hosting bulge binding energy $\sim M_{\text{bulge}}\sigma^2$: it would take a mechanical or radiative coupling efficiency of $\sim 1\%$ to blow away all the gas (Silk & Rees, 1998; Ostriker & Ciotti, 2005) and quench the galaxy SF. In fact, the histories of SF (SFH) (Lilly et al., 1996; Madau et al., 1996) and of BH growth in the Universe are similar (Figure 1.17, right panel; see Madau & Dickinson, 2014, for a review), both peaking at $z \sim 2$. For the same reason for which it may quench SF, AGN feedback may also explain the "cooling flow problem" in galaxy clusters (Fabian, 1994; Binney & Tabor, 1995; Ciotti & Ostriker, 1997), i.e. the absence of cool gas that one would expect in the high-density X-ray-emitting intracluster medium. Finally, the observed galaxy mass function drops more steeply at high masses than the predictions from the ΛCDM cosmological model (Planck Collaboration et al., 2016); this disagreement can be solved if high-M_{BH} AGNs can prevent late galaxy growth (Bower et al., 2006; Croton et al., 2006).

These were all indirect indications of the impact that the AGN has in shaping the host galaxy evolution. Direct proofs are more difficult to collect, and usually refer to
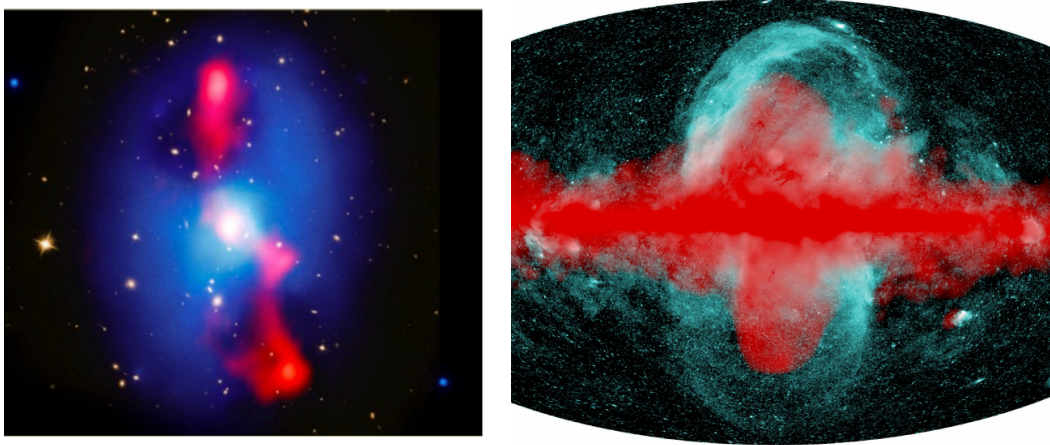
Figure 1.18: Direct evidence of AGN feedback. *Left panel.* X-ray (blue), radio (red) and optical images of the MS0735 galaxy cluster, of size $\sim 750 \times 750$ kpc^2. Figure from McNamara & Nulsen (2012). *Right panel.* Fermi γ-ray (in red) and eROSITA soft X-ray (in cyan) composite image of the Galactic plane (taken all-sky). Figure from Predehl et al. (2020).

single sources. The strongest case regards the spatial coincidence between X-ray cavities and radio jets in giant ellipticals and galaxy clusters (McNamara & Nulsen, 2007, 2012; Cavagnolo et al., 2010; Fabian, 2012, see Figure 1.18, left panel). This is often called the maintenance or jet mode of AGN feedback, since it maintains the gas hot through the mechanical action of the jets, preventing further galaxy growth. The other cases regard the detection of massive outflows of gas in different phases (see e.g. Veilleux et al., 2005, 2020; Cicone et al., 2014; Genzel et al., 2014; Harrison et al., 2014, 2018; Fiore et al., 2017). This is called the quasar or wind mode of feedback, and it relies on different kinds of pressure that can push the gas away (see Figure 1.18, right panel). We will discuss in more detail about AGN outflows in Section 1.4.

The direct and indirect evidence of AGN feedback suggests a coevolution of the AGN and its host galaxy (e.g. Hopkins et al., 2008; Somerville et al., 2008; Fiore et al., 2017). This coevolution extends to both SF and galaxy morphology (Schawinski et al., 2014, see also Figure 1.6). The complexity of the problem further arises from observational and theoretical evidence pointing to both positive and negative AGN feedback on SF (e.g. Silk, 2013; Zinn et al., 2013; Santoro et al., 2016; Maiolino et al., 2017; Zhuang & Ho, 2020; Smirnova-Pinchukova et al., 2022; Mercedes-Feliz et al., 2023).

AGN can negatively affect SF in three ways. Firstly, by heating and increasing the turbulence of cold gas, thereby suppressing the star formation efficiency (SFE, left panel of Figure 1.19). This mechanism has been invoked to explain the low SF efficiency of green valley and post-starburst (PSB) galaxies (e.g. Alatalo et al., 2015; Brownson et al., 2020; Smercina et al., 2022; Otter et al., 2022; French et al., 2023). Secondly, by
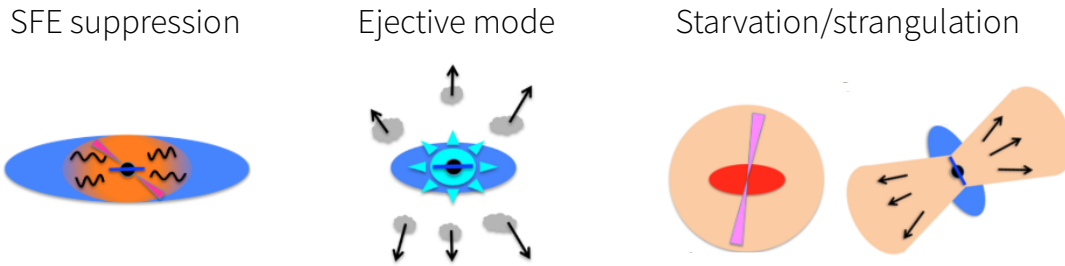
Figure 1.19: Three modes of negative AGN feedback. (*Left*) Suppression of star formation efficiency (SFE) via injection of turbulence and heating. (*Centre*) Ejection of the cold gas reservoir via wind/outflows. (*Right*) Prevention of further cold gas accretion via CGM heating by powerful jets (starvation/strangulation). Figure adapted from Maiolino (2018).

removing the cold gas (so-called *ejective* mode, central panel of Figure 1.19) through a powerful energy-driven wind (Zubovas & King, 2012; King & Pounds, 2015; Förster Schreiber et al., 2019; Herrera-Camus et al., 2019; Costa et al., 2020), or through a less dramatic momentum-driven or radiation pressure-driven wind (Costa et al., 2014, 2018; King & Pounds, 2015; Ishibashi et al., 2017; Bischetti et al., 2019). Thirdly, by preventing the cooling of gas in the circumgalactic medium (CGM), a phenomenon known as galaxy *starvation* or *strangulation* (right panel of Figure **??** Peng et al., 2015; Trussler et al., 2020). Additionally, it is necessary to determine the AGN duty cycle, i.e. the proportion of time during which the AGN is active (see e.g. Hopkins & Hernquist, 2006; Shankar et al., 2009; Bîrzan et al., 2012; Diamond-Stanic & Rieke, 2012; Sun et al., 2015). The AGN can, in fact, have a delayed effect on SF quenching (Leung et al., 2017; Woo et al., 2017).

On the other hand, AGN can have a positive impact on SF in two ways. Firstly, AGN-driven jets or winds increase molecular gas pressure, favouring conditions for SF. This has been demonstrated in both simulations (e.g. Blitz & Rosolowsky, 2006; Gaibler et al., 2012; Mukherjee et al., 2018) and observations (Croft et al., 2006; Cresci et al., 2015; Santoro et al., 2016). Secondly, SF can occur within the outflowing gas, owing to its dense and clumpy nature. This may have significant implications, including the formation of hypervelocity stars moving on radial orbits (Nayakshin & Zubovas, 2012; El-Badry et al., 2016; Ishibashi & Fabian, 2017; Wang & Loeb, 2018).

Finally, it is important to note that many phenomena typical of AGN feedback, such as ISM heating, wind launching, and galaxy starvation, can also be attributed to SF feedback (stellar winds, supernovae) and interactions with the environment (mergers, ram-pressure stripping with the intracluster medium). Moreover, AGN, SF, and environmental feedback often occur simultaneously. Therefore, when presented with a specific mechanism, identifying the dominant cause becomes challenging due to

potential degeneracies.

1.4 AGN feedback on molecular gas kinematics

In Section 1.2, we explored how AGN X-ray radiation heats and excites the surrounding molecular gas. Consequently, in Section 1.3, we reviewed the primary direct and indirect indications of AGN-galaxy coevolution. In this Section, our focus shifts to the impact of AGN radiation and winds on molecular gas kinematics. Molecular gas, traced by CO emission, typically forms a rotating disc associated with the galaxy's gravitational potential. The line profile of CO is also broadened by turbulence (see Section 1.2.5). Furthermore, molecular gas can exhibit bulk radial motions, either along elliptical orbits associated with a stellar bar (Sanders & Huntley, 1976; Bureau & Athanassoula, 1999; Casasola et al., 2011), or due to the AGN presence - either inflowing (referred to as AGN feeding, see e.g. García-Burillo et al., 2005; García-Burillo & Combes, 2012; Storchi-Bergmann & Schnorr-Müller, 2019), or outflowing (Feruglio et al., 2010; Combes et al., 2013; García-Burillo et al., 2014a; Morganti et al., 2015). Since the gas removal through molecular outflows is one of the main channels through which the AGN can regulate the galaxy growth, in this Section, we focus on this topic.

1.4.1 The physics of molecular outflows

The molecular outflows observed in AGNs most likely originate from a hot ionised wind, which may emanate from the accretion disc (see e.g. Tombesi et al., 2013; King & Pounds, 2015; Giustini et al., 2023). This sub-pc wind has been observed through the Doppler shift of absorption lines of highly ionised gas in X-rays, a phenomenon known as ultra-fast outflow (UFO) due to the high ($\sim 0.05 - 0.4$ c) velocities detected (Cappi, 2006; Tombesi et al., 2010; Gofford et al., 2013). Warm absorbers (WA Nandra & Pounds, 1994; Blustin et al., 2005) and broad absorption lines (BAL Murray et al., 1995; Hewett & Foltz, 2003) likely trace the same wind at lower velocities, ionisations and observed frequencies (Kazanas et al., 2012; Tombesi et al., 2013). Systematic studies of X-ray archival data has shown that the incidence of these fast winds in the radio-quiet population is > 35% (Tombesi et al., 2011), suggesting the significant role they could play in the context of AGN feedback.

We assume here that radiation pressure governs the momentum rate $\dot{P}_{\mathrm{wind}}$ of the hot wind:

$$\dot{P}_{\mathrm{wind}} \equiv \dot{M}_{\mathrm{wind}} v_{\mathrm{wind}} \simeq \frac{L_{\mathrm{AGN}}}{c} \equiv \dot{P}_{\mathrm{AGN}} \quad , \tag{1.10}$$
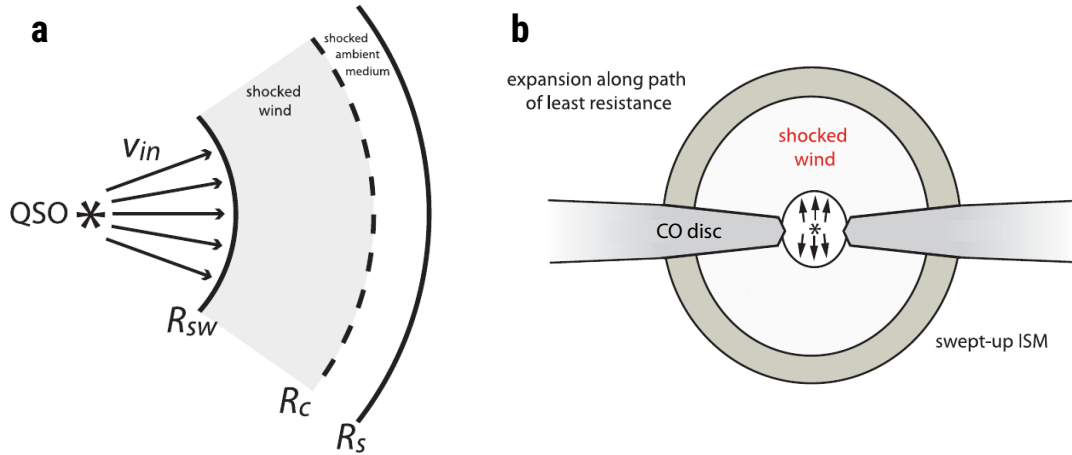
Figure 1.20: Schematic illustrations of the AGN wind structure. (*a*) The wind is launched from the galactic nucleus with velocity v_{in} and is shocked at radius R_{SW}. A second shock at R_S is driven into the ambient ISM. The two shocked gases are separated by a contact discontinuity at R_C. The swept-up ambient material piles up in a geometrically thin shell at $\approx R_S$. The geometrical thickness of the region between R_{SW} and R_C is determined by the cooling efficiency, and it distinguishes between energy-driven and momentum-driven winds. (*b*) When the wind encounters the molecular disc, it escapes preferentially along paths of least resistance. The swept-up ISM may include a fraction of cold gas from the disc. Figure adapted from Faucher-Giguère & Quataert (2012).

but other launching mechanisms have been investigated, including Compton heating (Begelman et al., 1983; Ciotti & Ostriker, 2007), magnetic driving (Fukumura et al., 2015), and line driving (Mizumoto et al., 2021). For comprehensive reviews on these processes, we refer to Crenshaw et al. (2003) and Veilleux et al. (2020).

The expanding AGN wind experiences abrupt deceleration upon interacting with the ambient ISM. Similar to stellar winds, the gas can be divided in four regions (Weaver et al., 1977; Dyson & Williams, 1997). In the left panel of Figure 1.20 a schematic representation of the wind structure is presented. In the innermost region, the AGN wind progresses outward unshocked, maintaining the initial velocity v_{in}. The interaction with the ambient ISM generates two shocks: one moving outward, sweeping up and shocking the ambient medium. and the other moving inward, slowing down and shocking the wind. Between these two regions of shocked gases there is a contact discontinuity, in which all thermodynamic variables, except pressure, experience a jump. The temperature of the shocked wind T_{sh} can be determined from the Rankine-Hugoniot jump conditions as:

$$T_{sh}(v_{sh}) = \frac{3\mu m_P}{16 k_B} v_{sh}^2 \approx 1.4 \times 10^9 \left(\frac{v_{sh}}{10^4 \, \text{km s}^{-1}} \right)^2 \, \text{K} \quad , \qquad (1.11)$$

where μ is the mean molecular weight, and the shock velocity in the wind reference

frame is $v_{sh} \simeq |v_{in}|$.

If the shocked wind can cool efficiently, the shocked region becomes very narrow, and most of the pre-shock energy is radiated - resulting in a momentum-driven outflow. Conversely, in the limit where cooling is negligible, the post-shock gas retains the mechanical input energy and expands adiabatically into the ambient ISM, constituting an energy-driven outflow. Detailed calculations for the different cooling processes of the shocked wind can be found in Faucher-Giguère & Quataert (2012).

Energy-driven outflows are generally more powerful than momentum-driven ones. This is due to the conservation of the wind kinetic energy rate $\dot{E}_{wind} = 0.5\dot{M}_{wind}v_{wind}^2$. The momentum rate of the outflowing gas ($\dot{P}_{out}$) is augmented with respect to the initial one ($\dot{P}_{AGN}$) by a boost factor defined as:

$$\frac{\dot{P}_{out}}{\dot{P}_{AGN}} \simeq \frac{\dot{P}_{out}}{\dot{P}_{wind}} \approx f_{wind}\frac{v_{wind}}{v_{out}} \quad , \tag{1.12}$$

where the first equality comes from Equation (1.10), and $f_{wind} \approx 0.5$ (Faucher-Giguère & Quataert, 2012) represents the fraction of the sub-pc wind energy that goes into the bulk motion of the swept-up gas.

Momentum-driven outflows are generally confined within ~ 1 kpc of the AGN, and have $\dot{P}_{out}/\dot{P}_{AGN} \sim 1$ (King & Pounds, 2015). Notably, these less powerful outflows have been shown to induce the observed $M_{BH} - \sigma$ relation (Fabian, 1999; King, 2003).

An interesting case of momentum-conserving outflow is a dusty wind driven by radiation pressure (Thompson et al., 2015), which may be launched from the inner part of the AGN torus. Hönig (2019) estimates a dusty molecular outflow with a mass outflow rate given by

$$\dot{M}_{out}^{mol} \approx 2.5\sqrt{\left(\frac{L_{AGN}}{10^{44} \text{ erg s}^{-1}}\right)\left(\frac{\lambda_{Edd}}{0.05}\right)\left(\frac{R_{\tau=1}}{5\,\text{pc}}\right)} \quad M_{\odot} \text{ yr}^{-1} \quad , \tag{1.13}$$

where $R_{\tau=1}$ is the radius at which the wind transitions from optically thick to optically thin to the UV radiation coming from the interior, which can be estimated from the IR emission size (Hönig, 2019).

The winds described so far predominantly occur in radiative-mode AGNs (see Figure 1.16). However, molecular outflows can also be initiated through ram pressure generated by a collimated relativistic jet (e.g. Tadhunter et al., 2014). It has been observed that an excessively powerful jet ($P_{jet} \gg 10^{43}$ erg s^{-1}) may traverse the host-galaxy ISM without effectively transferring energy or momentum (Scheuer, 1974; Mukherjee et al., 2016). In contrast, optimal jet feedback occurs when $P_{jet}/L_{Edd} \gtrsim 10^{-4}$ (Wagner et al.,

2012, 2013).

Molecular clouds exhibit resilience against interactions with hot winds, relativistic jets, and radiation pressure, due to efficient cooling (Aalto et al., 2012; Leroy et al., 2015; Cicone et al., 2020). This enables them to increase in density (Cooper et al., 2009) and even accrete more cold mass (Marinacci et al., 2010; Armillotta et al., 2016, 2017). Moreover, magnetic field lines contribute to cloud stabilization (Orlando et al., 2008; McCourt et al., 2015; Leaman et al., 2019). Simultaneously, the hot gas may undergo thermal instability, condense, and rapidly cool to form molecular gas (Richings & Faucher-Giguère, 2018a,b). This process is particularly favoured in the presence of massive hot winds (Thompson et al., 2016).

Upon encountering the molecular disc, the AGN wind typically follows the path of least resistance, preserving the molecular disc structure (see the right panel of Figure 1.20). This is because the outward force of the wind is generally lower than the inward gravitational force of the disc (Faucher-Giguère & Quataert, 2012). This interaction can divert an initially spherical wind into a bipolar shape (King & Pounds, 2015), extending to kpc-scale, as predicted in zoom-in 3D simulations (Costa et al., 2014; Gabor & Bournaud, 2014; Nelson et al., 2019). The kpc-scale wind is often detected, for nearby galaxies, through the asymmetric broadening of the [OIII]λ5007Å line, tracing the ionised gas of the NLR (Heckman et al., 1981; Veilleux, 1991; Greene & Ho, 2005; Fischer et al., 2013; Harrison et al., 2014; Davies et al., 2020; Musiimenta et al., 2023). This component is commonly referred to as the ionised wind. Another wind component, also extended on kpc scales, is the neutral one, mostly detected through absorption of HI or NaI D (Morganti et al., 2005; Cazzoli et al., 2016; Morganti et al., 2016; Rupke et al., 2017).

1.4.2 Observational findings

In the Local Universe, estimates of the molecular mass outflow rate in Seyfert galaxies range from $\sim$ 1 to a few tens of M$_\odot$ yr^{-1} (Combes et al., 2013; García-Burillo et al., 2014a; Morganti et al., 2015; Alonso-Herrero et al., 2019, 2023). More powerful AGNs can exhibit molecular gas outflow rates on the scale of $10^2 - 10^3$ M$_\odot$ yr^{-1} (Feruglio et al., 2010; Cicone et al., 2014; Veilleux et al., 2017; Fluetsch et al., 2019; Lutz et al., 2020). For reference, the mass outflow rates of the highly ionised (UFO, WA) and ionised winds, which likely underlie the neutral and molecular outflows, are in the range of $0.01 - 1$ M$_\odot$ yr^{-1} (Gofford et al., 2015; Morganti, 2017; Davies et al., 2020).

A tight correlation between the molecular mass outflow rate $\dot{M}_{\rm mol}$ and AGN luminosity ($L_{\rm AGN}$) was initially identified by Cicone et al. (2014) in a study of 19 nearby galaxies,
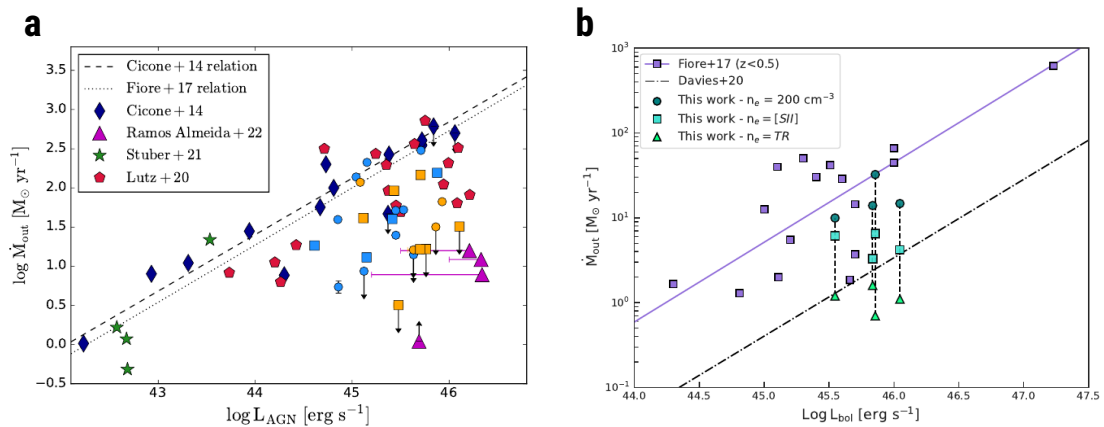
Figure 1.21: Mass outflow rate vs. AGN bolometric luminosity for molecular (left) and ionised (right) gas phases. (*a*) Molecular outflows from different samples, with additional data not present in the legend (starburst galaxies in blue, AGNs in orange, interacting systems as circles, mergers as squares) analysed by Lamperti et al. (2022). The diagonal lines show the sub-linear relations found by Cicone et al. (2014) and Fiore et al. (2017). In particular, more recent works find sources below those relations up to a factor ~ 100 in $\dot{M}_{\mathrm{out}}$. Figure from Lamperti et al. (2022). (*b*) Ionised outflows from different samples: purple line and squares from Fiore et al. (2017), which assumed a constant $n_{\mathrm{e}} = 200$ cm^{-3}, black line from Davies et al. (2020) best-fit, which used different n_{e} estimators, and green circles, cyan squares, and light-green triangles representing the same four type-2 QSOs analysed by Speranza et al. (2023) with different n_{e} estimators (namely a constant 200 cm^{-3} value, the [SII] doublet method, or the trans-auroral lines method, respectively). Figure from Speranza et al. (2023).

as $\dot{M}_{\mathrm{mol}} \propto L_{\mathrm{AGN}}^{0.7 \pm 0.1}$. This correlation was subsequently confirmed and extended to a broader sample of AGNs with molecular outflows by Fiore et al. (2017), who reported a similar slope of 0.76 ± 0.06. Notably, Fiore et al. (2017) also observed correlations between the outflow rate in highly ionised and ionised winds and L_{AGN}. One caveat of the aforementioned studies is that the samples were composed of AGNs with already detected outflows. More recent results, stemming from blind searches for molecular outflows in diverse AGN samples (Lamperti et al., 2022; Ramos Almeida et al., 2022), suggest that the correlation might not be as tight, and that the relation proposed by Fiore et al. (2017) might apply only to the most luminous sources (left panel of Figure 1.21). At the same time, more detailed studies on ionised outflows (Baron & Netzer, 2019; Davies et al., 2020; Speranza et al., 2023) emphasize substantial uncertainties in estimating mass outflow rates, particularly in relation to ionised gas density, with variations of up to ~ 10 times (as shown in the right panel of Figure 1.21). Further exploration of this matter will be undertaken in Section 4.5.3.

Another identified correlation exists between the mass outflow rate and the black hole mass (M_{BH}). Rupke et al. (2017) demonstrated, using a sample of 10 objects selected
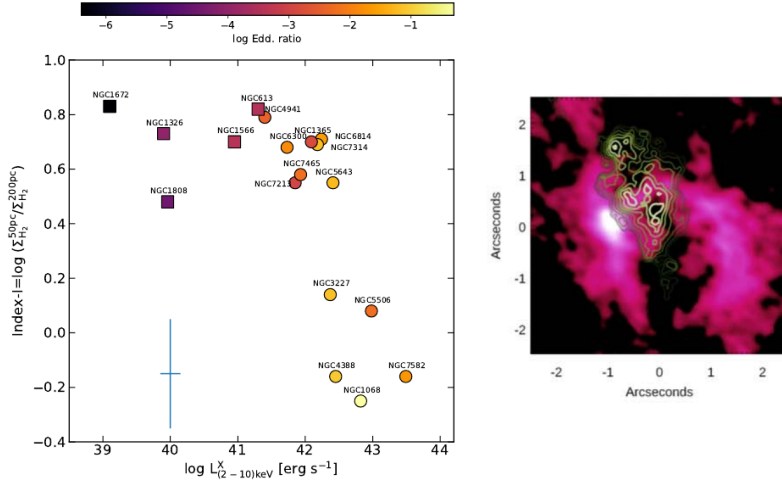
Figure 1.22: *Left panel.* Concentration index of molecular gas (*y*-axis) vs. X-ray (2 − 10 keV) intrinsic luminosity (*x*-axis). The concentration index is defined as the ratio between Σ_{H_2} measured within $r \leq 50$ pc and $r \leq 200$ pc. The sources are colour-coded on their Eddington ratio, and they are plotted as squares or circles if they come from the Nuclei of Galaxies sample (NUGA García-Burillo et al., 2003a) or from the GATOS sample. Figure from García-Burillo et al. (2021). *Right panel* Intensity of continuum-subtracted CO(3 − 2) emission (observed by ALMA, García-Burillo et al., 2019) with green contours representing [OIII] emission (HST/WFPC2 narrowband imaging, Schmitt et al., 2003; Fischer et al., 2018) of the central $\sim 5''$ (≈ 240 pc) of nearby Seyfert NGC 1068. North is up and east is to the left. Figure adapted from Fischer et al. (2023).

without prior outflow criteria, a $\dot{M}_{\text{out,tot}} \propto M_{\text{BH}}^{0.7\pm0.3}$ dependence. Here, $\dot{M}_{\text{out,tot}}$ represents the sum of the different measured outflow phases (ionised, neutral, and molecular). This discovery has been confirmed by Fluetsch et al. (2019) with a sample of 45 galaxies.

It is still debated whether these massive outflows can effectively quench large-scale star formation or induce morphological changes in the host galaxy. Apart from a few isolated cases (e.g. NGC 6240 Cicone et al., 2018), the outflow typically carries at most $\sim 10 - 20\%$ of the molecular mass reservoir (Cicone et al., 2014; Veilleux et al., 2017; Fluetsch et al., 2019; Lutz et al., 2020), suggesting that the ejection of cold gas may not be a primary quenching mechanism. To approach this from a different angle, one can calculate the outflow depletion time, defined as $t_{\text{dep,out}} \equiv M_{\text{gas}}/\dot{M}_{\text{out}}$. In comparing molecular outflows in SF- and AGN-dominated local objects, Fluetsch et al. (2019) found that the molecular outflow depletion time is shorter than the SF depletion time τ_{dep} in AGNs, whereas $t_{\text{dep,out}} \sim \tau_{\text{dep}}$ in the case of SF-dominated galaxies. However, when adding the contribution of HI to M_{gas}, the $t_{\text{dep,out}}$ in AGNs increased from ~ 10 Myr to ~ 1 Gyr. This suggests that AGN-driven outflows can effectively clear the central part of galaxies, where the molecular phase dominates, but they are less likely to deplete the gas content of the entire galaxy.

Zooming-in on the central kpc of nearby AGNs, García-Burillo et al. (2021), as part of the Galaxy Activity, Torus, and Outflow Survey (GATOS), found a suggestive negative trend between the molecular gas nuclear concentration and the AGN X-ray luminosity (left panel of Figure 1.22). This concentration index is defined as the ratio between the surface density Σ_{H_2} measured at two spatial scales: $r \leq 50$ pc, fully covering the torus region, and $r \leq 200$ pc, representing the circumnuclear disc (CND). An illustrative example is provided in the right panel of Figure 1.22, where the CO(3 − 2) emission of NGC 1068 shows a deficit in the nuclear region, from which it emerges a [OIII] wind (Fischer et al., 2023). These high-resolution (~ 10 pc) observations likely capture the initial interaction between the AGN wind and the molecular torus/disc depicted in the right panel of Figure 1.20. A similar case will be presented in Chapter 4.

1.5 Thesis outline

In this Thesis we are mainly interested in the influence of the AGN on the host galaxy. We investigate this process by evaluating the impact of the AGN on the molecular gas, since this is the fuel for star formation. We have introduced the molecular gas and the radiative feedback from stars and AGN in Section 1.2). In Section 1.3 we have described the AGN-galaxy coevolution, and in Section 1.4 we have introduced the topic of kinematic feedback (i.e. the concepts of outflows and winds) on the molecular gas. In Chapter 2 we present a study of the radiative impact of the AGN on the molecular gas in the central 500 pc for a sample of 35 local ($z \leq 0.15$) galaxies. In Chapter 3 we present a new model for estimating the molecular line emission in active galaxies. In Chapter 4 we present a case study of multiphase outflow (ionised and molecular) in a local Seyfert galaxy. Finally, in Chapter 5 we draw our conclusions on the impact of AGN on the molecular gas.

<div style="text-align: right; font-size: 3em; font-style: italic;">2</div>

Molecular gas excitation in AGN-host galaxies: observing the impact on galactic centres

This chapter is drawn from "*Molecular gas excitation in AGN-host galaxies: observing the impact on galactic centres*", **Esposito F.**, Vallini L., Pozzi F., Casasola V., Mingozzi M., Vignali C., Gruppioni C., and Salvestrini F., 2022, MNRAS, 512, 686.

2.1   Introduction

The purpose of this Chapter is to investigate the possible relation between the AGN activity and the conditions of molecular gas in a sample of local active galaxies with well-sampled CO SLED. We will assess whether, and to what extent, the excitation of the CO ladder shows correlations with X-ray and FUV tracers and whether the CO SLED can be used to infer the effect of SF versus AGN heating on the whole host galaxy and within the nuclear region.

The Chapter is structured as follows: in Section 2.2 we introduce the sample and the selection criteria. In Section 2.3 we describe the data collection from the sub-mm to the X-ray band. In Section 2.4 we derive the CO emission on a galactic scale, and we study the Schmidt–Kennicutt relation. In Section 2.5 we derive the physical parameters for the PDR and XDR analysis and we discuss the results we find. For the relevant calculations, we assume a ΛCDM cosmology with $H_0 = 70$ km s^{-1} Mpc^{-1}, $\Omega_m = 0.3$ and $\Omega_\Lambda = 0.7$.

2.2   Sample selection

To investigate the impact of AGN activity onto the molecular gas, we select a sample of local galaxies adopting the following criteria: (*i*) a properly sampled CO SLED in the mid/high-*J* regimes from *Herschel* observations; (*ii*) an intrinsic $2 - 10$ keV luminosity

Table 2.1: Properties of the sample of 35 AGN.

Name	RA (deg)	Dec (deg)	$D_{\rm L}$ (Mpc)	D_{25} ('')	$\log L_{\rm X}$ (erg/s)	$\log N_{\rm H}$ (cm^{-2})	$\log L_{\rm IR}$ (L$_\odot$)	$\log M_{\rm mol}$ (M$_\odot$)	SFR (M$_\odot$/yr)	Sample
N34	2.78	-12.11	85	69	42.11	23.72	11.44	9.97	31	klrvx
IZw1	13.40	12.69	264	29	43.60	–	11.95[d]	10.17	34	kx
N1068	40.67	-0.01	16	370	42.38	24.70	11.27	10.14	17	klmrtwx
N1275	49.95	41.51	76	128	43.98	21.68	11.20	9.63	9.0	klw
N1365	53.40	-36.14	23	721	42.32	22.21	11.00	10.10	17	krwx
IF05189-2524	80.26	-25.36	188	30	43.20	22.86	12.11	10.04	109	klprvwx
I07598+6508	121.14	65.00	704	39[c]	42.10	–	12.46[e]	10.54	–	kpx
U5101	143.97	61.35	174	72	43.08	24.08	11.95	10.21	105	klpuwx
N3227	155.88	19.87	17	239	42.10	20.95	10.13	9.02	0.56	kwx
N4151	182.64	39.41	14	173	42.31	22.71	10.20	7.42	0.25	kwx
N4388	186.45	12.66	36	322	42.60	23.50	10.00	9.40	3.7	kvwx
T1238-364	190.22	-36.76	47	76	43.40	24.95	10.62	8.94	4.1	kv
Mrk231	194.06	56.87	186	85	42.50	22.85	12.51	10.39	278	klpmrx
MCG-3-34-64	200.60	-16.73	72	81	43.18	23.80	11.24	–	5.7	klvwx
N5128	201.37	-43.02	8	1542	42.39	23.02	10.11	10.17	6.7	kw
N5135	201.43	-29.83	59	144	41.97	24.47	11.17	10.17	17	klrv
Mrk463	209.01	18.37	224	64	43.28	23.83	11.77[e]	9.92	–	kpvwx
IC4518a	224.42	-43.13	71	55	42.64	23.36	11.13	–	5.6	klw
Mrk848[a]	229.53	42.75	177	39	42.30	23.93	11.89	10.37	72	klx
PKS1549-79	239.25	-79.24	725	–	44.71	20.00	12.36[d]	10.01[h]	–	kw
PG1613+658	243.49	65.72	605	27	44.19	20.00	12.00	10.24	44	kw
N6240	253.25	2.40	107	131	43.58	24.20	11.85	10.58	70	klmprxwt
I19254-7245[b]	292.84	-72.66	277	38	42.80	23.58	12.06[e]	10.34	104	kpx
CygA	299.87	40.73	250	33	44.37	23.38	< 11.75[g]	< 8.88	35	kw
MCG+4-48-2	307.15	25.73	60	60	43.13	23.86	11.06	9.64	10	klw
IC5063	313.01	-57.07	49	161	42.87	23.42	10.85	9.36	2.6	kvw
I20551-4250	314.61	-42.65	190	41	42.30	23.69	12.00	10.25	105	klpx
3C433	320.94	25.07	468	19	44.16	23.01	< 11.66[g]	< 9.71	10	kw
N7130	327.08	-34.95	70	93	42.30	24.10	11.35	10.10	22	klvtw
N7172	330.51	-31.87	37	151	42.76	22.91	10.45	9.58	2.5	kwx
N7465	345.50	15.97	28	64	41.97	21.46	10.10	8.88	0.76	kw
N7469	345.82	8.87	71	83	43.19	20.53	11.59	10.09	35	klrwx
I23128-5919	348.95	-59.05	198	56	43.20	–	12.00	10.05	108	klpx
N7582	349.60	-42.37	23	415	42.53	24.20	10.87	9.64	7.1	ktwx
N7674	351.99	8.78	127	67	43.60	–	11.50	10.46	15	klx

Notes. In the Name column, N stands for NGC, I for IRAS, IF for IRAS Faint, U for UGC, T for TOL. RA, Dec from NED. $D_{\rm L}$ is the luminosity distance, calculated from the redshift (taken from NED) according to the adopted cosmology. D_{25} is the optical diameter, measured at the isophotal level 25 mag arcsec^{-2} in the B-band, taken from HyperLEDA. $L_{\rm X}$ is the 2–10 keV intrinsic (i.e. corrected for source absorption) luminosity, taken from the works indicated in the Sample column (see Section 2.3.1 for details). $L_{\rm IR}$ is the 8–1000 μm luminosity, from Sanders et al. (2003) unless otherwise specified. $M_{\rm mol}$ is the total molecular mass, calculated as described in Section 2.3.3. SFR is the star formation rate, calculated as described in Section 2.5.1. In the Sample column, references for the CO *Herschel* fluxes are: (*r*) Rosenberg et al. (2015); (*m*) Mashian et al. (2015); (*p*) Pearson et al. (2016); (*k*) Kamenetzky et al. (2016); (*l*) Lu et al. (2017). References for the X-ray data are: (*x*) Brightman & Nandra (2011); (*w*) Ricci et al. (2017a); (*t*) Marchesi et al. (2019); (*u*) La Caria et al. (2019); (*v*) Salvestrini et al. (in prep.).

Additional notes. (*a*) RA, Dec from Kojoian et al. (1981). (*b*) RA, Dec from Westmoquette et al. (2012). (*c*) D_{25} from NED. (*d*) $L_{\rm IR}$ from Moshir et al. (1990). (*e*) $L_{\rm IR}$ from Pearson et al. (2016). (*f*) $L_{\rm IR}$ from the IRAS PSC (1988). (*g*) Upper limit for $L_{\rm IR}$ from Golombek et al. (1988). (*h*) $M_{\rm H_2}$ from Oosterloo et al. (2019).

$L_X \geq 10^{42}$ erg s^{-1}. Moreover, we collect low/mid-J CO data by considering both sub-mm/mm single-dish observations, and interferometric ALMA data, which ensure a high spatial resolution.

Selecting sources with intrinsic $L_X \geq 10^{42}$ erg s^{-1} is the standard criterion for identifying AGN, since stellar processes alone (e.g. X-ray binaries, hot ionised ISM) rarely reach this X-ray luminosity (Hickox & Alexander, 2018). We look for AGN with a well-sampled CO SLED, to be able to study the high-J lines ($J_{upp} \geq 8$), where we expect to find the imprint of the AGN influence on the molecular gas.

The adopted criteria lead to a sample of 35 active galaxies (see Table 2.1), with redshifts in the range $0.0015 < z < 0.15$ (median $z = 0.02$), corresponding to luminosity distances (D_L) in the range $4 - 720$ Mpc.

Considering the classification from the optical spectra, 92% of our AGN are classified as Seyfert galaxies and two (Mrk 848 and IRAS 20551–4250) as low-ionisation nuclear emission line regions (LINERs). One of our sources (PKS 1549–79) is a quasar (see Netzer 2015 for a review on AGN classification), while PKS 1549-79, NGC 1275 (Perseus A, 3C84), Cygnus A (3C405), and 3C433 are also known as radio sources.

The $8 - 1000$ μm infrared luminosities L_{IR} (from Sanders et al., 2003) cover the range $10^{10} L_\odot < L_{IR} < 10^{12.5} L_\odot$. A substantial fraction (43%) of our sample consists of luminous infrared galaxies (LIRGs, $10^{11} \leq L_{IR}/L_\odot < 10^{12}$), while ultra-luminous infrared galaxies (ULIRGs, $L_{IR} \geq 10^{12} L_\odot$) account for 27% of the sample; the remaining 30% have $10^{10} < L_{IR} < 10^{11} L_\odot$. It is thought that the (U)LIRG phenomenon is mainly linked to merger activity (Lonsdale et al., 2006), especially for $L_{IR} \geq 10^{11.5}$ L$_\odot$ (Hung et al., 2014; Pérez-Torres et al., 2021a), as during mergers the gas can reach very high gas densities, triggering intense SF (Larson & Tinsley, 1978). Mergers and interactions can also trigger AGN activity for the very same reason: the gas has the opportunity to lose its angular momentum and fall from kpc-scale distances to the inner parsecs from the nucleus (Alonso-Herrero et al., 2012; Treister et al., 2012; Ricci et al., 2017b; Ellison et al., 2019). Both SF and AGN phenomena heat the dust, hence boosting the IR luminosity of the host galaxies. Within our sample, at least five galaxies show an evolved merging phase: IRAS 23128-5919 (Leslie et al., 2014), IRAS 19254-7245 (Superantennae, Bendo et al., 2009), NGC 6240 (Komossa et al., 2003), Mrk 463 (Bianchi et al., 2008) and Mrk 848 (Perna et al., 2019). Seven more galaxies have a very close companion: NGC 3227 (~15 kpc, Mundell et al., 2004), NGC 7465 (~15 kpc, Merkulova et al., 2012), NGC 7469 (~20 kpc, Zaragoza-Cardiel et al., 2017), NGC 7674 (~20 kpc, Larson et al., 2016), MCG+04-48-002 (~25 kpc, Koss et al., 2016), TOL1238-364 (~25 kpc, Temporin et al., 2003), and IC4518a (~1 kpc, Bellocchi et al., 2016). Two additional sources (NGC 34 and IRAS 20551–4250) have a disturbed morphology, sign of a past galactic interaction.

Moreover, some of the galaxies of this sample (notably NGC 1275, NGC 5128 and Cygnus A) are known to be part of groups or clusters, so their morphology is unsettled by probable continuous interactions with nearby satellite galaxies. Same as for the (U)LIRGs, interacting galaxies and systems with disturbed morphologies are typically characterized by higher molecular gas content and star-formation activity than isolated galaxies that may be due to tidal torques able to produce gas infall from the surrounding regions (e.g. Combes et al., 1994; Casasola et al., 2004; Pan et al., 2018; Moreno et al., 2019).

2.3 Data collection

2.3.1 X-ray data

We collect the best X-ray data available for our sample, namely the intrinsic 2–10 keV luminosity (L_X), the column density (N_H) of the obscuring material, and the photon index Γ (Reynolds, 1997; Osterbrock & Ferland, 2006; Singh et al., 2011) of the X-ray spectrum. To minimize both the contribution from host galaxy X-ray emission processes such as X-ray binaries, and the obscuration of the AGN (Hickox & Alexander, 2018), we prioritize hard-X *NuSTAR* (3-78 keV, Harrison et al., 2013) and *Swift/BAT* (15-150 keV, Gehrels et al., 2004; Barthelmy et al., 2005; Krimm et al., 2013) observations.

The data are taken from Ricci et al. (2017a), Marchesi et al. (2019); La Caria et al. (2019) and Salvestrini et al. (in prep.). When not available in these works, we take the L_X and N_H derived from *XMM-Newton* in the 0.5–10 keV band by Brightman & Nandra (2011). In Table 2.1 we list the data together with their references. The final sample has a median[1] $\log L_\mathrm{X}$ [erg s^{-1}] = $42.8^{+0.8}_{-0.5}$.

L_X is the intrinsic (i.e. unobscured) luminosity of the AGN, after taking into account the obscuration of the gas along the line of sight. Obscuration of AGN radiation is usually measured in terms of column density (N_H), and it originates from the immediate vicinity of the accretion disc, in the form of a compact (~0.1–10 pc) dusty torus (Ramos Almeida & Ricci, 2017). However, as pointed out by recent works (e.g. Buchner & Bauer, 2017; D'Amato et al., 2020), the obscuring gas can also be associated with the host galaxy on larger (~10 pc–1 kpc) scales. For our sample, the median N_H is $\log(N_\mathrm{H}/\mathrm{cm}^{-2}) = 23.5^{+0.7}_{-1.8}$, with 27 of them being type 2 AGN (i.e. they have $N_\mathrm{H} > 10^{22}$ cm^{-2}, Hickox & Alexander 2018), and six Compton-thick AGN ($N_\mathrm{H} \geq 1.5 \times 10^{24}$ cm^{-2}, Matt et al. 2000; Comastri 2004). Assuming that this gas is distributed over a sphere of

---

[1]The errors on the medians presented in this work always refer to the 16th and the 84th percentile of the data distribution.

Table 2.2: CO SLED transitions in units of $\log(L/L_\odot)$

CO transition Name	1–0	2–1	3–2	4–3	5–4	6–5	7–6	8–7	9–8	10–9	11–10	12–11	13–12
N34	5.22	5.83	–	<6.26	6.57	6.67	6.72	6.75	6.72	6.57	6.63	6.48	6.37
IZw1	5.42[a]	6.25[a]	6.92[a]	–	–	<7.08	<7.01	<7.15	7.22	<7.14	<7.18	<7.04	<7.17
N1068	5.39[b]	5.62[b]	6.20[a]	6.28	6.27	6.28	6.24	6.24	6.17	6.15	6.12	6.08	5.83
N1275	4.85[c]	4.48[d]	5.92[e]	<6.48	6.39	6.32	6.25	6.33	6.41	6.45	6.32	6.31	6.13
N1365	5.35	5.50	5.96	6.53	6.60	6.58	6.54	6.48	6.30	6.14	6.08	5.86	<5.77
IF05189-2524	5.28[a]	6.02[a]	6.49[a]	<7.04[a]	7.06	7.11	7.14	7.22	7.04	7.23	7.15	7.09	7.06
I07598+6508	5.78[f]	6.57[f]	–	–	<8.08	<7.70	<7.77	<7.62	–	<8.06	<8.00	<8.05	<8.02
U5101	5.38[g]	6.37[h]	6.78[a]	–	7.00	7.10	6.95	7.02	6.89	7.05	6.87	6.36	6.69
N3227	4.15[g]	4.82[h]	5.23[h]	5.41	5.48	5.44	5.30	5.34	5.19	5.11	5.24	5.15	<5.25
N4151	2.55[i]	3.23[j]	–	<5.14	–	<4.84	4.66	<5.02	<5.14	5.26	<5.24	<5.18	5.03
N4388	4.40[h]	5.15[h]	5.16[h]	6.05	5.91	5.94	5.84	5.83	5.78	5.71	<5.96	<5.93	<5.90
T1238-364	4.18[k]	5.15[k]	–	<5.92[k]	5.79	5.49	5.30	5.58	5.90	<5.98	<6.06	<5.90	<6.16
Mrk231	5.54[a]	6.39[a]	6.83[a]	7.25[a]	7.28	7.33	7.41	7.44	7.35	7.45	7.36	7.29	7.23
MCG-3-34-64	–	–	–	<6.22	<6.20	5.97	5.96	<6.25	<6.31	6.38	6.05	6.09	6.14
N5128	4.85[l]	4.57[m]	4.90[m]	4.51	4.57	4.48	4.32	4.29	<4.48	<4.27	<4.19	<4.24	<4.62
N5135	5.19[a]	6.00[a]	6.38[a]	6.51	6.61	6.61	6.49	6.37	6.31	6.13	6.03	5.95	5.65
Mrk463	5.12[n]	5.08[o]	–	–	<7.05	6.81	6.67	6.61	<7.03	6.37	<7.05	<7.08	–
IC4518a	–	–	–	6.66	6.28	6.24	5.99	6.14	<6.29	<6.16	6.25	<6.07	<6.28
Mrk848	5.61[a]	5.78[p]	6.59[a]	–	7.04	6.83	6.95	6.89	<7.04	6.77	6.79	6.79	6.70
PKS1549-79	–	–	–	–	<8.26	<7.95	<7.71	–	–	<7.92	<7.81	<7.98	<7.99
PG1613+658	5.49[f]	–	–	–	<7.99	<8.00	7.75	<7.59	–	<7.83	7.65	<7.94	<7.87
N6240	5.63[a]	6.59[a]	7.10[a]	7.46	7.59	7.69	7.75	7.78	7.75	7.72	7.65	7.59	7.52
I19254-7245	5.59[n]	–	–	–	–	7.01	7.31	7.20	7.32	7.21	7.04	6.85	7.07
CygA	<4.12[c]	–	–	–	<7.21	<7.01	<6.85	–	<7.21	–	<7.06	–	<7.13
MCG+4-48-2	4.88[q]	–	–	<6.61	6.32	6.11	6.13	6.18	<6.25	<6.33	<6.33	<6.18	<6.34
IC5063	4.51[h]	–	–	–	<6.17	<5.88	5.77	<6.00	<6.10	<6.15	–	<6.12	<6.17
I20551-4250	5.50[f]	–	6.30[s]	–	7.22	7.13	7.30	7.36	7.22	7.37	7.33	7.25	7.18
3C433	<4.96[c]	–	–	–	<7.76	<7.63	<7.38	<7.40	–	<7.37	<7.54	<7.55	–
N7130	5.34[q]	5.72[p]	–	6.70	6.71	6.66	6.62	6.51	6.58	6.43	6.34	6.18	6.11
N7172	4.75[p]	5.25[t]	–	<6.10	<5.79	5.64	<5.41	<5.62	<5.59	<5.64	<5.67	–	<5.77
N7465	4.13[g]	4.52[u]	4.92[e]	<5.59	5.38	<5.35	<5.24	<5.61	<5.66	<5.64	<5.42	–	–
N7469	5.24[a]	6.02[a]	6.44[a]	6.69	6.83	6.80	6.71	6.62	6.58	6.40	6.35	6.20	6.15
I23128-5919	5.29[a]	–	–	–	6.99	7.04	7.15	7.13	7.14	7.09	7.02	6.89	7.03
N7582	4.57[h]	5.53[t]	–	5.95	6.03	6.04	5.94	5.87	5.83	5.66	5.51	<5.41	<5.64
N7674	5.70[v]	5.93[h]	6.26[h]	<6.95	<6.57	6.32	6.09	6.36	<6.68	<6.59	<6.63	6.59	<6.64

Notes. All the CO line luminosities are taken from Rosenberg et al. (2015); Mashian et al. (2015); Pearson et al. (2016); Kamenetzky et al. (2016); Lu et al. (2017) unless otherwise specified. (a) Data from Papadopoulos et al. (2012): CO(1–0) was observed with IRAM-30m (FWHM: 22″), CO(2–1) (FWHM: 20″), CO(3–2) (FWHM: 14″) and CO(4–3) (FWHM: 11″) with JCMT. (b) Data from Curran et al. (2001); (c) Data from Evans et al. (2005): NGC 1275 and 3C433 were observed with NRAO-12m (FWHM: 55″), Cygnus A was observed with IRAM-30m (FWHM: 22″). (d) Data from Salomé et al. (2011), observed with IRAM-30m (FWHM: 11″). (e) Data from Mao et al. (2010), observed with HHT (FWHM: 22″). (f) Data from Xia et al. (2012): CO(1–0) (FWHM: 22″) and CO(2–1) (FWHM: 11″) were observed with IRAM-30m. (g) Data from Maiolino et al. (1997), observed with NRAO-12m (FWHM: 55″). (h) Data from Israel (2020); (i) Data from Dumas et al. (2010); (j) Data from Rigopoulou et al. (1997), observed with JCMT (FWHM: 20″). (k) Data from Pereira-Santaella et al. (2013); (l) Data from Espada et al. (2019); (m) Data from Israel (1992), observed with SEST (FWHM: 23″), CO(3–2) was observed with CSO (FWHM: 20″). (n) Data from Gao & Solomon (1999): IRAS23128-5919 and IRAS19254-7245 were observed with SEST (FWHM: 44″), Mrk0463 was observed with IRAM-30m (FWHM: 24″). (o) Data from Alloin et al. (1992), observed with IRAM-30m (FWHM: 13″). (p) Data from Albrecht et al. (2007); (q) Data from Gao & Solomon (2004); (r) Data from Ueda et al. (2014); (s) Data from Imanishi et al. (2017); (t) Data from Rosario et al. (2018); (u) Data from Monje et al. (2011); (v) Data from Young et al. (1995);

250 pc radius[2], the average gas density is $\log(n/\text{cm}^{-3}) = 2.6^{+0.7}_{-1.7}$.

2.3.2 Herschel CO data

In the Local Universe, the mid-J and high-J CO transitions have been observed with the *Herschel* Space Observatory (Pilbratt et al., 2010b). In particular, the transitions from CO(4–3) (CO(5–4) for galaxies with $D_L > 150$ Mpc) to CO(13–12) have been observed with the Spectral and Photometric Imaging Receiver (SPIRE) Fourier Transform Spectrometer (FTS) instrument (Griffin et al., 2010) aboard *Herschel*. The beam full width at half maximum (FWHM) of the SPIRE-FTS *Herschel* observations (Lu et al., 2017) ranges from 16″6 at 200 μm to 42″8 at 650 μm, corresponding to the rest-frame wavelengths of CO(13–12) and CO(4–3), respectively. The beam FWHMs correspond to physical scales in the range ∼6–14 kpc at the median redshift $z = 0.02$ of our sample.

We collect SPIRE data from Rosenberg et al. (2015); Mashian et al. (2015); Pearson et al. (2016); Kamenetzky et al. (2016); Lu et al. (2017), which altogether account for CO fluxes from 226 galaxies. In Table 2.2 we report the CO fluxes used in this work and, in case of multiple observations, we adopt the mean and the standard deviation of the observed fluxes as fiducial values.

2.3.3 Low-J CO data

To complete the CO SLEDs observations from *Herschel* discussed in Section 2.3.2, we collect (see Table 2.2) the low-J fluxes available in the literature, from CO(1–0) to CO(3–2). These transitions have been observed using several single-dish telescopes: the 14-m Five College Radio Astronomy Observatory (FCRAO), the 15-m Swedish-ESO Submillimeter Telescope (SEST), the 30-m Institut de Radioastronomie Millimétrique Pico Veleta telescope (IRAM-30m), the 12-m Atacama Pathfinder Experiment (APEX), and the 15-m James Clerk Maxwell Telescope (JCMT).

We expect these low-J CO lines to trace a larger area than mid-J and high-J lines, since they are characterized by lower n_{crit} and lower excitation temperatures. CO(1–0) is especially important since its flux is the most widely used proxy for the total molecular gas mass of a galaxy (Bolatto et al., 2013). For the closest galaxies, their projection on the sky could result larger than the telescope collecting area. For this reason, when multiple observations are available, we prioritize mosaics and larger beams.

Many authors have found that CO(1–0) emitting gas has a exponential radial profile, and that there is a relation between the CO(1–0) scale length r_{CO} and the optical radius

---

[2]See Section 2.3.4 for a definition of this radius
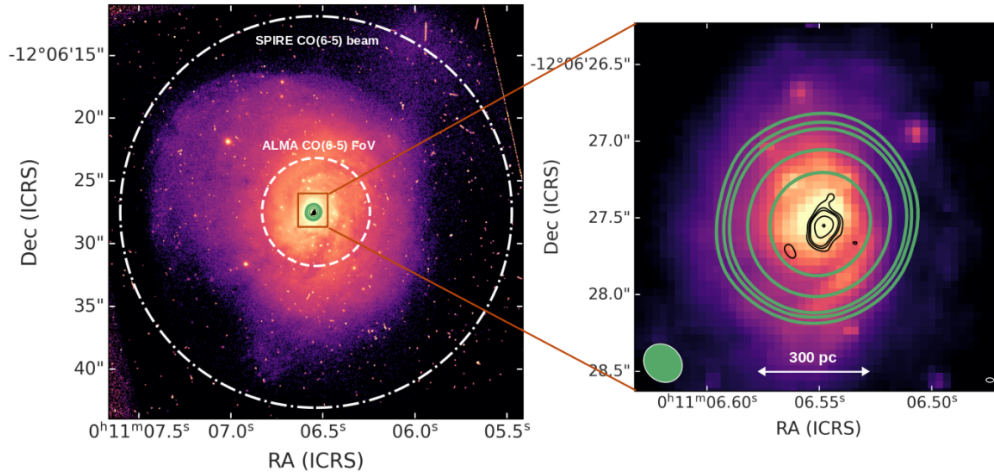
Figure 2.1: *Left panel:* HST WFPC2 F606W image of NGC 34 (from Malkan et al. 1998) with superimposed the contours of two ALMA CO(6–5) observations, in green at the resolution of 200 mas, in black of 35 mas. Both the contours are at the respective $(3, 4, 5, 10, 20) \times \sigma$, where $\sigma = 3.1$ Jy beam^{-1} km s^{-1} for the green lines and $\sigma = 0.27$ Jy beam^{-1} km s^{-1} for the black lines. The inner white dashed circle indicates the FoV of both ALMA observations, with a radius of 4″3 (~1.7 kpc), while the outer dash-dotted circle represents the *Herschel*/SPIRE-FTS beam FWHM for CO(6–5) observations, with a 15″6 radius. *Right panel:* zoom of the inner 1 kpc. Restored ALMA beams of the 200 and 35 mas images are shown as ellipses with white edges, at the bottom left (with the green area) and right (with the black area), respectively. The 35 mas ALMA image has not been primary-beam corrected.

r_{25} (Leroy et al., 2008; Schruba et al., 2011; Villanueva et al., 2021). Since the ~30% of our sample contains highly inclined galaxies ($i \geq 60°$), we follow Boselli et al. (2014) and Casasola et al. (2020) assuming that the CO(1–0) emission is well described by an exponential decline both along the radius r and above the galactic plane on the z direction (3D method):

$$S_{\rm CO}(r, z) = S_{\rm CO}(0)\, e^{-r/r_{\rm CO}}\, e^{-|z|/z_{\rm CO}} \quad , \tag{2.1}$$

where $r_{\rm CO} = 0.17\, r_{25}$ and $z_{\rm CO} = 0.01\, r_{25}$, as in Casasola et al. (2017) and Boselli et al. (2014). We stress that for galaxies with low inclination, the 3D method is analogous to the standard 2D approach, such as that developed by Lisenfeld et al. (2011). The adopted approach provides a median $r_{\rm CO} = 3.07^{+2.06}_{-1.48}$ kpc for our sample.

2.3.4 ALMA ancillary data

In local ($D \sim 1$ Mpc) sources, the Atacama Large Millimeter Array (ALMA) is able to resolve the morphology of CO emission at ~100 pc scales, from CO(1–0) to the mid-*J* CO(6–5) line. Higher-*J* lines, which trace the dense/warm molecular gas possibly influenced by the X-ray photons, fall unfortunately out of the ALMA bands at low

redshift. From the ALMA archive[3] we therefore collect all the available maps of the highest possible CO transition – namely the CO(6–5) – for the galaxies in our sample. We use these maps to infer the size of the high-density molecular gas region that cannot be estimated from the *Herschel* data given their poor spatial resolution. As the critical density of the CO transitions increases with J ($n_{\text{crit}} \propto (J + 1)^3$), and given that the gas density increases as we get closer to the galaxy centre, we expect the higher-J lines to originate from an area extended at most like CO(6–5) (see e.g. Mingozzi et al., 2018). We thus use the typical size of the CO(6–5) emitting region as an upper limit for the AGN sphere of influence on the molecular gas.

Figure 2.1 shows –as an illustrative example– the spatially resolved CO(6–5) emission from NGC 34, a LIRG in our sample, hosting an obscured ($N_{\text{H}} = 10^{23.7}$ cm^{-2}) AGN (Brightman & Nandra, 2011; Mingozzi et al., 2018). For this source, we retrieved two different ALMA observations, 2011.0.00182.S (PI: Xu) and 2016.1.01223.S (PI: Baba), both carried out in Band 9, where the field of view (FoV) is $\sim 8''6$, but with different spatial resolutions (200 and 35 mas, respectively) and maximum recoverable scales (2$''$ and 0$''$5, respectively). These scales correspond to 800 and 200 pc at the NGC 34 distance ($D = 85$ Mpc). The total flux of the CO(6–5) detection with a resolution of 200 mas is $S_{\text{CO(6–5)}} = 707 \pm 106$ Jy km s^{-1}, obtained by Mingozzi et al. (2018), using CASA 4.5.2 (McMullin et al., 2007) and a natural weighting scheme. This flux, which is shown with the green contours in Figure 2.1 (see also Xu et al., 2014; Mingozzi et al., 2018), is within 2σ from the one recovered by *Herschel*/SPIRE (920 $\pm$ 56 Jy km s^{-1}) within a much larger beam of 31$''$2. This means that this ALMA observation, despite having a smaller FoV with respect to that of SPIRE, recovers all the CO(6–5) emission from the galaxy.

The high-resolution data (project ID 2016.1.01223.S, PI: Baba) are plotted with black contours in Figure 2.1 and have never been published so far. We used the already calibrated and cleaned data cube from the ALMA Archive. For this data cube, calibration and imaging have been done manually, with a Briggs weighting (robust parameter of 0.5), and passed the QA2 stage. Using CASA 5.6 (McMullin et al., 2007), we produced the moment 0 map from the data cube with the task `immoments`. To estimate the flux, we performed a 2D Gaussian fit with the task `imfit`, which returned 62 $\pm$ 3 Jy km s^{-1}, less than 10% of the total flux measured by SPIRE-FTS. The reason for this discrepancy is that this observation is limited by a much smaller maximum recoverable scale, compared to the 200-mas data. The emission consists of a single clump of $r \lesssim 50$ pc, but due to the missed flux at larger scale we did not use this information.

In addition to NGC 34, we analysed ALMA CO(6–5) maps available for NGC 1068

---

[3]https://almascience.eso.org/asax/

(García-Burillo et al., 2014b), IRAS F05189–2524 (still unpublished), NGC 5128 (Espada et al., 2017), NGC 5135 (Sabatini et al., 2018), NGC 6240 (still unpublished) and NGC 7130 (Zhao et al., 2016). The images are shown in Appendix A.2. All these sources are characterized by spatially resolved CO(6–5) emission arising from the galaxy centre and extending up to $150 - 1000$ pc, with median $r = 250$ pc. We therefore assume that the bulk of higher-J CO line luminosity – for which we have only *Herschel* at low resolution – arise from a comparable region of radius $r = 250$ pc. In what follows we use this size as an upper limit for $J \geq 6$ transitions emitting region.

2.3.5 Dust continuum emission as a proxy for star formation

Dust in active galaxies can be heated by both the UV/optical photons coming from black hole accretion, and UV/optical photons associated to star-formation processes (e.g. Hatziminaoglou et al., 2008; Pozzi et al., 2010; Gruppioni et al., 2016). In the first case, the dust is mostly circumnuclear, which means it occupies the central 100 pc at most (e.g. Hickox & Alexander, 2018); in the second case the dust grains reside in the star-forming regions through the galaxy structure. The emission of two dust components peaks at different infrared (IR) wavelengths, due to the different temperatures: the circumnuclear dust ($T \approx 60 - 100$ K) peaks in the mid-IR, around $10 - 30 \,\mu$m (Alonso-Herrero et al., 2011; Feltre et al., 2012), while the galactic diffuse dust is colder ($T \approx 20 - 30$ K), peaking in the far-IR around $70 \sim 100 \,\mu$m (da Cunha et al., 2008).

For this reason we adopt the $70 \,\mu$m emission maps from the *Herschel* Photoconductor Array Camera and Spectrometer (PACS, Poglitsch et al., 2010) as a proxy for SF in our sample galaxies. In this regime the AGN contamination, if any, accounts for a few percent, and the spatial resolution at $70 \,\mu$m (FWHM = 5″.6, corresponding to ~0.17–13 kpc for our sample) is better than at longer wavelengths. We find suitable maps for all the sources, except IRAS 07598+6508, Mrk 463 and PKS 1549-79. We keep anyway these three galaxies in our sample for completeness.

The 5″.6 spatial resolution allows us to map the distribution of SF, assuming that all the $70 \,\mu$m photons trace the original stellar UV radiation. From visual inspection, SF is occurring mostly in the central regions ($r \sim 2$ kpc) of our galaxies. The procedure to extract the star formation rate (SFR) and the radial profile of the Habing field from the $70 \,\mu$m data is outlined in Section 2.5.1.

2.4 CO emission on global galactic scales

Before investigating the PDR vs. XDR contribution to the molecular gas heating in the centre of our sample galaxies, we want to see if, on the scale of the whole galaxy, it is already possible to see the influence of the AGN on the molecular gas phase. We check how our active galaxies compare to other active and non-active samples on the Schmidt–Kennicutt plane (Schmidt, 1959; Kennicutt, 1998c), which links the molecular gas surface density Σ_{mol} and the SFR surface density Σ_{SFR}, i.e. the star formation to its fuel.

We calculate the surface densities Σ_{mol} and Σ_{SFR} within the CO radius r_{CO}, defined as a fraction of the optical radius r_{25} (see Section 2.3.3). We derive the molecular mass from the CO(1–0) flux in the following way. For each source, we have the CO(1–0) flux S_{CO}, measured within the telescope beam, with FWHM 2θ, in angular units (the factor 2 is due to the fact that the FWHM is a diameter, while we want a radius). In physical units (e.g. in pc) in the source reference frame, this corresponds to a radius r_θ, so that the flux recovered by the telescope is:

$$
\begin{aligned}
S_{\text{CO}}(r_\theta) &= 2\pi \int_{-r_\theta}^{r_\theta} \int_0^{r_\theta} r\, S_{\text{CO}}(r,z)\, dr\, dz = \\
&= S_{\text{CO,tot}} \left(1 - e^{-r_\theta/z_{\text{CO}}}\right) \left[1 - e^{-r_\theta/r_{\text{CO}}}(r_\theta/r_{\text{CO}} + 1)\right] \quad ,
\end{aligned}
\tag{2.2}
$$

where we used Equation 2.1 and $S_{\text{CO,tot}}$ being the total CO(1–0) flux. If we put r_{CO} instead of r_θ in Equation 2.2, we obtain that $S_{\text{CO}}(r_{\text{CO}}) \approx 0.264 S_{\text{CO,tot}}$. Given that we know $S_{\text{CO}}(r_\theta)$ from observations, we can calculate the CO(1–0) flux within r_{CO}:

$$
S_{\text{CO}}(r_{\text{CO}}) = \frac{0.264\, S_{\text{CO}}(r_\theta)}{\left(1 - e^{-r_\theta/z_{\text{CO}}}\right) \left[1 - e^{-r_\theta/r_{\text{CO}}}(r_\theta/r_{\text{CO}} + 1)\right]} \quad .
\tag{2.3}
$$

We find a median ratio $S_{\text{CO}}(r_{\text{CO}})/S_{\text{CO}}(r_\theta) = 0.70^{+0.30}_{-0.06}$, with only one galaxy (NGC 5128) having $S_{\text{CO}}(r_{\text{CO}})/S_{\text{CO}}(r_\theta) > 2$. From the CO(1–0) flux calculated within r_{CO}, we estimate the molecular mass by using the following equation from Bolatto et al. (2013):

$$
M_{\text{mol}} = 1.05 \times 10^{-16} X_{\text{CO}} \frac{S_{\text{CO}} D_{\text{L}}^2}{1+z} M_\odot ,
\tag{2.4}
$$

where S_{CO} is the CO(1–0) flux in Jy km s^{-1}, D_{L} is the luminosity distance in Mpc, z is the redshift, and X_{CO} is the CO-to-H$_2$ conversion factor. These molecular gas masses take into account the contribution of helium and heavy elements (a $\sim 36\%$ correction based on cosmological abundances). To line up with the other samples included in our comparison, we adopt a Milky Way value of $X_{\text{CO}} = 2 \times 10^{20}$ cm^{-2} (K km s^{-1})$^{-1}$,

corresponding to $\alpha_{CO} = 4.3$ M$_\odot$ (K km s^{-1} pc^{-2})$^{-1}$ (see Section 1.2.1).

We find M_{mol} between $10^{7.4}$ and $10^{10.6}$ M$_\odot$, with median $\log(M_{mol}/M_\odot) = 10.1^{+0.3}_{-0.7}$. These M_{mol} are calculated within r_{CO}: to extrapolate the results to the whole galaxy ($r \rightarrow +\infty$), a multiplicative factor of $1/0.264$ is needed. The molecular masses calculated using Equations 2.4 and 2.4 are reported in Table 2.1, while the uncorrected (i.e. the observed) CO luminosities are the ones in Table 2.2. We note that these masses could be upper limits, since we are adopting a Milky Way value of α_{CO}, while it is thought that dusty (U)LIRGs and starburst galaxies have a lower $\alpha_{CO} \approx 0.8$ M$_\odot$ (K km s^{-1} pc^{-2})$^{-1}$ (Downes & Solomon, 1998; Bolatto et al., 2013).

The SFRs are estimated from the radial profile $F_{70}(r)$ of the 70 μm photometry maps: $\log \text{SFR} = \log L_{70} - 43.23$ (Calzetti et al., 2010; Kennicutt & Evans, 2012), where L_{70} is in units of erg s^{-1} and comes from the integration of $F_{70}(r)$ up to r$_{CO}$. This SFR calibration depends on the quantity of dust (it works better for dusty starburst galaxies) and the stellar population mix, and works better for galaxies with $L_{70} > 4.4 \times 10^9$ L$_\odot$ (Calzetti et al., 2010), which is satisfied by the $\sim 90\%$ of our galaxies. Using this SFR calibration, we find a median SFR $= 12.5^{+34.9}_{-9.8}$ M$_\odot$ yr^{-1}.

In Figure 2.2, we show our galaxies in the $\Sigma_{mol} - \Sigma_{SFR}$ plane, comparing them with starburst (SB) galaxies from Kennicutt & De Los Reyes 2021b (K21, hereafter), AGN observed with Swift/BAT from the BASS sample (Ricci et al., 2017a), star-forming galaxies (SFG) from the xCOLD GASS survey (Saintonge et al., 2017), and IR luminous galaxies from SLUGS (Dunne et al., 2000). The latter three samples were gathered by Lamperti et al. 2020 (L20, hereafter).

Our estimates of Σ_{mol} and Σ_{SFR} mainly depend on the assumed CO exponential profile and the SFR–70 μm calibration. Following K21, we assign a conservative error of $\pm 20\%$ to both Σ_{mol} and Σ_{SFR}. Since we could not recover the data errors from every point of L20, we adopt the same $\pm 20\%$ uncertainty also for their points.

We want to see if there is a difference between normal SFGs and AGN on the $\Sigma_{mol} - \Sigma_{SFR}$ plane. As shown in Figure 2.2, our sample of AGN fit well in between the starburst galaxies of K21 and the mixed (AGN/SFGs) sources from L20. We note a gap between the K21 and L20 sources, probably due to the difference in the area assumed for deriving the surface densities: K21 calculate a circumnuclear starburst region differently for every galaxy, finding $r = 2.8^{+3.3}_{-1.2}$ kpc; L20 instead use the CO observation beam area, which has a FWHM of 15″ for the SLUGS sample and $\sim 20 - 22''$ for both the xCOLD GASS and the BASS sample (hence radii of $\sim 0.4 - 11$ kpc). Overall, we find that, on the kpc-scale, an AGN effect on the SF is not evident, thus confirming earlier findings from Lamperti et al. (2020), and from Casasola et al. (2015), who studied the Schmidt–Kennicutt relation for four AGN from the NUGA sample (García-Burillo et al.,
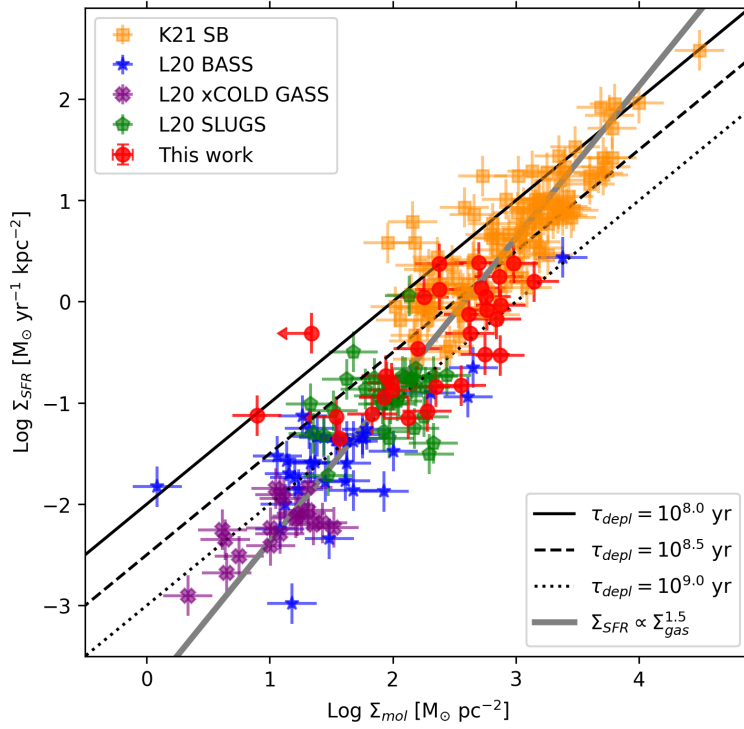
Figure 2.2: Schmidt–Kennicutt relation for our sample of active galaxies (red circles), the starburst sample from Kennicutt & De Los Reyes 2021b (orange squares), and the AGN sample (blue stars) and normal SFG (pink crosses and green pentagons) from Lamperti et al. (2020). Lines of constant molecular gas depletion times are overlayed to the data. The gray solid line is the best fit for a single relation as reported by Kennicutt & De Los Reyes (2021b), namely $\log \Sigma_{\mathrm{SFR}} = 1.5 \log \Sigma_{\mathrm{mol}} - 3.87$. All molecular surface densities were derived using the Milky Way value $\alpha_{\mathrm{CO}} = 4.3 \ \mathrm{M_\odot \ (K \ km \ s^{-1} \ pc^{-2})^{-1}}$.

2003b).

In Fig. 2.2 we highlight the lines corresponding to constant depletion time, $\tau_{depl} = \Sigma_{mol}/\Sigma_{SFR} = [10^8, 10^{8.5}, 10^9]$ yr, respectively. For the galaxies in our sample, we find a median $\log(\tau_{depl}/yr) = 8.9^{+0.4}_{-0.6}$, similar to other studies of Seyferts (e.g. Salvestrini et al., 2020), and slightly lower than typical values for local inactive SFGs (Bigiel et al., 2008; Utomo et al., 2018; Leroy et al., 2021, all find a median $\tau_{depl} \sim 2 \times 10^9$ yr). Conversely, typical progenitors of ellipticals or proto-spheroids galaxy models (Calura et al., 2014) require $\tau_{depl} \sim 2 \times 10^7$ yr, while dusty sub-millimeter galaxies (SMG), which are mostly hyperluminous infrared galaxies (HyLIRG, $L_{IR} \geq 10^{13}$ L$_\odot$) at moderately high redshift ($z \sim 3$) can have even shorter $\tau_{depl} \leq 10^7$ yr (Carilli & Walter, 2013), but these are probably extreme and rare objects (Heckman & Best, 2014).

From a classical evolutionary perspective, active, interacting (U)LIRGs are thought to be an intermediate stage between a late-type SFG and a quiescent early-type galaxy (Hopkins et al., 2008). From more recent works it seems that interacting and merging systems can account only for the formation of the most massive ellipticals, while slow secular processes (in the Local Universe) or rapid instabilities in clumpy gaseous discs (at high z) are responsible for the evolution of the bulk of the galaxies (Heckman & Best, 2014). Within the limits of our analysis, we do not see a strong effect of AGN feedback on τ_{depl} at kpc-scales, but that its impact also depends on the choice of α_{CO}.

2.5 CO emission in the galaxy centres

We now focus on the CO emission in the inner 500 pc (i.e. up to $r = 250$ pc from the centre) with the aim of assessing the relative contribution of PDR and/or XDR to the molecular gas in the vicinity of the AGN. To this goal, we exploit the line ratios with respect to CO(1–0) and CO(6–5): $L'_{CO(J\to J-1)}/L'_{CO(1-0)}$ (i.e. high-J/low-J ratios) and $L'_{CO(J\to J-1)}/L'_{CO(6-5)}$ (i.e. high-J/mid-J ratios), where all L'_{CO} are in units of K km s^{-1} pc^{-2}. We use the CO(1–0) theoretical profile (Equation 2.2) to calculate the flux within $r = 250$ pc:

$$S_{CO}(250 \text{ pc}) = S_{CO,tot}(1 - e^{-250pc/z_{CO}}) \left[1 - e^{-250pc/r_{CO}} \left(\frac{250pc}{r_{CO}} + 1 \right) \right] \qquad (2.5)$$

Conversely, we do not correct the other CO lines: we know (Section 2.3.4) that CO(6–5) emission is mostly confined within the central 250 pc, and the same should likely apply for higher-J lines. There are few studies that map the size of other low-J lines than CO(1–0): Casasola et al. (2015) compares CO(1–0), CO(2–1) and CO(3–2) images for 4 nearby active galaxies (none of which is part of this sample), finding a similar physical

size for the first two transitions and a halved size (mean ~ 500 pc) for the available CO(3–2) maps; NGC 1068, however, has a CO(3–2) emission which extends beyond the central 2 kpc (García-Burillo et al., 2014b). Among our sample of galaxies, Dasyra et al. (2016) have published a CO(4–3) image of IC 5063, which has a similar size (~ 1 kpc) to its CO(2–1) emission. CO(4–3) images of IRAS F05189–2524, NGC 5135, IRAS 20551–4250, NGC 7130, NGC 7469 and IRAS 23128–5919, among other (U)LIRGs, are published by Michiyama et al. (2021), who find emitting sizes for the aforementioned galaxies between 1 and 5 kpc. Since these low-J CO transitions are not the focus of the present work, and since we do not have a theoretical radial profile to correct them, we leave them unaltered, and put the relative plots only in the Appendix A.1.

In the next two subsections, we derive the fluxes of FUV and X-ray photons, which are the heating drivers in PDRs and XDRs, respectively, and we compare them with the CO line ratios.

2.5.1 PDR

The FUV flux (also often referred to as interstellar radiation field) is measured in Habing units G_0, where $G_0 = 1$ corresponds to its value in the solar neighbourhood: 1.6×10^{-3} erg cm^{-2} s^{-1} in the FUV band (Habing, 1968). As discussed in Section 2.3.5, the FUV photons are efficiently absorbed by dust grains, which re-emit energy in the infrared (IR), especially around 70μm (given typical dust temperatures; da Cunha et al., 2008). Since our systems are powerful IR-emitters (with median $\log(L_{\mathrm{IR}}/L_\odot) = 11.4^{+0.6}_{-0.9}$), we assume that all the FUV photons are processed by dust and re-emitted at 70 μm.

We use *Herschel*/PACS 70 μm High Level Images[4] to extract a value for G_0. To do so, we fit the radial profile of the 70 μm photometric map with a Sersic function:

$$F(R) = F_e \exp\left\{-b_n\left[\left(\frac{R}{R_e}\right)^{1/n} - 1\right]\right\}. \tag{2.6}$$

The free parameters of this fit are F_e, R_e and n, while b_n is a constant that depends on n (Sérsic, 1963). We then divide the normalization flux F_e by 1.6×10^{-3} erg cm^{-2} s^{-1}, obtaining a profile in G_0 units. In this way we find values corresponding to the radius R_e, with median $\log G_0(R_e) = 2.6^{+0.5}_{-0.8}$, which is similar to what Farrah et al. (2013) and Díaz-Santos et al. (2017) found for local (U)LIRGs, in the HERUS ($10^{2.2} < G_0 < 10^{3.6}$) and the GOALS ($10^1 < G_0 < 10^{3.5}$) samples, respectively. It is important to note that in these works, as in most of the literature, G_0 is derived from PDR calculations fitting the observed line emission, thus relying on PDR codes as e.g. the PDR Toolbox (Pound

---

[4]https://irsa.ipac.caltech.edu/data/Herschel/HHLI/overview.html
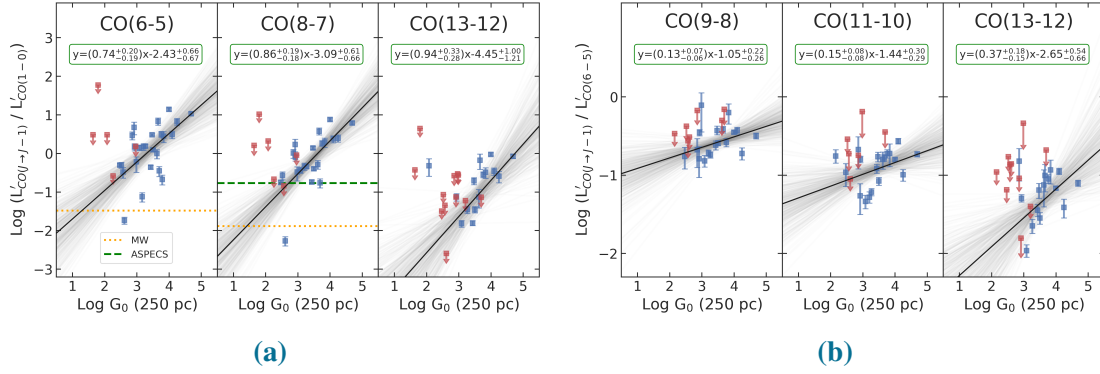
Figure 2.3: CO line ratios as a function of the Habing field, G_0, measured at $r = 250$ pc (see Section 2.5.1). We consider both the luminosity ratios $L'_{CO(J\to J-1)}/L'_{CO(1\to 0)}$ with respect to the CO(1–0) (left panel, 2.3a) and $L'_{CO(J\to J-1)}/L'_{CO(6\to 5)}$ with respect to the CO(6–5) line luminosity (right panel, 2.3b). The luminosities L' are in units of K km s^{-1} pc^{-2}, and J is indicated on the top of each panel. Blue squares indicate 3σ detections, while red squares with downward arrow indicate $< 3\sigma$ detections in the higher-J line (i.e. censored data). The solid black line is the regression fit, with the underlying grey lines showing the fits drawn from the posterior distribution. When available, the Milky Way (dotted orange line, data from Fixsen et al. 1999) and the ASPECS AGN (green dashed line, data from Boogaard et al. 2020) CO ratios are also shown.

& Wolfire, 2008) and Cloudy (Ferland et al., 2017). Here, instead, we observationally derive G_0 and we use the fitted profile to estimate its value at different radii. G_0 increases at smaller radii due to the higher SFR in the circumnuclear region, and the consequent high FUV irradiation. At $r = 250$ pc, we find a median $\log G_0(250\text{pc}) = 3.1^{+0.7}_{-0.8}$. We look then for correlations between the CO line ratios and G_0 (from now on when we refer to G_0 values we mean measured at $r = 250$ pc), to understand if the FUV irradiation can explain by itself the observed CO emission at the centre of local active galaxies.

In Figure 2.3 we show the CO(6–5)/CO(1–0), CO(8–7)/CO(1–0), and CO(13–12)/CO(1–0) luminosity ratios on the left panel, and the CO(9–8)/CO(6–5), CO(11–10)/CO(6–5) and CO(13–12)/CO(6–5) ratios on the right panel, as a function of G_0. All the other CO line ratios are presented in the Appendix A.1. We see an overall trend, for high-G_0 galaxies, to show increasing high-J/low-J and high-J/mid-J ratios.

We fit a regression line with the `Linmix` algorithm (Kelly, 2007), which evaluates the likelihood in presence of censored data (i.e. upper limits). Linmix computes the likelihood function by convolving multiple (we use two, since adding more has a negligible effect on our results) hierarchical Gaussian distributions. We also tried to fit only the detections with an ordinary least squares regression and with a bootstrapped version of the same algorithm, finding limited differences with respect to the Linmix regression, which includes the censored data. Since an important fraction (between 20 and 50 %, depending on the transition) of the high-J CO fluxes are actually upper limits

(see Table 2.2), we plot the Linmix results in Figures 2.3 and 2.4 and in Appendix A.1.

We find steeper slopes for the ratios computed with respect to the CO(1-0) line luminosity, and a trend of increasing steepness with J for both ratios. However, almost all the regression slopes return a sub-linear relation between the CO line ratios and G_0, with slopes $0.3 - 1.1$ for the ones with respect to the CO(1-0), and $0.1 - 0.4$ for ones with respect to the CO(6-5). These findings suggest that other excitation mechanisms, as X-ray irradiation, may contribute to the CO line emission.

We also plot in Figure 2.3 the median line ratios for the Milky Way (Fixsen et al., 1999, MW,) and the AGN from the ASPECS (Walter et al., 2016) AGN sample (Boogaard et al., 2020). The MW has a lower CO ratio than most of our sources, which is expected since our galaxies are forming stars at a higher rate than the MW and host an AGN. The ASPECS AGNs are instead bright ($L_{IR} \sim 10^{12} L_\odot$) and have a median CO ratio comparable to our active galaxies. These AGNs are located at $z \sim 1 - 3$, at the peak of the cosmic SF history (Madau & Dickinson, 2014).

2.5.2 XDR

We use the L_X and N_H derived for our sample (see Section 2.3.1 for details) to estimate the unobscured X-ray flux, $F_X = L_X/(4\pi r^2)$, illuminating the GMCs located at $r = 250$ pc from the centre of our galaxies. We find a median $\log(F_X/\mathrm{erg\ s^{-1} cm^{-2}}) = -0.1^{+0.8}_{-0.5}$.

In accordance with theoretical studies (Kawakatu & Wada, 2008) and observational investigations (Davies et al., 2007; Esquej et al., 2014; Motter et al., 2021), the circum-nuclear star-forming region directly influenced by the AGN is reported to have a ≈ 100 pc radius. However, our analysis, based on the available ALMA data (Section 2.3.4), is limited to the mid-J CO(6-5) emission, which, on average, extends only up to a ~ 250 pc radius. Consequently, we derive our X-ray fluxes at $r = 250$ pc. An alternative approach involves estimating F_X through XDR numerical modelling, as done by van der Werf et al. (2010); Pozzi et al. (2017); Mingozzi et al. (2018). Notably, these studies consistently report higher values of F_X for three galaxies in our sample, namely Mrk 231, NGC 7130, and NGC 34. This raises the possibility that the selected radius $r = 250$ pc for the central XDR may be excessively large.

The X-ray flux F_X does not account for the obscuration of the X-ray photons before they strike the molecular gas. It is therefore useful to calculate the local (i.e. accounting for the absorption) X-ray energy deposition rate per particle H_X. It can be estimated from the following formula (Maloney et al., 1996):

$$H_X \approx 7 \times 10^{-22} L_{44}\, r_2^{-2} N_{22}^{-1}\ \ \mathrm{erg\ s^{-1}}, \tag{2.7}$$

where the X-ray luminosity is $L_X = 10^{44}L_{44}$ erg s^{-1}, the distance to the X-ray source is $r = 10^2 r_2$ pc and the attenuating column density is $N_H = 10^{22}N_{22}$ cm^{-2}. We find a median $\log(H_X/(\text{erg s}^{-1}) = -25.3^{+1.1}_{-0.9}$. We use the N_H measured from the X-ray spectrum (Section 2.3.1) to estimate H_X. Although a Compton-thick gas ($N_H > 10^{24}$ cm^{-2}) is generally associated to small-scale structures like a dusty molecular torus, Compton-thin gas (as it is for 65% of our sample) may be part of the same circumnuclear gas we are studying from molecular and IR emission (Ballantyne, 2008; Hickox & Alexander, 2018). In this case, the $H_X \propto N_H^{-1}$ we calculate from Equation 2.7 could be underestimated, since there would be a lower N_H between the XDR and the AGN.

A key physical quantity affecting the XDR emission, and directly proportional to H_X/n, is the effective ionisation parameter, defined (Maloney et al., 1996; Galliano et al., 2003; Motter et al., 2021) as:

$$\xi_{\text{eff}} = 1.06 \times 10^{-2} L_{44}\, r_2^{-2}\, N_{22}^{-\alpha}\, n_5^{-1} \ \ \text{erg cm}^3 \text{ s}^{-1}, \qquad (2.8)$$

where the density of the XDR gas is $n = 10^5 n_5$ cm^{-3}, $\alpha = (\Gamma + 2/3)/(8/3)$ depends on the photon index Γ of the X-ray spectrum (Kawamuro et al., 2020) and the other quantities are the same defined above for H_X. For a representative fixed value of $n_5 = 0.1$ we find a median $\log \xi_{\text{eff}}/(\text{erg cm}^3\text{s}^{-1}) = -4.2^{+1.9}_{-1.0}$. These values are very low when compared to the theoretical values found in Maloney et al. (1996) models (e.g. their Figure 7) and to the observed values found in Motter et al. (2021), who calculated ξ_{eff} for the active galaxy NGC 34, also present in our sample. Motter et al. (2021) used N_H derived from radio observations (which is 1 dex lower than the one we use for NGC 34, derived from X-rays), and calculated ξ_{eff} at distances from the AGN between 40 and 120 pc, thus finding values ~ 2 dex higher than us. When taking into account these differences, the results are compatible. Again, this may be a clue that at $r = 250$ pc we cannot yet see the AGN impact.

In Figure 2.4 we plot the same luminosity line ratios (CO(6–5)/CO(1–0), CO(8–7)/CO(1–0) and CO(13–12)/CO(1–0) on the left panel, CO(9–8)/CO(6–5), CO(11–10)/CO(6–5) and CO(13–12)/CO(6–5) on the right panel) analysed in Figure 2.3, as a function of F_X only, since both H_X and ξ_{eff} were showing, compared to F_X, less defined trends. The other CO line ratios and their regression fits, as function of F_X, are presented in Appendix A.1.

Compared to the PDR results shown in Figure 2.3, for the XDR we find lower regression slopes: $0.1 - 0.5$ for the CO(1–0) ratios, $0 - 0.2$ for the CO(6–5) ratios. We interpret this as a sign that F_X is not the dominant driver of these CO lines either. Given the physics of high-J CO line emission, which originates from warm molecular gas, the
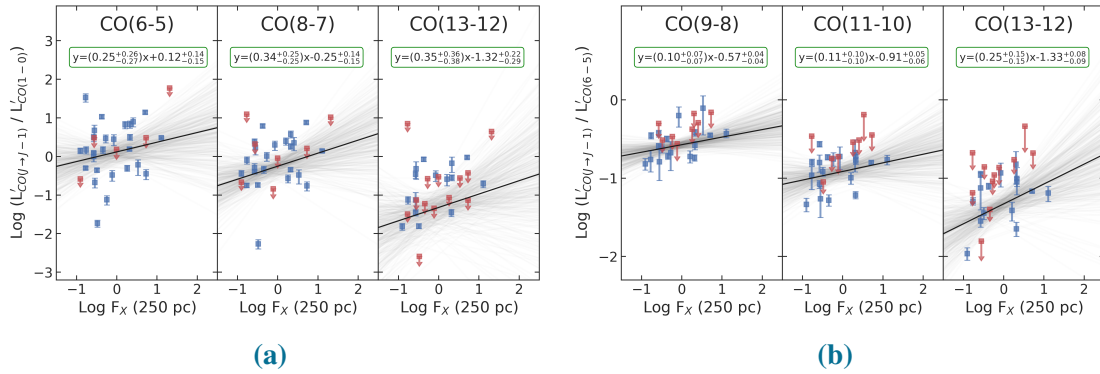
Figure 2.4: CO ratios as a function of F_X, in units of erg s^{-1} cm^{-2}, derived at $r = 250$ pc (see Section 2.5.2). We consider both the luminosity ratios $L'_{CO(J \rightarrow J-1)}/L'_{CO(1 \rightarrow 0)}$ with respect to the CO(1–0) (left panel, 2.4a) and $L'_{CO(J \rightarrow J-1)}/L'_{CO(6 \rightarrow 5)}$ with respect to the CO(6–5) line luminosity (right panel, 2.4b). The luminosities L' are in units of K km s^{-1} pc^{-2}, and J is indicated on the top of each panel. Blue squares indicate 3σ detections in both lines; red squares with downward arrow indicate $< 3\sigma$ detections in the higher-J line. The solid black line is the regression fit, with the underlying grey lines showing the fits drawn from the posterior distribution.

X-ray influence was expected to show up in the correlation with the line ratios, especially those with respect to the low-J CO lines, as found by many theoretical (Maloney et al., 1996; Meijerink & Spaans, 2005; Meijerink et al., 2007) and observational (van der Werf et al., 2010; Pozzi et al., 2017; Mingozzi et al., 2018) works on XDR. A plausible explanation is that at $r = 250$ pc we are still outside the actual AGN sphere of influence of the molecular gas: several studies on Seyfert galaxies (Davies et al., 2007; Kawakatu & Wada, 2008; Esquej et al., 2014; Motter et al., 2021) indeed place it within the central $r = 100$ pc. At larger radii, we cannot isolate the contribution of X-rays due to dilution with stellar FUV photons. Unfortunately, our *Herschel* CO observations have limited spatial resolution to reach such a nuclear region, and ALMA is still limited to the low/mid-J lines, at least in the Local Universe.

2.5.3 Comparison with models

We use predictions from numerical models presented in Vallini et al. (2019) to interpret the observations, in order to shed light on the dominant heating source in the molecular ISM of our galaxies. For this purpose, we use CLOUDY (Ferland et al., 2017) to compute the CO line intensities emerging from a 1-D gas slab of density n, illuminated by either FUV flux G_0 (PDR models) or a X-ray flux F_X (XDR models). The results of these simulations mainly apply for a single cloud, while we are dealing with entire galaxies (or at least their inner regions); it is therefore especially convenient to study the effect on the line ratios, rather than line fluxes or luminosities, assuming that both numerators and
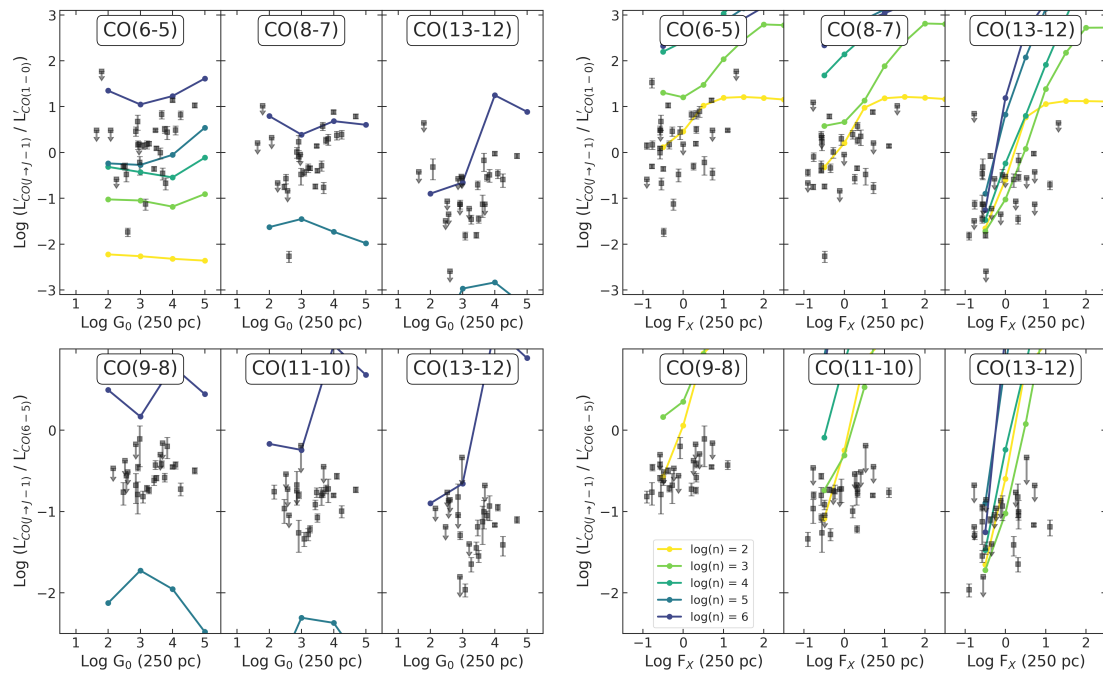
Figure 2.5: *Top-left*: G_0 vs. CO ratio to the nuclear ($r = 250$ pc) fraction of CO(1–0). *Bottom-left*: G_0 vs. CO ratio to the CO(6–5) line. *Top-right*: F_X vs. CO ratio to the nuclear ($r = 250$ pc) fraction of CO(1–0). *Bottom-right*: F_X vs. CO ratio to the CO(6–5) line. In all the plots, the points are the same of Figure 2.3 and Figure 2.4. Both G_0 and F_X are measured at $r = 250$ pc. The coloured overplotted lines are from numerical Cℒουdy models of different gas densities n, namely 10^2 (yellow), 10^3 (light green), 10^4 (aqua green), 10^5 (light blue) and 10^6 (dark blue) cm^{-3}.

denominators originate from the same area.

The gas density n is a fundamental missing quantity in our analysis of PDR and XDR. We do have some indications of its possible value: from the X-ray-derived column density, we estimated mean volume densities between $n \approx 10^{1-3}$ cm^{-3} (Section 2.3.1) within $r = 250$ pc. It is however possible, from the comparison of observed CO ratios with PDR and XDR CLOUDY models outputs, to estimate the density of the dissociation region from which the observed CO lines originate.

In the four panels of Figure 2.5, we examine the predictions for PDR and XDR models, with gas density $\log(n/\text{cm}^{-3}) = [2, 3, 4, 5]$, and with incident fluxes $\log G_0 = [2, 3, 4, 5]$ and $\log[F_X/(\text{erg s}^{-1} \text{ cm}^{-2})] = [-0.5, 0, 0.5, 1, 1.5, 2, 2.5]$, respectively. Again we explore the CO line ratio to CO(1–0) and CO(6–5), using the same three mid-/high-J lines as in Figure 2.3 and 2.4. The same plots with all the CO lines can be found at the end of Appendix A.1. The modelled points are plotted in the panels of Figure 2.5, colour coded with n.

In the PDR case, almost all our galaxies are reproduced considering densities in the $n = 10^{5-6}$ cm^{-3} range, except for the line ratios up to CO(6–5), as can be seen on the leftmost panel ($L'_{CO(6-5)}/L'_{CO(1-0)}$) of Figure 2.5, and even better in the first lines of Figure A.5 and A.6. Previous PDR studies did not find such high densities. The only exception is Mrk 231, for which van der Werf et al. (2010) obtained a warm PDR component with $G_0 = 10^{3.5}$ and $n = 10^5$ cm^{-3}; however, such a high density is necessary to reproduce the mid-J emission, while a colder PDR component, with $n = 10^{3.5}$ cm^{-3}, reproduces the low-J emission and accounts for most of the gas volume. Díaz-Santos et al. (2017) observed instead that on average, and on the scale of the whole galaxy, local (U)LIRGs start from a minimum $G_0/n \sim 10^{-1}$, and that this ratio increases with the IR luminosity surface density; this would place an upper limit to the gas density at a fixed G_0. In the top panels of Figure 2.5, instead, our galaxies, for $J_{\text{upp}} \geq 8$, lie in the range $\log(G_0/n) = [-4, -1]$, given the modelled gas densities. It is necessary for PDR models to have high densities to produce bright mid-J transitions (Vallini et al., 2018), and it is known (e.g. McKee & Ostriker, 2007) that such densities are typical of clumps and cores in single star-forming molecular clouds (as shown by Joblin et al., 2018, in e.g. the Orion Bar). Nonetheless, it is unlikely that the central 500 pc of galaxies have an average gas density of 10^{5-6} cm^{-3}, so we expect these high-density regions to have a very low volume filling factor.

In the XDR case, on the contrary, the models with low density ($n \approx 10^{2-3}$ cm^{-3}) can reproduce the observed CO line ratios, at least in the regions of the parameters space where the lines with such densities are clearly separable from the others. This result is in line with the densities ($n \approx 10^{1-3}$ cm^{-3}) calculated from the X-ray-derived N_{H}, and

from what we expect from the available XDR studies for local (U)LIRGs (van der Werf et al., 2010; Pozzi et al., 2017; Mingozzi et al., 2018). From Figure 2.5 it is clear that the observed high-J line ratios (especially $J_{upp} \geq 12$) can be reproduced by either a high F_X or a high n, a degeneracy also found in the semi-analytic model by Vallini et al. (2019). However, both our high-J line ratios and our calculated F_X are lowered by the nuclear radius we are using ($r = 250$ pc), so a detailed numerical modelling at different distances from the AGN is needed to really see the impact of XDR on the molecular emission.

We note here that stars and AGN can also affect the heating of molecular gas through outflows/winds, resulting in shock-heated regions (Kazandjian et al., 2012; Aalto et al., 2012; García-Burillo et al., 2014b) where the brightness of high-J CO lines is enhanced too. Disentangling the contribution of shock heating from that produced in XDRs is a challenging task (Hollenbach & McKee, 1989; Meijerink et al., 2013; Mingozzi et al., 2018). However, the study of mechanical heating is beyond the scope of this work.

2.6 Summary

In this work, we investigate the relative impact of star formation and AGN activity on the CO rotational line emission. In this respect, we collect multiwavelength (mm, IR and X-ray) data for a sample of 35 local active galaxies. The sources are selected with a well-sampled CO SLED (from $J = 1 - 0$ to $J = 13 - 12$) and intrinsic $L_X \geq 10^{42}$ erg s^{-1} in the 2–10 keV range. From the multiband data we derive, in a homogeneous way, key integrated physical quantities, as the molecular gas mass (M_{mol}), the star formation FUV flux (G_0) and the AGN X-ray flux, F_X. Moreover, by analysing the ALMA images of the highest available CO emission, we estimate the emitting area of mid-J/high-J CO lines, finding it concentrated within $r = 250$ pc from the centre. To determine whether AGN activity influences the molecular gas in its vicinity, we measure FUV and X-ray radiation, producing PDR and XDR, respectively, from the observational data in a self-consistent way. The FUV flux is parametrized in terms of G_0, gauged from the 70 μm, spatially resolved, dust emission, the F_X is calculated from the intrinsic L_X. Our main results can be summarized as follows:

1. On the kpc-scale of the whole galaxy (namely within a median $r_{CO} = 3.1^{+2.1}_{-1.5}$ kpc) we do not find measurable evidence for the AGN influence on the star formation. Our sample results well mixed with other samples of non-active galaxies on the Schmidt-Kennicutt (Σ_{mol} vs. Σ_{SFR}) plane. If we use a Milky Way CO-to-H$_2$ conversion factor $\alpha_{CO} = 4.3$ M$_\odot$ (K km s^{-1} pc^{-2})$^{-1}$, we find a median $\log(M_{mol}/M_\odot) = 9.9^{+0.3}_{-0.8}$ for our sample, and a median depletion time

$$\log(\tau_{\text{depl}}/\text{yr}) = 8.9^{+0.4}_{-0.6}.$$

2. We measure within $r = 250$ pc the irradiation of PDR and XDR by deriving G_0 and F_X, finding $\log G_0 = 3.1^{+0.7}_{-0.8}$ and $\log(F_X/(\text{erg s}^{-1}\text{cm}^{-2})) = -0.1^{+0.8}_{-0.5}$ for our sample. These values are comparable with the literature for local active galaxies, for both observational and theoretical works.

3. We find that neither G_0 nor F_X alone can produce the observed molecular emission, traced by two different CO line ratios, namely to the nuclear ($r = 250$ pc) fraction of CO(1–0) and to CO(6–5).

4. From the comparison of CO emission and observed G_0 with grids of PDR numerical models, we can conclude that PDR emission can reproduce observed high-J line ratios only assuming unlikely extreme gas densities ($n > 10^5$ cm^{-3}), while it is more efficient at moderate densities ($n \sim 10^{3-4}$ cm^{-3}) up to CO(6–5).

5. From the comparison between XDR observations and models, we find that F_X can reproduce the observed low-/mid-J CO line ratios only at low densities ($n \sim 10^2$ cm^{-3}), similar to those estimated from X-ray column densities ($n \sim 10^{1-3}$ cm^{-3}). At high-J we find increasing (with J) degeneracy between F_X and n, so we can not find a typical gas density for our sample. This is probably an indication that the nuclear scale at which we are considering the XDR is still too large to see a strong AGN effect on the CO SLED.

From our analysis, we conclude that, on scales of $\approx$250 pc from the galaxy centre, a mix of PDR and XDR is necessary to explain the observed CO emission, since neither of them is the dominant mechanism. The use of the CO SLED to disentangle the contribution of FUV and/or X-rays photons to the molecular gas heating in local galaxies is currently limited by the low spatial resolution at the high-J frequencies ($\sim$ 17 arcsec for CO(13–12) with *Herschel*/PACS). Conversely, high-z galaxies have their high-J CO emission redshifted into the observation bands of ALMA and NOEMA, which are able to reach sub-arcsec resolution. These extreme CO lines have been observed and modelled already by several works (Gallerani et al., 2014; Carniani et al., 2019; Pensabene et al., 2021). It would be therefore interesting to extend the analysis performed in this work on a high-redshift sample of active galaxies with spatially resolved CO emission, and assess possible differences with local AGN.

3

Modelling molecular clouds and
CO excitation in AGN-host galaxies

This chapter is drawn from "*Modelling molecular clouds and CO excitation in AGN-host galaxies*", **Esposito F.**, Vallini L., Pozzi F., Casasola V., Alonso-Herrero A., García-Burillo S., Decarli R., Calura F., Vignali C., Mingozzi M., Gruppioni C., and Sengupta D., 2024, MNRAS, 527, 8727.

3.1   Introduction

Two radiation sources dominate the molecular gas heating in active galaxies: OB stars, emitting far-ultraviolet (FUV, $6 - 13.6$ eV) radiation, and the AGN, through hard X-rays ($E > 1$ keV) emission. FUV and X-ray photons create the so-called photo-dissociation regions (PDRs, Hollenbach & Tielens, 1997; Wolfire et al., 2022) and X-ray dominated regions (XDRs, Maloney et al., 1996; Wolfire et al., 2022), respectively. Usually, low-J CO lines trace FUV-heated gas within PDRs, while high-J lines are XDR tracers (Wolfire et al., 2022). This is due to the increasing critical density and excitation temperatures of the CO rotational transitions as a function of their quantum number J ($n_{\mathrm{crit}} \propto (J + 1)^3$) and to the fact that X-rays can penetrate at larger column densities with respect to FUV photons (Maloney et al., 1996; Meijerink & Spaans, 2005), thus keeping the dense gas warmer.

Many works in literature exploit the observed CO SLED of active galaxies (e.g. van der Werf et al., 2010; Pozzi et al., 2017; Mingozzi et al., 2018) to infer the global molecular gas properties (e.g. density, temperature) and the heating mechanism acting on the molecular gas (FUV from star formation, and/or X-ray from AGN). This is done by searching for the best-fit PDR and XDR models reproducing the CO SLED. PDR and XDR models are radiative transfer calculations that compute the line emissivity given

the incident radiation field, the gas density, the metallicity, and other free parameters set by the user (see Wolfire et al., 2022, for a recent review). This approach is obviously a simplification, because the gas density and the heating mechanism inferred from the CO SLED fitting are global average values over the whole galaxy. In fact, most of the PDR and XDR models do not account for the spatial distribution of GMCs in the galaxy and/or for their internal structure.

In Section 2.5.3 we used alike single-density models to interpret the CO SLED of a sample of 35 local AGN-host galaxies, for which we gathered a wealth of multiwavelength observations. We found that PDR models could reproduce the high-J CO lines only by using very high density ($n > 10^5$ cm^{-3}), while XDR models need more moderate ($n \sim 10^3$ cm^{-3}) densities.

With the aim of improving the characterization of the molecular gas properties in AGN-host galaxies we build a new, physically-motivated, model that couples PDR and XDR radiative transfer (RT) calculation with the internal structure of GMCs, and their observed distribution within the galaxy disc. This is done by integrating single-density single-flux RT predictions, performed with Cloudy (Ferland et al., 2017), into a more complex model able to catch the gas distribution properties of a galaxy, building upon previous analysis by Vallini et al. (2017, 2018, 2019). We apply the model to the sample analysed in Chapter 2, but the general goal is that of providing a flexible modelling tool exploitable for any AGN-host source.

This Chapter is structured as follows: in Section 3.2 we describe how we model (i) the internal structure of GMCs, (ii) the RT within the GMCs, and (iii) the mass distribution of GMCs within a galaxy. We test the model on a sample of AGN-host galaxies, described in Section 3.3, and in Section 3.4 we present the model results. We discuss them in Section 3.5 and we draw our conclusions in Section 3.6. For all the revelant calculations, we assume a ΛCDM cosmology with $H_0 = 70$ km s^{-1} Mpc^{-1}, $\Omega_m = 0.3$ and $\Omega_\Lambda = 0.7$.

3.2 Model outline

We build a physically motivated model[1] that decribes the interaction of the radiation from AGN and star formation with the molecular gas in galaxies. This model takes the Vallini et al. (2017, 2018, 2019) works - focused on the far-infrared (FIR) and molecular line emission from GMCs in high-z galaxies - as starting point. In those works, single GMCs were modelled as collections of clumps in a log-normal density distribution, their CO SLEDs were computed with radiative transfer calculations, and a galaxy was filled with

---

[1]We publicly release the code, called `galaxySLED`, on GitHub (`https://federicoesposito.github.io/galaxySLED/`) along with a Jupyter notebook tutorial.
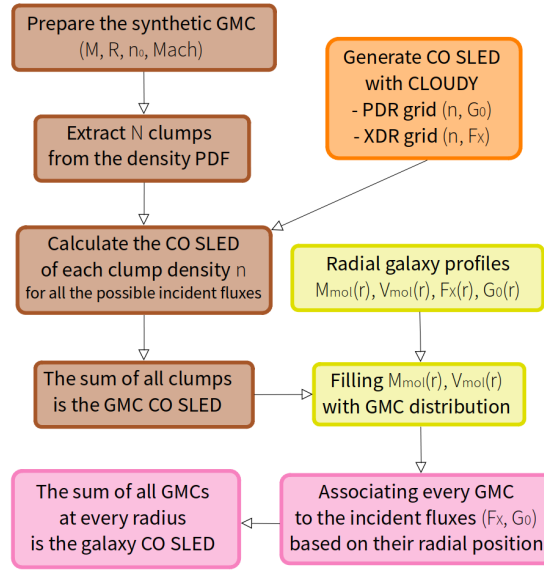
Figure 3.1: A sketch of the workflow followed in this Chapter. First, we define a synthetic GMC with four physical variables $(M, R, n_0, \mathcal{M})$, which define the density distribution of its molecular clumps (as described in Section 3.2.1). We combine CLOUDY results to generate the CO SLED of each clump and of the synthetic GMC (see Section 3.2.2). Having collected the four radial profiles for a real galaxy $(M_{\mathrm{mol}}(r), V_{\mathrm{mol}}(r), G_0(r), F_{\mathrm{X}}(r))$, we filled it with the GMC distribution described in Equation (3.4), we associate every GMC with the corresponding incident fluxes, and eventually we have the CO SLED of the studied galaxy.

a uniform distribution of identical GMCs. The aim of the present work is to extend such analysis, including different GMCs in single galaxies (following a mass distribution), and illuminating them with a differential radiative flux (following observed radial profiles).

Figure 3.1 shows a sketch that summarizes its modular structure, which from the sub-pc scales of clumps within GMCs (see Sec. 3.2.1) progressively zooms-out to the kpc scales of the gas distribution within galaxies (see Sec. 3.2.3). More precisely, Section 3.2.1 deals with the analytical description of the internal structure and mass distribution of GMCs, Section 3.2.2 outlines the RT modelling implemented to compute the CO emission, whereas in Sec. 3.2.3 we present our assumptions concerning the molecular gas distribution on kpc-scales and the resulting total CO emission from galaxies.

3.2.1 GMC internal structure and mass distribution

We characterize GMCs with four physical parameters: the total mass (M), the GMC radius (R), the mean density (ρ_0) and the Mach number $(\mathcal{M})$. The density structure of GMCs (see e.g. Hennebelle & Falgarone, 2012) is well described by a log-normal distribution (Vazquez-Semadeni, 1994; Padoan & Nordlund, 2011; Federrath et al., 2011;

68
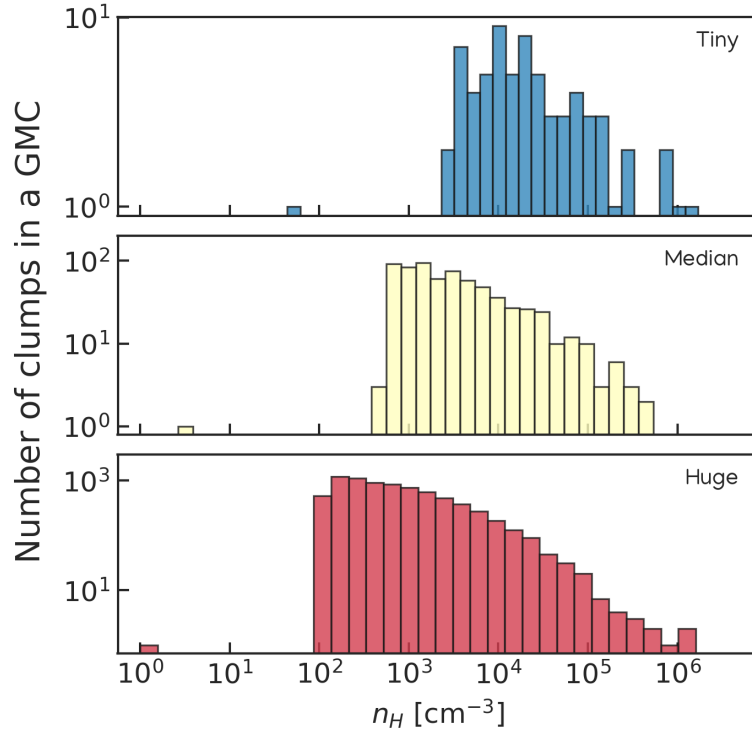
Figure 3.2: Histograms of clumps density distributions within the three GMCs listed in Table 3.1. The shapes are set from Equation 3.1, and mainly depend on each GMC mean number density n_0.

Vallini et al., 2017). The volume-weighted probability distribution function (PDF) of gas density ρ, in a supersonically turbulent, isothermal cloud of mean density ρ_0, is

$$p_s \, ds = \frac{1}{\sqrt{(2\pi\sigma_s^2)}} \exp\left[-\frac{1}{2}\left(\frac{s-s_0}{\sigma_s}\right)^2\right] ds \quad , \tag{3.1}$$

where $s = \ln(\rho/\rho_0)$ is the logarithmic density, with mean value $s_0 = -\sigma_s^2/2$. The standard deviation of the distribution, σ_s, depends on $\mathcal{M}$ and on the b factor, which parametrizes the kinetic energy injection mechanism (often referred to as forcing) driving the turbulence (Molina et al., 2012):

$$\sigma_s^2 = \ln\left(1 + b^2\mathcal{M}^2\right) \quad . \tag{3.2}$$

We assume $b = 0.3$, which is the value for purely solenoidal forcing (Federrath et al., 2008; Molina et al., 2012).

We define a GMC as a spherical collection of clumps, whose densities are distributed following the PDF in Equation (3.1). Accounting for the presence of clumps within the GMCs is one of the fundamental features of this work, as dense clumps emit the bulk
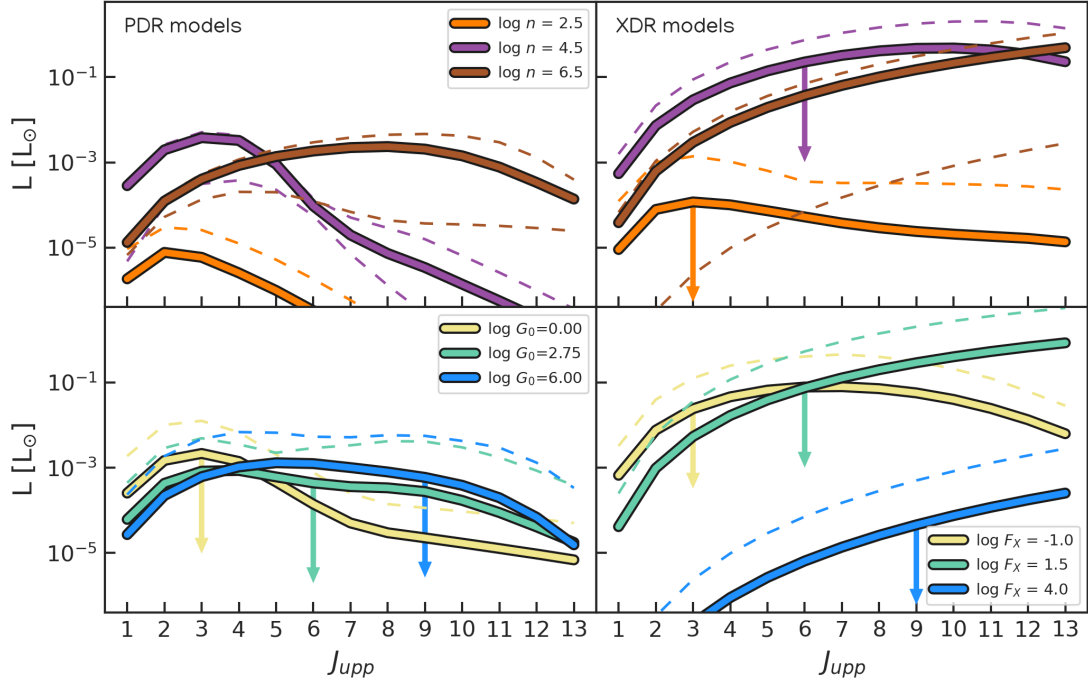
Figure 3.3: Synthetic CO SLEDs from CO(1 − 0) to CO(13 − 12) for spherical molecular clumps of radius $R = R_J$ (Equation 3.3). The clump fluxes have been converted to solar units. Left and right panels are PDR and XDR models, respectively. In the upper panels the orange, purple, and brown lines represent the mean CO SLED for $\log n = 2.5, 3.5, 4.5$ cm^{-3}, respectively, with the incident flux (G_0 for PDRs, F_X for XDRs) left free to vary over the ranges $10^0 - 10^6$ and $10^{-1} - 10^4$ erg s^{-1} cm^{-2}, respectively. In the lower panels the yellow, green, and blue lines represent the median CO SLED for $\log G_0 = 0.0, 2.75, 6.0$ (bottom-left panel) and for $\log F_X = -1.0, 1.5, 4.0$ erg s^{-1} cm^{-2} (bottom-right panel), respectively, while the volume density is left free to vary over the range $10^0 - 10^{6.5}$ cm^{-3}. In all panels the solid lines represent the mean CO SLED, while the dashed lines with the same colors show the minimum and maximum CO SLEDs at the given density or incident flux. If the minimum luminosity of a given SLED is out of the plot, then the median curve is plotted with a downward arrow to highlight the presence of very low luminosities.

Name	M [$M_\odot$]	R [pc]	n_0 [cm^{-3}]	N_{clumps}
Tiny	1.3×10^3	1.5	2755.6	69
Median	3.2×10^4	7.7	549.8	674
Huge	7.9×10^5	38.6	109.7	7644

Table 3.1: Main properties of the smallest, median and largest GMCs in the mass distribution described in Section 3.2.1. The columns are the mass, radius, mean number density and number of extracted clumps.

of the CO luminosity ($n_{\text{crit}} > 10^4$ cm^{-3} for $J \geq 2$, Carilli & Walter, 2013). We then randomly extract clumps with $\rho \geq \rho_0$ from the PDF and for each of them we calculate its Jeans mass, $M_J = (4\pi/3)R_J^3 \mu m_p n$, and the Jeans radius:

$$R_J(n) = \sqrt{\frac{\pi c_s^2}{G\rho}} \quad . \tag{3.3}$$

Here $c_s = \sqrt{\gamma k_B T/(\mu m_p)}$ is the sound speed, that depends, after we set the adiabatic index to $\gamma = 5/3$ and the mean molecular weight to $\mu = 1.22$, only on the gas temperature T and the clump number density n. We assume a fixed temperature of $T = 10$ K for all our clumps, which is the typical value for dense clumps in molecular clouds (Spitzer, 1978; Hughes et al., 2016; Elia et al., 2021). We proceed with the clumps extraction until we fill the entire GMC mass (with a 10% tolerance). Following Vallini et al. (2017), we distribute the leftover mass through the whole GMC, accounting for what we define *intraclump* medium (ICM).

We consider 15 different GMC models, with masses in the range $M = 10^3 - 10^6$ M$_\odot$ (0.2 dex steps), and a fixed surface density $\Sigma = 170$ M$_\odot$ pc^{-2} (McKee & Ostriker, 2007). This translates into GMCs radii in the range $R = 1 - 40$ pc, and mean number densities, $n_0 = 3M/(\mu m_p 4\pi R^3)$, in the range $n_0 = 10^2 - 3 \times 10^3$ cm^{-3}. The Mach number is set to $\mathcal{M} = 10$ for all the GMCs in this work (Krumholz & McKee, 2005). In Figure 3.2 we plot the distribution in density of the clumps within the three GMCs listed in Table 3.1: different GMCs (shown with different colors) have a different peak in the clumps density distribution, since they have a different mean density n_0. The ICM appears, in Figure 3.2, in single clumps at low-end densities.

The observed GMC mass distribution in galaxies is well approximated by a power-law (see Chevance et al., 2023b, for a recent review). In particular, we follow Roman-Duval et al. (2010) and Dutkowska & Kristensen (2022) and we set the mass distribution as follows:

$$\frac{dN}{dM} \propto M^{-1.64}. \tag{3.4}$$
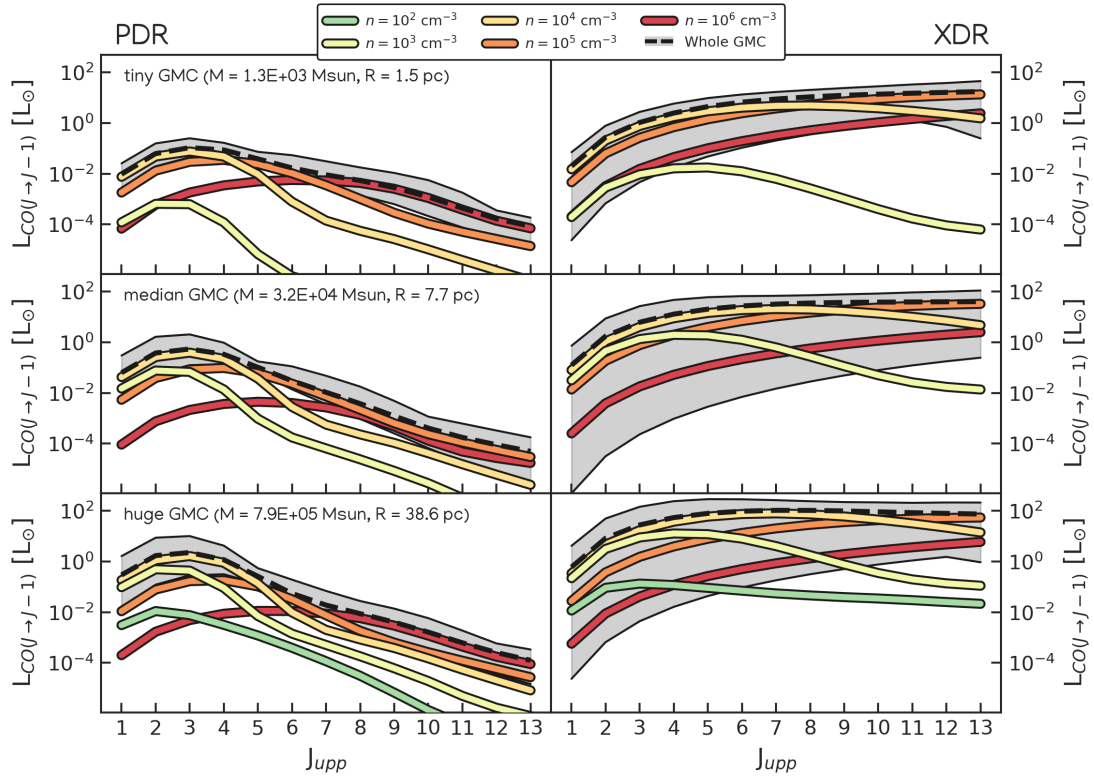
Figure 3.4: CO SLED of the three GMCs listed in Table 3.1. The dashed black lines represent the CO SLED of the tiny (upper panels), median (middle panels), huge (lower panels) GMC models, while the grey shaded area highlights the variation in the GMC CO SLED produced by changing the incident flux. Left panels are for PDR models (i.e. the incident flux range is $10^0 \leq G_0 \leq 10^6$), right panels are for XDR models (i.e. the incident flux range is $10^{-1} \leq F_X/(\text{erg s}^{-1} \text{ cm}^{-2}) \leq 10^4$). The colored lines highlight the contribution of the clumps within each GMC, as a function of their density n.

Equation (3.4) has been derived by fitting the observed GMC mass distribution in the Milky Way with a power-law, albeit only in the mass range $M = 10^5 - 10^6$ M$_\odot$ due to observational limits that make it hard to sample the distribution towards the low-mass end (Roman-Duval et al., 2010). Dutkowska & Kristensen (2022) extrapolate the relation down to $M = 10^4$ M$_\odot$, but in this work we extrapolate Equation (3.4) down to $M = 10^3$ M$_\odot$, because we expect the majority of GMCs in galaxies to be small and with low masses (e.g. Fukui & Kawamura, 2010; Colombo et al., 2014; Rosolowsky et al., 2021).

We verified that the choice of different power-law exponents for Equation (3.4), namely 1.39, 1.89 and 2.5, corresponding to the lowest and highest values in Roman-Duval et al. (2010) and the highest value from Chevance et al. (2023b) does not greatly affect our results. In Table 3.1, we list the two extremes in mass, labelled as "Tiny" and "Huge", respectively, and the "Median" GMCs, extracted from the distribution.

3.2.2   Radiative transfer modelling

We use Cloudy (version 17.02, Ferland et al., 2017) to model the CO line emission from a 1-D gas slab with constant density n and irradiated by a stellar or AGN incident flux. In what follows we label a Cloudy run as "PDR-model" if the incident far-ultraviolet (FUV) photons flux is produced by a stellar population. As it is a standard in PDR studies (Wolfire et al., 2022) the FUV flux (G_0) is parametrized in terms of the Habing field 1.6×10^{-3} erg s^{-1} cm^{-2} (Habing, 1968), which equates to $G_0 = 1$. Conversely, we label a run as "XDR-model" if the incident flux F_X (in the $1 - 100$ keV range) comes from an AGN.

For PDR models we adopt the Spectral Energy Distribution (SED) of the incident radiation from the stellar population synthesis code Starburst99 (Leitherer et al., 1999), assuming a continuous star formation model with age $t = 10$ Myr and solar metallicity, and $\log(G_0) = 0 - 6$. In the XDR models, we use $\log[F_X/(\text{erg s}^{-1} \text{ cm}^{-2})] = -1 - 4$, and the SED is set with the Cloudy command `table xdr`, that generates a truncated AGN X-ray SED, $f_\nu \propto h\nu^{-0.7}$, in the 1–100 keV range (see Maloney et al., 1996, for details).

The second free parameter in the PDR and XDR models is the gas density n. To cover the density range of clumps and ICM in GMCs (see Section 3.2.1), we consider a grid of Cloudy runs spanning $\log(n/\text{cm}^{-3}) = 0 - 6.5$. The ranges of n, G_0 and F_X have logarithmic steps of 0.25 dex. All our Cloudy runs assume solar metallicity for the gas, and elemental abundances from Grevesse et al. (2010). Moreover, we account for the Cosmic Microwave Background ($T_{CMB} = 2.7$ K), the Milky Way cosmic ray ionisation rate, $\zeta = 2 \times 10^{-16}$ s^{-1} (Indriolo et al., 2007), and we set the turbulence velocity $\upsilon = 1.5$ km s^{-1} (see Pensabene et al., 2021).

Cloudy solves the RT through the gas slab by dividing it into a large number of thin layers. Starting at the illuminated face of the slab, it computes the cumulative emergent flux at every layer. While in this work we are interested in the CO lines from CO($1 - 0$) to CO($13 - 12$), Cloudy also computes other molecular and atomic lines (e.g. HCN, HCO$^+$, [CII]) that we store in our database. We compute the emergent line emission up to a total gas column density of $\log(N_H/\text{cm}^{-2}) = 24.5$: this choice allows us to fully sample the molecular part of the irradiated gas clouds, typically located at $N_H > 2 \times 10^{22}$ cm^{-2} (McKee & Ostriker, 2007). The CO emission from a GMC is obtained by interpolating the Cloudy outputs at the density n_i and radius R_i for each i-th clump and then summing up all the clumps luminosities.

3.2.2.1 The CO SLED of single clumps and GMCs

In what follows, we first discuss the resulting CO SLED from clumps of different densities within a given GMC, noting that the luminosity of each i-th clump is $L = 4\pi R_i^2 F_{CO}(R_i)$, where $F_{CO}(R_i)$ is the flux computed by Cloudy. This is shown in Figure 3.3.

As shown in the upper panel of Figure 3.3 the CO SLEDs for XDR clump models are overall brighter at a given gas density, with respect to the CO SLEDs of PDR clump models. Leaving the incident flux free to vary (upper panels of Figure 3.3) has a limited effect in the CO cooling energy output of PDR models (top-left panel). Varying the incident flux seems more important in XDR models (top-right panel), since the derived CO SLED luminosities can decrease by more than four orders of magnitudes (as pointed by the downward arrows in the top-right panel of Figure 3.3).

Leaving the density free to vary while fixing the incident flux, however, could make the CO SLED luminosity range over several orders of magnitude for any possible value of incident flux, both for PDR and XDR models (bottom panels of Figure 3.3). The very low-luminosity SLEDs correspond to the lowest densities computed ($\log n/\text{cm}^{-3} = 0$). It is interesting to note that the highest F_X values, which correspond to clumps closer to the AGN, return very faint CO SLEDs: this is because high X-ray photon fluxes lead to the CO dissociation (see Wolfire et al., 2022, for a recent review of XDR processes).

As detailed in Section 3.2.1, for a given modelled cloud we have a list of extracted clumps. Once the contribution from the various clumps in the GMC is accounted for, by summing up their CO luminosity, the global CO SLED of a GMC depends on the incident flux only. In Figure 3.4, we show the CO SLED for the three GMCs listed in Table 3.1. The variation in the GMC CO SLED introduced by spanning the whole G_0 and F_X ranges is highlighted by a grey shaded area. We note that varying G_0 has a limited effect on the predicted CO SLEDs (left panels in Figure 3.4), as opposed to varying F_X (right panels).

In Figure 3.4 we plot the contribution of clumps of different densities to the global GMC CO SLED. PDR models (left panels of Figure 3.4) are dominated by clumps with density $n = 10^4, 10^5, 10^6$ cm^{-3} in the low ($J \leq 4$), medium ($5 \leq J \leq 7$) and high-J ($J \geq 8$) transitions, respectively. In the XDR case (right panels of Figure 3.4), instead, the very high-density clumps ($n \sim 10^6$ cm^{-3}) never dominate the CO SLED: their contribution is always at least one order of magnitude lower than clumps with $n = 10^4 - 10^5$ cm^{-3}. However, as can be noticed in Figure 3.3, the very high-density clumps can sustain a high XDR emission only when a large incident flux ($F_X \sim 10^4$ erg s^{-1} cm^{-2}) is present. This is because at high volume and, thus, column densities ($N_H = nR_J \propto n^{1/2}$), the molecular gas is efficiently shielded from external radiation, so
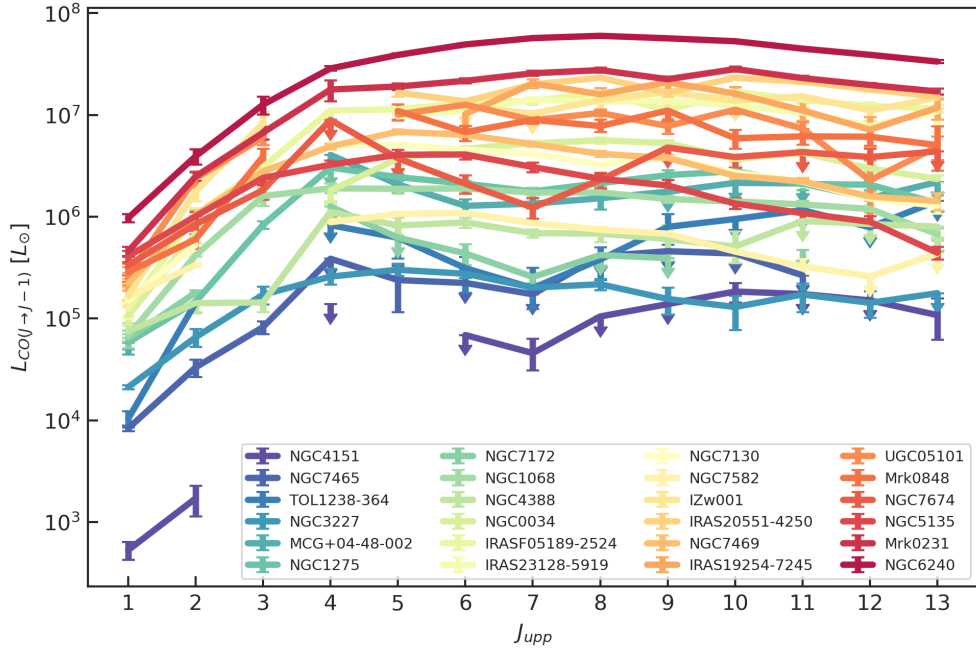
Figure 3.5: Observed CO SLED of our AGN sample, composed of 24 galaxies. The order of the objects depends on their molecular mass within a radius of $2r_{CO}$ (blue is low, red is high, with the range being $[5 \times 10^7 - 9 \times 10^{10}]$ M$_\odot$ when calculated with a Milky-Way α_{CO}). Downward arrows are upper limits.

that only a large incident flux can penetrate the gas. The same argument applies to PDRs.

3.2.3 Galaxy radial profiles

In this Section we describe how we distribute the GMCs throughout the galaxy volume, and how we associate to each GMC an incident flux (G_0 or F_X) depending on the position within the galaxy. To do so, we need the radial profiles of the molecular mass $M_{mol}(r)$, the molecular volume $V_{mol}(r)$, the FUV flux $G_0(r)$, and the X-ray flux $F_X(r)$. Spatially resolved observations of nearby galaxies have shown that low-J CO emission is well described by an exponential profile along the galactocentric radius r (Boselli et al., 2014; Casasola et al., 2017, 2020), with scale factor $r_{CO} = 0.17r_{25}$, where r_{25} is the radius of the galaxy at the isophotal level 25 mag arcsec^{-2} in the B-band. The CO$(1-0)$ emission can be converted into the molecular mass by adopting a CO-to-H$_2$ conversion factor α_{CO} (e.g. Bolatto et al., 2013, for a review). We adopt the Milky Way value of $\alpha_{CO} = 4.3$ M$_\odot$ (K km s^{-1} pc^2)$^{-1}$ (which includes the helium contribution) as our initial fiducial value, but we will discuss the effect of relaxing this assumption in Section 3.5.1. We thus obtain the following cumulative molecular mass radial profile:

$$M_{mol}(r) = 2.08 \times 10^4 \, \alpha_{CO} \, L_{CO,tot} \, [1 - e^{-r/r_{CO}}(r/r_{CO} + 1)] \qquad (3.5)$$

75

where $L_{CO,tot}$ is the CO(1 − 0) luminosity of the whole galaxy in $L_{\odot}$, M_{mol} is in $M_{\odot}$. This molecular gas mass is also confined within a volume radial profile $V(r)$. We approximate the galaxy as a disc, with half-height $z_{CO} = 0.01r_{25}$ (Boselli et al., 2014; Casasola et al., 2020), in its external part, while in its inner part ($r < 1.5\,z_{CO}$) we use the equation for a sphere:

$$V_{mol}(r) = \begin{cases} (4/3)\pi r^3 & \text{for } r \leq 1.5\,z_{CO} \\ 2\pi z_{CO} r^2 & \text{for } r \geq 1.5\,z_{CO} \end{cases} \tag{3.6}$$

The profile $V(r)$ changes at $r = 1.5z_{CO}$ to ensure a smooth transition between the spherical and the disc-like regions. Equations (3.5) − (3.6) imply that the molecular gas volume density $\rho_{mol}(r)$ increases towards small radii. The gas surface density $\Sigma(r)$ is instead roughly constant in the central part (i.e. at $r \lesssim r_{CO}$), and decreases exponentially as $\Sigma_{mol}(r) = \Sigma_{mol}(0)e^{-r/r_{CO}}$.

In our model the molecular gas – distributed according to Equations (3.5) − (3.6) – is irradiated by a FUV or X-ray flux that depend on the galactocentric radius. Following Chapter 2, we model $G_0(r)$ with a Sersic function (Sérsic, 1963):

$$G_0(r) = G_0(r_e) \exp\left\{-b_n \left[\left(\frac{r}{r_e}\right)^{1/n} - 1\right]\right\} \tag{3.7}$$

which is characterized by three parameters: the effective radius r_e, the shape parameter n and the normalization $G_0(r_e)$. We assume a minimum $G_0 = 1$ at every radius, which is equal to the Milky Way interstellar radiation field (ISRF).

The X-ray profile, $F_X(r)$, is derived from the intrinsic X-ray luminosity L_X, in the $1 − 100$ keV range. Given the importance of the attenuation of the X-ray flux due to obscuring gas, usually measured in terms of gas column density $N_H(r)$, we use the following formula (Maloney et al., 1996; Galliano et al., 2003):

$$F_X(r) = \frac{L_X}{4\pi r^2} N_{22}(r)^{-0.9} \tag{3.8}$$

where $N_{22}(r) = N_H(r)/10^{22}$ cm^{-2}.

From the derived radial profiles of the molecular mass and volume, we can easily compute the column density radial profile as

$$N_H(r) = \int_0^r n_H(x)\, dx = \int \frac{M_{mol}(x)}{\mu m_p V_{mol}(x)}\, dx \quad . \tag{3.9}$$

Whenever the gas column density $N_H(r) < 10^{22}$ cm^{-2}, due to the marginal impact on the X-rays attenuation (e.g. Hickox & Alexander, 2018), we use the classical definition

$F_X(r) = L_X/(4\pi r^2)$. We term this "Baseline model", as it is also possible to fit the average N_H value from the observed CO SLEDs (see Section 3.4). We will discuss in detail the effect of $N_H(r)$ in Section 3.5.2.

3.3   The dataset

In Chapter 2, we gathered a wealth of observational data for a sample of 35 local ($z \leq 0.15$) AGN-host galaxies. For each source we collected: CO line luminosities from CO($1-0$) to CO($13-12$), mostly coming from *Herschel* observations; the optical radius r_{25} (from the HyperLeda[2] database); the total IR luminosity L_{IR} ($8-1000\ \mu$m), mostly from IRAS observations; the intrinsic X-ray luminosity L_X ($2-10$ keV) and the obscuring column density of the X-ray photons, $N_{H, X\text{-ray}}$, from a variety of X-ray observatories; and the FIR flux (observed by *Herschel*) from which we derived the FUV field radial profile, $G_0(r)$ (i.e. the three parameters of Equation 3.7: $G_0(r_e)$, r_e, and n). Any change in the data with respect to Chapter 2 is reported in Appendix B.1.

First of all, we select a sub-sample of the 35 galaxies analysed in Chapter 2. We adopt the following selection criteria: (i) the availability of the CO($1-0$) detection, necessary for the derivation of the molecular gas mass of a galaxy; (ii) the availability of both incident flux radial profiles, i.e. $G_0(r)$ and $F_X(r)$; (iii) an apparent optical radius $r_{25} \leq 250\ ''$, since larger objects would have a r_{CO} larger than the CO beams; (iv) at least three CO detections (i.e. without counting the upper limits) between CO($1-0$) and CO($13-12$), to ensure we have enough data points to make a meaningful comparison with the model output. These selection criteria reduce our sample to 24 active galaxies. We list, in Table 3.2, the r_{CO}, the median $G_0(r)$, the L_X and the $N_{H, X\text{-ray}}$ of each galaxy in the sample.

The parent sample was selected considering the availability of *Herschel* data, and being their intrinsic X-ray luminosity $L_X \geq 10^{42}$ erg s^{-1} in the $2-10$ keV range. The sample of 24 objects considered in this work is composed by nearby ($z \leq 0.062$) moderately powerful ($L_X \leq 10^{44}$ erg s^{-1}) AGN-host galaxies, but at the same time they display a wide variety of physical properties. Four galaxies of our sample (IRAS 19254$-$7245, IRAS 23128$-$5919, Mrk 848, and NGC 6240) are clear mergers, while other six (IRAS F05189$-$2524, IRAS 20551$-$4250, Mrk 231, NGC 34, NGC 1275, and UGC 5101) show some signs of interaction as tidal tails. The rest of the sample has a spiral-like morphology. Half of the galaxies (12/24) are luminous infrared galaxies (LIRGs: $10^{11} \leq L_{IR} < 10^{12}$ L$_\odot$), while 5 are ultra-LIRGs (ULIRGs: $L_{IR} \geq 10^{12}$ L$_\odot$).

---

[2] http://leda.univ-lyon1.fr

Almost all of the galaxies (22/24) have their nuclear activity classified as Seyfert, with the exceptions of Mrk 848 and IRAS 20551−4250 which are classified as low-ionisation nuclear emission-line regions (LINERs). NGC 1275 (also known as 3C 84, Perseus A) is the only radio-galaxy of our sample, and it is also the central dominant galaxy in the Perseus Cluster. Two of the furthest galaxies (Mrk 231 and I Zw 1) are also commonly classified as quasi-stellar objects (QSOs). We refer to Chapter 2 for further details on the galaxy sample and data collection. The CO SLEDs of all the objects in our sample are shown in Figure 3.5.

3.4 Results

The model takes into account the radial profiles defined in Equations (3.5) − (3.9) to spatially distribute the 15 GMCs described in Section 3.2.1 in a real galaxy. The profiles for all the galaxies in the sample are presented in Figure B.1. We divide these profiles into logarithmically-spaced radial bins. Based on some tests, we adopt a 0.05 dex bin size, starting from $r_{\min} = 10^{-3}$ kpc, and up to $r_{\max} = 2r_{\mathrm{CO}}$. First, since for every bin we know the molecular mass and the molecular volume, we extract random GMCs from the distribution (Equation 3.4), until we fill up the entire mass and/or volume of the bin. Then, we associate each GMC, in each radial bin, with the matching incident fluxes $G_0(r)$, $F_{\mathrm{X}}(r)$, and finally produce the expected CO SLED of each galaxy.

3.4.1 The different models

The molecular mass of a galaxy is highly dependent on the choice of the CO-to-H_2 conversion factor α_{CO}, while the X-ray flux can be strongly attenuated by gas clouds between the AGN and the GMCs which we parametrize in terms of a hydrogen column density profile $N_{\mathrm{H}}(r)$.

The model discussed in Section 3.2 assumes a default Milky-Way value of $\alpha_{\mathrm{CO}} = 4.3$ M$_\odot$ (K km s^{-1} pc^2)$^{-1}$, and the intrinsic $N_{\mathrm{H}}(r)$ profile from Equation (3.9). We label this "Baseline model".

For each galaxy we search also for the "Best-fit model" following the Bayesian Markov chain Monte Carlo (MCMC) method: we use the χ^2 likelihood function to fit the observed CO SLED and determine the posterior probability distribution of the model parameters, i.e. α_{CO} and N_{H}, with uniform prior distributions $\alpha_{\mathrm{CO}} = [0.43, 43]$ M$_\odot$ (K km s^{-1} pc^2)$^{-1}$ and $N_{\mathrm{H}} = [10^{22}, 10^{25}]$ cm^{-2}. In this model, N_{H} has a constant value at every radius, and it acts as an average N_{H} seen by the GMCs. To run the MCMC algorithm, we use the open-source Python package emcee (Foreman-Mackey et al.,

Table 3.2: Properties and results on the sample of 24 AGN.

Name	r_{CO} (kpc)	$\log M_{mol}$ (M$_\odot$)	$\log G_0$	$\log L_X$ (erg s^{-1})	$\log N_{H,X}$ (cm^{-2})	$f_{PDR}^{(1-0)}$	$f_{XDR}^{(1-0)}$	$f_{PDR}^{(4-3)}$	$f_{XDR}^{(4-3)}$	α_{CO}	$\log N_H$ (cm^{-2})
I Zw 1	2.78	10.36	1.64	43.6	–	0.76	0.20	0.24	0.80	$6.6^{+1.7}_{-1.7}$	$23.50^{+0.37}_{-0.28}$
IRAS F05189−2524	2.15	9.74	3.83	43.2	22.86	0.17	0.02	0.83	0.98	$2.1^{+0.4}_{-0.2}$	$22.09^{+0.12}_{-0.04}$
IRAS 19254−7245	3.83	10.55	3.94	42.8	23.58	0.57	0.11	0.43	0.89	$7.3^{+1.5}_{-0.9}$	$22.11^{+0.10}_{-0.05}$
IRAS 20551−4250	2.92	10.46	4.22	42.3	23.69	0.64	0.14	0.36	0.86	$7.2^{+0.9}_{-0.6}$	$22.04^{+0.04}_{-0.02}$
IRAS 23128−5919	4.18	10.15	3.71	43.2	–	0.46	0.07	0.54	0.93	$5.5^{+1.0}_{-0.4}$	$22.08^{+0.10}_{-0.03}$
MCG +04−48−002	1.45	9.85	2.54	43.1	23.86	0.81	0.27	0.19	0.73	$7.3^{+1.3}_{-1.3}$	$23.96^{+0.10}_{-0.12}$
Mrk 231	5.99	10.95	4.77	42.5	22.85	0.86	0.34	0.14	0.66	$9.4^{+0.5}_{-0.5}$	$22.02^{+0.01}_{-0.02}$
Mrk 848	2.62	10.26	3.72	42.3	23.93	0.66	0.15	0.34	0.85	$3.1^{+0.4}_{-0.3}$	$22.05^{+0.04}_{-0.03}$
NGC 34	2.33	10.20	2.93	42.1	23.72	0.77	0.21	0.23	0.79	$7.1^{+0.5}_{-0.8}$	$22.07^{+0.03}_{-0.04}$
NGC 1068	2.46	9.88	3.69	42.4	24.70	0.80	0.24	0.20	0.76	$5.4^{+0.9}_{-0.5}$	$22.40^{+0.04}_{-0.04}$
NGC 1275	3.89	8.78	3.60	44.0	21.68	0.25	0.02	0.75	0.98	$0.5^{+0.1}_{-0.0}$	$22.11^{+0.17}_{-0.08}$
NGC 3227	1.62	8.94	3.00	42.1	20.95	0.74	0.16	0.26	0.84	$2.0^{+0.2}_{-0.3}$	$22.53^{+0.07}_{-0.09}$
NGC 4151	1.01	7.30	2.28	42.3	22.71	0.66	0.11	0.34	0.89	$1.8^{+0.7}_{-0.5}$	$22.66^{+1.02}_{-0.47}$
NGC 4388	4.74	9.16	2.90	42.6	23.50	0.87	0.30	0.13	0.70	$0.9^{+0.1}_{-0.1}$	$22.02^{+0.01}_{-0.02}$
NGC 5135	3.42	10.27	3.11	42.0	24.47	0.86	0.32	0.14	0.68	$2.2^{+0.2}_{-0.2}$	$22.03^{+0.06}_{-0.03}$
NGC 6240	5.51	10.60	4.10	43.6	24.20	0.54	0.07	0.46	0.93	$2.0^{+0.1}_{-0.1}$	$22.05^{+0.02}_{-0.02}$
NGC 7130	2.60	10.05	3.68	42.3	24.10	0.76	0.19	0.24	0.81	$3.6^{+0.5}_{-0.5}$	$22.08^{+0.08}_{-0.05}$
NGC 7172	2.28	9.75	2.67	42.8	22.91	–	–	–	–	–	–
NGC 7465	0.74	8.91	2.48	42.0	21.46	0.96	0.64	0.04	0.36	$4.7^{+0.7}_{-0.7}$	$23.94^{+0.65}_{-0.48}$
NGC 7469	2.34	10.39	3.30	43.2	20.53	0.83	0.29	0.17	0.71	$5.3^{+0.5}_{-0.7}$	$23.54^{+0.05}_{-0.09}$
NGC 7582	3.82	9.58	3.25	42.5	24.20	0.46	0.06	0.54	0.94	$1.1^{+0.2}_{-0.1}$	$22.29^{+0.10}_{-0.07}$
NGC 7674	3.32	10.27	4.06	43.6	–	0.94	0.54	0.06	0.46	$2.7^{+0.4}_{-0.4}$	$24.08^{+0.11}_{-0.12}$
TOL 1238-364	1.44	9.14	3.45	43.4	24.95	0.83	0.28	0.17	0.72	$6.5^{+1.2}_{-1.1}$	$24.09^{+0.14}_{-0.14}$
UGC 5101	4.78	10.58	4.36	43.1	24.08	0.78	0.22	0.22	0.78	$6.9^{+1.3}_{-1.2}$	$22.51^{+0.10}_{-0.11}$

Notes. The molecular masses M_{mol} are calculated within a $2\,r_{CO}$ radius and by using the best-fit α_{CO} (except for NGC 7172, for which we used $\alpha_{CO} = 4.3$). G_0 is the median value of the $G_0(r)$ profile. $N_{H,X}$ is the column density derived from the X-ray SED. The best-fit $f_{PDR}^{(1-0)}$, $f_{XDR}^{(1-0)}$, $f_{PDR}^{(4-3)}$, and $f_{XDR}^{(4-3)}$ are the fractions to the total CO(1 − 0) and CO(4 − 3) luminosities, respectively, due to PDR and XDR emission, respectively. Best-fit α_{CO} is in units of M$_\odot$ (K km s^{-1} pc^2)$^{-1}$. For both α_{CO} and $\log N_H$, we report the median values of the marginalized posterior distributions, with 1σ width as errors.
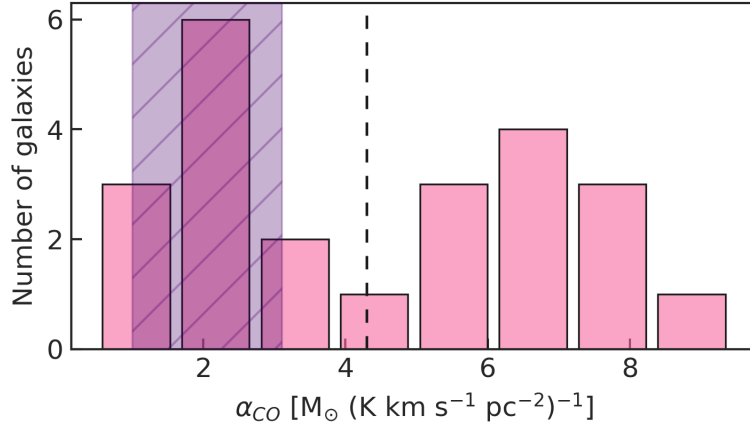
Figure 3.6: Histogram representing the best-fit CO-to-H$_2$ conversion factor α_{CO}, selected through the minimization of the χ^2_ν, for our sample of 24 galaxies. The dashed line is for the Milky Way value (Bolatto et al., 2013), while the shaded hatched area highlights the values associated to ULIRGs (Pérez-Torres et al., 2021b).

2013), which implements the Goodman and Weare's Affine Invariant MCMC Ensemble sampler (Goodman & Weare, 2010). In this way we are able to fully characterize any degeneracy between our model parameters, while also providing the 1σ spread of the posterior distribution for each of them. To be able to include also upper limits in the likelihood function, we follow the approach described in Sawicki (2012) and Boquien et al. (2019), splitting the χ^2 formula in two sums:

$$\chi^2 = \sum_{j=1}^{13} \left(\frac{f_j - m_j}{\sigma_j} \right) - 2 \sum_{j=1}^{13} \ln \left\{ \frac{1}{2} \left[1 + \mathrm{erf} \left(\frac{f_{\mathrm{ul},j} - m_j}{\sqrt{2}\sigma_j} \right) \right] \right\} \tag{3.10}$$

where the first sum contains the detections f_j and their errors σ_j (j covers the first 13 lines of the CO SLED), the second one containing the 3σ upper limits $f_{\mathrm{ul},j}$ (whereas we used the 1σ upper limit as the measured error σ_j), and in both sums m_j are the model values.

Finally, we produce a third set of synthetic CO SLEDs by keeping the default $\alpha_{\mathrm{CO}} = 4.3$ M$_\odot$ (K km s^{-1} pc^2)$^{-1}$ but using the column density $N_{\mathrm{H, X\text{-}ray}}$ derived from the absorption of X-rays along the line of sight (Brightman & Nandra, 2011; Ricci et al., 2017a; Marchesi et al., 2019; La Caria et al., 2019, and Salvestrini in prep.). We label these CO SLED predictions "$N_{\mathrm{H, X\text{-}ray}}$ model". Also in this case we set $N_{\mathrm{H, X\text{-}ray}}$ constant at every radius.
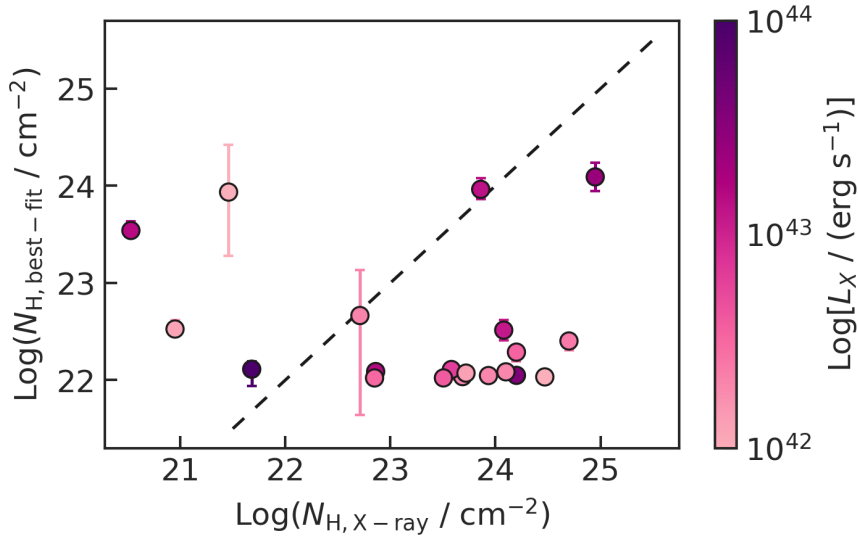
Figure 3.7: A comparison of the column densities N_H from our fitting procedure (on the y-axis) and the $N_{H,\,X\text{-ray}}$ derived by modelling the absorption of X-rays (on the x-axis). The colour of each circle (i.e. of each galaxy) depends on the intrinsic X-ray luminosity L_X ($2 - 10$ keV). The dashed line is the 1:1 line.

3.4.2 Best-fit model results

We run `emcee` with 10 walkers exploring the parameter space for 10^4 chain steps. The chains have been initialized by distributing the walkers around $\alpha_{CO} = 4.3$ M$_\odot$ (K km s^{-1} pc^2)$^{-1}$ and the median $N_H(r)$ for each galaxy (if larger than 10^{22} cm^{-2}, 10^{22} cm^{-2} otherwise). For each walker, we first run the algorithm with a burn-in chunk of 5000 steps which we later discard. The procedure gives a mean autocorrelation length $\tau = 65$ for both α_{CO} and N_H, and a mean acceptance fraction of 0.59. In the following we report the median values of the marginalized posterior probability distributions for the two parameters, with a 68% confidence interval as errors. The MCMC code did not converge for NGC 7172, due to the dominance of upper limits (7, with only 3 detections): in the subsequent paragraphs and sections, we only consider the remaining 23 galaxies of our sample.

The best-fit procedure returns median values $0.5 \leq \alpha_{CO} < 9.5$ M$_\odot$ (K km s^{-1} pc^2)$^{-1}$, as shown in Figure 3.6. The median CO-to-H$_2$ conversion factor for our galaxy sample is $\alpha_{CO} = 4.7^{+2.4}_{-2.8}$, where the lower and upper errors are the 16th and 84th percentiles of the sample distribution, respectively. This value is comparable to that of the Milky Way, and the range agrees well with the available literature (e.g. Bolatto et al., 2013; Leroy et al., 2015; Mashian et al., 2015; Accurso et al., 2017; Seifried et al., 2017; Casasola et al., 2017; Dunne et al., 2022).

The best-fit values of N_H are shown in Figure 3.7 against $N_{H,\,X\text{-ray}}$. We find values
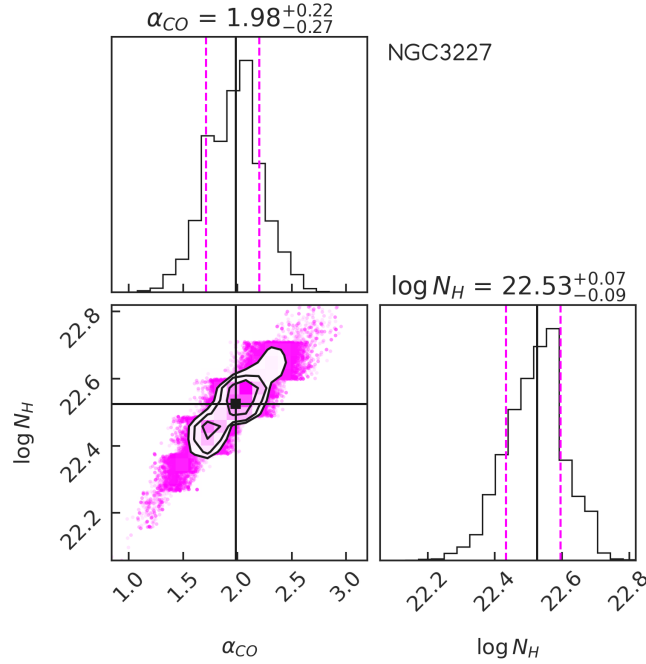
Figure 3.8: Corner plot showing the marginalized posterior distributions of α_{CO} (in $M_\odot$ (K km s^{-1} pc^2)$^{-1}$) and N_H (in cm^{-2}) for the galaxy NGC 3227. The contours represent $(1, 1.5, 2)\sigma$ levels for the 2D distribution. The best-fitting parameters and the 16th and 84th percentiles are plotted with solid black lines and square and dashed magenta lines, respectively.

$10^{22.0} \leq N_H \leq 10^{24.1}$ cm^{-2} with a median of $\log(N_H/\text{cm}^{-2}) = 22.1^{+1.6}_{-0.1}$. By comparison, the 21/24 galaxies for which we have $N_{H, \text{X-ray}}$ have a median $\log(N_{H, \text{X-ray}}/\text{cm}^{-2}) = 23.7^{+0.5}_{-1.8}$.

The maximum fitted obscuration of our sample is in TOL 1238-364 ($N_H = 10^{24.1}$ cm^{-2}), which also has the maximum $N_{H, \text{X-ray}} = 10^{25}$ cm^{-2}. As shown in Figure 3.7, however, the N_H values, derived from the fit of the CO SLED and from the fit of the X-ray spectrum, do not correlate. This, anyway, does not constitute a critical issue of our modelling, as will be explained in Section 3.5.2.

We find a degeneracy between the α_{CO} and N_H sampled values in almost all the galaxies (see e.g. Figure 3.8 for NGC 3227). This is not unexpected, since it is known that α_{CO} depends on the optical depth (Bolatto et al., 2013; Teng et al., 2023), which in turn depends on N_H. Increasing α_{CO} in a galaxy means more molecular mass within the same volume, hence N_H has to increase accordingly. The galaxies for which the sampled parameters do not show degeneracy are also among the ones for which our model works worse (e.g. Mrk 231, NGC 4151, NGC 4388, see Appendix B.3).

In Appendix B.3, together with observed and modelled CO SLEDs for all the galaxies, we also plot the relative (i.e. normalized to the best-fit model) residuals between observed data and best-fit model. We find relative residual values ≥ 2 for at least two detected CO
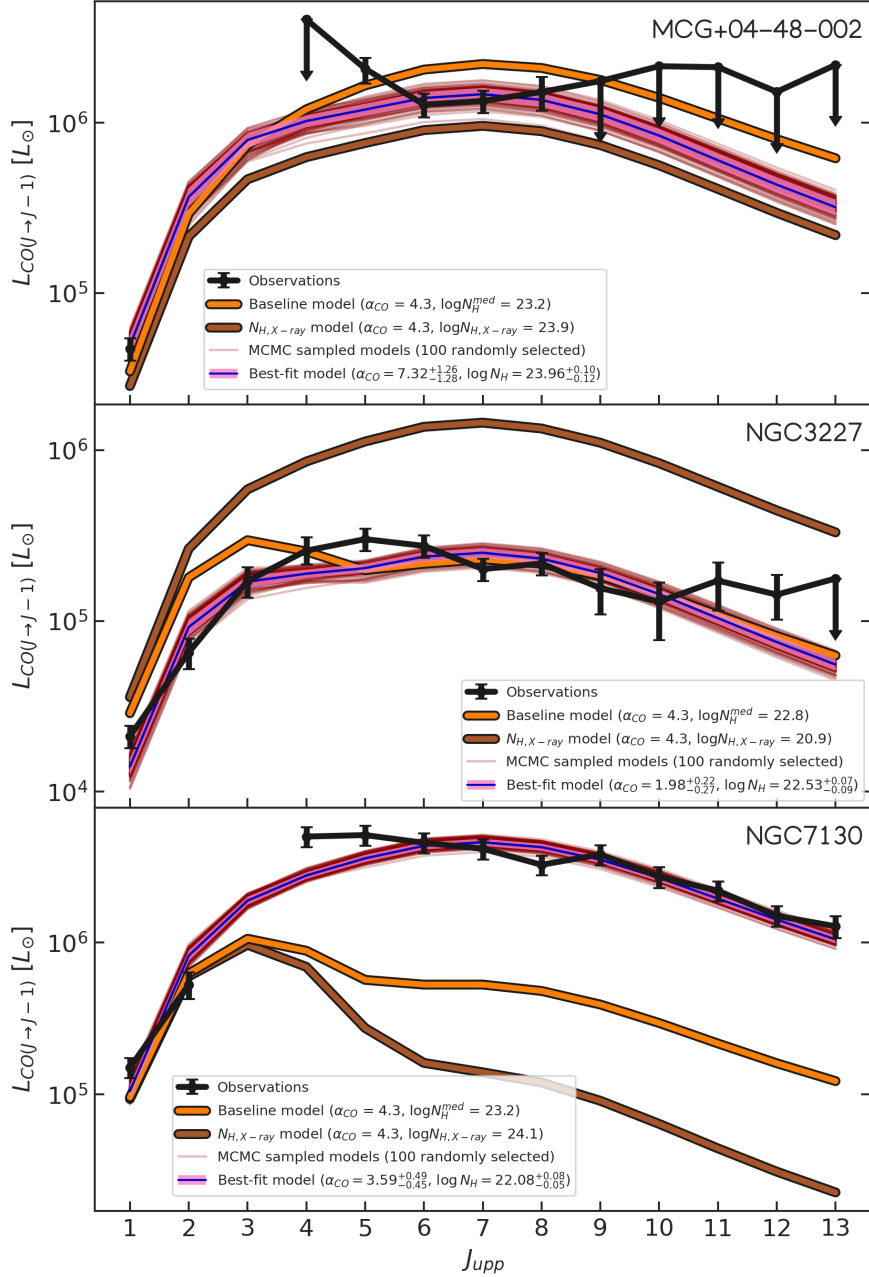
Figure 3.9: The modelled CO SLEDs of 3 galaxies (from the top to the bottom panel: MCG+04−48−002, NGC 3227 and NGC 7130) of our sample, in physical units of $L_\odot$. For each panel, the black line is the observed CO SLED (with downward arrows indicating censored data points), and the orange, brown, red, and pink lines are the modelled CO SLEDs: our baseline model without fitting any free parameter and with a negligible $N_H(r)$, the baseline model with a constant $N_{\mathrm{H,X\text{-}ray}}$ derived by modelling the absorption of X-rays, 100 MCMC modelled SLEDs randomly picked from the parameters posterior distributions, and the best-fit model covering the 1σ spread of such distributions, respectively. The x-axis represents the upper rotational quantum number J of each CO line, from CO$(1-0)$ to CO$(13-12)$.

lines in 4 galaxies: IRAS 20551−4250, Mrk 231, NGC 4151, and NGC 4388. Apart from NGC 4388, which has a very peculiar CO SLED shape that our model is not able to reproduce, for the other three galaxies our model fails to reach such high luminosities for the high-J lines. This may be due to an additional source of excitation (other than FUV and X-ray flux), as shocks or cosmic rays. In fact, IRAS 20551−4250 and Mrk 231 are known to host powerful CO outflows, with velocities up to 500 and 700 km s^{-1}, respectively (Lutz et al., 2020). NGC 4388 has also a detected CO outflow, reaching 150 km s^{-1} (Domínguez-Fernández et al., 2020), while for NGC 4151 we only have a detected H$_2$ outflow travelling at 300 km s^{-1} (May et al., 2020). It is tempting to intepret these results as evidences of AGN mechanical feedback on CO excitation, but this is beyond the purpose of this work.

The best-fit α_{CO} and N_H, together with the 1σ spread of their posterior distributions, are listed, for each galaxy, in Table 3.2, together with the molecular mass within a $2r_{CO}$ radius (recalculated with the best-fit α_{CO}).

3.4.3 Three examples of modelled galaxies

In Figure 3.9 we show the comparison between the observed CO SLED and that resulting from the "Baseline", "Best-fit", and "$N_{H,\,X\text{-ray}}$" modelling, where the "Best-fit" model is calculated with the $\pm 1\sigma$ values of the (α_{CO}, $\log N_H$) posterior distributions. We show three sample galaxies: MCG+04−48−002, NGC 3227 and NGC 7130, chosen to be representative (due to the spread of their best-fit parameters) of the results obtained by means of our fitting procedure, with best-fit median values α_{CO} = [7.32, 1.98, 3.59] M$_\odot$ (K km s^{-1} pc^2)$^{-1}$, respectively, and N_H = [$10^{23.96}$, $10^{22.53}$, $10^{22.08}$] cm^{-2}, respectively. In Appendix B.3 we gather the observed and theoretical CO SLEDs for the whole galaxy sample.

MCG+04−48−002 (top panel of Figure 3.9) has very similar "$N_{H,\,X\text{-ray}}$", "Baseline" and "Best-fit" CO SLEDs, due to their similar N_H values. The effect of a high N_H on the CO SLED is visible especially at high J. The effect of changing α_{CO} (by a factor of $\sim 80\%$) is evident by comparing the "$N_{H,\,X\text{-ray}}$", and "Best-fit" CO SLEDs.

In NGC 3227 (middle panel of Figure 3.9) we can notice the difference between the "Baseline" and "Best-fit" CO SLEDs due to different α_{CO} and N_H: a higher α_{CO} would boost the luminosity of all the CO lines, but a higher N_H decreases the high-J lines, exposing a typical PDR bump in the low-Js (cfr. Figures 3.3 and 3.4). The "$N_{H,\,X\text{-ray}}$" SLED is very bright due to its low $N_{H,\,X\text{-ray}}$, which boosts the XDR emission.

NGC 7130 (bottom panel of Figure 3.9) has instead three very different modelled CO SLEDs. In the "Baseline" and "$N_{H,\,X\text{-ray}}$" models we can clearly see the PDR bump
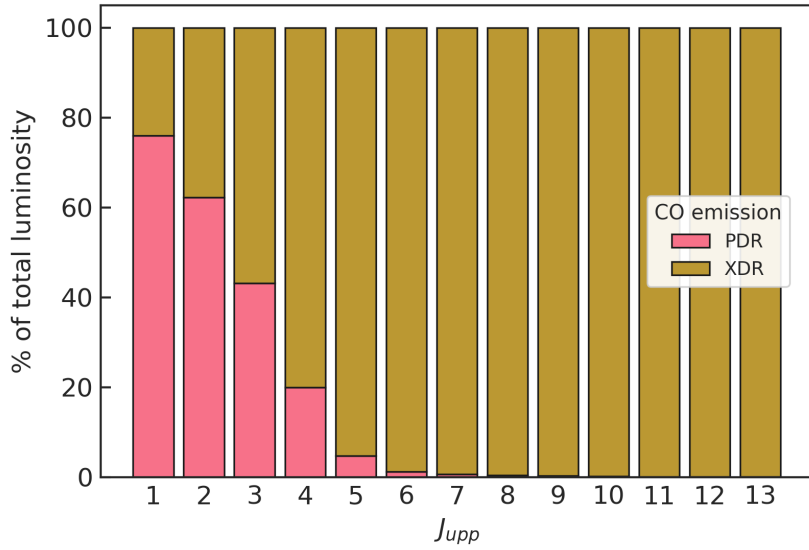
Figure 3.10: Bar plot showing the relative percentage to the total modelled luminosity of PDR (pink side) and XDR (brown side) emission for each analysed CO line, from CO(1 − 0) to CO(13 − 12).

at low-J, due to the high N_H which absorbs the X-rays. The higher $N_{H, X-ray}$ makes its SLED to dramatically decrease towards the high-J lines, where the XDR emission is dominant. The "Best-fit" CO SLED has instead a lower PDR component due to its low $\alpha_{CO} = 3.59$, which better reproduces the observed CO SLED.

3.4.4 PDR vs. XDR emission

In Figure 3.10 we plot the relative importance of PDR and XDR emission as a function of J for our galaxy sample as resulting from the "Best-fit" model. It is remarkable the fact that from CO(4 − 3) going upwards the CO luminosity is almost all due to XDR emission, even after taking into account the effect of X-ray flux attenuation with a best-fit N_H. This confirms what is shown in Figure 3.3 for single molecular clumps, and in Figure 3.4 for single GMCs, i.e. the XDR models dominate the overall CO luminosity, with the exception of the low-J lines. These results are extensively discussed in Section 3.5.3.

3.4.5 The CO SLED radial build-up

Since we modelled the GMC distribution and their CO emission as a function of galactocentric radius, we can study the spatial distribution of different CO lines. In Figure 3.11 we plot the radius at which the luminosity of a given CO transition reaches 90% of the total value for our sample of galaxies, $r_{90\%}$. It is immediate to see that there is a separation between low-J lines, dominated by PDR emission (Figure 3.10), which
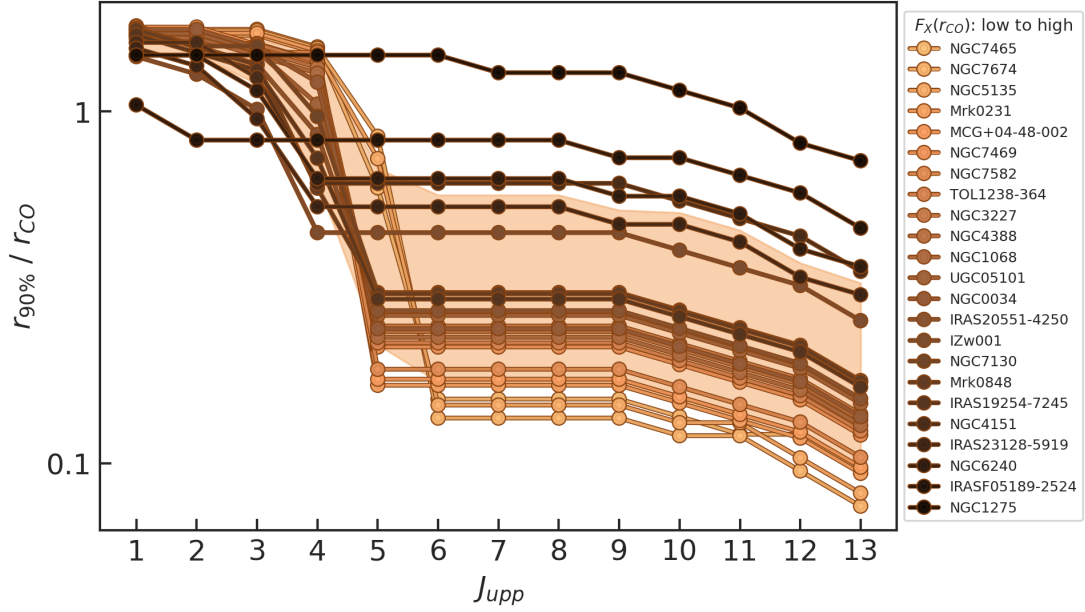
Figure 3.11: Galactocentric radius at which the luminosity of a given CO transition reaches 90% of the total value for our sample of galaxies, divided by their r_{CO}. The filled circles, linked with solid lines, mark the $r_{90\%}$ for every galaxy, color-coded according to their $F_{\mathrm{X}}(r_{\mathrm{CO}})$, while the brown shaded area represents the values between 16% and 84% of the radii distributions for our sample.

emit up to several kpc (i.e. through the whole star-forming galaxy disc), and mid- and high-J lines, dominated by XDR emission, which emit most of their luminosity within $r = 1$ kpc. The spread in radii for a given CO line is due to the different sizes of the studied galaxies, but also, at least for the mid-/high-J, to the different incident F_{X}: a higher F_{X} indeed produces a larger XDR emission (as in Meijerink & Spaans, 2005).

3.5 Discussion

In this section we discuss the implications of the derived values of the CO-to-H$_2$ conversion factor α_{CO} and the gas column densities N_{H} for our galaxy sample. Finally, we discuss about the relative importance of PDRs and XDRs to the CO luminosity.

3.5.1 The CO-to-H$_2$ conversion factor α_{CO}

The best-fit procedure returns reasonable values for α_{CO}. We find a median value of $\alpha_{\mathrm{CO}} = 4.8^{+2.4}_{-2.8}$ M$_\odot$ (K km s^{-1} pc^2)$^{-1}$, which is similar to the Milky-Way adopted value. Less than a third (8/24) of our sample has a ULIRG-like $\alpha_{\mathrm{CO}} = 1.8^{+1.3}_{-0.8}$ M$_\odot$ (K km s^{-1} pc^2)$^{-1}$ (Herrero-Illana et al., 2019; Pérez-Torres et al., 2021b), even though only one of
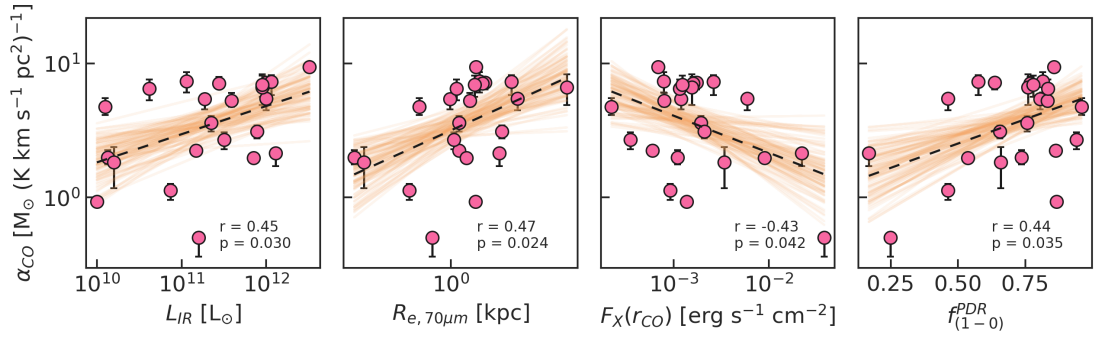
Figure 3.12: Scatter plot of best-fit α_{CO} (on the *y*-axis) against, from left to right, the total IR luminosity, the effective radius of the 70 μm maps, the X-ray flux at r_{CO}, and the PDR fraction of the total CO$(1-0)$ modelled emission, for the whole galaxy sample. The dashed black line is the regression fit between the quantities on the *x* and *y* axes, and the brown lines are 100 bootstrapped fits, which highlight the confidence interval of the regression fit. The Pearson correlation coefficient *r* and the *p*-value appear on every panel on the bottom right.

them (IRAS F05189−2524) is a ULIRG, and four (Mrk 848, NGC 5135, NGC 6240, and NGC 7674) are LIRGs.

For some targets we have independent measures of α_{CO} from the literature to compare with. By modelling the gas dynamics, Fei et al. (2023) found, for I Zw 1, $\alpha_{CO} = 1.6 \pm 0.5$ $M_\odot$ (K km s^{-1} pc^2)$^{-1}$, which is lower than our result ($\alpha_{CO} = 6.6 \pm 1.7$ $M_\odot$ (K km s^{-1} pc^2)$^{-1}$); however, their analysis is limited to the central 1 kpc, whereas our model extends up to $2r_{CO}$ (i.e. 5.6 kpc for I Zw 1). By comparing gas and dust emission, García-Burillo et al. (2014a) found values in the range $0.43 - 1.43$ $M_\odot$ (K km s^{-1} pc^2)$^{-1}$ for the central 700 pc of NGC 1068 (whereas we find $\alpha_{CO} = 5.4^{+0.9}_{-0.5}$ $M_\odot$ (K km s^{-1} pc^2)$^{-1}$ up to a diameter of 4.9 kpc). In NGC 6240, the quiescent gas and the outflowing one have different $\alpha_{CO} = 3.2 \pm 1.8$ $M_\odot$ (K km s^{-1} pc^2)$^{-1}$ and $\alpha_{CO} = 2.1 \pm 1.2$ $M_\odot$ (K km s^{-1} pc^2)$^{-1}$, respectively (Cicone et al., 2018): our value for this galaxy ($\alpha_{CO} = 2.0 \pm 0.1$ $M_\odot$ (K km s^{-1} pc^2)$^{-1}$) is closer to the outflowing gas, which is where the bulk of the molecular mass is, according to Cicone et al. (2018). The circumnuclear region (up to a 175 pc radius) of NGC 7469 has a α_{CO} between 1.7 and 3.4 $M_\odot$ (K km s^{-1} pc^2)$^{-1}$ according to Davies et al. (2004). Our model gives a higher result ($\alpha_{CO} = 5.3^{+0.5}_{-0.7}$ $M_\odot$ (K km s^{-1} pc^2)$^{-1}$) but it is derived for the molecular gas extending up to a 4.7 kpc radius.

Surprisingly, we find a positive, moderate (Pearson coefficient $r = 0.45$, $p = 0.03$), correlation between α_{CO} and the total IR luminosity L_{IR}, as shown in the first panel of Figure 3.12. The value of α_{CO} is predicted to decrease for higher gas temperatures, hence for starburst galaxies as (U)LIRGs (Bolatto et al., 2013). However, high gas volume and column densities are expected to increase α_{CO}: for example, Teng et al. (2023) found α_{CO} to increase in the central region of local barred galaxies due to the high CO optical

depth, which they find to be a more dominant driver than the gas temperature. A limit of the present analysis is the fact that we used a single α_{CO} for every radius, while it is likely to vary with different local conditions, as metallicity, temperature, density and optical depth (Bolatto et al., 2013; Teng et al., 2023). Another important point to make is that our (U)LIRGs (17/24 galaxies have $L_{IR} \geq 10^{11}$ L$_\odot$) are AGN, so that a fraction of the IR luminosity is due to AGN activity rather than SF (e.g. Nardini et al., 2010; Alonso-Herrero et al., 2012). For example, the largest value we derive is $\alpha_{CO} = 9.41$ M$_\odot$ (K km s^{-1} pc^2)$^{-1}$ for Mrk 231, the only quasar of our sample, with $L_{IR} = 10^{12.5}$ L$_\odot$, the highest of our sample.

We observe a moderate correlation between α_{CO} and the effective radius $R_{e,70\mu m}$ of the 70 μm emission ($r = 0.47$, $p = 0.02$, second panel of Figure 3.12). These radii result from the Sersic fit applied to the *Herschel* maps analysed in Chapter 2. A weak correlation ($r = -0.12$, $p = 0.58$) is evident between α_{CO} and r_{CO}, indicating that the optical and molecular radii ($r_{CO} = 0.17\,r_{25}$) do not significantly impact the CO-to-H$_2$ conversion factor. Instead, it appears influenced by the size of the star-forming region traced by the 70 μm emission in our analysis. Furthermore, a strong correlation is found between L_{IR} and $R_{e,70\mu m}$ ($r = 0.72$, $p = 8 \times 10^{-5}$), suggesting that only one of the two correlations might be meaningful. A weak correlation ($r = 0.13$, $p = 0.56$) is observed between α_{CO} and the median G_0 listed in Table 3.2 or $G_0(R_{e,70\mu m})$. Thus, it seems that G_0 is not the primary driver of the variation in α_{CO}.

Some insights can come from the way we implemented α_{CO} in the model, where it serves as a normalization factor for the "Best-fit model". A bright IR galaxy exhibits CO emission at every J (e.g. Kamenetzky et al., 2016). However, there exists a complex interplay between the combined effects of α_{CO} and N_H in our model. For instance, in the case of MCG+04−48−002 (top panel of Figure 3.9), which has a high $\alpha_{CO} = 7.32$ M$_\odot$ (K km s^{-1} pc^2)$^{-1}$, the "Baseline model" with a lower α_{CO} appears brighter for some CO lines. This is attributed to the high N_H derived for this galaxy, which suppresses the XDR emission. While a weak correlation ($r = 0.28$, $p = 0.20$) exists between the two best-fit parameters (α_{CO}, N_H), a moderate anti-correlation ($r = -0.43$, $p = 0.04$) is observed between α_{CO} and F_X measured at a distance r_{CO} from the AGN and obscured with the best-fit N_H (third panel of Figure 3.12). A high F_X is indeed expected to boost the XDR CO emission, thereby lowering α_{CO}.

In the last panel of Figure 3.12, we present a positive and moderate ($r = 0.44$, $p = 0.04$) correlation between α_{CO} and the PDR fractions of the total CO(1−0) modelled emission. For certain galaxies (e.g. MCG+04−48−002, exhibiting a high $f_{PDR}^{(1-0)} = 0.81$ – see Table 3.2) this correlation arises from the combined effect of α_{CO} and N_H: a high N_H suppresses the XDR emission, necessitating a high α_{CO} to boost the otherwise low

PDR emission and increase the likelihood.

We stress that the characterization of a class of objects (local AGN as in our study) or even more of individual galaxies by constraining galaxy properties such as α_{CO}, is in line with some recent studies (e.g., Ellison et al., 2021a; Casasola et al., 2022; Salvestrini et al., 2022; Thorp et al., 2022). These works highlight the heterogeneity of properties of the local galaxies, in addition to provide observational constraints to theoretical models and for high-redshift studies.

3.5.2 The X-ray attenuation column density

Taking into account the 1σ uncertainty, we find non-negligible (i.e. $N_H > 10^{22}$ cm^{-2}, see Equation 3.8) X-ray attenuation for most (14/23 galaxies) of our sample. The median is $\log(N_H/\text{cm}^{-2}) = 22.1^{+1.6}_{-0.1}$, and the range $[10^{22}, 10^{24}]$ cm^{-2}. By comparison the column density derived from the X-ray SED, for 20/23 galaxies, has median $\log(N_{H,\,X\text{-ray}}/\text{cm}^{-2})$ $= 23.7^{+0.5}_{-2.0}$ and range $[10^{20.5}, 10^{25}]$ cm^{-2}.

Although our best-fit N_H approximately has the same range of $N_{H,\,X\text{-ray}}$, the two values do not correlate (Figure 3.7). This uncorrelation can be due to the different locations of the X-ray absorbers: in the case of $N_{H,\,X\text{-ray}}$, the X-ray flux is attenuated by gas clouds along the line of sight only, while the N_H we derive is due to clouds between the AGN and the GMCs in the whole galaxy volume (i.e. considering multiple lines of sight).

Lately, more complex models of X-ray absorption are leading to different estimates of N_H, measuring the obscuration along the line of sight plus a reflective component from the nuclear torus (Yaqoob, 2012; Esparza-Arredondo et al., 2021). Several works targeting local AGNs show that these different N_H, both estimated from the X-ray SED, fail to correlate between each other (Torres-Albà et al., 2021; Sengupta et al., 2023).

García-Burillo et al. (2021) compared instead different estimates of N_H, from X-ray absorption, and from high-resolution (7-10 pc) ALMA CO observations, for a sample of 19 local Seyferts, finding similar median values but with a large dispersion around the 1:1 line. As our estimates of Figure 3.7, they also find less absorbed galaxies (with $N_{H,X\text{-ray}} < 10^{22}$ cm^{-2}) to systematically lie above the 1:1 line, and vice versa. This could be expected if, in less absorbed galaxies, $N_{H,X\text{-ray}}$ is dominated by gas clouds smaller than our spatial resolution, which is dictated by the diameter of our smallest modelled GMC (3 pc, see Table 3.1).

It is believed that, at least in local AGNs, most of the obscuration is due to the nuclear torus rather than gas on galactic scales (see Hickox & Alexander 2018 for a recent review, and Gilli et al. 2022 for high-redshift systems). However, the orientation, filling factor

and opening angle of the torus are all important quantities that affect the measurement of $N_{\text{H, X-ray}}$. With our analysis we give a way to measure the attenuation of AGN obscuration on the molecular gas in all the possible directions.

3.5.3 PDR vs. XDR emission

As shown in Figures 3.3 and 3.4, the CO luminosity is dominated, for our modelled clumps and GMCs, by XDR emission, at least at $J > 3$. We find the same by fitting the observed CO SLEDs (Figure 3.10). The fact that high-J lines need X-rays to be radiatively excited is well known and studied (Bradford et al., 2009; van der Werf et al., 2010; Rosenberg et al., 2015; Kamenetzky et al., 2017), however this is the first time a detailed study of CO emission, coming from different gas sizes (clumps, GMCs), produces this same result. The majority of the studies have found, so far, CO excitation to be consistent with PDRs up to CO(6 − 5) (van der Werf et al., 2010; Hailey-Dunsheath et al., 2012; Pozzi et al., 2017). One notable exception is the work by Mingozzi et al. (2018), where their fiducial model for the CO SLED of NGC 34 has a XDR component which starts dominating the luminosity at $J_{\text{upp}} = 3$.

All these studies used a combination of two or three PDR and XDR components, each with a single density and incident flux. To be able to reproduce PDR emission consistent with observations at mid-/high-J, these models need very high gas densities ($n_{\text{H}} \gtrsim 10^5$ cm^{-3}), more typical of high-redshift, turbulent star-forming regions (Calura et al., 2022). The mass fraction of such dense clumps within the modelled GMCs is $\sim 2\%$, being most of the molecular mass in the range $[10^2, 10^4]$ cm^{-3}, where only XDRs are able to emit significant high-J CO emission (see also Figure 3.4). This also confirms the findings of Chapter 2, i.e. that only unlikely extreme gas densities PDR models can reproduce the CO emission.

As a caveat, we note that our model does not include (*i*) variations in the cosmic ray ionisation rate (CRIR), and (*ii*) the effect of shocks. It is known that both high cosmic-ray fluxes (Vallini et al., 2019; Bisbas et al., 2023) and shocks (Meijerink et al., 2013; Mingozzi et al., 2018; Bellocchi et al., 2020) influence the CO SLED, especially the high-J lines. Further developments of our model may be able to include a varying CRIR and the treatment of large scale shocks, as in the case of galaxies with winds and outflows (García-Burillo et al., 2014a; Morganti et al., 2015; Fiore et al., 2017; Speranza et al., 2022) or mergers (Ueda et al., 2014; Larson et al., 2016; Ellison et al., 2019).

3.6 Summary

We have presented a new physically-motivated model for computing the CO SLED in AGN-host galaxies, which takes into account the internal structure of GMCs, the radiative transfer of external FUV and X-ray flux on the molecular gas, and the mass distribution of GMCs within a galaxy volume. The assumptions are that the molecular clumps in a GMC follow a log-normal density distribution, the clumps size is equal to their Jeans radius, and that the GMC masses, in a galaxy, follow a power-law distribution. The model can predict the CO SLED of a galaxy from the radial profiles of molecular mass $M_{\mathrm{mol}}(r)$, FUV flux $G_0(r)$ and X-ray flux $F_{\mathrm{X}}(r)$. We also set two free parameters: the CO-to-H_2 conversion factor α_{CO}, and the X-ray attenuation column density N_{H}. We have used Cloudy to predict the CO lines emission of clumps and GMCs, through a combination of PDR and XDR simulations, and by taking into account the observed radial profiles.

To test the validity of our model, we extracted, from the galaxy sample described in Chapter 2, a sub-sample of 24 X-ray selected AGN-host galaxies with a well-sampled CO SLED. The sample represents a good variety of local ($z \leq 0.06$) moderately luminous ($10^{42} \leq L_{\mathrm{X}}[\mathrm{erg\ s^{-1}}] \leq 10^{44}$, $10^{10} \leq L_{\mathrm{IR}}[\mathrm{L_\odot}] \leq 10^{12.5}$) AGNs. We compared the CO SLEDs produced by our model with the observed ones, and we selected the best-fit α_{CO} and N_{H} with a MCMC analysis for each galaxy. Our main results are here summarized:

- the best-fit procedure returned, for our galaxy sample, median values of $\alpha_{\mathrm{CO}} = 4.8^{+2.4}_{-2.8}$ $\mathrm{M_\odot}$ $(\mathrm{K\ km\ s^{-1}\ pc^2})^{-1}$ and $\log(N_{\mathrm{H}}/\mathrm{cm^{-2}}) = 22.1^{+1.6}_{-0.1}$, where the lower and upper errors are the 16th and 84th percentiles, respectively; we find α_{CO} consistent with the Galactic value, and N_{H} that do not correlate with $N_{\mathrm{H,\ X\text{-}ray}}$;

- XDRs are fundamental to reproduce observed CO SLEDs of AGN-host galaxies, particularly for $J_{\mathrm{upp}} \gtrsim 3$.

We argue that the larger importance of X-rays to the CO luminosity, with respect to other works in the literature, is mainly due to the fact that the majority of molecular gas mass in a galaxy is at $n_{\mathrm{H}} \sim 10^2 - 10^4$ $\mathrm{cm^{-3}}$. This conclusion comes from a physically-motivated structure for the molecular gas, rather than from single-density radiative transfer models.

The model predictions can be used to estimate α_{CO} in AGN-host galaxies, by constraining both the relative and absolute intensity of several CO lines. They can also be useful to estimate the effective attenuation of X-ray photons on the molecular gas in a spatially-resolved way, rather than only on the line-of-sight (i.e., $N_{\mathrm{H,\ X\text{-}ray}}$).

Moving forward, the model is able to predict the emission of other molecular species, as HCN, HCO^+, H_2, H_2O. These molecules have been increasingly used in detailed

studies of local AGN (Butterworth et al., 2022; Eibensteiner et al., 2022; Huang et al., 2022). The model is also built to exploit a wealth of observed galaxy data, and compare different molecular lines spatially resolved by ALMA (as done with NGC 1068 in García-Burillo et al., 2019; Nakajima et al., 2023) with our model predictions.

4

The AGN kinematic feedback:
the case study of nearby Seyfert NGC 5506

This chapter is drawn from "*AGN feedback in the Local Universe: the multiphase outflow of Seyfert galaxy NGC 5506*", **Esposito F.**, Alonso-Herrero A., García-Burillo S., Casasola V., Combes F., Dallacasa D., Davies R., García-Bernete I., García-Lorenzo B., Hermosa Muñoz L., Peralta de Arriba L., Pereira-Santaella M., Pozzi F., Ramos Almeida C., Taro Shimizu T., Vallini L., Bellocchi E., González-Martín O., Hicks E., Hönig S., Labiano A., Levenson N., Ricci C., and Rosario D., submitted to A&A.

4.1   Introduction

Analysing AGN feedback is a complex task due to its impact on different phases of the interstellar medium (ISM) across different physical scales, from the sub-pc highly ionised ultra-fast outflows (UFOs, Tombesi et al., 2010; Fukumura et al., 2015; Nomura et al., 2016), warm absorbers (Blustin et al., 2005; Laha et al., 2014), and broad absorption lines (BALs, Weymann et al., 1991; Proga et al., 2000), to the kpc-scale ionised (McCarthy et al., 1996; Baum & McCarthy, 2000; Liu et al., 2013; Perna et al., 2020; Fluetsch et al., 2021) and molecular (Feruglio et al., 2010; Cicone et al., 2014; Bischetti et al., 2019; Ramos Almeida et al., 2022) outflows, up to the Mpc-scale emission of giant radio galaxies (GRGs, Ishwara-Chandra & Saikia, 1999; Kuźmicz et al., 2018; Dabhade et al., 2020) and X-ray groups and clusters (McCarthy et al., 2010; Fabian et al., 2011; McNamara & Nulsen, 2012; Pasini et al., 2020).

Furthermore, AGN activity is considered to be intermittent over the course of a galaxy's lifetime (King et al., 2004; Hopkins & Hernquist, 2006; Schawinski et al., 2015; King & Nixon, 2015), or even on time scales of days or less (Dultzin-Hacyan et al., 1992; Wagner & Witzel, 1995). Consequently, comprehending the overall impact of AGN

feedback is highly challenging, requiring the use of multiwavelength, multi-scale, and multi-time observations as essential tools.

The molecular phase of the ISM is of paramount importance, since it is the fuel for star formation and the phase in which resides the bulk of the gaseous mass in star-forming galaxies (see Section 1.2). The AGN radiation heats the molecular gas by creating X-ray dominated regions within the ISM (described in Section 1.2.3), and it perturbs its kinematics, driving outflows (Cicone et al., 2014; Fiore et al., 2017; Veilleux et al., 2020; Lamperti et al., 2022).

Molecular gas typically forms a rotating disc associated with the galaxy gravitational potential. As described in Section 1.4, in AGN-host galaxies, a common form of perturbation involves the interaction between the molecular disc and the AGN hot wind, which manifests as outflowing ionised gas observable in X-rays (Cappi, 2006; Tombesi et al., 2013; Giustini et al., 2023), UV (Hewett & Foltz, 2003; Rankine et al., 2020) and optical (Fabian, 2012; Mullaney et al., 2013) wavelengths (see also the review by Veilleux et al., 2020, and references therein, for the hot-cold gas coupling). In this regard, a multiwavelength approach is essential to effectively trace the multiphase outflow (Davies et al., 2014; Cicone et al., 2018; García-Bernete et al., 2021; Speranza et al., 2023). Nearby AGN serve as a perfect laboratory for studying these feedback signatures in detail, particularly with the increasingly improved spatial resolution and spectral coverage of today's instruments.

The Galactic Activity, Torus, and Outflow Survey (GATOS) aims to understand the obscuring material (torus) and the nuclear gas cycle (inflows and outflows) in the immediate surroundings of the nuclear region of local AGN (García-Burillo et al., 2021; Alonso-Herrero et al., 2021; García-Bernete et al., 2023). The GATOS sample includes Seyfert galaxies with distances $10 - 40$ Mpc, selected from the 70-month Swift/BAT catalogue of AGN (Baumgartner et al., 2013), some of which have been observed at different wavelengths, including optical and near-infrared integral field unit (IFU) spectroscopy, JWST, and ALMA observations.

One of the key findings of the GATOS survey is the existence of an anti-correlation between the molecular gas nuclear concentration and the AGN power (García-Burillo et al., 2021, and see Figure 1.22), which may be due to the AGN wind pushing the molecular gas away from the central region. These outflows have been observed and analysed in detail for some GATOS selected sources, in the molecular and ionised phases (Alonso-Herrero et al., 2018, 2019, 2023; García-Bernete et al., 2021; Peralta de Arriba et al., 2023).

In this Chapter, we investigate the molecular and ionised gas phases of NGC 5506, a Sa spiral galaxy in the GATOS sample at a redshift-independent distance of 26 Mpc

(Karachentsev et al., 2006). At this distance the spatial scale is 125 pc/″. NGC 5506 has an AGN bolometric luminosity of $\sim 1.3 \times 10^{44}$ erg s^{-1} (Davies et al., 2014) and is classified as a optically obscured Narrow Line Seyfert 1 (NLSy1 Nagar et al., 2002). The black hole mass is $M_{\mathrm{BH}} = 2.0^{+8.0}_{-1.6} \times 10^7$ M$_\odot$ (Gofford et al., 2015), yielding an Eddington ratio of $\lambda_{\mathrm{Edd}} \equiv L_{\mathrm{bol}}/L_{\mathrm{Edd}} = 0.05^{+0.21}_{-0.04}$. NGC 5506 is notable in the GATOS sample for having one of the highest molecular gas nuclear deficiencies (see Figure 18 of García-Burillo et al., 2021), suggesting a potential imprint of AGN feedback on the molecular gas. Furthermore, NGC 5506 hosts a sub-pc bent radio jet (Roy et al., 2000, 2001; Kinney et al., 2000) and a UFO (Gofford et al., 2013, 2015), making it an intriguing target for investigating multiphase (and multiscale) outflows. As a NLSy1, NGC 5506 is expected to be in a young AGN phase, characterized by a small black hole mass and a high accretion rate (see e.g. Crenshaw et al., 2003; Tarchi et al., 2011; Salomé et al., 2023).

Evidence of complex kinematics from the long-slit optical spectrum was found by Wilson et al. (1985), who suggested radial motion for the ionised gas. Maiolino et al. (1994) refined this model, identifying outflowing velocities of up to 400 km s^{-1} for [OIII], [NII], and Hα, with the outflow cone inclined at $-15°$ from the north. Additionally, Fischer et al. (2013) estimated an ionised outflow velocity of 500 km s^{-1} using slitless *Hubble* Space Telescope (HST) observations (see also Ruiz et al., 2005), modelling a biconical outflow. Davies et al. (2020) carried out a detailed analysis of optical data from observations made with X-shooter at VLT, finding a [OIII] outflow with a maximum velocity of 792 km s^{-1} and $\dot{M}_{\mathrm{out}} = 0.21$ M$_\odot$ yr^{-1}. Riffel et al. (2017, 2021) and Bianchin et al. (2022) studied the outflow of the ionised gas in the near-IR (with GEMINI NIFS), finding a mass outflow rate ranging from 0.11 to 12.49 M$_\odot$ yr^{-1} (by adopting two fixed n_e values - 500 cm^{-3} and 10^4 cm^{-3} - and exploring different geometries). The highest outflow values would result in a kinetic efficiency $\dot{E}_{\mathrm{out}}/L_{\mathrm{bol}} = 0.71$. They also calculate, from L_{bol}, a mass accretion rate to the SMBH of 0.067 M$_\odot$ yr^{-1}.

In this Chapter, we present new IFU observations made with the Multi-Espectrógrafo en GTC de Alta Resolución para Astronomía (MEGARA) at the Gran Telescopio Canarias (GTC), which covers several optical emission lines, together with ALMA Band 7 observations of the CO$(3-2)$ transition. The Chapter is structured as follows. In Section 4.2 we present the ALMA Band 7 and GTC/MEGARA observations In Section 4.3 we describe the morphology of the molecular and ionised gas emission lines, while we model the kinematics of the two phases in Sections 4.4 and 4.5, respectively. In Section 4.6 we discuss the results of this work and we compare our data with the available literature, and we draw our conclusions in Section 4.7.

Table 4.1: Fundamental parameters for NGC 5506.

Parameter	Value	Reference[a]
α_{2000}	$14^h 13^m 14.877^s$	(1)
δ_{2000}	$-03°12'27.67''$	(1)
V_{hel}[b]	1882 ± 11 km s^{-1}	(1)
RC3 Type	Sa pec edge-on	(2)
Nuclear activity	Optically obscured NLSy1	(3)
Distance	26 Mpc ($1'' = 125$ pc)	(4)
D_{25}	$2.82'$	(5)
Inclination	$80°$	(1)
Position Angle	$265°$	(1)
M_{BH}	$2.0^{+8.0}_{-1.6} \times 10^7$ M$_\odot$	(6)
L_{bol}	1.3×10^{44} erg s^{-1}	(7)
L_{IR}	3.1×10^{10} L$_\odot$	(8)
λ_{Edd}	$0.05^{+0.21}_{-0.04}$	(1)

Notes. [a] (1) This work; (2) de Vaucouleurs et al. (1991); (3) Nagar et al. (2002); (4) Karachentsev et al. (2006); (5) Baillard et al. (2011); (6) Gofford et al. (2015); (7) Davies et al. (2020); (8) Sanders et al. (2003). [b] Heliocentric velocity is the mean between the systemic velocities derived for the molecular and the ionised gas

4.2 Observations

4.2.1 ALMA Band 7

We observed NGC 5506 with the Band 7 ALMA receiver and a single pointing (project-ID: #2017.1.00082.S; PI: S. García-Burillo). We analysed the moderate resolution datacube from García-Burillo et al. (2021). The datacube has a $0.21'' \times 0.13''$ (26 pc × 16 pc) beam (with PA = $-60°$, measured anticlockwise from the north direction), a $17''$ (2.1 kpc) field of view (FoV) and a largest angular scale of $4''$ (0.5 kpc).

To check the astrometry, we first aligned the HST/F606W image (top panel of Figure 4.1) with the position of stars (from the Gaia mission), and then we aligned the ALMA continuum peak and the HST peak, resulting in $\alpha_{2000} = 14^h 13^m 14.877^s$, $\delta_{2000} = -03°12'27.67''$ (as in García-Burillo et al., 2021).

4.2.2 GTC/MEGARA Bands B and R

We observed the central region of NGC 5506 on 20/03/2021 (Program GTC27-19B; PI: A. Alonso-Herrero), with MEGARA in IFU mode (Gil de Paz et al., 2016; Carrasco
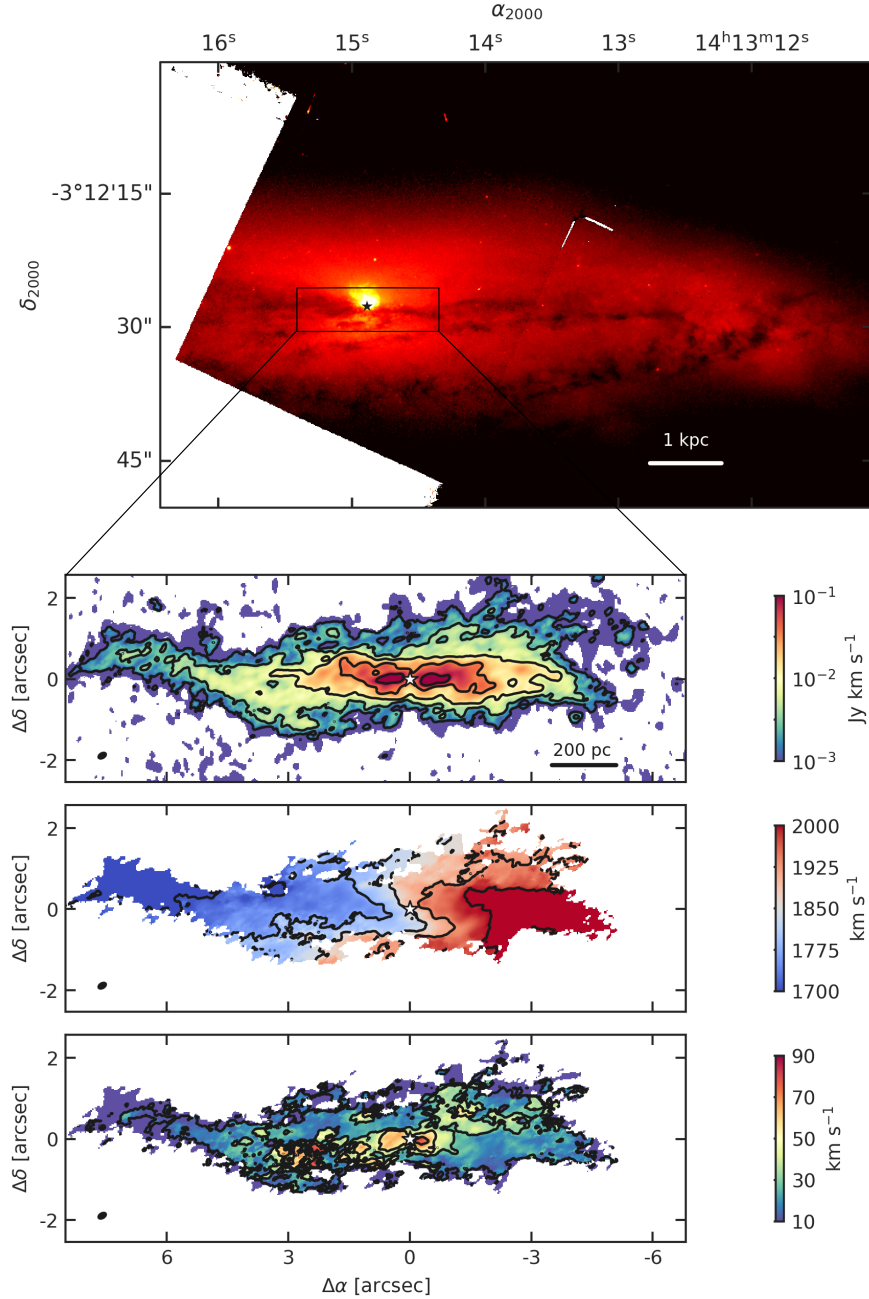
Figure 4.1: *Top panel*: HST/F606W image of NGC 5506 from Malkan et al. (1998). The black rectangle identifies a region of $15.3'' \times 5.1''$ (corresponding to 1.9×0.6 kpc^2). *Bottom panels*: ALMA CO(3 − 2) intensity, velocity and velocity dispersion maps, clipped at a signal-to-noise ratio of 3. The contours are between 10^{-3} and 10^{-1} Jy km s^{-1} (with 0.5 dex steps) for the intensity map, between 1700 and 2000 km s^{-1} (with 75 km s^{-1} steps) for the velocity map, and between 10 and 90 km s^{-1} (with 20 km s^{-1} steps) for the velocity dispersion map. North is up and east is left, and offsets in the ALMA maps are measured relative to the the 870 μm continuum peak (as in García-Burillo et al., 2021), marked with a star symbol in every panel. The ALMA beam $(0.21'' \times 0.13'')$ appears in every bottom panel as a black ellipse in the lower left.
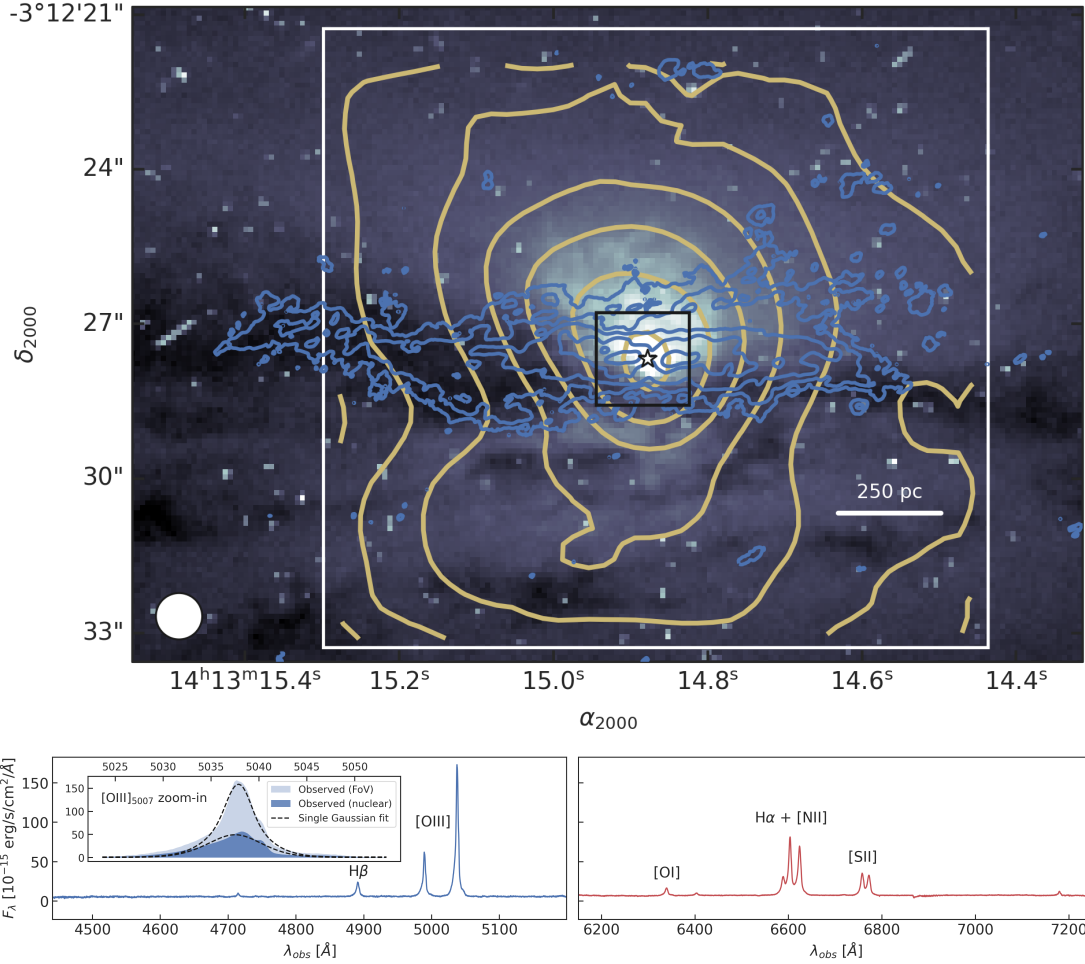
Figure 4.2: *Top*. The GTC/MEGARA [OIII] ($\lambda_e = 5007$ Å, in orange) and CO ($\lambda_e = 870\mu m$, in blue) contours over the HST/F606W image of NGC 5506 (Malkan et al., 1998). The [OIII] contour levels, from the single-component Gaussian fit, have a logarithmic spacing from 3σ to 80% of the peak intensity in steps of 0.5 dex, while the CO(3 − 2) contours are the same of Figure 4.1. The white star symbol is the AGN position. The black and white squares are the nuclear region, with size 1.8 arcsec ∼ 225 pc, observed by X-shooter (see Davies et al., 2020), and the MEGARA FoV ($12.5'' \times 11.3'' \sim 1.5$ kpc $\times$ 1.4 kpc), respectively. The white circle in the bottom left is the MEGARA seeing conditions (diameter $0.9''$). *Bottom*. Left and right panels contain the spectra (integrated within the MEGARA FoV) revealed with the MEGARA LR-B and LR-R gratings, respectively, with names of identified emission lines and doublets. The inset is the zoom-in of a [OIII] line (after continuum subtraction): the blue shadings are the observed spectra of the MEGARA FoV and of the nuclear region, the black dashed lines are the fits with a single Gaussian. The inset axes have the same units of the outer panel.

et al., 2018). We used two low resolution (LR) volume phase holographic gratings: the LR-B (spectral range $\sim 4300 - 5200$ Å, resolution $R \sim 5000$), to observe Hβ and the [OIII]$\lambda\lambda4959, 5007$ doublet (exposure time 480 s), and the LR-R ($\sim 6100 - 7300$ Å, $R \sim 5900$), to observe Hα, [OI]$\lambda6300$, and the [NII]$\lambda\lambda6548, 6583$ and [SII]$\lambda\lambda6716, 6731$ doublets (exposure time 400 s). The observed FoV is $12.5'' \times 11.3''$, corresponding to 1.6×1.4 kpc^2.

The data reduction was performed by following Peralta de Arriba et al. (2023) and using the official MEGARA pipeline (Pascual et al., 2021). The resolution of the GTC/MEGARA observations was limited by the seeing conditions. We plotted it with a circle of diameter $0.9''$. The final datacubes were produced with a spaxel size of $0.3''$, as recommended by the pipeline developers (Pascual et al., 2021; Peralta de Arriba et al., 2023): this corresponds to a physical spaxel size of 37.5 pc. We corrected the maps astrometry from the two configurations by aligning their continuum peaks with the ALMA Band 7 (870 μm) and HST (F606W filter) ones; throughout the Chapter we will refer to this point as the AGN position. We note that optical extinction may have an impact on the observed optical nucleus and actual AGN location on scales below the MEGARA seeing of $0.9''$.

4.3 Morphology and kinematics

4.3.1 ALMA CO(3-2)

Figure 4.1 shows the Hubble Space Telescope (HST) image and the ALMA CO($3 - 2$) first three moments maps. The CO intensity map reveals an edge-on disc with a nuclear deficit (with respect to the circumnuclear region) of diameter ~ 100 pc. This molecular gas depletion in the very centre has already been observed and analysed in García-Burillo et al. (2021). The circumnuclear disc is symmetric up to a diameter of $\sim 7'' = 875$ pc. At radii larger than $3 - 4''$ there is an extended gas tail in the eastern direction, which traces the dust lane visible in the HST image (see also Figure 4.2).

The bottom panels of Figure 4.1 show the velocity and velocity dispersion of CO($3-2$). The velocity field is centred at 1850 km s^{-1}. It appears to be dominated by rotation, redshifted on the western side and blueshifted on the eastern side. However, it also exhibits perturbations due to non-circular motion. The velocity dispersion has a median value of 17 km s^{-1}, and displays higher values along the NW-SE axis, with a maximum value of 86 km s^{-1} at $\delta\alpha \sim 3''$.
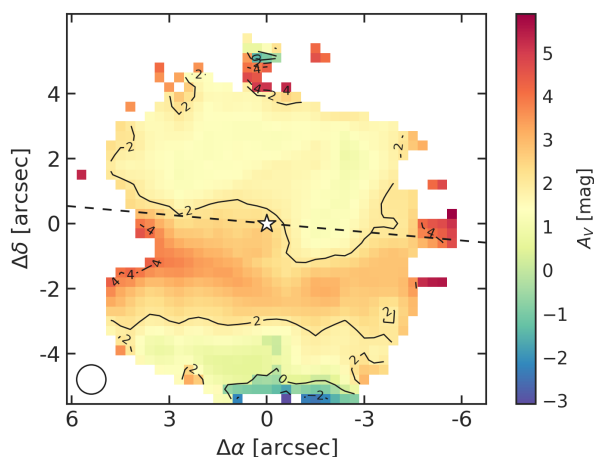
Figure 4.3: The visual extinction map of the MEGARA FoV, calculated from the Hα/Hβ ratio and with R_V = 3.1 (Cardelli et al., 1989). The white star symbol is the AGN position, and distances are relative to it. The dashed black line is our fiducial major kinematic axis with PA = 265° (see Section 4.4). The white circle in the bottom left is the MEGARA seeing conditions.

4.3.2 GTC/MEGARA emission lines

To derive the line intensity and kinematics, we extracted and fitted every spaxel of the MEGARA FoV with the ALUCINE[1] (Ajuste de Líneas para Unidades de Campo Integral de Nebulosas en Emisión, Peralta de Arriba et al., 2023), initially with a single Gaussian and an amplitude-over-noise (AoN) of 3 or higher. Figure 4.2 shows the contours of the [OIII] doublet intensity, which are the brightest lines in the MEGARA spectrum (also in Figure 4.2). The other identified emission lines, namely Hβ, [OI], Hα + [NII] doublet, and [SII] doublet, are labelled in Figure 4.2.

The [OIII] emission of Figure 4.2 nicely follows the HST image, and it is shaped as a bicone, typical of narrow line regions (NLRs Pogge, 1988; Wilson et al., 1993; Schmitt et al., 2003). The bicone emerges almost vertically in projection from the dusty molecular disc (~ 20° anticlockwise from north, as reported by Fischer et al., 2013; García-Burillo et al., 2021). We note here that Fischer et al. (2013) detected a one-sided ionisation cone (the northern side), which is also evident in the HST map (Figures 4.1 and 4.2). With MEGARA we detect the southern side as well, although it appears more extinguished. To check this we derived, following Cardelli et al. (1989), the visual extinction map from the Hα/Hβ line ratios (whereas the line fluxes come from the single Gaussian fit spaxel-by-spaxel). The resulting map (Figure 4.3) shows a clear dust band crossing the southern side of NGC 5506 nuclear region. This piece of information also suggests that the southern side is the near side of the galaxy (in accordance with García-Burillo et al., 2021, analysis).

---

[1]Available at https://gitlab.com/lperalta_ast/alucine
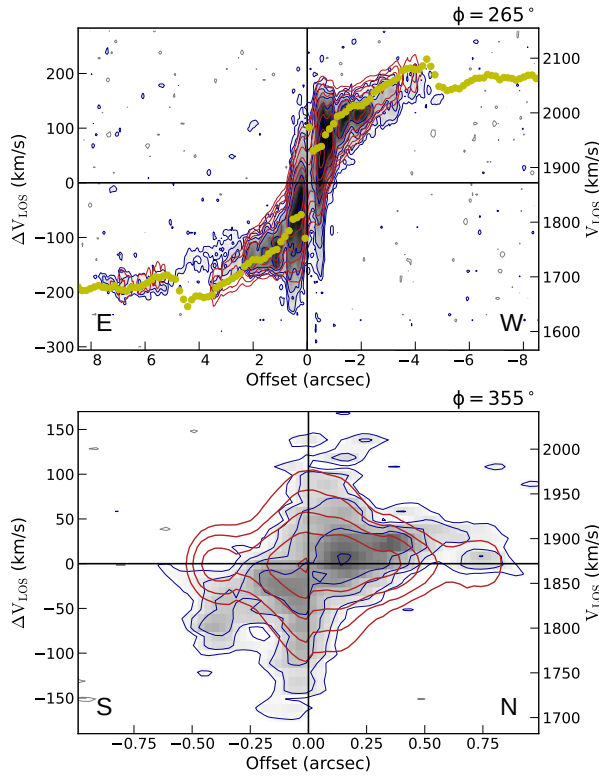
Figure 4.4: ALMA CO(3 − 2) PV diagrams generated with 3DB along the kinematic major (*top panel*) and minor (*bottom panel*) axes. Details for this 3DB run can be found in Section 4.4.1. The gray scale and blue contours are the ALMA CO(3 − 2) observations $> 3\sigma$, while the red contours are the 3DB rotating disc model (without a radial velocity component). The yellow dots are the fitted rotation curve. The approximate east, west, south and north directions are marked in the panels.

It is tempting to interpret the comparison of [OIII] and CO contours in Figure 4.2 as an ionised outflow that escapes the galaxy disc following the path of less resistance (Faucher-Giguère & Quataert, 2012). We will explore this possibility in Section 4.6.

4.4 Modelling the molecular gas kinematics

The CO(3 − 2) velocity field map (Figure 4.1) shows the typical signatures of a rotating disc with some deviations from non-circular motions. We modelled the CO(3 − 2) datacube with ^{3D}BAROLO[2] (Di Teodoro & Fraternali, 2015, hereafter 3DB), which creates a disc model for the rotating gas by dividing the emission into concentric rings, and fits the following parameters for every ring: the kinematic centre coordinates, the scale-height of the disc (z_0), the inclination (i) of the disc with respect to the line of sight, the position angle (PA, measured anticlockwise from the north direction for the receding side of

---

[2]Available at `https://bbarolo.readthedocs.io`
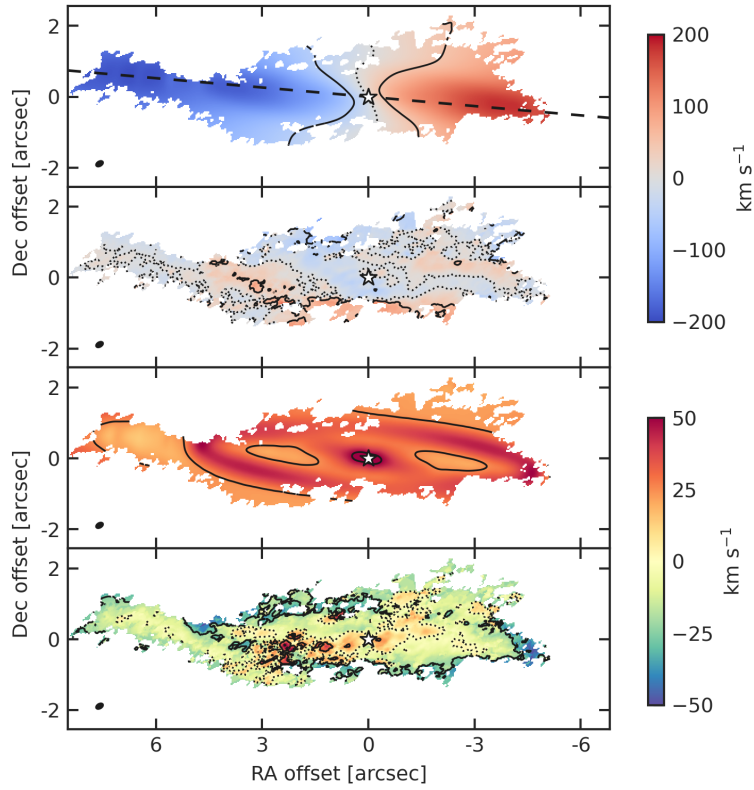
Figure 4.5: The best-fit model and residuals (i.e. observation minus the model) obtained with 3DB for the rotating disc with radial velocity component. Top and bottom panels show the mean velocity field and the velocity dispersion field of CO(3 − 2), respectively. In the first panel, $v_{sys} = 1872$ km s^{-1} has been subtracted from the model velocities. Velocity contours (top panels) are at −50 and 50 km s^{-1} (solid) and at 0 km s^{-1} (dotted), while dispersion contours (bottom panels) are at −50, −25, 25, and 50 km s^{-1} (solid) and at 0 km s^{-1} (dotted). The dashed black line in the first panel is the kinematic major axis with PA = 265°. The ALMA beam appears in every panel as a black ellipse in the bottom left.

the rotating disc) of the major kinematic axis, the systemic velocity v_{sys} with which the whole galaxy is receding from us, the rotational velocity (v_{rot}) of the gas, the velocity dispersion (σ_{gas}), and the radial velocity (v_{rad}).

We note here that 3DB is designed to model the gas kinematics within a rotating disc (plus a radial velocity component). Our strategy is to use 3DB to identify and quantify any radial motion within the disc, which may point to an inflow or outflow of gas. If the radial flow forms an angle θ_{out} with the galaxy disc, only the velocity projected on the disc, i.e. $v_{out} \cos \theta_{out}$, will be detected by 3DB (see also Di Teodoro & Peek, 2021; Bacchini et al., 2023).

We fixed the kinematic centre at the position of the continuum peak. We set a ring radial size of 0.15″ (≃ 19 pc), similar to the ALMA beam (0.21″ × 0.13″), and a total of 60 rings, thus reaching out to a distance of 9″ (≃ 1.1 kpc) from the centre.

4.4.1 Rotating disc

We performed a first 3DB run with $v_{rad} = 0$ km s^{-1}, and z_0, i, PA, v_{sys}, v_{rot}, and σ_{gas} as free parameters. In this way we derived $z_0 = 0.2'' \simeq 25$ pc, $i = 80°$, PA = 265°, and $v_{sys} = 1872 \pm 10$ km s^{-1} (where the error is given by the ALMA datacube spectral step). The inclination is the same as that found by García-Burillo et al. (2021) with the software `kinemetry` (Krajnović et al., 2006), while the PA is slightly different (they found PA = 275°). The v_{sys} value is in agreement with several works: Fischer et al. (2013) reported 1823 km s^{-1}, Riffel et al. (2017) 1878 km s^{-1}, Davies et al. (2020) 1962 km s^{-1}, García-Burillo et al. (2021) 1840 km s^{-1}, and the average of these values is 1876 km s^{-1}, only 4 km s^{-1} over our estimate.

We then performed a 3DB run with v_{rot} and σ_{gas} as the only free parameters, while the others were fixed to the values determined in the first run. This approach assumes the absence of radial motions associated with molecular inflows or outflows. Figure 4.4 displays the position-velocity (PV) diagrams resulting from this run. Overall, the 3DB model contours (red lines in Figure 4.4) reasonably reproduce the observed PV values (plotted with blue colours). From the major-axis PV diagram (Figure 4.4, top panel) we can appreciate the goodness of the v_{sys} estimate, as the CO(3 − 2) emission is symmetric with respect to v_{sys}. Along the kinematic minor axis (Figure 4.4, bottom panel), there are indications of non-circular motions in the central 1″, which we explore further in the next section.

4.4.2 Rotating disc with a radial velocity component

Within the approximate inner (projected) 1″, the minor axis PV diagram shows redshifted motions to the north of the AGN and blueshifted to the south (see top-left and bottom-right quadrants, respectively, of Figure 4.4, bottom panel). Since the south is the near side of the galaxy (see Figure 4.3 and related discussion in Section 4.3.2), this suggests the presence of a CO outflow component in the plane of the disc. We thus run another 3DB model including a radial velocity (v_{rad}) component. The other free parameters are v_{rot} and σ_{gas}, while the others have been set as the previous run.

Figure 4.5 shows the 3DB models and residuals for this run, for the first and second moments (mean velocity and mean velocity dispersion). The velocity and velocity dispersion absolute residuals have median values of 16 km s^{-1} and 14 km s^{-1}, respectively. The highest velocity residuals (Figure 4.5, second panel) are in the SE direction, where also the highest values of dispersion (Figure 4.1, bottom panel) and dispersion residuals (Figure 4.5, fourth panel) reside.

Figure 4.6 shows the PV diagrams of this run, where we can appreciate a better fit
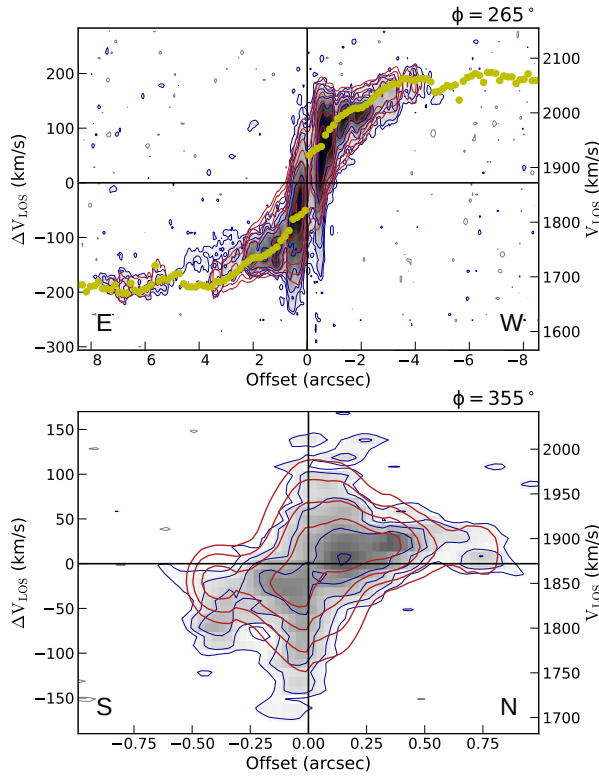
Figure 4.6: Same as Figure 4.4, but for the 3DB run with a radial velocity component.

along the minor axis (Figure 4.6, bottom panel). Especially, the 3DB model now follows the northern red - southern blue asymmetry along the CO(3 − 2) minor axis. We also plot the mean velocities along the minor axis in Figure 4.7, where we compare the 3DB results for the two models (with and without the radial velocity component). While not perfect, the model incorporating v_{rad} more closely aligns with the observed data, particularly at positive offsets from the centre (i.e. in the northern direction). The yellow dots in the top panel of Figure 4.6 represent the mean v_{rot} (also plotted in the second panel of Figure 4.8). We find v_{rot} reaching $193 \, \mathrm{km \, s^{-1}}$ at $r = 3.5''$ (440 pc), in reasonable agreement with the rotational velocity of $181 \pm 5 \, \mathrm{km \, s^{-1}}$ measured from HI absorption (Gallimore et al., 1999).

The four panels in Figure 4.8 show, from top to bottom, the CO(3 − 2) surface density $\Sigma_{CO(3-2)}$, and the modelled rotational velocity v_{rot}, velocity dispersion σ_{gas}, and radial velocity v_{out}^{mol} (which is the same as v_{rad}, with the positive sign meaning outflowing and negative meaning inflowing gas). We distinguish significative changes in the curve profiles at two particular radii: $0.4''$ and $5''$.

At $r \sim 0.4''$ (50 pc) we find the maximum value of $\Sigma_{CO(3-2)}$, which corresponds to the inner radius of the ring. Within this radius $v_{out}^{mol} < 0$, which is indicative of inflowing gas: it could be an indication of AGN feeding from the molecular disc (see e.g. Combes,
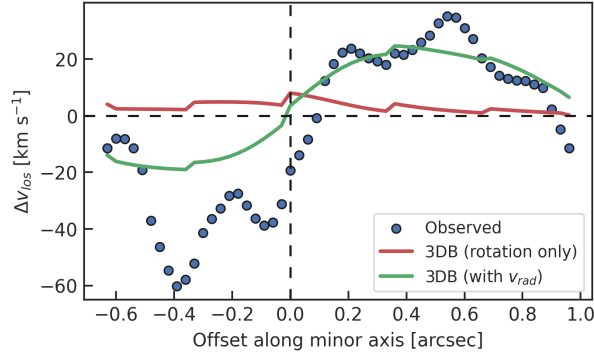
Figure 4.7: Relative velocities of CO(3 − 2) along the minor axis, extracted and averaged from a slit width of 3 pixels (corresponding to a projected width of 0.09″). The blue circles are the observed values, not weighted for the emitted flux. The green and red lines are the 3DB models with and without a radial velocity component.

2021), but since we only have two radial points we could not confirm this finding. At $r \sim 0.4''$ we also have a peak in the σ_{gas} and v_{out}^{mol} profiles: this means that the molecular ring is not only rotating, but also outflowing (as in NGC 1068, see García-Burillo et al., 2019).

At $r \sim 5''$ (610 pc) there is another peak of σ_{gas}, and v_{out}^{mol} goes from positive to negative, suggesting a transition from outflow to inflow (García-Burillo et al., 2014a, found a similar result for NGC 1068). However, at $r > 5''$ there is a lot of oscillation between inflow and outflow, probably due to the small number of datapoints (see the asymmetry of the CO emission in Figure 4.1) and to loss of sensitivity on large scales in the ALMA data, so we did not take into consideration these outer radii.

The CO(3 − 2) radial motion on the molecular plane could be explained with *(i)* inflowing/outflowing gas (García-Bernete et al., 2021; Ramos Almeida et al., 2022) or *(ii)* elliptical orbits associated with a bar (Buta & Combes, 1996; Casasola et al., 2011; Audibert et al., 2019). Since the presence of a bar is not evident on the CO(3 − 2) PV diagrams (Figures 4.4 and 4.6, cf. Alonso-Herrero et al., 2023), it probably does not dominate the motion of the molecular gas. Nevertheless, due to this possibility, we conservatively assume that the outflow velocities we derive between $R_{out,min}^{mol} = 0.4''$ (50 pc) and $R_{out,max}^{mol} = 5''$ (610 pc) are upper limits. We will discuss the presence of a bar in NGC 5506 in Section 4.6.1.

4.4.3   The molecular mass outflow rate

We used the CO(3 − 2) emission between $R_{out,min}^{mol} = 0.4''$ (50 pc) and $R_{out,max}^{mol} = 5''$ (610 pc) to calculate the main properties of the outflow, such as the amount of molecular gas it is driving outward (M_{out}^{mol}). To do so, we first converted it to CO(1 − 0), using
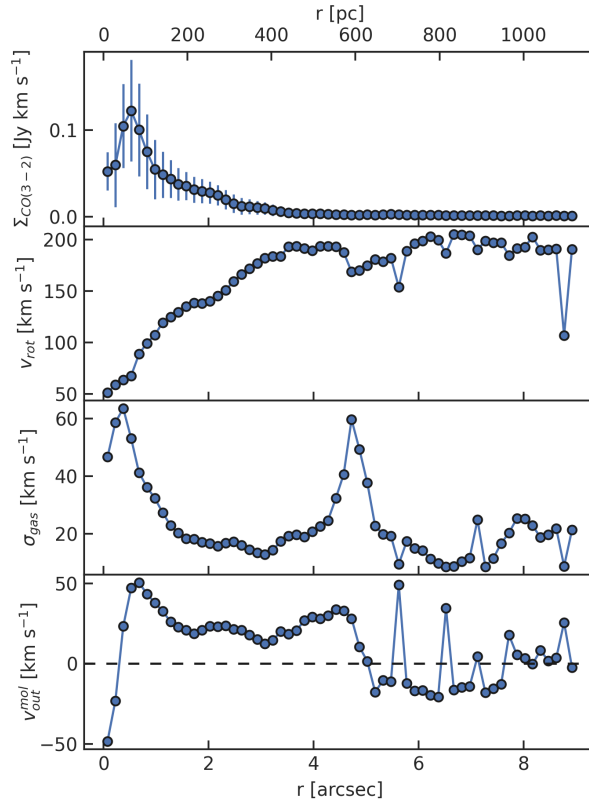
Figure 4.8: Radial profiles of molecular gas derived with 3DB. From top to bottom: the CO(3 − 2) surface density, the rotational velocity (same as the yellow dots in the top panel of Figure 4.6), the velocity dispersion and the outflow velocity, all as a function of deprojected distance from the AGN (on the plane of the galaxy). The dashed black line in the bottom panel is the zero line, dividing between ouflow ($v_{\text{out}}^{\text{mol}} > 0$) and inflow ($v_{\text{out}}^{\text{mol}} < 0$).
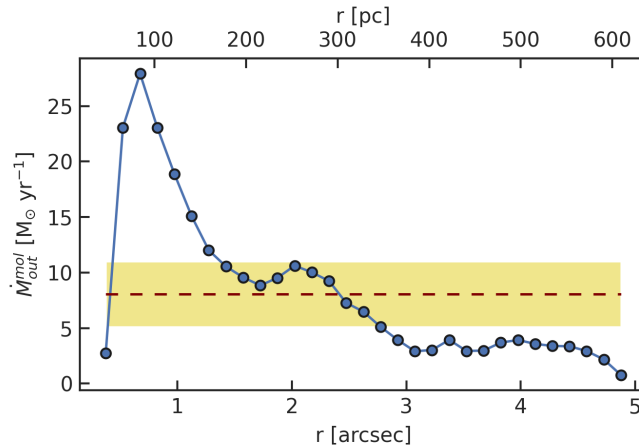
Figure 4.9: Molecular gas mass outflow rate as a function of deprojected distance from the AGN (on the plane of the galaxy). The molecular gas mass includes the helium contribution. The blue dots correspond to the values computed with the 3DB model radial velocities and CO(3 − 2) intensities of Figure 4.8. The red dashed line is the integrated mass outflow rate, $8 \pm 3 \ \text{M}_\odot \ \text{yr}^{-1}$, with the shaded yellow region representing its uncertainty.

a typical brightness temperatures ratio for galaxy discs of $T_{B,CO(3-2)}/T_{B,CO(1-0)} = 0.7$: this is the average value found by Israel (2020) in 126 nearby galaxy centres, and we adopt it for consistency with García-Burillo et al. (2021). We then used a Galactic CO-to-H_2 conversion factor of $X_{CO} = 2 \times 10^{20}$ mol cm^{-2} (K km s^{-1})$^{-1}$ (Bolatto et al., 2013). We chose the Galactic value to better compare our results with most of the literature, and also because NGC 5506 does not show any indication of merger and is not particularly luminous in the infrared ($L_{IR} = 10^{10.49}$ L$_\odot$ Sanders et al., 2003). We calculate $M_{out}^{mol} = 1.75 \times 10^8$ M$_\odot$ between $R_{out,min}^{mol}$ and $R_{out,max}^{mol}$. This result is affected by our choice of $T_{B,CO(3-2)}/T_{B,CO(1-0)}$ and X_{CO}. Specifically, a higher brightness temperatures ratio, as found in the central $\sim 1''$ of NGC 1068 (García-Burillo et al., 2014a; Viti et al., 2014), would decrease M_{out}^{mol}. Also a lower X_{CO}, usually associated to starburst galaxies (Bolatto et al., 2013; Pérez-Torres et al., 2021b), would decrease M_{out}^{mol}.

Assuming a simple shell geometry (as in Alonso-Herrero et al., 2023), we can write the mass outflow rate as

$$\dot{M}_{out}^{mol} = \frac{M_{out}^{mol} \, v_{out}^{mol}}{R_{out}^{mol}} \quad , \tag{4.1}$$

where v_{out}^{mol} is defined as the average velocity measured between $R_{out,min}^{mol}$ and $R_{out,max}^{mol}$. By taking the standard deviation as its uncertainty, we find $v_{out}^{mol} = 25.6 \pm 9.4$ km s^{-1}, from which we infer a molecular mass outflow rate of $\dot{M}_{out}^{mol} = 8 \pm 3$ M$_\odot$ yr^{-1} (which includes the helium contribution). Figure 4.9 shows the radial profile of the mass outflow rate, i.e. the same calculation of Equation 4.1 for every radial ring. We find a strong peak of $\dot{M}_{out}^{mol}$ at the inner radius of the molecular ring ($R \sim 85$ pc), which is outflowing (while rotating) up to $\dot{M}_{out,max}^{mol} = 28$ M$_\odot$ yr^{-1}. A second (minor) peak is visible around 250 pc ($\sim 2''$), within which resides half of the molecular mass, and which corresponds to a small v_{out} peak (bottom panel of Figure 4.8).

The average value of $\dot{M}_{out}^{mol} = 8 \pm 3$ M$_\odot$ yr^{-1} is similar to those of other local Seyferts, which range from ~ 1 M$_\odot$ yr^{-1} to a few tens of M$_\odot$ yr^{-1} (Combes et al., 2013; García-Burillo et al., 2014a; Morganti et al., 2015; Alonso-Herrero et al., 2019; Domínguez-Fernández et al., 2020; García-Bernete et al., 2021; Alonso-Herrero et al., 2023).
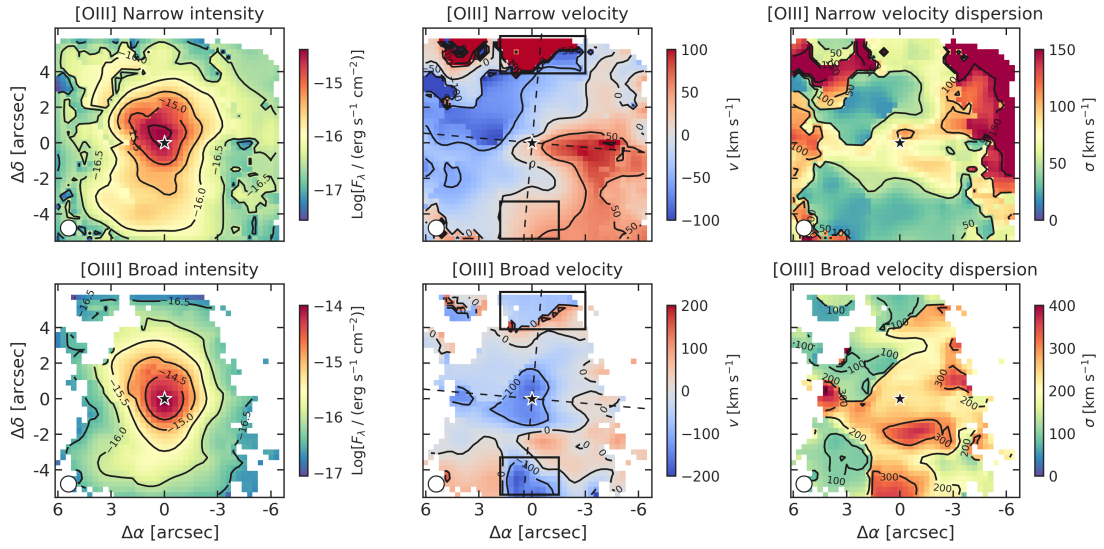
Figure 4.10: [OIII] double Gaussian fit made with ALUCINE. Top and bottom rows are for the narrow and broad component, respectively. From left to right, the three columns show the intensity, velocity, and velocity dispersion of both components. The AGN position is marked with a black star symbol, and distances are measured from it. The white circle in the bottom left of each panel is the MEGARA seeing conditions. The velocity panels (central column) show the PA = 265° and 355° dashed black lines, and two black rectangles that highlight the northern and southern edges of the velocity field.

4.5 Modelling the ionised gas kinematics

4.5.1 Gaussian decomposition

In the inset of Figure 4.2 we presented the single Gaussian fit of the [OIII] line. It is evident that a single Gaussian cannot accurately reproduce the complex shape of the line profile. Consequently, we decided to fit the observed lines (listed in Figure 4.2) with two Gaussians, spaxel by spaxel. The ALUCINE code determines, based on the AoN > 3 cut, whether one or two Gaussians are necessary for each spaxel. As input parameters, ALUCINE needs also the wavelength range for subtracting the continuum, and a systemic velocity. At first we set $v_{sys,CO} = 1872$ km s^{-1} as the CO$(3-2)$, but we achieved better results by setting $v_{sys,[OIII]} = 1893$ km s^{-1}. It is worth noting that this 21 km s^{-1} difference is only 1.5 times the MEGARA spectral step (~ 14 km s^{-1}). A detailed comparison of v_{sys} values from the literature is available in Davies et al. (2020) and in Section 4.4.1.

We name the two Gaussians "narrow" and "broad" component, where their width is the discriminant factor. We focus mainly on the [OIII] line in the analysis, since it shows the highest signal (Figure 4.2) and is the one usually studied for AGN ionised winds (Weedman, 1970; Heckman et al., 1981; Veilleux, 1991; Crenshaw & Kraemer,
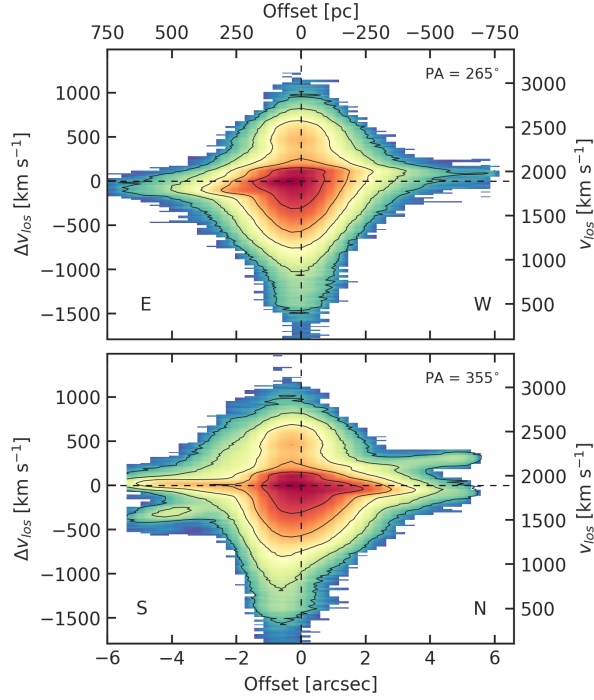
Figure 4.11: PV diagrams of the observed [OIII] ($\lambda_e = 5007\text{Å}$) line, clipped at 3σ, along major (*top panel*) and minor (*bottom panel*) kinematic axes, with PA = 265° and 355°, respectively. Contours are at $[10, 30, 100, 300, 1000]\sigma$. The vertical dashed line is the AGN position, and the horizontal dashed line is the systemic velocity $v_{sys}^{ion} = 1893$ km s^{-1}. The approximate east, west, south and north directions are marked in the panels. At $\Delta v_{los} < -1500$ km s^{-1} contamination with the secondary [OIII] line ($\lambda_e = 4959\text{Å}$) is probable.

2000; Harrison et al., 2014). The results for the [OIII] line are in Figure 4.10. The top panels show the narrow component: from the velocity map we can identify a rotation pattern, with velocities up to -100 and 100 km s^{-1}, oriented roughly in the same way of the CO disc (Figure 4.1). The external parts of the narrow component can be hardly associated to rotation however: at the northern end of the FoV the gas reaches 340 km s^{-1} (with relatively low dispersions around 60 km s^{-1}), while at NE and NW there are areas with very high dispersion (up to ~ 200 km s^{-1}). It could be that these extreme northern regions trace the external part of the ionised outflow.

The broad component of [OIII] (bottom panels of Figure 4.10) contains fewer pixels than the narrow one, since for some spaxels a single Gaussian component was sufficient to obtain a proper modelling (or the broad Gaussian had AoN< 3). The velocity map of this component displays a central blueshifted region (up to -170 km s^{-1}), and some positive and negative velocities all over the FoV. The velocity dispersion map reaches higher values than the narrow one (up to 400 km s^{-1}).

The Gaussian decomposition made with ALUCINE is able to separate the [OIII] rotation from the outflow component (except for the extreme northern regions at high
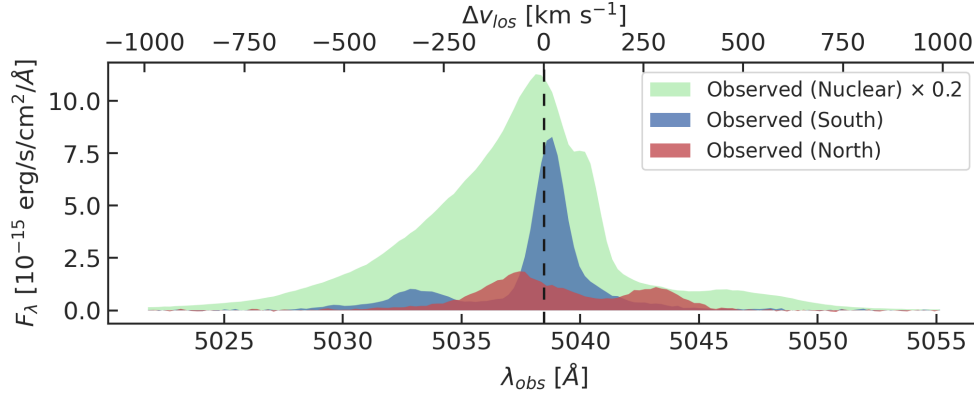
Figure 4.12: Observed spectra (continuum-subtracted) of the [OIII]λ5007 line at three locations along the kinematical minor axis (PA = 355°). In green, blue, and red, the spectra extracted within the nuclear region (black square in Figure 4.2), the southern region, and the northern region (black rectangles in Figure 4.10), respectively. The nuclear spectrum is multiplied by a 0.2 factor for a better comparison. The vertical dashed line is the redshifted (with v_{sys}^{ion} = 1893 km s^{-1}) [OIII] line.

velocity or velocity dispersion). The same applies for the other emission lines in the MEGARA spectrum, for which the results are shown in Appendix C.2. Compared to [OIII], the narrow component intensity maps of [NII], [SII], and [OI] are more consistent with an ionised rotating disc (aligned with the HST and ALMA discs, i.e. with PA $\sim$ 265°), while the broad component is more elongated on the north-south direction, (as [OIII], Hα and Hβ). This north-south elongation is especially evident in the velocity dispersion of the broad components of [NII] and [SII] (Figures C.4 and C.5).

We also show, in Appendix C.3, the Baldwin, Phillips, Telervich (BPT) diagrams (Baldwin et al., 1981; Veilleux & Osterbrock, 1987; Kewley et al., 2001; Kauffmann et al., 2003) made with the same fitted lines. From such diagrams (Figures C.7 - C.9) we can conclude that most of the observed central emission is due to the AGN activity rather than star formation, both for the narrow and broad components.

We will use this decomposition to calculate the [OIII] mass of the broad component in Section 4.5.3. However, the velocities obtained with ALUCINE represent mean velocities within each spaxel. To explore the full range of velocities of the ionised gas, we produced [OIII] PV diagrams (Figure 4.11), along the same PAs as the CO emission (Figure 4.6). In both major- and minor-axis PV diagrams, the ionised gas exhibits velocities exceeding 1000 km s^{-1}, both redshifted and blueshifted. The most extreme blueshifted velocities (Δv_{los} < −1500 km s^{-1}) are possibly contaminated with emission from the secondary [OIII] doublet line (λ_e = 4959 Å). The major-axis PV diagram (Figure 4.11, top panel) displays a rotation curve between −100 and 100 km s^{-1}. However, most of the emission, along both PAs, appears to be dominated by the outflowing gas. Along the minor axis

(bottom panel of Figure 4.11), there is also an observable X shape, elongated at large radii, likely due to the northern red and southern blue regions in the central panels of Figure 4.10 (within the black rectangles). These regions may represent the locations where the outflow is emerging from the nuclear zone.

To have a better understanding of the observed PV diagrams, we show, in Figure 4.12, the [OIII] line profile at three locations along the minor axis. The northern (in red) and southern (in blue) regions exhibit two distinct components: one travelling at approximately the systemic velocity, and the other outflowing at $\sim \pm 300$ km s^{-1}. The southern blue emission also displays a stronger centred emission, which is evident in the PV diagram (Figure 4.11, bottom panel) at $\gtrsim 4''$ south (while its northern counterpart is fainter). In the Gaussian decomposition (Figure 4.10), the northern region with high redshifted velocities likely belongs to the outflowing/broad component rather than to the rotational/narrow one. However, the associated flux (and consequently, the ionised mass within it) is negligible in our analysis (see Section 4.5.3).

We note here that, even if several works allow three or more Gaussians to fit the emission of [OIII] in AGN with possible outflows (e.g Harrison et al., 2014; Dall'Agnol de Oliveira et al., 2021; Speranza et al., 2022; Hermosa Muñoz et al., 2023), we limited our analysis to two components to have a simpler interpretation of them: we associated the narrow component to the ionised gas rotation, and the broad one to the outflow. Adding more Gaussians to the ALUCINE fit would result in higher velocities and velocity dispersions for the broader components (but we refer to the next section for a better characterization of the outflow velocities). However, such broader components would add a small contribution to the modelled flux (see Figure C.1), hence to the outflow mass.

4.5.2 Non-parametric [OIII] velocities

In the previous section we saw that the ionised gas (traced by [OIII]) shows very high velocities probably due to an AGN wind. However, due to the complex line profiles, it is hard to see the different velocities from the Gaussian decomposition of Figure 4.10. In this section, we make use of a non-parametric method to measure the outflow velocities.

We followed the method described by Harrison et al. (2014) to spatially resolve the velocities of the [OIII] emission line. This method uses the [OIII] line produced as the sum of the two fitted Gaussians (Section 4.5.1). For every spaxel we calculate the velocities corresponding to different percentiles of the flux contained in the modelled line profile, namely the velocities at the 2nd, 5th, 10th, 90th, 95th, and 98th percentiles, respectively called v_{02}, v_{05}, v_{10}, v_{90}, v_{95}, and v_{98}. We also calculate, for every spaxel, the velocity of the emission line peak v_p.
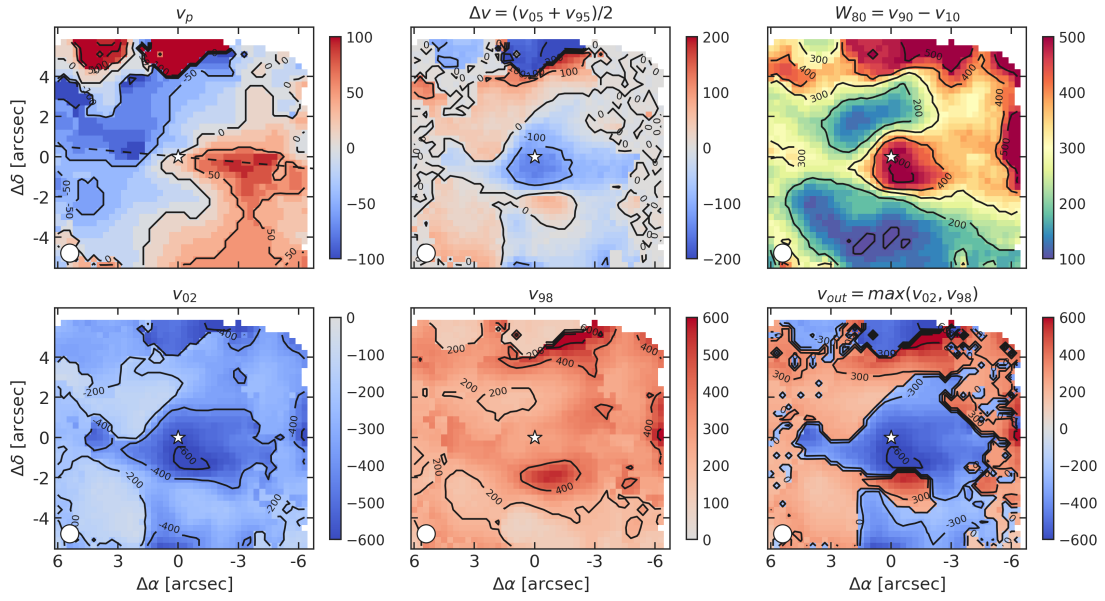
Figure 4.13: Non-parametric velocity components for the [OIII] line. The top panels show, from left to right, the peak velocity v_p, the broad velocity Δv, and the 80% width W_{80}. The bottom panels show, from left to right, the velocity at the 2$^{\text{nd}}$ flux percentile (v_{02}), at the 98$^{\text{th}}$ (v_{98}), and the positive or negative velocities that have the maximum absolute value between these two (for every spaxel), which is our estimate for the outflow velocity v_{out}. The white star symbol marks the AGN position, and the dashed black line in the top-left panel is the kinematic major axis (PA = 265°). The white circle in the bottom left of each panel is the MEGARA seeing conditions. Velocities in all the panels are in km s^{-1}.

The results are illustrated in Figure 4.13. The top-left panel shows v_p, which is similar to the velocity of the narrow component of the Gaussian decomposition (cf. Figure 4.10). It has been shown that v_p traces the ionised gas rotation (Rupke & Veilleux, 2013; Harrison et al., 2014). In the case of NGC 5506, v_p is similar to the mean-velocity field of the molecular gas, whose kinematic PA = 265° is plotted with a dashed black line. The region $\sim$ 5″ N from the AGN, redshifted at $\sim$ 300 km s^{-1}, is not following the rotation pattern.

The top-central panel of Figure 4.13 shows the $\Delta v = (v_{05} + v_{95})/2$ map. This is very similar to the velocity map of the broad component modelled by ALUCINE (cf. Figure 4.10), and so represents its velocity offset. There are differences between the two maps though, especially around $\sim$ 3″ NE from the nucleus, where the Δv plot shows redshifted velocities around 50 km s^{-1}. This may be an outflow feature lost in the ALUCINE decomposition map.

The top-right panel of Figure 4.13 is the $W_{80} = v_{90} - v_{10}$ width, which represents the width containing 80 percent of the [OIII] emitted flux. In the case of a single modelled Gaussian, this would correspond approximately to the FWHM. In our decomposition, W_{80} is, in a way, a combination of the velocity dispersions of the two components of Figure 4.10. However, W_{80} exhibits larger values across the entire FoV, particularly at the AGN position (reaching up to 500 km s^{-1}) and in the $\sim$ 5″ N region (with an average $< W_{80,N} > \sim$ 500 km s^{-1}). The maximum value observed is $W_{80,max} = 826$ km s^{-1} located $\sim$ 6″ W.

The bottom three panels of Figure 4.13 show the velocities found in the 2nd and 98th percentiles of the flux (the third panel is showing the positive or negative velocities that have the maximum absolute value among the two). These correspond to the projected maximum values for the outflow velocities (as in Rupke & Veilleux, 2013; Harrison et al., 2014; Davies et al., 2020). We find the highest blueshifted velocities around the AGN (-565 km s^{-1} at the AGN position, -620 km s^{-1} at $\sim$ 1″ S-SW) and in the $\sim$ 5″ N region (up to -702 km s^{-1}). The highest redshifted values are found at $\sim$ 1.6″ (200 pc) S-SW from the AGN (up to 551 km s^{-1}), and very close to the $\sim$ 5″ N region (up to 689 km s^{-1}).

The prevalence of blueshifted velocities in the nuclear region was previously identified in the X-shooter spectrum, extracted with a FoV of 1.8×1.8 arcsec^2 (Davies et al., 2020), which is also visible in Figure 4.12 (green profile). With the MEGARA data, we observe high-velocity components, not associated with rotation, both blueshifted and redshifted, in all panels of Figure 4.13 and in nearly every direction, particularly in the central 4×4 arcsec^2, as evident in Figure 4.11. This may be due to a wide bicone aperture, where any given line of sight intersects both approaching and receding clouds of gas simultaneously.

We isolate the [OIII] rotation velocity (v_{rot}) by taking the median absolute value of v_p along the PA = 265° line (the dashed line in the v_p panel of Figure 4.13) with a width of 4 pixels (corresponding to 1.2″ ~ 150 pc). In Figure 4.14, we plot the mean radial profiles of v_{rot}, Δv, W_{80}, and v_{out}. The [OIII] rotational velocity v_{rot} flattens out at 83 km s^{-1} around ~ 320 pc from the centre (Figure 4.14, top panel), whereas the CO(3 − 2) flattens out at 193 km s^{-1} around $r = 440$ pc (Figure 4.8, top panel). We point out that [OIII] is not the best tracer for the ionised disc rotation, and in fact it is the slowest rotator among the MEGARA lines: Hα flattens at 120 km s^{-1}, Hβ at 113 km s^{-1}, [NII] at 120 km s^{-1}, [SII] at 118 km s^{-1}, and [OI] at 110 km s^{-1} (see Appendix C.4 for the mean velocity radial profiles of all the MEGARA lines).

Interestingly, the ionised gas seems to be rotating at 60% the velocity of the molecular gas. Davis et al. (2013) found that, in CO-rich ATLAS^{3D} galaxies (Cappellari et al., 2011), the difference between molecular and ionised rotation velocities was larger for [OIII]-bright galaxies (up to a Δv_{rot} ~ 80 km s^{-1}), due to the different ionisation sources: a bright [OIII] emission (with respect to Hβ) traces a dynamically hotter component of ionised gas than HII regions embedded in the cold star-forming disc. Also Levy et al. (2018) and Su et al. (2022) found the ionised gas to rotate slower than the molecular gas in EDGE-CALIFA (Bolatto et al., 2017) and ALMaQUEST (Lin et al., 2019) galaxies, but with a smaller difference of ~ 25 km s^{-1}.

The radial profiles of Δv, W_{80}, and v_{out} have similar shapes, with a smooth decrease of absolute velocities from the centre up to a radial distance of ~ 400 pc. For these three quantities, the distance is the projected distance along every direction, so one has to be careful when comparing them to v_{rot} or to the molecular radial profiles of Figures 4.8 and 4.9. We will use the v_{out} radial profile of Figure 4.14 to calculate the other ionised outflow properties, as the mass outflow rate (see Section 4.5.4).

4.5.3 The [OIII] outflow mass

In this section we calculate the electron density and mass of the ionised outflow. To do so, we make use of the ALUCINE decomposition (Section 4.5.1), and we consider the flux of the broad component as the outflow (whereas the narrow component is associated to the ordered gas rotation). We will calculate the outflow properties using the [OIII] emission line (Figure 4.10), but we will exploit as well the modelled broad components of Hα, Hβ, and [NII] (Figures C.2-C.4).

One of the challenges in the estimation of the ionised outflow mass is to properly calculate the gas volume density n, usually expressed as the electron density n_e (where for ionised gas we expect $n_e \sim n$). Many studies assume constant fiducial values for n_e
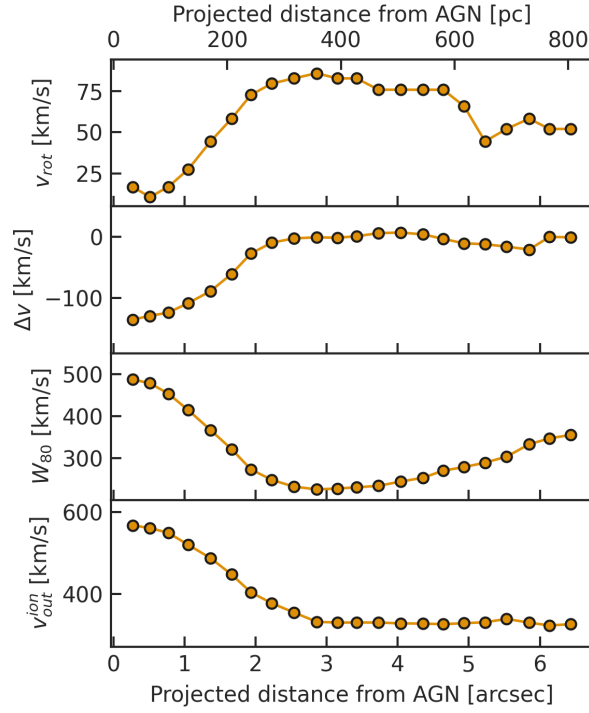
Figure 4.14: Radial profiles for the different mean velocities of the [OIII] line, all as a function of projected distance from the AGN. Panels show, from top to bottom: the rotational velocity $v_{\rm rot}$ along the kinematic axis, the broad velocity Δv, the 80% width W_{80}, and our estimate for the mean outflow velocity of the ionised gas $v_{\rm out}^{\rm ion}$.
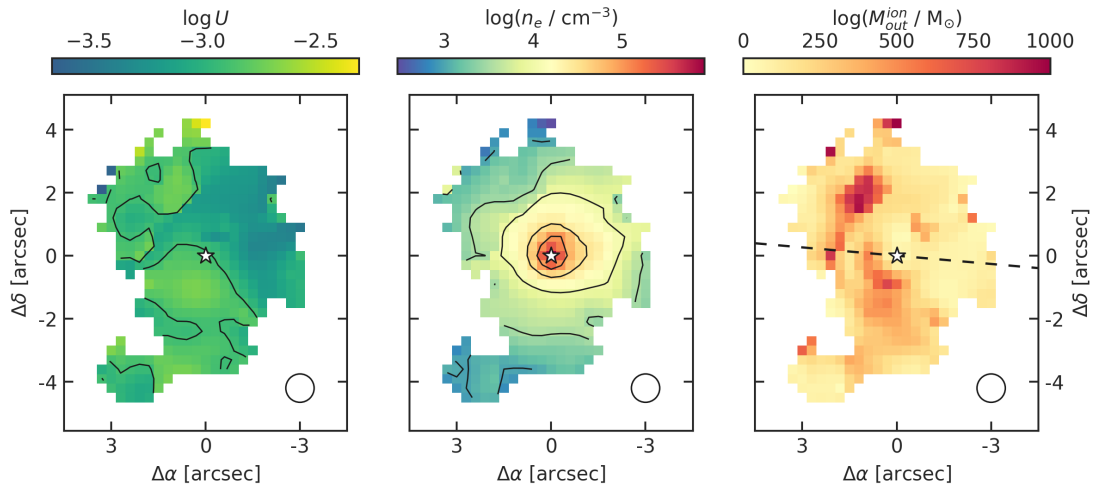
Figure 4.15: From left to right: outflowing [OIII] ionisation parameter $\log U$, electron density n_e, and mass $M_{\rm out}^{\rm ion}$. Contours are at $\log U = -2.9$ (i.e. its median value), $\log(n_e\ {\rm cm}^{-3}) = (3, 3.5, 4, 4.5, 5)$. The white star symbol marks the AGN position, and the dashed black line in the top-right panel is the kinematic major axis (PA = 265°). The white circle in the bottom right of each panel is the MEGARA seeing conditions.

(e.g. Harrison et al., 2014; Fiore et al., 2017) for all the spaxels (or for a whole sample of galaxies). The most commonly used method to estimate n_e pixel-by-pixel is based on the [SII] doublet ratio (Osterbrock & Ferland, 2006). However, this method has known biases, one of which is that the doublet ratio saturates above 10^4 cm^{-3}. We refer the interested reader to Davies et al. (2020) for a structured discussion on this topic and for a comparison between different methods to estimate n_e.

We follow Baron & Netzer (2019), Davies et al. (2020), and Peralta de Arriba et al. (2023), in estimating the ionised gas density from the ionisation parameter $\log U$, defined as the number of ionising photons per atom, $U = Q_H/(4\pi r^2 n_H c)$, where Q_H is the rate of hydrogen-ionising photons (in s^{-1} units), r is the distance from the ionising source, $n_H \sim n_e$ is the hydrogen density, and c is the speed of light. Since Q_H can be estimated from the AGN bolometric luminosity (Baron & Netzer, 2019), we can find n_e given the ionisation parameter.

Since the [OIII]/Hβ and [NII]/Hα line ratios are widely used in AGN studies (Veilleux & Osterbrock, 1987; Kewley et al., 2001), and both depend on $\log U$, Baron & Netzer (2019), by exploiting a sample of 234 type II AGN with outflow signatures, empirically determined (with a scatter of 0.1 dex) the following expression:

$$
\begin{aligned}
\log U = &-3.766 + 0.191 \log\left(\frac{[OIII]}{H\beta}\right) + 0.778 \log^2\left(\frac{[OIII]}{H\beta}\right) \\
&- 0.251 \log\left(\frac{[NII]}{H\alpha}\right) + 0.342 \log^2\left(\frac{[NII]}{H\alpha}\right) \quad .
\end{aligned}
\tag{4.2}
$$

The resulting $\log U$ map for the broad component of [OIII] is in the left panel of Figure 4.15. There are fewer pixels than the broad [OIII] map (Figure 4.10, bottom panels), since we had to use also the broad Hα, Hβ, and [NII] maps, and only the pixels featured in all four maps are left (with Hβ being the most limiting one). We recover a median value of $\log U = -2.9$, in agreement with the integrated value of -2.87 ± 0.12 found by Davies et al. (2020) within the X-shooter FoV (1.8×1.8 arcsec^2).

From the $\log U$ definition, we follow Baron & Netzer (2019) and calculate the electron density as

$$
n_e \approx 3.2 \left(\frac{L_{\mathrm{bol}}}{10^{45}\ \mathrm{erg\ s^{-1}}}\right) \left(\frac{r}{1\ \mathrm{kpc}}\right)^{-2} \left(\frac{1}{U}\right)\ \ \mathrm{cm}^{-3}
\tag{4.3}
$$

where we used the $\log(L_{\mathrm{bol}}/\mathrm{erg\ s^{-1}}) = 44.1 \pm 0.09$ obtained by Davies et al. (2020) from the X-ray luminosity given by Ricci et al. (2017a).

We show the spatially-resolved n_e map in the central panel of Figure 4.15. We find n_e to decrease at increasing distance from the centre, as found by other works on local AGN (e.g. Freitas et al., 2018; Shimizu et al., 2019; Davies et al., 2020; Peralta

de Arriba et al., 2023). The maximum $n_{e,\text{max}} = 8.5 \times 10^5$ cm^{-3} is exactly at the AGN position. To compare our values with the results of Davies et al. (2020) for NGC 5506, we calculate the median n_e at the edge of a 1.8×1.8 arcsec^2 FoV (the black square in Figure 4.2), finding $\log(n_e/\text{cm}^{-3}) = 3.95$, which is very close to their integrated value of $\log(n_e/\text{cm}^{-3}) = 4.03 \pm 0.14$.

Before calculating the ionised outflow mass from the broad [OIII] luminosity, we have to correct it for the extinction. To do so, we assume an intrinsic ratio $H\alpha/H\beta = 3.1$, and we use the Cardelli et al. (1989) extinction law ($R_V = 3.1$). We find the [OIII] outflow area (i.e. the same of the three panels in Figure 4.15) to have a median $A_V = 1.9$ mag and an extinction-corrected total luminosity $L_{\text{broad [OIII]}} = 10^{41.6}$ erg s^{-1}. If we limit the FoV to 1.8×1.8 arcsec^2 we find $10^{41.3}$ erg s^{-1}, in excellent agreement with the Davies et al. (2020) value of $10^{41.2}$ erg s^{-1}.

Finally, the ionised outflow mass $M_{\text{out}}^{\text{ion}}$ is given by (see Rose et al., 2018; Baron & Netzer, 2019):

$$M_{\text{out}}^{\text{ion}} = \frac{\mu m_H L_{\text{broad [OIII]}}}{\gamma_{\text{[OIII]}} n_e} \quad , \tag{4.4}$$

where $\mu = 1.4$ is the mean molecular weight, m_H is the hydrogen mass, $L_{\text{broad [OIII]}}$ is the extinction-corrected broad [OIII] luminosity, n_e is the outflowing gas electron density, and $\gamma_{\text{[OIII]}}$ is the effective line emissivity, which depends on the ionisation parameter (see Equations 5 and 6 in Baron & Netzer, 2019). We interpolated the values listed in Baron & Netzer (2019), Table 2, to calculate $\gamma_{\text{[OIII]}}$ for every spaxel.

The resulting spatial distribution of the outflowing [OIII] mass is presented in the right panel of Figure 4.15. We calculated a total ionised outflowing mass of $M_{\text{out}}^{\text{ion}} = 9.8 \times 10^4$ M$_\odot$. In comparison, the mass reported by Davies et al. (2020) is 3.2×10^4 M$_\odot$. The discrepancy arises because the MEGARA aperture is significantly larger than the X-shooter one (as indicated by the white and black squares in Figure 4.2). Additionally, Davies et al. (2020) used a single value for all the quantities involved in Equation 4.4, whereas we considered spatial variations, resulting in a more dispersed distribution of $M_{\text{out}}^{\text{ion}}$.

4.5.4 The ionised mass outflow rate

We calculate the ionised mass outflow rate following, as for the molecular gas, Equation 4.1 (as in Rose et al., 2018; Baron & Netzer, 2019; Davies et al., 2020). The outflow velocity and mass have been calculated following Sections 4.5.2 and 4.5.3. If we take, as typical outflow radius, $R_{out,95}^{\text{ion}} = 525$ pc (i.e. the one that contains 95% of M_{out}), we find $v_{\text{out}}^{\text{ion}} = 422 \pm 97$ km s^{-1}, from which we infer a ionised mass outflow rate of
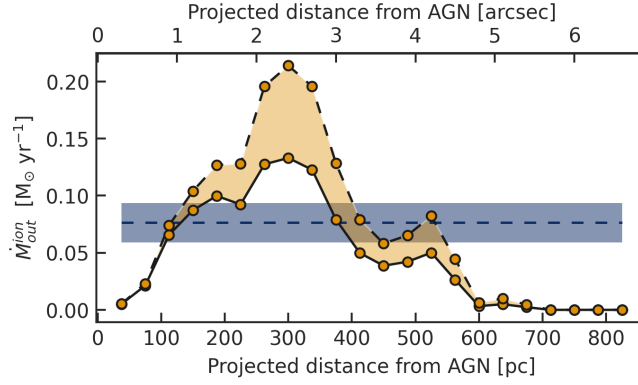
Figure 4.16: Radial profile of the ionised mass outflow rate $\dot{M}_{out}^{ion}$ as a function of average projected distance from the AGN. Solid and dashed lines are estimates of $\dot{M}_{out}^{ion}$ by using the average and the maximum v_{out}^{ion} at every radius. The blue dashed line is the integrated mass outflow rate, $0.076 \pm 0.017\ \mathrm{M}_\odot\ \mathrm{yr}^{-1}$, with the blue shading representing its uncertainty.
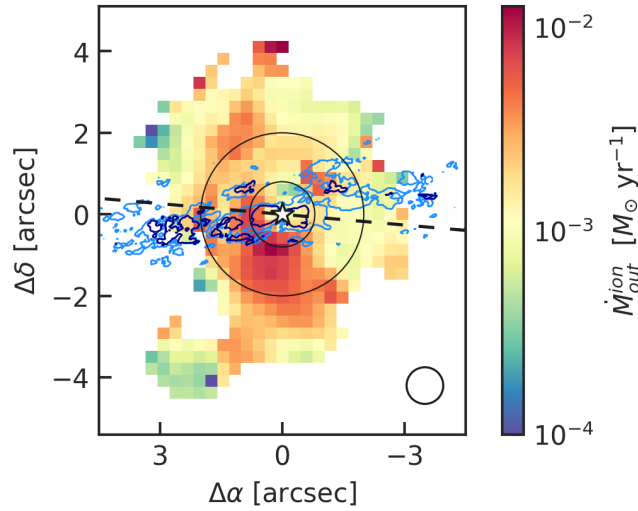
Figure 4.17: Coloured map of the ionised mass outflow rate, with contours of observed $CO(3-2)$ velocity dispersion (as Figure 4.1, bottom panel), at 30 and 50 km s^{-1} in light and dark blue, respectively. The two black circles have a radius of 100 and 250 pc (i.e. ~ 0.8 and 2 arcsec, respectively) from the white star symbol, which marks the AGN position. The dashed line is the kinematic major axis. The white circle in the bottom right is the MEGARA seeing conditions.

$\dot{M}_{\text{out}}^{\text{ion}} = 0.076 \pm 0.017 \, \text{M}_\odot \, \text{yr}^{-1}$, where the uncertainty comes from the standard deviation of the different measured radial velocities.

This is significantly lower than the $0.21 \, \text{M}_\odot \, \text{yr}^{-1}$ value reported in Davies et al. (2020). A factor of ~ 2 discrepancy is due to the different velocity (they measured 792 km s^{-1}). Another difference is the outflow size, that dilutes the averaged value (their aperture radius was of 117 pc). We can recover the Davies et al. (2020) value if we plot the radial profile of $\dot{M}_{\text{out}}$ (Figure 4.16) using, for each radius, the maximum outflow velocity available (dashed black line) rather than the average one (solid black line).

The spatially resolved map of ionised mass outflow rate (Figure 4.17) reveals an excess of $\dot{M}_{\text{out}}^{\text{ion}}$, extending from $\sim 0.8''$ up to $\sim 2.5''$ south of the AGN. This is the region where the most extreme blueshifted velocities of 620 km s^{-1} reside (see Figure 4.13). It is also a region which exhibits some excess of M_{out} (see Figure 4.15, right panel), hence the local high $\dot{M}_{\text{out}}$. Some minor $\dot{M}_{\text{out}}$ clumps are visible at $\sim 1.5''$ NW and $\sim 2.5''$ NE from the AGN. Interestingly, this NE clump (which is very clear in the M_{out} map) is located just after the separation between blueshifted and redshifted velocities (on the red side) in the bottom-right panel of Figure 4.13. All together these clumps contribute to the two main bumps in the $\dot{M}_{\text{out}}$ radial profile (Figure 4.16).

The farthest (from the AGN) peak, at $\sim 4'' \sim 500$ pc north, visible in both Figure 4.16 and 4.17, is due to the pixels in the northern region highlighted in the central panels of Figure 4.10, and whose spectrum is plotted in red in Figure 4.12. Most of this northern region has been excluded from our analysis since it is out of the $\log U$ map (Figure 4.15, left panel) and therefore of all the subsequent maps (this is mainly due to the limited size of the broad component of the Hβ line, see Figure C.3), but probably it is part of the ionised outflow. Interestingly, some molecular clouds are visible just north of the MEGARA FoV edge in Figure 4.2.

Another region left out by Figure 4.15 is the NW arc with high W_{80} values (Figure 4.13), associated with LINER/shock emission in Figures C.8 and C.9. This arc begins at the western edge of the $CO(3-2)$ emission, but it may be linked to the high dispersion values we see going towards NW (bottom panel of Figures 4.1 and 4.17). These two regions may indicate that the outflow (both in the ionised and molecular phases) has a larger size than the ones we derive with the present analysis. However, a more detailed mapping of the aforementioned areas is needed to draw meaningful conclusions.

The immediate vicinity of the AGN is relatively devoid of $\dot{M}_{\text{out}}^{\text{ion}}$, due to the small amount of $M_{\text{out}}^{\text{ion}}$ (see Figure 4.15) in this region. This may stem from the observed ionised wind being a past outflow episode, now situated ~ 100 pc from the centre, where it encounters resistance from the surrounding ISM. This corresponds to the same distance at which we observe a peak in the molecular mass outflow rate (Figure 4.9), with the
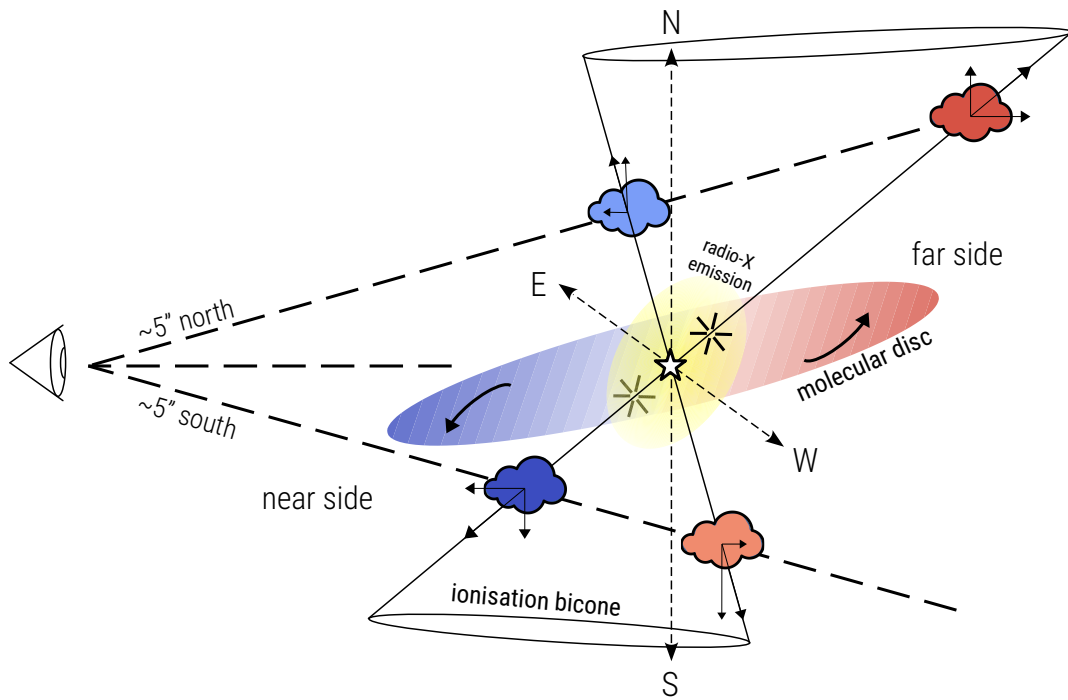
Figure 4.18: A scenario (not to scale) for the intersection between the molecular disc (the red and blue ellipse) and the ionisation bicone. In the disc of the galaxy, traced by the molecular gas, we mark the AGN position (white star) and the proposed interactions between the two gas phases (black asterisk symbols). The 300-pc radio (at 8.46 GHz) and soft X-ray (below 1 keV) emission is depicted in yellow. Along the ±5″ lines of sight, we draw clouds on the edge of the bicone, color-coded depending on whether the gas is blueshifted or redshifted.

caveat that we are seeing projected distances for the ionised outflow, and deprojected distances (on the disc plane) for the molecular outflow. We will compare in detail the two phases in the next Section.

4.6 Discussion

4.6.1 The case for elliptical motions due to a bar

Being highly inclined, it is challenging to prove (or disprove) the presence of a bar in NGC 5506. de Vaucouleurs et al. (1991) classified this galaxy as a peculiar edge-on Sa, while Baillard et al. (2011), by analysing SDSS images, signalled the presence of a "barely visible" stellar bar (with confidence ranging from "no bar" to "bar long about half D_{25}"). By inspecting PanSTARRS images we could in fact recognize a X-shape, typical of edge-on barred galaxies (Baba et al., 2022).

The presence of a bar is not evident on the molecular PV diagrams (Figures 4.4 and 4.6): we do not see two distinct components on either of the axes, as instead on the major axis of NGC 7172 (Alonso-Herrero et al., 2023, Figures 8 and 10), which is also a highly inclined galaxy. With the exception of the X-shape on the minor axis (explained in Section 4.5.1, see also Figure 4.12), the same applies for the PV diagrams of the ionised gas (Figure 4.11), to be compared with the collection of PV diagrams of edge-on galaxies in Bureau & Athanassoula (1999). This, however, could be to an unfavourable orientation of the bar, being too close to the minor axis to produce any apparent perturbation. It is also worth noting that NLSy1s as NGC 5506 are usually associated with the presence of a bar (Crenshaw et al., 2003).

The fact that we see disturbed molecular clouds on the north-west and south-east (Figure 4.1, bottom panel), may be an indication of interaction of the ionised outflow with the molecular disc (Figure 4.17). In the following section, we aim to provide a more comprehensive description of the interaction. However, it is important to note that we cannot rule out the potential existence of a bar within the central kpc. Consequently, in our analysis of molecular inflow/outflow velocities (Figure 4.8, bottom panel), we treat these results as upper limits.

4.6.2 Comparing molecular and ionised outflows

In Section 4.4 we modelled the ALMA CO(3 − 2) kinematics, finding a rotating disc along PA = 265°, within which the gas is also outflowing. The most intense region of the molecular outflow is at $r \sim 100$ pc, with $v_{out,max}^{mol} = 50$ km s^{-1} and $\dot{M}_{out,max}^{mol} = 28$ M$_\odot$

yr^{-1}. This is also where most of the molecular mass resides. Another region of interest is at $r \sim 250$ pc, where we found a second, more modest, peak of $\dot{M}_{\text{out}}^{\text{mol}}(250 \text{ pc}) = 11$ M$_\odot$ yr^{-1}. We plotted the circles of radii 100 and 250 pc in Figure 4.17. If we follow the PA = 265° dashed line on the eastern side, we find enhanced values of $\dot{M}_{\text{out}}^{\text{ion}}$ at such radii. This could be an evidence of interaction between the ionised AGN wind and the molecular disc, where we are seeing perhaps two different outflow episodes, in which case, from the 150 pc distance between the episodes, we can calculate, given a 500 km s^{-1} velocity, a $\Delta t_{\text{out}} = 0.3$ Myr (similar to the AGN flickering timescale derived by Schawinski et al., 2015; King & Nixon, 2015).

We can have a closer look at the interaction between the ionised and molecular gas by plotting the CO(3 − 2) dispersion contours against the ionised mass outflow rate map, as in Figure 4.17: not only do the $\dot{M}_{\text{out}}^{\text{ion}}$ regions at 100 and 250 pc east from the AGN correlate with high CO dispersion ($\sigma_{CO} \geq 50$ km s^{-1}), but also the region $\sim 1.5''$ NW has both a local excess of $\dot{M}_{\text{out}}^{\text{ion}}$ and high σ_{CO} (up to 61 km s^{-1}). From Figure 4.17 (but also from Figure 4.1) it seems NGC 5506 would be in the weak coupling scenario described by Ramos Almeida et al. (2022), i.e. where the biconical ionised outflow intercepts the molecular disc only partially, launching a modest molecular outflow (see also Alonso-Herrero et al., 2023). This would be in agreement with the bicone model fitted by Fischer et al. (2013) for NGC 5506: they found the inclination between the bicone and the host galaxy disc to be 32°, less than the maximum half-opening angle of the bicone (40°, see Table 6 in Fischer et al., 2013).

We draw a tentative sketch of the relative positions of the molecular disc and the ionised bicone in Figure 4.18. Every line of sight intercepts both approaching and receding sides of the bicone, resulting in a mix of blueshifted and redshifted velocities (as in Figure 4.13). Once we are far enough from the disc plane ($\sim 5''$ north and south), the edges of the bicone start to appear distinct on the spectra (Figure 4.12): this would point out a hollow bicone. The southern nearest and northern farthest bicone edges intercept the molecular disc, hence rising the CO velocity dispersion and causing the molecular ring to outflow on the disc plane: this results in high CO dispersion on the SE-NW direction (Figure 4.17), and in an asymmetry in the CO(3 − 2) PV diagram on the redshifted northern - blueshifted southern directions (Figure 4.6, bottom panel).

An exception to the spatial correlation between σ_{CO} and $\dot{M}_{\text{out}}^{\text{ion}}$ is in the immediate vicinity of the AGN: there the CO line broadening is probably due to the presence, in a small space, of multiple components of CO velocities, even due to ordered rotation alone. Nevertheless, this region also has a deficit of CO emission (see Figure 4.1 and García-Burillo et al., 2021), which may be another indication of multiphase feedback.

If we adopt the scenario drawn in Figure 4.18, then the ionised outflow velocities we

Table 4.2: Results for the molecular and ionised phases of the AGN outflow. The distance from the AGN R_{out} is in different directions for the two phases.

Property	Molecular	Ionised
R_{out} [pc]	610	525
v_{out} [km s^{-1}]	26 ± 9	422 ± 97
M_{out} [M$_\odot$]	1.7×10^8	9.4×10^4
$\dot{M}_{\text{out}}$ [M$_\odot$ yr^{-1}]	8 ± 3	0.08 ± 0.02
$\dot{E}_{\text{out}}$ [10^{39} erg s^{-1}]	1.7 ± 1	4.3 ± 1.7
$\dot{P}_{\text{out}}$ [10^{32} dyn]	13.1 ± 6.7	2.0 ± 0.7

Notes. Molecular v_{out}, $\dot{M}_{\text{out}}$, $\dot{E}_{\text{out}}$, and $\dot{P}_{\text{out}}$ are upper limits, due to the possible presence of elliptical motions associated with a nuclear bar. All the ionised values (except M_{out} and $\dot{M}_{\text{out}}$) are lower limits, since R_{out} and v_{out} are projected (on the plane of the sky) measurements.

measured, especially the redshifted ones in the north and the blueshifted in the south, are lower limits due to projection effects. We did not perform a modelling of the bicone (so its opening angle in Figure 4.18 is only qualitative), but if we adopt an half-opening angle of 40° (Fischer et al., 2013), we can derive a multiplicative factor of $1/\sin(40°) = 1.56$, which would result in an average deprojected $v_{\text{out}}^{\text{ion}} = 657 \pm 151$ km s^{-1}. Being the deprojected $R_{\text{out}}^{\text{ion}}$ affected in the same way, this would not change the $\dot{M}_{\text{out}}^{\text{ion}}$.

If the AGN wind seen with the [OIII] and the outflowing CO ring are physically connected, we expect the kinetic energy rate ($\dot{E}_{\text{out}}$) or the momentum rate ($\dot{P}_{\text{out}}$) to be conserved (see King & Pounds, 2015, and references therein). These two quantities can be straightforwardly calculated as $\dot{E}_{\text{out}} = \dot{M}_{\text{out}} v_{\text{out}}^2 / 2$ and $\dot{P}_{\text{out}} = \dot{M}_{\text{out}} v_{\text{out}}$. The values (listed in Table 4.2) point to a energy-driven rather than momentum-driven outflow (King & Pounds, 2015; Veilleux et al., 2020): in such outflows, the momentum undergoes a boost (e.g. Veilleux et al., 2020; Longinotti et al., 2023), which in our case is $\dot{P}_{\text{mol}}/\dot{P}_{\text{ion}} = 7$. However, if we use the values derived by Davies et al. (2020) for the ionised outflow, the ratio of the momentum rates would be ~ 1.2, rather indicating a momentum-driven outflow. Given the observed L_{bol} and λ_{Edd} (see Table 4.1), a radiation pressure-driven wind would predict an outflow of ~ 3 M$_\odot$ yr^{-1} (Hönig, 2019), not too far from our $\dot{M}_{\text{out}}^{\text{mol}}$ value: this also would point to a momentum-driven scenario.

We highlight that the dichotomy between energy and momentum conservation refers to single or continuous outflow episodes. In the case of NGC 5506, we may be observing the stratification of multiple outflows, a possibility explored also in the next section. Taking everything into account, if the ionised wind is pushing and dragging the molecular
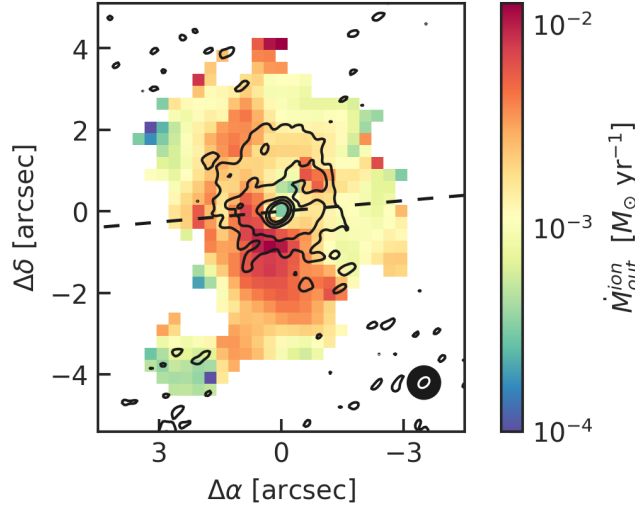
Figure 4.19: Same as Figure 4.17 but with the Schmitt et al. (2001) 3.6 cm VLA contours, at $\log(S_\nu/\text{Jy beam}^{-1}) = (-4, -3.5, -3, -2.5, -2)$, in black. The black circle in the bottom right is the MEGARA seeing conditions, with the VLA beam ellipse within it in white.

gas, it currently seems to impact only the inner part of the molecular ring. At this stage, the AGN wind appears to be relatively ineffective in clearing the entire galaxy (which is common in local systems, see e.g. Fluetsch et al., 2019).

4.6.3 Extending the spectrum: radio and X-ray literature

Despite its classification as a radio-quiet galaxy (Terao et al., 2016), NGC 5506 has been detected in the radio band in several studies. Wehrle & Morris (1987) detected, with the VLA at 5 GHz, a radio bubble, NW from the nucleus, also visible in the 8.46 GHz VLA A-array continuum image presented by Schmitt et al. (2001). In Figure 4.19 we plot the contours of Schmitt et al. (2001) VLA image against the ionised mass outflow rate map, where we can see that the radio bubble observed by Wehrle & Morris (1987) perfectly overlaps with the $\sim 1.5''$ region that has both high $\dot{M}_{\text{out}}^{\text{ion}}$ and high σ_{CO}. The extended ~ 300 pc VLA emission in Figure 4.19 is well aligned with the galactic disc (PA = 265°), but extends below and (mostly) over it, following the [OIII] emission. Orienti & Prieto (2010) measured, for this diffuse radio emission, a steep spectral index $\alpha = 0.9$, which combined with the size < 1 kpc, would make it a compact steep spectrum (CSS) radio source (e.g. Dallacasa et al., 2013; O'Dea & Saikia, 2021).

The VLA contours shown in Figure 4.19 are also spatially coincident with the soft X-ray (below 1 keV) emission observed, with the *Chandra* X-ray Observatory, by Bianchi et al. (2003). Their main explanation is that the photoionised gas (that we clearly see with MEGARA, Figure 4.2, even if more extended than 300 pc) is reprocessing

the nuclear X-ray emission. However, since we detect velocities up to ~ 600 km s^{-1} out to 300 pc from the AGN, the expected temperature of the shocked emission is $kT \approx 1.3(v_{shock}/10^3)^2$ keV ≈ 0.5 keV (Fornasini et al., 2022), which could suggest a thermal emission for the *Chandra* soft X-ray observation (see also Paggi et al., 2012).

High-resolution radio observations made with the Very Long Basement Array (VLBA) at different frequencies (1.6 - 15 GHz, Roy et al., 2000), show a sub-relativistic ($v_{jet} \leq 0.25c$) one-sided jet, initially oriented 70° anticlockwise from the north (so roughly as the CO disc), and then bending 90° towards south (Kinney et al., 2000), at 3.4 pc ($\sim 0.03''$) from the core emission. In Roy et al. (2001) they argue that the counterjet is not visible because of free-free absorption (rather than doppler boosting), and that the bend might be a sign of interaction between the jet and the NLR gas on parsec scales. Middelberg et al. (2004) collected different-epochs EVN, MERLIN and VLBA observations, and reported a 3σ upper limit of $0.50c$ for the jet motion with respect to the core. Gallimore et al. (2006) argue that the diffuse emission on the 300-pc scale (Figure 4.19 and Schmitt et al., 2001), is attributed to the pc-scale jet observed by Roy et al. (2000). The misalignment between the jet trajectory (initially pointing at $\sim 70°$ anticlockwise from north and later bending $\sim 90°$ towards south) and the elongation of the diffuse radio emission towards the north direction can be explained by either jet precession or jet-ISM interactions (Gallimore et al., 2006, and also Xanthopoulos et al., 2010 come to the same conclusions).

Interestingly, such high velocities are also seen via absorption of the hard X-ray Fe XXVI Lyα line. The UFO in NGC 5506 has been observed and studied by Gofford et al. (2013) and Gofford et al. (2015), where they find $v_{UFO} = 0.246 \pm 0.006$ c. The momentum rate released by such a UFO ranges between 5×10^{33} and 5×10^{35} dyn, where this large uncertainty mostly comes from the estimation of the distance between the UFO and the AGN (see Tombesi et al., 2013, for a detailed derivation of the UFO parameters). Even the lower limit of $\dot{P}_{\text{out}}^{UFO}$ is 3.8 times the molecular one (see Figure 4.20). If we accept as good all these different measurements, a plausible explanation for this momentum decrease (instead of the boost required in the energy-driven scenario, or the constant $\dot{P}_{\text{out}}$ in the momentum-driven scenario) is, again, that we are seeing different outflow episodes, among which the UFO is the most recent (also Sebastian et al., 2020, suggest multiple activity episodes for NGC 5506 from analysing polarized radio data). X-ray observations have shown in fact continuous rapid variation among different epochs (McHardy & Czerny, 1987; Uttley & McHardy, 2005; Sun et al., 2018), even suggesting the presence of a supermassive black hole binary system (Manchanda, 2006).

Both relativistic jets (e.g. Mukherjee et al., 2018; Audibert et al., 2023, but also low-power jets, e.g. Venturi et al., 2021; Pereira-Santaella et al., 2022) and UFOs (e.g.
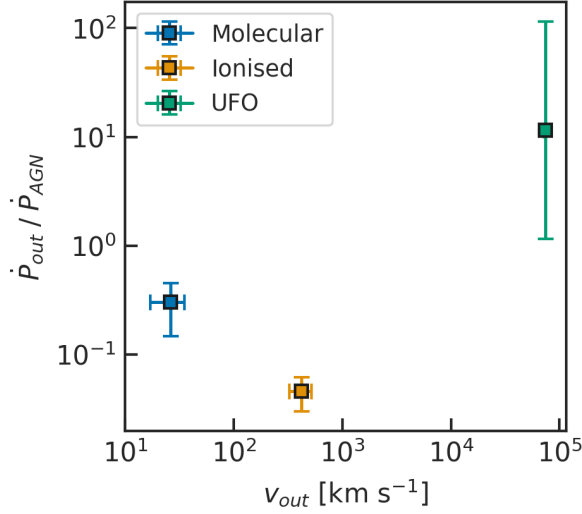
Figure 4.20: Outflow momentum rate divided by the AGN radiation momentum rate L_{bol}/c (also called *wind momentum load*) as a function of the outflow velocity v_{out} for the molecular gas (in blue), the ionised gas (in orange), and the UFO (in green).

Marasco et al., 2020; Longinotti et al., 2023; Salomé et al., 2023) are thought to be the initial trigger of galaxy-scale ionised and molecular outflows (see Singha et al., 2023, for a recent discussion). Another possibility is that the VLBI radio structures seen by Roy et al. (2000) are shock signatures left by the X-ray UFO (Longinotti et al., 2018).

4.7 Summary

We presented new GTC/MEGARA optical IFU observations of NGC 5506, complemented with ALMA Band 7 observations of the CO(3 − 2) transition (García-Burillo et al., 2021). NGC 5506 is a nearby ($D = 26$ Mpc) luminous ($L_{\text{bol}} \sim 1.3 \times 10^{44}$ erg s^{-1}) Seyfert galaxy, part of the GATOS sample (García-Burillo et al., 2021; Alonso-Herrero et al., 2021). The angular resolution of the ALMA observation ($0.21'' \times 0.13''$) allows us to probe regions on physical scales of ~ 25 pc for the molecular gas. The GTC/MEGARA observation, with a seeing of $0.9''$ (corresponding to ~ 113 pc at the distance of NGC 5506), offers a spectral resolution enabling the analysis of velocities as low as ~ 14 km s^{-1}.

The CO(3 − 2) map reveals a highly inclined ($i = 80°$) cold molecular gas ring, symmetric up to a radius of $3.5'' \sim 438$ pc, with an eastern tail extending up to a $8'' \sim 1$ kpc radius. The cold molecular gas mass of the ring is $\sim 2.3 \times 10^8$ M$_\odot$, calculated assuming a brightness temperature ratio of $T_{B,CO(3−2)}/T_{B,CO(1−0)} = 0.7$ and a Galactic CO-to-H$_2$ conversion factor. The CO(3 − 2) kinematics reveal a rotating disc, flattening at 193 km s^{-1} around $r = 440$ pc, with clear signatures of non-circular motions.

A ^{3D}Barolo model of a rotating disc with a radial velocity component reproduces reasonably well the observed CO kinematics, interpreted as a rotating and outflowing molecular ring. Within a 0.4″ radius, fitted radial velocities are directed towards the centre, potentially indicating AGN feeding, though this finding could not be confirmed since this radius is very close to the ALMA beam size. At larger radii, the radial velocity is directed outwards, decreasing from a maximum of 50 km s^{-1} to an average of 26 km s^{-1}. The maximum molecular outflow radius is 610 pc, within which we calculate an integrated molecular gas mass outflow rate of $\sim 8 \pm 3$ M$_\odot$ yr^{-1}.

We detected several bright emission lines in the MEGARA spectra, with [OIII]λ5007 standing out as the brightest. The spatially-resolved BPT diagnostic diagrams predominantly reveal Sy-like excitation, ruling out a significant contribution from star formation over a projected region of 1.5 kpc × 1.4 kpc. The [OIII] kinematics appear to be dominated by the outflowing gas. Nevertheless, we separated disc rotation from non-circular motion spaxel-by-spaxel, employing both parametric and non-parametric methods. The ionised gas exhibits a slower rotation speed than the molecular gas ($\sim$ 190 km s^{-1}), with Hα, [NII] and [SII] reaching 120 km s^{-1}. Conversely, we detected [OIII] radial velocities up to 1000 km s^{-1}, both approaching and receding. By employing a non-parametric analysis of the line wings of [OIII] emission, we derived an average ionised gas outflow velocity of 422 km s^{-1} within a radius of 525 pc. To estimate the outflowing mass, we utilized the broad component intensity maps from the double Gaussian decomposition. We calculated the electron density in every spaxel using the ionisation parameter method. This analysis yielded an outflowing mass of 9.8×10^4 M$_\odot$, resulting in an ionised mass outflow rate of $\dot{M}_{\text{out}}^{\text{ion}} = 0.076 \pm 0.017$ M$_\odot$ yr^{-1}.

We compared the spatially resolved map of $\dot{M}_{\text{out}}^{\text{ion}}$ with the CO(3−2) velocity dispersion map, identifying spatial correlation between the two. The ionised outflow does not appear perpendicular to the plane of the galaxy; instead, it likely lies at a small angle relative to the disc. This results in a good geometrical coupling between the two phases. We also found diffuse radio and soft X-ray emission to spatially correlate with the observed [OIII] emission and $\dot{M}_{\text{out}}^{\text{ion}}$.

Various results, both from this study and the literature, suggest a diverse history of outflows for NGC 5506. These outflows may be associated with the presence of a pc-scale radio jet, a $0.25c$ UFO, or a combination of both. New ALMA and JWST observations, offering a higher resolution view of the nuclear region of NGC 5506, will soon become available as part of the GATOS project. These observations may eventually enhance our understanding of the complex interactions between the sub-pc radio jet, the UFO, the ionised wind, and the molecular torus and disc.

5

Conclusions

One of the central questions in contemporary astrophysics is whether the energy and momentum released by AGNs can effectively quench star formation in the host galaxy, driving its morphological transition from spiral to elliptical. The problem is inherently complex due to:

- Different scales involved, ranging from the sub-pc size of accretion discs to the Mpc-size of the CGM of large galaxies.

- Delayed effects between AGN radiation, wind expansion, star formation and the ejection of enriched material. Adding to this is the continuous flickering on and off of the AGN.

- Involvement of different gas phases, each associated with distinct physical processes and requiring different observational instruments and techniques to characterize them.

- The obvious fact that every galaxy is unique, and a strong observational/statistical and theoretical effort must be devoted to highlight the shared key properties (e.g. the galaxy bimodality). Additionally, galaxies are not isolated entities; they are interconnected in groups, clusters, cosmic filaments, and frequently interact and merge over their lifetime.

Molecular gas is the primary fuel for both star formation and black hole accretion, making its fate crucial for our central question. Through this Thesis, I contribute to this research field by analysing the impact of AGN on molecular gas excitation and kinematics in the Local Universe. In the following, I provide a summary of the main results, the conclusions drawn, and a discussion on future perspectives.

5.1 Highlights of the presented work

Molecular gas excitation in AGN-host galaxies: observing the impact on galactic centres

High-energy radiation from the nucleus of active galaxies heats and influences the chemistry of the molecular gas (Section 1.2.3). To assess its impact on CO emission, and to disantangle its effect from stellar radiation (Section 1.2.2), I presented, in Chapter 2, a new observational study of a sample of local AGN taking advantage of the exquisite multiwavelength data available, including continuum emission from far-IR to X-ray bands, and sub-mm line (CO) emission. I selected the sample from the *Herschel* CO observations, applying a $L_X(2 - 10\,\text{keV}) \geq 10^{42}$ erg s^{-1} threshold, which resulted in 35 objects. Apart from being X-ray luminous and primarily (77%) type-2 AGNs, the galaxies in the sample exhibit diverse morphologies, environments, merger stages, and IR luminosities (Sections 2.2 and 2.3).

I calculated large values for the molecular gas mass ($\sim 3 \times 10^8 - 7 \times 10^{10}$ M$_\odot$) and spread-out SFR values (in the range $\sim 0.3 - 300$ M$_\odot$ yr^{-1}). When measured on the r_{CO} scale ($\sim 2 - 5$ kpc), the surface densities Σ_{mol} and Σ_{SFR} appear consistent with other samples of non-active galaxies (see the Schmidt-Kennicutt plane in Figure 2.2). This suggests that the AGN does not significantly influence the star formation and the molecular gas of the entire host galaxy.

In contrast to low-J CO lines (used for calculating M_{mol}), mid- and high-J CO transitions are emitted from smaller regions containing the AGN and the bulk of high-density molecular gas and SF. The median size of this region, based on spatially resolved ALMA CO(6 − 5) images (Section 2.3.4), is $r \sim 250$ pc for this sample. Despite checking for correlations between FUV (G_0) and X-ray fluxes (F_X) at this radius with different CO line ratios, I found only sublinear relations. My conclusion is that neither G_0 nor F_X alone can explain the observed CO SLEDs, and probably a mix of SF and AGN feedback is responsible.

Finally, I compared the CO line ratios with grids of simple single-density PDR and XDR models. I found that (i) PDR models can reproduce the observed high-J ratios only when assuming extremely high gas densities ($n > 10^5$ cm^{-3}), and (ii) XDR models can reproduce the observed ratios across all Js with more realistic densities ($n \sim 10^2 - 10^3$ cm^{-3}), albeit with a degeneracy observed at $J_{\text{upp}} \gtrsim 12$, where widely different densities can reproduce the data.

Notably, the data presented in Esposito et al. (2022) were used by Bisigello et al. (2022, including FE) for implementing the evolution of the CO luminosity function in a new semi-analytical model called SPRITZ (http://spritz.oas.inaf.it/).

Modelling molecular clouds and CO excitation in AGN-host galaxies

Building upon our earlier findings (see also Section 2.6), I decided to refine the PDR and XDR model grids by incorporating a more physically-motivated model. The molecular gas exhibits a well-structured density field (see Section 1.2.5), a factor that must be considered when examining CO heating and cooling processes. To address this, I developed a novel model, introduced in Chapter 3, which accounts for (i) the internal density structure of GMCs, (ii) the heating associated with SF and AGN feedback (i.e. PDR and XDR), and (iii) the mass distribution of GMCs within the galaxy. To my knowledge, this is the first instance of such a model being developed and utilized to investigate molecular emission.

The model operates in two ways. Firstly, it can predict the CO SLED of a galaxy based on its optical size r_{25}, molecular mass, X-ray luminosity, and the radial profile of the FUV flux $G_0(r)$. Secondly, it can fit an observed CO SLED using a MCMC algorithm, which returns the posterior distribution of two physical parameters: the CO-to-H_2 conversion factor, α_{CO}, and the X-ray attenuation column density, N_H. I tested the model on a sub-sample of 24 AGNs from Chapter 2 (see Section 3.3 for the selection criteria). The median values obtained were $\alpha_{CO} \sim 5$ $M_\odot$ (K km s^{-1} pc^{-2})$^{-1}$ and N_H $\sim 10^{22}$ cm^{-2}. The α_{CO} values are largely consistent with the Galactic value, suggesting that the AGN does not significantly impact the overall molecular gas (though interpreting α_{CO} is nuanced, as discussed in Section 3.5.1). The notably low values for N_H indicate that, despite the majority of the test sample comprising type-2 AGNs, X-rays can easily escape the torus and irradiate the GMCs. In other words, our line of sight and that of the GMCs within the host galaxy differ.

The most noteworthy outcome from the model is that the CO SLED of the examined galaxies is entirely reproduced by an XDR component from CO(4 − 3) upwards. The increased relevance of X-rays in influencing CO luminosity, compared to other works in the literature, can be mainly attributed to the utilization of a physical distribution for the molecular gas (described in Section 1.2.5), which predicts the majority of the molecular gas mass in a galaxy to exist at moderate densities ($n \sim 10^2 - 10^4$ cm^{-3}). This is in contrast to the extreme densities that PDR models typically require to excite mid- and high-J CO lines. This conclusion arises from a physically-motivated structure for the molecular gas, as opposed to relying on single-density radiative transfer models.

The AGN kinematic feedback: the case study of the nearby Seyfert galaxy NGC 5506

High-energy photons emitted by the AGN not only heat and influence the chemistry of GMCs but also generate hot winds capable of pushing the gas outward in both the torus

and the galaxy disc. This multiphase radial motion is observable through an analysis of gas kinematics. In Chapter 4, I presented a case study of such a multiphase outflow in NGC 5506, a nearby, highly inclined Seyfert galaxy and a member of the Galactic Activity, Torus, and Outflow Survey (GATOS). This source is notably characterized by (i) one of the highest nuclear deficiencies in molecular gas (as shown in Figure 1.22); (ii) the coexistence of a sub-pc radio jet, exhibiting signs of interaction with the ambient ISM, and an UFO; and (iii) its classification as a NLSy1, suggesting a potential young phase in the AGN evolution.

I analyzed and modelled the kinematics of the molecular gas, traced by $CO(3-2)$, and of the ionised gas, traced by [OIII]. The observations resulted in spatially-resolved maps covering the central $1-2$ kpc of NGC 5506. For the molecular gas, by using the public code ^{3D}Barolo, I identified a nuclear ring exhibiting both rotational and outflowing motions on the galaxy plane (see Section 4.4). I modelled the ionised gas by using both a Gaussian decomposition (with the public code ALUCINE) and a non-parametric method. The kinematics of the ionised gas were predominantly influenced by non-circular motions, interpreted as an AGN wind expanding mostly over and below the galaxy plane (see Section 4.5). However, due to the complexity of the velocity fields, I could not delineate a biconical shape. Despite the [OIII] wind expanding faster (up to $\approx 10^3$ km s^{-1}, with $\dot{M}_{out} \approx 0.08$ M$_\odot$ yr^{-1}), the CO outflow entrains the largest mass rate (≈ 8 M$_\odot$ yr^{-1}, with $v_{out}^{max} \approx 50$ km s^{-1}). Remarkably, the map of the ionised mass outflow rate shows spatial correlation with diffuse radio and soft X-ray emissions originating from the galaxy center (Figure 4.19). It is worth noting that the UFO momentum rate is higher, at least by a factor of ≈ 4, than the ionised and molecular rates. This discrepancy suggests that they might be unrelated (see Figure 4.20)

My interpretation of these multiphase observations suggests that the AGN hot wind, traced by [OIII] and also observed in the radio and soft-X emissions, interacts with the molecular gas in the disc. This interaction results in the outward motion of the molecular gas, leading to a nuclear gas deficit. To support this interpretation, we observe kinematic perturbations in both phases at the same radii, indicating an interaction. Additionally, assuming that the [OIII] outflow has a biconical shape, the presence of high-velocity clouds at the edge of the observed region suggests that the bicone is inclined with respect to the galaxy disc, further indicating a possible interaction (see a schematic view in Figure 4.18). An alternative explanation considers the influence of radiation pressure from the AGN on the molecular outflow. Equation 1.13 predicts a $\dot{M}_{mol} \sim 3$ M$_\odot$ yr^{-1}, which aligns closely with the measured value. While I do not present physical quantities related to the sub-pc radio jet, we can hypothesize its role in inducing the molecular outflow. Regarding the UFO, given its larger momentum rate, it is probable that we are

witnessing a different, more recent outflow episode. This conclusion is further supported by several observations of X-ray variability in this AGN.

5.2 Final summary and open questions

To summarize the overall findings of the investigation presented in this Thesis, it is evident that AGN play a significant role in influencing the gas within the central kpc. This influence is manifested through the creation of XDRs, which in turn drive heating and cooling rates of CO, as well as by exerting pressure on the multiphase gas, leading to the generation of winds and outflows. However, it becomes apparent that the AGN impact does not extend to directly affecting the large-scale structure of the host galaxy, at least in the context of nearby ($D \lesssim 100$ Mpc) and moderately powerful ($L_X \lesssim 10^{44}$ erg s^{-1}) Seyfert galaxies. This outcome holds particularly true for the ejective mode of AGN feedback (as discussed in Section 1.3.2), a perspective consistently supported by contemporary literature (e.g. Fluetsch et al., 2019; Ellison et al., 2021b; Lamperti et al., 2022; Ramos Almeida et al., 2022). The analysis of NGC 5506, along with the analysis of other very nearby ($D < 40$ Mpc) galaxies carried out within the GATOS collaboration, allows us to also rule out the preventive mode of AGN feedback (i.e. galaxy starvation), as the observed outflows lack the required power to reach and heat the CGM.

Another plausible scenario is the suppression of SF efficiency (SFE) through the heating and injection of turbulence into the ISM (e.g. Wylezalek et al., 2020; Piotrowska et al., 2022). In Figure 5.1 I replot the Schmidt-Kennicutt for the sample of AGN analysed in Chapter 2, together with the samples of AGNs and non-AGNs we displayed in Figure 2.2. In Section 2.4, one of the conclusions was that the AGNs and non-AGNs are well-mixed on the $\Sigma_{SFR} - \Sigma_{mol}$ plane. However, a fresh look at Figure 5.1 reveals that, contrarywise to star-forming galaxies, (i) AGNs rarely reach low depletion times ($\sim 10^8$ yr) or equivalently high SFE= τ_{dep}^{-1}, and (ii) AGNs do not exhibit very high values of Σ_{SFR} and Σ_{mol}. This could indicate a constraint on the SFE (but not in every case) and the suppression of the formation of high-density gas regions, which might otherwise evolve into starburst regions. To explore this possibility further, a more careful evaluation is required. This involves selecting galaxies with and without AGN, and with and without starburst activity, coupled with high spatial resolution ($\lesssim 100$ pc) mapping of both dense molecular gas (which better traces ongoing or imminent SF) and the SFR, both near and far (beyond 1 kpc) from the galactic nucleus.

Even with more detailed observations, detecting such a subtle effect of AGN feedback in action may prove challenging, particularly due to delayed manifestations. Once the AGN has initiated the suppression of SF, it could already be in an off-state, potentially
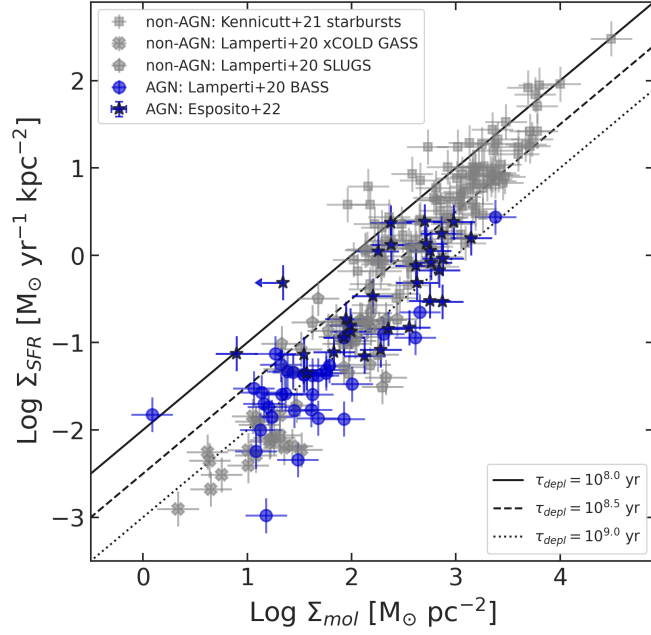
Figure 5.1: Schmidt-Kennicutt relation for the samples analysed in Chapter 2. Blue and gray points are for AGN and non-AGN host galaxies. Different symbols are for different samples (see Figure 2.2 for details). The three black lines represent different constant depletion times.

nullifying observed relations. To address this challenge, time-dependent models, informed by the physical effects of AGN and stellar feedback, need to be employed and compared to observations. While zoom-in MHD simulations could naturally facilitate this, they often lack the necessary spatial resolution for resolving microphysics, leading to reliance on empirical relations. Additionally, certain fundamental processes relevant to our problem, such as star formation, black hole accretion, and the launching of jets and winds, still lack a complete physical explanation. The solution will likely emerge from a communal effort in joining updated simulations, theoretical advances, large statistical samples, and detailed observational studies on selected sources.

5.3 Future perspectives

The past few decades have underscored the fundamental importance of constraining AGN feedback on the host galaxy. This Thesis aimed to contribute to this research field both observationally, through the analysis of a sample of local Seyfert galaxies, and from a theoretical standpoint. In Chapter 3, I presented a new physically-motivated model for estimating the molecular line emission in active galaxies. This model has been publicly released under the name `galaxySLED`, and is now available on GitHub at the address `https://federicoesposito.github.io/galaxySLED/` (see Figure 5.2).

Figure 5.2: Screen capture of the `galaxySLED` homepage at https://federicoesposito.github.io/galaxySLED/.

The model is now able to predict the CO SLED of an active galaxy given some observables, and to fit the observed CO SLED to estimate the CO-to-H_2 conversion factor α_{CO} and the X-ray attenuation column density N_H. I plan to extend `galaxySLED` in two directions.

Beyond the CO SLED

Firstly, by exploiting the predictive power of the underlying `Cloudy` simulations, I plan to include predictions on other ISM lines, complementary to CO. These lines are now commonly observed by ALMA, which revolutionised the field of molecular astrophysics, and JWST, which is already playing a similarly crucial role. I divide the lines in three groups.

A first group comprises the rotational lines of HCN, HCO$^+$, and HNC, which trace the high-density ($\gtrsim 10^6$ cm^{-3}) clumps and cores within GMCs. I also plan to explore the use of more molecular species in the same wavelength range (i.e. the one observable by ALMA), such as CS, CN, C$_2$H, SiO, and H$_2$O. A possible outcome of this inclusion is the production of diagnostic diagrams to disentangle AGN, SF and shock excitation, similarly to what BPT diagrams do with ionised emission lines.

A second group is composed by the widely observed carbon and oxygen transitions that trace the upper layers of GMCs and PDRs, i.e. the [CI], [CII], and [OI] far-IR lines. To achieve this, some more sophisticated models of the cold gas distribution are

needed, as these lines do not originate from the nearly collapsing gas we considered in `galaxySLED` so far, but mostly trace atomic and lowly ionised gas (with the inclusion of the CO-dark molecular gas). Such a model could have a strong impact on interpreting the ISM observations of both local and distant galaxies, where these lines are commonly observed.

A third group consists of the rotational lines of H_2. These lines trace the warm ($T \gtrsim 100$ K) molecular gas, and are now routinely observed using the medium resolution spectroscopy (MRS) instrument, which operates in the range $5 - 28$ μm) and is equipped on the JWST. Considered the high temperatures involved, H_2 lines mostly originate in shock-heated regions, so this has to be taken into account in the model implementation. In this perspective, a comparison with MHD simulations of shocks within the molecular gas could be useful. The resulting new model could then be exploited to fully characterize the molecular ISM with means of multiwavelength observations (IR and mm/sub-mm).

Estimating the mass of gas

The use of low-J CO transitions to estimate the molecular mass M_{mol} relies on a number of assumptions and are undermined by many uncertainties (I discussed it in Section 1.2.1). The `galaxySLED` code is now able to infer the CO-to-H_2 conversion factor from the CO SLED fit, which may already serve as a way to estimate M_{mol}. However, at its present state, the code utilizes a single fixed surface density Σ_{mol} for the GMCs, which is constraining possible calculations of M_{mol}.

I plan to extend the current model to overcome these limitations, and to be able to directly calculate M_{mol} from the fit of the CO SLED. This proposed effort would require also a calibration with secure measures of M_{mol} in different samples, and validation.

Further GATOS observations

The GATOS sample (described in García-Burillo et al., 2021; Alonso-Herrero et al., 2021; García-Bernete et al., 2023) comprises Seyfert galaxies within a distance range of $10 - 40$ Mpc, selected from the 70-month Swift/BAT catalogue of AGN (Baumgartner et al., 2013). Ongoing observations include data from optical and near-IR IFU, JWST, and ALMA. The project aims to investigate the properties of the obscuring material (torus) and the nuclear gas cycle (inflows and outflows) in the immediate surroundings of the nuclear region of local AGNs.

New ALMA Band 7 and JWST MIRI MRS observations, providing a higher resolution view of the nuclear region of NGC 5506, will soon be available. Specifically, the forthcoming ALMA observations will trace the CO($3 - 2$) and HCO$^+$($4 - 3$) emission

lines at a spatial resolution of $2 - 4$ pc. JWST observations will include the mid-IR H_2 lines in the $5 - 29\ \mu$m range, namely the quadrupole rotational transitions from the 17 μm S(1) to the 5 μm S(8) (see e.g. the work on NGC 7469 by Armus et al., 2023). The MIRI spectrum has been published by García-Bernete et al. (2023), but the emission lines have not undergone analysis yet.

These observations may eventually enhance our understanding of the relative behaviour of molecular gas at different temperatures and densities when exposed to AGN radiation. Furthermore, we may gain insights into the complex interactions between the sub-pc radio jet, the UFO, the ionised wind, and the molecular torus and disc.

Bibliography

Aalto S., Spaans M., Wiedner M. C., Hüttemeister S., 2007, A&A, 464, 193

Aalto S., Garcia-Burillo S., Muller S., Winters J. M., van der Werf P., Henkel C., Costagliola F., Neri R., 2012, A&A, 537, A44

Abramowicz M. A., Fragile P. C., 2013, Living Reviews in Relativity, 16, 1

Abramowicz M. A., Czerny B., Lasota J. P., Szuszkiewicz E., 1988, ApJ, 332, 646

Accurso G., et al., 2017, MNRAS, 470, 4750

Aird J., et al., 2010, MNRAS, 401, 2531

Alatalo K., et al., 2015, ApJ, 798, 31

Albrecht M., Krügel E., Chini R., 2007, A&A, 462, 575

Alexander D. M., Hickox R. C., 2012, New Astron. Rev., 56, 93

Alloin D., Barvainis R., Gordon M. A., Antonucci R. R. J., 1992, A&A, 265, 429

Alonso-Herrero A., et al., 2011, ApJ, 736, 82

Alonso-Herrero A., Pereira-Santaella M., Rieke G. H., Rigopoulou D., 2012, ApJ, 744, 2

Alonso-Herrero A., et al., 2018, ApJ, 859, 144

Alonso-Herrero A., et al., 2019, A&A, 628, A65

Alonso-Herrero A., et al., 2021, A&A, 652, A99

Alonso-Herrero A., et al., 2023, A&A, 675, A88

Andersson B. G., Lazarian A., Vaillancourt J. E., 2015, ARA&A, 53, 501

Antonucci R., 1993, ARA&A, 31, 473

Antonucci R. R. J., Miller J. S., 1985, ApJ, 297, 621

Armillotta L., Fraternali F., Marinacci F., 2016, MNRAS, 462, 4157

Armillotta L., Fraternali F., Werk J. K., Prochaska J. X., Marinacci F., 2017, MNRAS, 470, 114

Armus L., et al., 2023, ApJ, 942, L37

Asensio Ramos A., Elitzur M., 2018, A&A, 616, A131

Astropy Collaboration et al., 2013, A&A, 558, A33

Astropy Collaboration et al., 2018, AJ, 156, 123

Audibert A., et al., 2019, A&A, 632, A33

Audibert A., et al., 2021, A&A, 656, A60

Audibert A., et al., 2023, A&A, 671, L12

Azeez J. H., Hwang C. Y., Abidin Z. Z., Ibrahim Z. A., 2016, Scientific Reports, 6, 26896

Bañados E., et al., 2018, Nature, 553, 473

Baade W., Minkowski R., 1954, ApJ, 119, 206

Baan W. A., Henkel C., Loenen A. F., Baudry A., Wiklind T., 2008, A&A, 477, 747

Baba J., Kawata D., Schönrich R., 2022, MNRAS, 513, 2850

Bacchini C., et al., 2023, ApJ, 950, 24

Baillard A., et al., 2011, A&A, 532, A74

Baker W. M., Maiolino R., Bluck A. F. L., Lin L., Ellison S. L., Belfiore F., Pan H.-A., Thorp M., 2022, MNRAS, 510, 3622

Baldry I. K., Glazebrook K., Brinkmann J., Ivezić Ž., Lupton R. H., Nichol R. C., Szalay A. S., 2004, ApJ, 600, 681

Baldwin J. A., Phillips M. M., Terlevich R., 1981, PASP, 93, 5

Ballantyne D. R., 2008, ApJ, 685, 787

Ballesteros-Paredes J., Klessen R. S., Mac Low M. M., Vazquez-Semadeni E., 2007, in Reipurth B., Jewitt D., Keil K., eds, Protostars and Planets V. p. 63 (`arXiv:astro-ph/0603357`), doi:10.48550/arXiv.astro-ph/0603357

Ballesteros-Paredes J., et al., 2020, Space Sci. Rev., 216, 76

Barnard E. E., 1919, ApJ, 49, 1

Baron D., Netzer H., 2019, MNRAS, 486, 4290

Barthelmy S. D., et al., 2005, Space Sci. Rev., 120, 143

Barvainis R., 1987, ApJ, 320, 537

Barvainis R., Lehár J., Birkinshaw M., Falcke H., Blundell K. M., 2005, ApJ, 618, 108

Baum S. A., McCarthy P. J., 2000, AJ, 119, 2634

Baumgartner W. H., Tueller J., Markwardt C. B., Skinner G. K., Barthelmy S., Mushotzky R. F., Evans P. A., Gehrels N., 2013, ApJS, 207, 19

Begelman M. C., McKee C. F., Shields G. A., 1983, ApJ, 271, 70

Bell T. A., Roueff E., Viti S., Williams D. A., 2006, MNRAS, 371, 1865

Bellocchi E., Arribas S., Colina L., 2016, A&A, 591, A85

Bellocchi E., et al., 2020, A&A, 642, A166

Bender R., 1988, A&A, 193, L7

Bendo G. J., Clements D. L., Khan S. A., 2009, MNRAS, 399, L29

Benedettini M., et al., 2020, A&A, 633, A147

Bergin E. A., Tafalla M., 2007, ARA&A, 45, 339

Bianchi S., Balestra I., Matt G., Guainazzi M., Perola G. C., 2003, A&A, 402, 141

Bianchi S., Chiaberge M., Piconcelli E., Guainazzi M., Matt G., 2008, MNRAS, 386, 105

Bianchin M., et al., 2022, MNRAS, 510, 639

Bigiel F., Leroy A., Walter F., Brinks E., de Blok W. J. G., Madore B., Thornley M. D., 2008, AJ, 136, 2846

Binney J., Tabor G., 1995, MNRAS, 276, 663

Binney J., Tremaine S., 1987, Galactic dynamics

Bîrzan L., Rafferty D. A., Nulsen P. E. J., McNamara B. R., Röttgering H. J. A., Wise M. W., Mittal R., 2012, MNRAS, 427, 3468

Bisbas T. G., Bell T. A., Viti S., Yates J., Barlow M. J., 2012, MNRAS, 427, 2100

Bisbas T. G., van Dishoeck E. F., Hu C.-Y., Schruba A., 2023, MNRAS, 519, 729

Bischetti M., Maiolino R., Carniani S., Fiore F., Piconcelli E., Fluetsch A., 2019, A&A, 630, A59

Bisigello L., et al., 2022, A&A, 666, A193

Bland-Hawthorn J., Gerhard O., 2016, ARA&A, 54, 529

Bland-Hawthorn J., et al., 2019, ApJ, 886, 45

Blandford R., Meier D., Readhead A., 2019, ARA&A, 57, 467

Blanton M. R., Moustakas J., 2009, ARA&A, 47, 159

Blasi P., 2013, A&ARv, 21, 70

Blitz L., Rosolowsky E., 2006, ApJ, 650, 933

Blustin A. J., Page M. J., Fuerst S. V., Branduardi-Raymont G., Ashton C. E., 2005, A&A, 431, 111

Boch T., Fernique P., 2014, in Manset N., Forshay P., eds, Astronomical Society of the Pacific Conference Series Vol. 485, Astronomical Data Analysis Software and Systems XXIII. p. 277

Bogdán Á., et al., 2023, Nature Astronomy,

Bok B. J., 1948, in , Vol. 7, Harvard Observatory Monographs. p. 53

Bok B. J., Reilly E. F., 1947, ApJ, 105, 255

Bolatto A. D., Leroy A. K., Rosolowsky E., Walter F., Blitz L., 2008, ApJ, 686, 948

Bolatto A. D., Wolfire M., Leroy A. K., 2013, ARA&A, 51, 207

Bolatto A. D., et al., 2017, ApJ, 846, 159

Bonnarel F., et al., 2000, A&AS, 143, 33

Boogaard L. A., et al., 2020, ApJ, 902, 109

Boquien M., Burgarella D., Roehlly Y., Buat V., Ciesla L., Corre D., Inoue A. K., Salas H., 2019, A&A, 622, A103

Boselli A., Cortese L., Boquien M., 2014, A&A, 564, A65

Bower R. G., Benson A. J., Malbon R., Helly J. C., Frenk C. S., Baugh C. M., Cole S., Lacey C. G., 2006, MNRAS, 370, 645

Bradford C. M., et al., 2009, ApJ, 705, 112

Bradley L., et al., 2020, astropy/photutils: 1.0.0, doi:10.5281/zenodo.4044744, https://doi.org/10.5281/zenodo.4044744

Brandt W. N., Alexander D. M., 2015, A&ARv, 23, 1

Brightman M., Nandra K., 2011, MNRAS, 413, 1206

Brinchmann J., Charlot S., White S. D. M., Tremonti C., Kauffmann G., Heckman T., Brinkmann J., 2004, MNRAS, 351, 1151

Broderick J. W., Fender R. P., 2011, MNRAS, 417, 184

Bron E., Le Bourlot J., Le Petit F., 2014, A&A, 569, A100

Brownson S., Belfiore F., Maiolino R., Lin L., Carniani S., 2020, MNRAS, 498, L66

Brunt C. M., Federrath C., Price D. J., 2010, MNRAS, 403, 1507

Buchner J., Bauer F. E., 2017, MNRAS, 465, 4348

Bureau M., Athanassoula E., 1999, ApJ, 522, 686

Burgers J. M., 1939, Verhandelingen der Koninklijke Nederlandse Akademie van Wetenschappen, Afdeeling Natuurkunde, 17, 1

Burkhart B., Lee M.-Y., Murray C. E., Stanimirović S., 2015, ApJ, 811, L28

Burtscher L., et al., 2013, A&A, 558, A149

Burtscher L., et al., 2016, A&A, 586, A28

Buta R., Combes F., 1996, Fundamentals Cosmic Phys., 17, 95

Butterworth J., Holdship J., Viti S., García-Burillo S., 2022, A&A, 667, A131

Cañameras R., et al., 2021, A&A, 645, A45

139

Calura F., Gilli R., Vignali C., Pozzi F., Pipino A., Matteucci F., 2014, MNRAS, 438, 2765

Calura F., et al., 2022, MNRAS, 516, 5914

Calzetti D., et al., 2010, ApJ, 714, 1256

Cappellari M., 2013, ApJ, 778, L2

Cappellari M., 2016, ARA&A, 54, 597

Cappellari M., et al., 2011, MNRAS, 416, 1680

Cappi M., 2006, Astronomische Nachrichten, 327, 1012

Capriotti E. R., 1965, ApJ, 142, 1101

Cardelli J. A., Clayton G. C., Mathis J. S., 1989, ApJ, 345, 245

Carilli C. L., Walter F., 2013, ARA&A, 51, 105

Carniani S., et al., 2019, MNRAS, 489, 3939

Carrasco E., et al., 2018, in Evans C. J., Simard L., Takami H., eds, Society of Photo-Optical Instrumentation Engineers (SPIE) Conference Series Vol. 10702, Ground-based and Airborne Instrumentation for Astronomy VII. p. 1070216, doi:10.1117/12.2313040

Casasola V., Bettoni D., Galletta G., 2004, A&A, 422, 941

Casasola V., Hunt L. K., Combes F., García-Burillo S., Neri R., 2011, A&A, 527, A92

Casasola V., Hunt L., Combes F., García-Burillo S., 2015, A&A, 577, A135

Casasola V., et al., 2017, A&A, 605, A18

Casasola V., et al., 2020, A&A, 633, A100

Casasola V., et al., 2022, A&A, 668, A130

Cattaneo A., et al., 2009, Nature, 460, 213

Cavagnolo K. W., McNamara B. R., Nulsen P. E. J., Carilli C. L., Jones C., Bîrzan L., 2010, ApJ, 720, 1066

Cazaux S., Tielens A. G. G. M., 2004, ApJ, 604, 222

Cazaux S., Tielens A. G. G. M., 2010, ApJ, 715, 698

Cazzoli S., Arribas S., Maiolino R., Colina L., 2016, A&A, 590, A125

Chabrier G., 2003, PASP, 115, 763

Chandrasekhar S., 1931, ApJ, 74, 81

Chatzikos M., et al., 2023, Rev. Mex. Astron. Astrofis., 59, 327

Chevance M., et al., 2020a, Space Sci. Rev., 216, 50

Chevance M., et al., 2020b, MNRAS, 493, 2872

Chevance M., Krumholz M. R., McLeod A. F., Ostriker E. C., Rosolowsky E. W., Sternberg A., 2023a, in Inutsuka S., Aikawa Y., Muto T., Tomida K., Tamura M., eds, Astronomical Society of the Pacific Conference Series Vol. 534, Protostars and Planets VII. p. 1 (arXiv:2203.09570), doi:10.48550/arXiv.2203.09570

Chevance M., Krumholz M. R., McLeod A. F., Ostriker E. C., Rosolowsky E. W., Sternberg A., 2023b, in Inutsuka S., Aikawa Y., Muto T., Tomida K., Tamura M., eds, Astronomical Society of the Pacific Conference Series Vol. 534, Protostars and Planets VII. p. 1 (arXiv:2203.09570), doi:10.48550/arXiv.2203.09570

Chomiuk L., Povich M. S., 2011, AJ, 142, 197

Cicone C., et al., 2014, A&A, 562, A21

Cicone C., et al., 2018, ApJ, 863, 143

Cicone C., Maiolino R., Aalto S., Muller S., Feruglio C., 2020, A&A, 633, A163

Cimatti A., Fraternali F., Nipoti C., 2020, Introduction to galaxy formation and evolution: from primordial gas to present-day galaxies

Ciotti L., Ostriker J. P., 1997, ApJ, 487, L105

Ciotti L., Ostriker J. P., 2007, ApJ, 665, 1038

Colless M., et al., 2001, MNRAS, 328, 1039

Colombo D., et al., 2014, ApJ, 784, 3

Comastri A., 2004, in Barger A. J., ed., Astrophysics and Space Science Library Vol. 308, Supermassive Black Holes in the Distant Universe. p. 245 (arXiv:astro-ph/0403693), doi:10.1007/978-1-4020-2471-9˙8

Comastri A., Gilli R., Marconi A., Risaliti G., Salvati M., 2015, A&A, 574, L10

Combes F., 2021, in Storchi Bergmann T., Forman W., Overzier R., Riffel R., eds, Vol. 359, Galaxy Evolution and Feedback across Different Environments. pp 312–317 (arXiv:2003.13280), doi:10.1017/S1743921320001544

Combes F., Prugniel P., Rampazzo R., Sulentic J. W., 1994, A&A, 281, 725

Combes F., et al., 2013, A&A, 558, A124

Combes F., et al., 2019, A&A, 623, A79

Compton A. H., 1923, Physical Review, 21, 483

Condon J. J., Ransom S. M., 2016, Essential Radio Astronomy

Cooper J. L., Bicknell G. V., Sutherland R. S., Bland-Hawthorn J., 2009, ApJ, 703, 330

Costa T., Sijacki D., Haehnelt M. G., 2014, MNRAS, 444, 2355

Costa T., Rosdahl J., Sijacki D., Haehnelt M. G., 2018, MNRAS, 473, 4197

Costa T., Pakmor R., Springel V., 2020, MNRAS, 497, 5229

Costagliola F., et al., 2011, A&A, 528, A30

Crenshaw D. M., Kraemer S. B., 2000, ApJ, 532, L101

Crenshaw D. M., Kraemer S. B., George I. M., 2003, ARA&A, 41, 117

Cresci G., et al., 2015, A&A, 582, A63

Croft S., et al., 2006, ApJ, 647, 1040

Croton D. J., et al., 2006, MNRAS, 365, 11

Crutcher R. M., 2012, ARA&A, 50, 29

Curran S. J., Polatidis A. G., Aalto S., Booth R. S., 2001, A&A, 368, 824

D'Amato Q., et al., 2020, A&A, 636, A37

Da Rio N., Robberto M., Soderblom D. R., Panagia N., Hillenbrand L. A., Palla F., Stassun K., 2009, ApJS, 183, 261

Dabhade P., et al., 2020, A&A, 635, A5

Dabrowski I., 1984, Canadian Journal of Physics, 62, 1639

Dalgarno A., Yan M., Liu W., 1999, ApJS, 125, 237

Dall'Agnol de Oliveira B., et al., 2021, MNRAS, 504, 3890

Dallacasa D., Orienti M., Fanti C., Fanti R., Stanghellini C., 2013, MNRAS, 433, 147

Dannerbauer H., Daddi E., Riechers D. A., Walter F., Carilli C. L., Dickinson M., Elbaz D., Morrison G. E., 2009, ApJ, 698, L178

Dasyra K. M., Combes F., Oosterloo T., Oonk J. B. R., Morganti R., Salomé P., Vlahakis N., 2016, A&A, 595, L7

Davies R. I., Tacconi L. J., Genzel R., 2004, ApJ, 602, 148

Davies R. I., Müller Sánchez F., Genzel R., Tacconi L. J., Hicks E. K. S., Friedrich S., Sternberg A., 2007, ApJ, 671, 1388

Davies R. I., et al., 2014, ApJ, 792, 101

Davies J. I., et al., 2017, PASP, 129, 044102

Davies R., et al., 2020, MNRAS, 498, 4150

Davis T. A., et al., 2013, MNRAS, 429, 534

Davis T. A., et al., 2014, MNRAS, 444, 3427

Decarli R., et al., 2020, ApJ, 902, 110

Delvecchio I., et al., 2014, MNRAS, 439, 2736

Di Teodoro E. M., Fraternali F., 2015, MNRAS, 451, 3021

Di Teodoro E. M., Peek J. E. G., 2021, ApJ, 923, 220

Diamond-Stanic A. M., Rieke G. H., 2012, ApJ, 746, 168

Díaz-Santos T., et al., 2017, ApJ, 846, 32

Dickman R. L., Snell R. L., Schloerb F. P., 1986, ApJ, 309, 326

Djorgovski S., Davis M., 1987, ApJ, 313, 59

Domínguez-Fernández A. J., et al., 2020, A&A, 643, A127

Downes D., Solomon P. M., 1998, ApJ, 507, 615

Draine B. T., 1978, ApJS, 36, 595

Dressler A., Richstone D. O., 1988, ApJ, 324, 701

Dressler A., Lynden-Bell D., Burstein D., Davies R. L., Faber S. M., Terlevich R., Wegner G., 1987, ApJ, 313, 42

Driver S. P., et al., 2011, MNRAS, 413, 971

Dultzin-Hacyan D., Schuster W. J., Parrao L., Pena J. H., Peniche R., Benitez E., Costero R., 1992, AJ, 103, 1769

Dumas G., Schinnerer E., Mundell C. G., 2010, ApJ, 721, 911

Dunham T. J., 1937, PASP, 49, 26

Dunne L., Eales S., Edmunds M., Ivison R., Alexander P., Clements D. L., 2000, MNRAS, 315, 115

Dunne L., Maddox S. J., Papadopoulos P. P., Ivison R. J., Gomez H. L., 2022, MNRAS, 517, 962

Dutkowska K. M., Kristensen L. E., 2022, A&A, 667, A135

Dyson J. E., Williams D. A., 1997, The physics of the interstellar medium, doi:10.1201/9780585368115.

Eibensteiner C., et al., 2022, A&A, 659, A173

Einstein A., 1916, Deutsche Physikalische Gesellschaft, 18, 318

El-Badry K., Wetzel A., Geha M., Hopkins P. F., Kereš D., Chan T. K., Faucher-Giguère C.-A., 2016, ApJ, 820, 131

Elia D., et al., 2018, MNRAS, 481, 509

Elia D., et al., 2021, MNRAS, 504, 2742

Elitzur M., Asensio Ramos A., 2006, MNRAS, 365, 779

Ellison S. L., Viswanathan A., Patton D. R., Bottrell C., McConnachie A. W., Gwyn S., Cuillandre J.-C., 2019, MNRAS, 487, 2491

Ellison S. L., Lin L., Thorp M. D., Pan H.-A., Scudder J. M., Sánchez S. F., Bluck A. F. L., Maiolino R., 2021a, MNRAS, 501, 4777

Ellison S. L., et al., 2021b, MNRAS, 505, L46

Elmegreen B. G., Falgarone E., 1996, ApJ, 471, 816

Enia A., et al., 2020, MNRAS, 493, 4107

Esin A. A., McClintock J. E., Narayan R., 1997, ApJ, 489, 865

Espada D., et al., 2017, ApJ, 843, 136

Espada D., et al., 2019, ApJ, 887, 88

Esparza-Arredondo D., Gonzalez-Martín O., Dultzin D., Masegosa J., Ramos-Almeida C., García-Bernete I., Fritz J., Osorio-Clavijo N., 2021, A&A, 651, A91

Esposito F., Vallini L., Pozzi F., Casasola V., Mingozzi M., Vignali C., Gruppioni C., Salvestrini F., 2022, MNRAS, 512, 686

Esquej P., et al., 2014, ApJ, 780, 86

Evans Neal J. I., 1999, ARA&A, 37, 311

Evans A., 2005, An ACS Survey of a Complete Sample of Luminous Infrared Galaxies in the Local Universe, HST Proposal

Evans A. S., Mazzarella J. M., Surace J. A., Frayer D. T., Iwasawa K., Sanders D. B., 2005, ApJS, 159, 197

Event Horizon Telescope Collaboration et al., 2019, ApJ, 875, L1

Event Horizon Telescope Collaboration et al., 2022, ApJ, 930, L12

Ewen H. I., Purcell E. M., 1951, Nature, 168, 356

Fabbiano G., 2006, ARA&A, 44, 323

Faber S. M., Jackson R. E., 1976, ApJ, 204, 668

Fabian A. C., 1994, ARA&A, 32, 277

Fabian A. C., 1999, MNRAS, 308, L39

Fabian A. C., 2012, ARA&A, 50, 455

Fabian A. C., et al., 2011, MNRAS, 418, 2154

Farrah D., et al., 2013, ApJ, 776, 38

Fath E. A., 1909, Lick Observatory Bulletin, 149, 71

Faucher-Giguère C.-A., Oh S. P., 2023, ARA&A, 61, 131

Faucher-Giguère C.-A., Quataert E., 2012, MNRAS, 425, 605

Federrath C., Klessen R. S., 2012, ApJ, 761, 156

Federrath C., Klessen R. S., Schmidt W., 2008, ApJ, 688, L79

Federrath C., Sur S., Schleicher D. R. G., Banerjee R., Klessen R. S., 2011, ApJ, 731, 62

Fei Q., Wang R., Molina J., Shangguan J., Ho L. C., Bauer F. E., Treister E., 2023, ApJ, 946, 45

Feltre A., Hatziminaoglou E., Fritz J., Franceschini A., 2012, MNRAS, 426, 120

Feretti L., Giovannini G., Govoni F., Murgia M., 2012, A&ARv, 20, 54

Ferland G. J., Korista K. T., Verner D. A., Ferguson J. W., Kingdon J. B., Verner E. M., 1998, PASP, 110, 761

Ferland G. J., et al., 2017, Rev. Mex. Astron. Astrofis., 53, 385

Ferrarese L., Merritt D., 2000, ApJ, 539, L9

Feruglio C., Maiolino R., Piconcelli E., Menci N., Aussel H., Lamastra A., Fiore F., 2010, A&A, 518, L155

Fiore F., et al., 2017, A&A, 601, A143

Fischer T. C., Crenshaw D. M., Kraemer S. B., Schmitt H. R., 2013, ApJS, 209, 1

Fischer T. C., et al., 2018, ApJ, 856, 102

Fischer T. C., Johnson M. C., Secrest N. J., Crenshaw D. M., Kraemer S. B., 2023, ApJ, 953, 87

Fixsen D. J., Bennett C. L., Mather J. C., 1999, ApJ, 526, 207

Fluetsch A., et al., 2019, MNRAS, 483, 4586

Fluetsch A., et al., 2021, MNRAS, 505, 5753

Foreman-Mackey D., 2016, The Journal of Open Source Software, 1, 24

Foreman-Mackey D., Hogg D. W., Lang D., Goodman J., 2013, PASP, 125, 306

Fornasini F. M., Elvis M., Maksym W. P., Fabbiano G., Bergmann T. S., Gandhi P., Whittle M., 2022, ApJ,

931, 65

Förster Schreiber N. M., et al., 2019, ApJ, 875, 21

Freitas I. C., et al., 2018, MNRAS, 476, 2760

French K. D., Earl N., Novack A. B., Pardasani B., Pillai V. R., Tripathi A., Verrico M. E., 2023, ApJ, 950, 153

Friedman H., Byram E. T., 1967, Science, 158, 257

Fukui Y., Kawamura A., 2010, ARA&A, 48, 547

Fukumura K., Tombesi F., Kazanas D., Shrader C., Behar E., Contopoulos I., 2015, ApJ, 805, 17

Gabor J. M., Bournaud F., 2014, MNRAS, 441, 1615

Gaches B. A. L., Offner S. S. R., Bisbas T. G., 2019, ApJ, 878, 105

Gaibler V., Khochfar S., Krause M., Silk J., 2012, MNRAS, 425, 438

Gallerani S., Ferrara A., Neri R., Maiolino R., 2014, MNRAS, 445, 2848

Galliano E., Alloin D., Granato G. L., Villar-Martín M., 2003, A&A, 412, 615

Galliano F., Galametz M., Jones A. P., 2018, ARA&A, 56, 673

Gallimore J. F., Baum S. A., O'Dea C. P., Pedlar A., Brinks E., 1999, ApJ, 524, 684

Gallimore J. F., Axon D. J., O'Dea C. P., Baum S. A., Pedlar A., 2006, AJ, 132, 546

Gallimore J. F., et al., 2016, ApJ, 829, L7

Ganguly S., Walch S., Clarke S. D., Seifried D., 2022, arXiv e-prints, p. arXiv:2204.02511

Gao Y., Solomon P. M., 1999, ApJ, 512, L99

Gao Y., Solomon P. M., 2004, ApJ, 606, 271

García-Bernete I., et al., 2021, A&A, 645, A21

García-Bernete I., et al., 2023, arXiv e-prints, p. arXiv:2310.09093

García-Burillo S., Combes F., 2012, in Journal of Physics Conference Series. p. 012050 (`arXiv:1205.0758`), doi:10.1088/1742-6596/372/1/012050

García-Burillo S., et al., 2003a, A&A, 407, 485

García-Burillo S., et al., 2003b, A&A, 407, 485

García-Burillo S., Combes F., Schinnerer E., Boone F., Hunt L. K., 2005, A&A, 441, 1011

García-Burillo S., et al., 2014a, A&A, 567, A125

García-Burillo S., et al., 2014b, A&A, 567, A125

García-Burillo S., et al., 2016, ApJ, 823, L12

García-Burillo S., et al., 2019, A&A, 632, A61

García-Burillo S., et al., 2021, A&A, 652, A98

Gebhardt K., et al., 2000, ApJ, 539, L13

Gehrels N., et al., 2004, ApJ, 611, 1005

Genzel R., Hollenbach D., Townes C. H., 1994, Reports on Progress in Physics, 57, 417

Genzel R., et al., 2014, ApJ, 796, 7

Gerssen J., van der Marel R. P., Axon D., Mihos J. C., Hernquist L., Barnes J. E., 2004, AJ, 127, 75

Giacconi R., Gursky H., Paolini F. R., Rossi B. B., 1962, Phys. Rev. Lett., 9, 439

Gil de Paz A., et al., 2016, in Evans C. J., Simard L., Takami H., eds, Society of Photo-Optical Instrumentation Engineers (SPIE) Conference Series Vol. 9908, Ground-based and Airborne Instrumentation for Astronomy VI. p. 99081K, doi:10.1117/12.2231988

Gilli R., et al., 2022, A&A, 666, A17

Ginsburg A., Robitaille T., Beaumont C., 2016, pvextractor: Position-Velocity Diagram Extractor, Astrophysics Source Code Library, record ascl:1608.010 (ascl:1608.010)

Ginsburg A., et al., 2019, radio-astro-tools/spectral-cube: v0.4.4, Zenodo, doi:10.5281/zenodo.2573901

Giustini M., et al., 2023, A&A, 679, A73

Gofford J., Reeves J. N., Tombesi F., Braito V., Turner T. J., Miller L., Cappi M., 2013, MNRAS, 430, 60

Gofford J., Reeves J. N., McLaughlin D. E., Braito V., Turner T. J., Tombesi F., Cappi M., 2015, MNRAS, 451, 4169

Goldbaum N. J., Krumholz M. R., Matzner C. D., McKee C. F., 2011, ApJ, 738, 101

Golombek D., Miley G. K., Neugebauer G., 1988, AJ, 95, 26

Goodman J., Weare J., 2010, Communications in Applied Mathematics and Computational Science, 5, 65

Greene J. E., Ho L. C., 2005, ApJ, 627, 721

Greenstein J. L., 1963, Nature, 197, 1041

Grenier I. A., Casandjian J.-M., Terrier R., 2005, Science, 307, 1292

Greve T. R., et al., 2014, ApJ, 794, 142

Grevesse N., Asplund M., Sauval A. J., Scott P., 2010, Ap&SS, 328, 179

Griffin M. J., et al., 2010, A&A, 518, L3

Gritschneder M., Naab T., Walch S., Burkert A., Heitsch F., 2009, ApJ, 694, L26

Gruppioni C., et al., 2016, MNRAS, 458, 4297

Guillard P., et al., 2012, ApJ, 747, 95

Gursky H., Kellogg E. M., Leong C., Tananbaum H., Giacconi R., 1971, ApJ, 165, L43

Habing H. J., 1968, Bull. Astron. Inst. Netherlands, 19, 421

Hailey-Dunsheath S., et al., 2012, ApJ, 755, 57

Han J. L., 2017, ARA&A, 55, 111

Hardouin Duparc O., 2009, International Journal of Materials Research, 100, 1162

Harris C. R., et al., 2020, Nature, 585, 357

Harrison F. A., et al., 2013, ApJ, 770, 103

Harrison C. M., Alexander D. M., Mullaney J. R., Swinbank A. M., 2014, MNRAS, 441, 3306

Harrison C. M., Costa T., Tadhunter C. N., Flütsch A., Kakkad D., Perna M., Vietri G., 2018, Nature Astronomy, 2, 198

Hatziminaoglou E., et al., 2008, MNRAS, 386, 1252

Hazard C., Mackey M. B., Shimmins A. J., 1963, Nature, 197, 1037

Heckman T. M., Best P. N., 2014, ARA&A, 52, 589

Heckman T. M., Miley G. K., van Breugel W. J. M., Butcher H. R., 1981, ApJ, 247, 403

Hennebelle P., Falgarone E., 2012, A&ARv, 20, 55

Hermosa Muñoz L., et al., 2023, arXiv e-prints, p. arXiv:2311.12552

Hernández-Vera C., et al., 2023, A&A, 677, A152

Herrera-Camus R., et al., 2019, ApJ, 871, 37

Herrero-Illana R., et al., 2019, A&A, 628, A71

Herschel W., 1785, Philosophical Transactions of the Royal Society of London Series I, 75, 213

Hewett P. C., Foltz C. B., 2003, AJ, 125, 1784

Heyer M. H., Brunt C. M., 2004, ApJ, 615, L45

Heyer M., Dame T. M., 2015, ARA&A, 53, 583

Heyer M., Krawczyk C., Duval J., Jackson J. M., 2009, ApJ, 699, 1092

Hickox R. C., Alexander D. M., 2018, ARA&A, 56, 625

Hollenbach D., Gorti U., 2009, ApJ, 703, 1203

Hollenbach D., McKee C. F., 1989, ApJ, 342, 306

Hollenbach D., Salpeter E. E., 1970, J. Chem. Phys., 53, 79

Hollenbach D., Salpeter E. E., 1971, ApJ, 163, 155

Hollenbach D. J., Tielens A. G. G. M., 1997, ARA&A, 35, 179

Hönig S. F., 2019, ApJ, 884, 171

Hönig S. F., et al., 2013, ApJ, 771, 87

Hopkins A. M., 2018, Publ. Astron. Soc. Australia, 35, e039

Hopkins P. F., Hernquist L., 2006, ApJS, 166, 1

Hopkins P. F., Hernquist L., Cox T. J., Kereš D., 2008, ApJS, 175, 356

Hopkins P. F., et al., 2018, MNRAS, 480, 800

Hoskin M. A., 1976, Journal for the History of Astronomy, 7, 169

Hoyle F., Fowler W. A., 1963, MNRAS, 125, 169

Huang K. Y., et al., 2022, A&A, 666, A102

Hubble E. P., 1926, ApJ, 64, 321

Hughes A., Meidt S., Colombo D., Schruba A., Schinnerer E., Leroy A., Wong T., 2016, in Jablonka P.,
    André P., van der Tak F., eds,   Vol. 315, From Interstellar Clouds to Star-Forming Galaxies: Universal
    Processes?. pp 30–37, doi:10.1017/S1743921316007213

Hung C.-L., et al., 2014, ApJ, 791, 63

Hunter J. D., 2007, Computing in Science & Engineering, 9, 90

Iben Icko J., 1967, ARA&A, 5, 571

Iben I. J., 1974, ARA&A, 12, 215

Iben I. J., Renzini A., 1983, ARA&A, 21, 271

Ichimaru S., 1977, ApJ, 214, 840

Imanishi M., Nakanishi K., Tamura Y., Oi N., Kohno K., 2007, AJ, 134, 2366

Imanishi M., Nakanishi K., Izumi T., 2016, ApJ, 822, L10

Imanishi M., Nakanishi K., Izumi T., 2017, ApJ, 849, 29

Indriolo N., Geballe T. R., Oka T., McCall B. J., 2007, ApJ, 671, 1736

Ishibashi W., Fabian A. C., 2017, MNRAS, 472, 2768

Ishibashi W., Banerji M., Fabian A. C., 2017, MNRAS, 469, 1496

Ishwara-Chandra C. H., Saikia D. J., 1999, MNRAS, 309, 100

Israel F. P., 1992, A&A, 265, 487

Israel F. P., 2020, A&A, 635, A131

Izumi T., Wada K., Fukushige R., Hamamura S., Kohno K., 2018, ApJ, 867, 48

Jansky K. G., 1933, Nature, 132, 66

Jeans J. H., 1902, Philosophical Transactions of the Royal Society of London Series A, 199, 1

Joblin C., et al., 2018, A&A, 615, A129

Jura M., 1975, ApJ, 197, 575

Kaaret P., Feng H., Roberts T. P., 2017, ARA&A, 55, 303

Kainulainen J., Beuther H., Henning T., Plume R., 2009, A&A, 508, L35

Kamenetzky J., Rangwala N., Glenn J., Maloney P. R., Conley A., 2014, ApJ, 795, 174

Kamenetzky J., Rangwala N., Glenn J., Maloney P. R., Conley A., 2016, ApJ, 829, 93

Kamenetzky J., Rangwala N., Glenn J., 2017, MNRAS, 471, 2917

Karachentsev I. D., Kudrya Y. N., Karachentseva V. E., Mitronova S. N., 2006, Astrophysics, 49, 450

Kauffmann G., et al., 2003, MNRAS, 341, 54

Kawakatu N., Wada K., 2008, ApJ, 681, 73

Kawamuro T., Izumi T., Onishi K., Imanishi M., Nguyen D. D., Baba S., 2020, ApJ, 895, 135

Kazanas D., Fukumura K., Behar E., Contopoulos I., Shrader C., 2012, The Astronomical Review, 7, 92

Kazandjian M. V., Meijerink R., Pelupessy I., Israel F. P., Spaans M., 2012, A&A, 542, A65

Kelly B. C., 2007, ApJ, 665, 1489

Kennicutt Robert C. J., 1989, ApJ, 344, 685

Kennicutt Robert C. J., 1998a, ARA&A, 36, 189

Kennicutt Robert C. J., 1998b, ApJ, 498, 541

Kennicutt Robert C. J., 1998c, ApJ, 498, 541

Kennicutt Robert C. J., De Los Reyes M. A. C., 2021a, ApJ, 908, 61

Kennicutt Robert C. J., De Los Reyes M. A. C., 2021b, ApJ, 908, 61

Kennicutt R. C., Evans N. J., 2012, ARA&A, 50, 531

Kewley L. J., Dopita M. A., Sutherland R. S., Heisler C. A., Trevena J., 2001, ApJ, 556, 121

Khachikian E. Y., Weedman D. W., 1974, ApJ, 192, 581

King A., 2003, ApJ, 596, L27

King A., Nixon C., 2015, MNRAS, 453, L46

King A., Pounds K., 2015, ARA&A, 53, 115

King A. R., Pringle J. E., West R. G., Livio M., 2004, MNRAS, 348, 111

Kinney A. L., Schmitt H. R., Clarke C. J., Pringle J. E., Ulvestad J. S., Antonucci R. R. J., 2000, ApJ, 537, 152

Klessen R. S., Hennebelle P., 2010, A&A, 520, A17

Kojoian G., Elliott R., Tovmassian H. M., 1981, AJ, 86, 811

Kolmogorov A., 1941, Akademiia Nauk SSSR Doklady, 30, 301

Komossa S., Burwitz V., Hasinger G., Predehl P., Kaastra J. S., Ikebe Y., 2003, ApJ, 582, L15

Kormendy J., 1977, ApJ, 218, 333

Kormendy J., Bender R., 1996, ApJ, 464, L119

Kormendy J., Djorgovski S., 1989, ARA&A, 27, 235

Kormendy J., Ho L. C., 2013, ARA&A, 51, 511

Kormendy J., Richstone D., 1995, ARA&A, 33, 581

Koss M. J., et al., 2016, ApJ, 824, L4

Koss M., et al., 2017, ApJ, 850, 74

Krajnović D., Cappellari M., de Zeeuw P. T., Copin Y., 2006, MNRAS, 366, 787

Krieger N., et al., 2020, ApJ, 897, 176

Krimm H. A., et al., 2013, ApJS, 209, 14

Krolik J. H., Begelman M. C., 1988, ApJ, 329, 702

Krolik J. H., Kallman T. R., 1983, ApJ, 267, 610

Krolik J. H., Lepp S., 1989, ApJ, 347, 179

Kroupa P., 2001, MNRAS, 322, 231

Kroupa P., Jeřábková T., Dinnbier F., Beccari G., Yan Z., 2018, A&A, 612, A74

Kruijssen J. M. D., et al., 2019, Nature, 569, 519

Krumholz M. R., McKee C. F., 2005, ApJ, 630, 250

Krumholz M. R., McKee C. F., Bland-Hawthorn J., 2019, ARA&A, 57, 227

Kuźmicz A., Jamrozy M., Bronarska K., Janda-Boczar K., Saikia D. J., 2018, ApJS, 238, 9

La Caria M. M., Vignali C., Lanzuisi G., Gruppioni C., Pozzi F., 2019, MNRAS, 487, 1662

Lada C. J., Lada E. A., 2003, ARA&A, 41, 57

Laha S., Guainazzi M., Dewangan G. C., Chakravorty S., Kembhavi A. K., 2014, MNRAS, 441, 2613

Lamperti I., et al., 2020, ApJ, 889, 103

Lamperti I., et al., 2022, A&A, 668, A45

Larson R. B., 1981, MNRAS, 194, 809

Larson R. B., Tinsley B. M., 1978, ApJ, 219, 46

Larson K. L., et al., 2016, ApJ, 825, 128

Latif M. A., Ferrara A., 2016, Publ. Astron. Soc. Australia, 33, e051

Lauer T. R., 1985, MNRAS, 216, 429

Lazareff B., Castets A., Kim D. W., Jura M., 1989, ApJ, 336, L13

Le Petit F., Nehmé C., Le Bourlot J., Roueff E., 2006, ApJS, 164, 506

Leaman R., et al., 2019, MNRAS, 488, 3904

Ledoux C., Petitjean P., Srianand R., 2003, MNRAS, 346, 209

Leitherer C., et al., 1999, ApJS, 123, 3

Lepp S., McCray R., 1983, ApJ, 269, 560

Leroy A. K., Walter F., Brinks E., Bigiel F., de Blok W. J. G., Madore B., Thornley M. D., 2008, AJ, 136, 2782

Leroy A. K., et al., 2013, AJ, 146, 19

Leroy A. K., et al., 2015, ApJ, 801, 25

Leroy A. K., et al., 2021, ApJS, 257, 43

Leslie S. K., Rich J. A., Kewley L. J., Dopita M. A., 2014, MNRAS, 444, 1842

Leung G. C. K., et al., 2017, ApJ, 849, 48

Levenson N. A., Heckman T. M., Krolik J. H., Weaver K. A., Życki P. T., 2006, ApJ, 648, 111

Levy R. C., et al., 2018, ApJ, 860, 92

Liang E. P. T., Price R. H., 1977, ApJ, 218, 247

Liang E. P. T., Thompson K. A., 1979, MNRAS, 189, 421

Licquia T. C., Newman J. A., 2015, ApJ, 806, 96

Lilly S. J., Le Fevre O., Hammer F., Crampton D., 1996, ApJ, 460, L1

Lin C. C., Shu F. H., 1964, ApJ, 140, 646

Lin L., et al., 2019, ApJ, 884, L33

Lindblad B., 1948, MNRAS, 108, 214

Lindblad P. O., 1960, Stockholms Observatoriums Annaler, 4, 4

Lique F., 2015, MNRAS, 453, 810

Lisenfeld U., et al., 2011, A&A, 534, A102

Lister M. L., Homan D. C., Kellermann K. I., Kovalev Y. Y., Pushkarev A. B., Ros E., Savolainen T., 2021, ApJ, 923, 30

Liu B. F., Mineshige S., Ohsuga K., 2003, ApJ, 587, 571

Liu G., Zakamska N. L., Greene J. E., Nesvadba N. P. H., Liu X., 2013, MNRAS, 436, 2576

Loenen A. F., Spaans M., Baan W. A., Meijerink R., 2008, A&A, 488, L5

Lombardi M., Lada C. J., Alves J., 2010a, A&A, 512, A67

Lombardi M., Alves J., Lada C. J., 2010b, A&A, 519, L7

Longinotti A. L., et al., 2018, ApJ, 867, L11

Longinotti A. L., et al., 2023, MNRAS, 521, 2134

Lonsdale C. J., Farrah D., Smith H. E., 2006, Ultraluminous Infrared Galaxies. p. 285, doi:10.1007/3-540-30313-8_9

López-Gonzaga N., Jaffe W., Burtscher L., Tristram K. R. W., Meisenheimer K., 2014, A&A, 565, A71

Lu N., et al., 2017, ApJS, 230, 1

Lupi A., Colpi M., Devecchi B., Galanti G., Volonteri M., 2014, MNRAS, 442, 3616

Lutz D., et al., 2020, A&A, 633, A134

Lynden-Bell D., 1969, Nature, 223, 690

Mac Low M.-M., Klessen R. S., 2004, Reviews of Modern Physics, 76, 125

MacAlpine G. M., 1985, in Miller J. S., ed., Astrophysics of Active Galaxies and Quasi-Stellar Objects. pp 259–288

Madau P., Dickinson M., 2014, ARA&A, 52, 415

Madau P., Ferguson H. C., Dickinson M. E., Giavalisco M., Steidel C. C., Fruchter A., 1996, MNRAS, 283, 1388

Magorrian J., et al., 1998, AJ, 115, 2285

Maiolino R., 2018, in AGN13: Beauty and the Beast. p. 72, doi:10.5281/zenodo.1482552

Maiolino R., Mannucci F., 2019, A&ARv, 27, 3

Maiolino R., Stanga R., Salvati M., Rodriguez Espinosa J. M., 1994, A&A, 290, 40

Maiolino R., Ruiz M., Rieke G. H., Papadopoulos P., 1997, ApJ, 485, 552

Maiolino R., et al., 2017, Nature, 544, 202

Makarov D., Prugniel P., Terekhova N., Courtois H., Vauglin I., 2014, A&A, 570, A13

Malkan M. A., Gorjian V., Tam R., 1998, ApJS, 117, 25

Maloney P. R., Hollenbach D. J., Tielens A. G. G. M., 1996, ApJ, 466, 561

Manchanda R. K., 2006, Advances in Space Research, 38, 1387

Mao R.-Q., Schulz A., Henkel C., Mauersberger R., Muders D., Dinh-V-Trung 2010, ApJ, 724, 1336

Marasco A., et al., 2020, A&A, 644, A15

Marchesi S., et al., 2019, ApJ, 872, 8

Marconi A., Hunt L. K., 2003, ApJ, 589, L21

Marconi A., Schreier E. J., Koekemoer A., Capetti A., Axon D., Macchetto D., Caon N., 2000, ApJ, 528, 276

Marcotulli L., et al., 2022, ApJ, 940, 77

Marinacci F., Binney J., Fraternali F., Nipoti C., Ciotti L., Londrillo P., 2010, MNRAS, 404, 1464

Mashian N., Sternberg A., Loeb A., 2015, J. Cosmology Astropart. Phys., 2015, 028

Matt G., Fabian A. C., Guainazzi M., Iwasawa K., Bassani L., Malaguti G., 2000, MNRAS, 318, 173

Matthews T. A., Sandage A. R., 1963, ApJ, 138, 30

Matzner C. D., 2002, ApJ, 566, 302

May D., Steiner J. E., Menezes R. B., Williams D. R. A., Wang J., 2020, MNRAS, 496, 1488

McCarthy P. J., Baum S. A., Spinrad H., 1996, ApJS, 106, 281

McCarthy I. G., et al., 2010, MNRAS, 406, 822

McCaughrean M. J., Pearson S. G., 2023, arXiv e-prints, p. arXiv:2310.03552

McConnell N. J., Ma C.-P., 2013, ApJ, 764, 184

McCourt M., O'Leary R. M., Madigan A.-M., Quataert E., 2015, MNRAS, 449, 2

McGaugh S. S., Schombert J. M., Bothun G. D., de Blok W. J. G., 2000, ApJ, 533, L99

McGuire B. A., 2022, ApJS, 259, 30

McHardy I., Czerny B., 1987, Nature, 325, 696

McKee C. F., Ostriker E. C., 2007, ARA&A, 45, 565

McKellar A., 1940, PASP, 52, 187

McMullin J. P., Waters B., Schiebel D., Young W., Golap K., 2007, in Shaw R. A., Hill F., Bell D. J., eds, Astronomical Society of the Pacific Conference Series Vol. 376, Astronomical Data Analysis Software and Systems XVI. p. 127

McNamara B. R., Nulsen P. E. J., 2007, ARA&A, 45, 117

McNamara B. R., Nulsen P. E. J., 2012, New Journal of Physics, 14, 055023

Meijerink R., Spaans M., 2005, A&A, 436, 397

Meijerink R., Spaans M., Israel F. P., 2007, A&A, 461, 793

Meijerink R., et al., 2013, ApJ, 762, L16

Mercedes-Feliz J., et al., 2023, MNRAS, 524, 3446

Merello M., et al., 2019, MNRAS, 483, 5355

Merkulova O. A., Karataeva G. M., Yakovleva V. A., Burenkov A. N., 2012, Astronomy Letters, 38, 290

Michiyama T., et al., 2021, ApJS, 257, 28

Middelberg E., et al., 2004, A&A, 417, 925

Miller G. E., Scalo J. M., 1979, ApJS, 41, 513

Mineo S., Gilfanov M., Sunyaev R., 2012, MNRAS, 419, 2095

Mingozzi M., et al., 2018, MNRAS, 474, 3640

Miura R. E., et al., 2021, MNRAS, 504, 6198

Miville-Deschênes M.-A., Murray N., Lee E. J., 2017, ApJ, 834, 57

Mizumoto M., Nomura M., Done C., Ohsuga K., Odaka H., 2021, MNRAS, 503, 1442

Molina F. Z., Glover S. C. O., Federrath C., Klessen R. S., 2012, MNRAS, 423, 2680

Molinari S., et al., 2010, A&A, 518, L100

Monje R. R., Blain A. W., Phillips T. G., 2011, ApJS, 195, 23

Moreno J., et al., 2019, MNRAS, 485, 1320

Morganti R., 2017, Frontiers in Astronomy and Space Sciences, 4, 42

Morganti R., Tadhunter C. N., Oosterloo T. A., 2005, A&A, 444, L9

Morganti R., Oosterloo T., Oonk J. B. R., Frieswijk W., Tadhunter C., 2015, A&A, 580, A1

Morganti R., Veilleux S., Oosterloo T., Teng S. H., Rupke D., 2016, A&A, 593, A30

Morselli L., et al., 2020, MNRAS, 496, 4606

Mortlock D. J., et al., 2011, Nature, 474, 616

Moshir M., et al., 1990, in Bulletin of the American Astronomical Society. p. 1325

Motter J. C., et al., 2021, MNRAS, 506, 4354

Mouschovias T. C., Spitzer L. J., 1976, ApJ, 210, 326

Mukherjee D., Bicknell G. V., Sutherland R., Wagner A., 2016, MNRAS, 461, 967

Mukherjee D., Bicknell G. V., Wagner A. Y., Sutherland R. S., Silk J., 2018, MNRAS, 479, 5544

Mullaney J. R., Alexander D. M., Fine S., Goulding A. D., Harrison C. M., Hickox R. C., 2013, MNRAS, 433, 622

Muller C. A., Oort J. H., 1951, Nature, 168, 357

Mundell C. G., James P. A., Loiseau N., Schinnerer E., Forbes D. A., 2004, ApJ, 614, 648

Murray N., Chiang J., Grossman S. A., Voit G. M., 1995, ApJ, 451, 498

Mushotzky R. F., Done C., Pounds K. A., 1993, ARA&A, 31, 717

Musiimenta B., et al., 2023, A&A, 679, A84

Naab T., Ostriker J. P., 2017, ARA&A, 55, 59

Nagar N. M., Oliva E., Marconi A., Maiolino R., 2002, A&A, 391, L21

Nakajima T., et al., 2023, ApJ, 955, 27

Nakamura F., Li Z.-Y., 2007, ApJ, 662, 395

Nakano T., 1976, PASJ, 28, 355

Nandra K., Pounds K. A., 1994, MNRAS, 268, 405

Narayan R., 2005, Ap&SS, 300, 177

Narayanan D., Krumholz M. R., 2014, MNRAS, 442, 1411

Nardini E., Risaliti G., Watabe Y., Salvati M., Sani E., 2010, MNRAS, 405, 2505

Nayakshin S., Zubovas K., 2012, MNRAS, 427, 372

Nelson D., et al., 2018, MNRAS, 475, 624

Nelson D., et al., 2019, MNRAS, 490, 3234

Netzer H., 2006, in Alloin D., ed., , Vol. 693, Physics of Active Galactic Nuclei at all Scales. p. 1,
    doi:10.1007/3-540-34621-X˙1

Netzer H., 2015, ARA&A, 53, 365

Neufeld D. A., Kaufman M. J., 1993, ApJ, 418, 263

Nomoto K., Kobayashi C., Tominaga N., 2013, ARA&A, 51, 457

Nomura M., Ohsuga K., Takahashi H. R., Wada K., Yoshida T., 2016, PASJ, 68, 16

Noterdaeme P., Ledoux C., Petitjean P., Srianand R., 2008, A&A, 481, 327

Nyland K., et al., 2020, ApJ, 905, 74

O'Dea C. P., Saikia D. J., 2021, A&ARv, 29, 3

Ogle P., Boulanger F., Guillard P., Evans D. A., Antonucci R., Appleton P. N., Nesvadba N., Leipski C.,
    2010, ApJ, 724, 1193

Oke J. B., 1963, Nature, 197, 1040

Omont A., 2007, Reports on Progress in Physics, 70, 1099

Oosterloo T., Morganti R., Tadhunter C., Raymond Oonk J. B., Bignall H. E., Tzioumis T., Reynolds C.,
    2019, A&A, 632, A66

Oppenheimer J. R., Volkoff G. M., 1939, Physical Review, 55, 374

Orienti M., Prieto M. A., 2010, MNRAS, 401, 2599

Orlando S., Bocchino F., Reale F., Peres G., Pagano P., 2008, ApJ, 678, 274

Osterbrock D. E., Ferland G. J., 2006, Astrophysics of gaseous nebulae and active galactic nuclei

Ostriker J. P., Ciotti L., 2005, Philosophical Transactions of the Royal Society of London Series A, 363,
    667

Otter J. A., et al., 2022, ApJ, 941, 93

Padoan P., Nordlund Å., 2011, ApJ, 730, 40

Padovani M., Hennebelle P., Marcowith A., Ferrière K., 2015, A&A, 582, L13

Padovani M., Marcowith A., Hennebelle P., Ferrière K., 2016, A&A, 590, A8

Paggi A., Wang J., Fabbiano G., Elvis M., Karovska M., 2012, ApJ, 756, 39

Pan H.-A., et al., 2018, ApJ, 868, 132

Papadopoulos P. P., van der Werf P., Isaak K., Xilouris E. M., 2010, ApJ, 715, 775

Papadopoulos P. P., van der Werf P. P., Xilouris E. M., Isaak K. G., Gao Y., Mühle S., 2012, MNRAS, 426,
    2601

Pascual S., Cardiel N., Picazo-Sanchez P., Castillo-Morales A., de Paz A. G., 2021, guaix-ucm/megaradrp:
    v0.11, doi:10.5281/zenodo.4588041, https://doi.org/10.5281/zenodo.4588041

Pasini T., et al., 2020, MNRAS, 497, 2163

Pasquini L., Bonifacio P., Randich S., Galli D., Gratton R. G., 2004, A&A, 426, 651

Paturel G., Petit C., Prugniel P., Theureau G., Rousseau J., Brouty M., Dubois P., Cambrésy L., 2003,

A&A, 412, 45

Pearson C., et al., 2016, ApJS, 227, 9

Pedregosa F., et al., 2011, Journal of Machine Learning Research, 12, 2825

Peng Y., Maiolino R., Cochrane R., 2015, Nature, 521, 192

Pensabene A., et al., 2021, A&A, 652, A66

Peralta de Arriba L., et al., 2023, A&A, 675, A58

Pereira-Santaella M., et al., 2013, ApJ, 768, 55

Pereira-Santaella M., et al., 2022, A&A, 665, L11

Pérez-Torres M., Mattila S., Alonso-Herrero A., Aalto S., Efstathiou A., 2021a, A&ARv, 29, 2

Pérez-Torres M., Mattila S., Alonso-Herrero A., Aalto S., Efstathiou A., 2021b, A&ARv, 29, 2

Perna M., Cresci G., Brusa M., Lanzuisi G., Concas A., Mainieri V., Mannucci F., Marconi A., 2019, A&A, 623, A171

Perna M., et al., 2020, A&A, 643, A139

Pessa I., et al., 2021, A&A, 650, A134

Pilbratt G. L., et al., 2010a, A&A, 518, L1

Pilbratt G. L., et al., 2010b, A&A, 518, L1

Pillepich A., Nelson D., Truong N., Weinberger R., Martin-Navarro I., Springel V., Faber S. M., Hernquist L., 2021, MNRAS, 508, 4667

Piotrowska J. M., Bluck A. F. L., Maiolino R., Peng Y., 2022, MNRAS, 512, 1052

Planck Collaboration et al., 2016, A&A, 594, A13

Pogge R. W., 1988, ApJ, 328, 519

Poglitsch A., et al., 2010, A&A, 518, L2

Portegies Zwart S. F., McMillan S. L. W., Gieles M., 2010, ARA&A, 48, 431

Pound M. W., Wolfire M. G., 2008, in Argyle R. W., Bunclark P. S., Lewis J. R., eds, Astronomical Society of the Pacific Conference Series Vol. 394, Astronomical Data Analysis Software and Systems XVII. p. 654

Pound M. W., Wolfire M. G., 2023, AJ, 165, 25

Powell M. C., Urry C. M., Cardamone C. N., Simmons B. D., Schawinski K., Young S., Kawakatsu M., 2017, ApJ, 835, 22

Pozzi F., et al., 2010, A&A, 517, A11

Pozzi F., Vallini L., Vignali C., Talia M., Gruppioni C., Mingozzi M., Massardi M., Andreani P., 2017, MNRAS, 470, L64

Predehl P., et al., 2020, Nature, 588, 227

Priestley F. D., Barlow M. J., Viti S., 2017, MNRAS, 472, 4444

Proga D., Stone J. M., Kallman T. R., 2000, ApJ, 543, 686

Querejeta M., et al., 2021, A&A, 656, A133

Rachford B. L., et al., 2002, ApJ, 577, 221

Ramos Almeida C., Ricci C., 2017, Nature Astronomy, 1, 679

Ramos Almeida C., et al., 2022, A&A, 658, A155

Ranalli P., Comastri A., Setti G., 2003, A&A, 399, 39

Rankine A. L., Hewett P. C., Banerji M., Richards G. T., 2020, MNRAS, 492, 4553

Reber G., 1944, ApJ, 100, 279

Renzini A., 1977, in Bouvier P., Maeder A., eds, Saas-Fee Advanced Course 7: Advanced Stages in Stellar Evolution. p. 151

Reynolds J. H., 1920, MNRAS, 80, 746

Reynolds C. S., 1997, MNRAS, 286, 513

Ricci C., Walter R., Courvoisier T. J. L., Paltani S., 2011, A&A, 532, A102

Ricci C., et al., 2017a, ApJS, 233, 17

Ricci C., et al., 2017b, MNRAS, 468, 1273

Ricci C., et al., 2023, ApJ, 959, 27

Richings A. J., Faucher-Giguère C.-A., 2018a, MNRAS, 474, 3673

Richings A. J., Faucher-Giguère C.-A., 2018b, MNRAS, 478, 3100

Riffel R. A., Storchi-Bergmann T., Riffel R., Dahmer-Hahn L. G., Diniz M. R., Schönell A. J., Dametto
    N. Z., 2017, MNRAS, 470, 992

Riffel R. A., et al., 2021, MNRAS, 504, 3265

Rigopoulou D., Papadakis I., Lawrence A., Ward M., 1997, A&A, 327, 493

Robberto M., et al., 2013, ApJS, 207, 10

Robertson B. E., 2022, ARA&A, 60, 121

Robitaille T., 2019, APLpy v2.0: The Astronomical Plotting Library in Python,
    doi:10.5281/zenodo.2567476, https://doi.org/10.5281/zenodo.2567476

Robitaille T., Bressert E., 2012, APLpy: Astronomical Plotting Library in Python (ascl:1208.017)

Robitaille T. P., Whitney B. A., 2010, ApJ, 710, L11

Röllig M., Ossenkopf V., Jeyakumar S., Stutzki J., Sternberg A., 2006, A&A, 451, 917

Röllig M., et al., 2007, A&A, 467, 187

Röllig M., Szczerba R., Ossenkopf V., Glück C., 2013, A&A, 549, A85

Roman-Duval J., Jackson J. M., Heyer M., Rathborne J., Simon R., 2010, ApJ, 723, 492

Rosario D. J., et al., 2018, MNRAS, 473, 5658

Rose M., Tadhunter C., Ramos Almeida C., Rodríguez Zaurín J., Santoro F., Spence R., 2018, MNRAS,
    474, 128

Rosenberg M. J. F., et al., 2015, ApJ, 801, 72

Rosolowsky E., 2005, PASP, 117, 1403

Rosolowsky E., et al., 2021, MNRAS, 502, 1218

Rowan-Robinson M., 1977, ApJ, 213, 635

Roy A. L., et al., 2000, in van Haarlem M. P., ed., Perspectives on Radio Astronomy: Science with Large
    Antenna Arrays. p. 173 (arXiv:astro-ph/9909105), doi:10.48550/arXiv.astro-ph/9909105

Roy A. L., et al., 2001, in Schilizzi R. T., ed., Vol. 205, Galaxies and their Constituents at the Highest
    Angular Resolutions. p. 70 (arXiv:astro-ph/0012159), doi:10.48550/arXiv.astro-ph/0012159

Ruiz J. R., Crenshaw D. M., Kraemer S. B., Bower G. A., Gull T. R., Hutchings J. B., Kaiser M. E.,
    Weistrop D., 2005, AJ, 129, 73

Rupke D. S. N., Veilleux S., 2013, ApJ, 768, 75

Rupke D. S. N., Gültekin K., Veilleux S., 2017, ApJ, 850, 40

Sabatini G., Gruppioni C., Massardi M., Giannetti A., Burkutean S., Cimatti A., Pozzi F., Talia M., 2018,
    MNRAS, 476, 5417

Saintonge A., Catinella B., 2022, ARA&A, 60, 319

Saintonge A., et al., 2011, MNRAS, 415, 61

Saintonge A., et al., 2017, ApJS, 233, 22

Saito T., et al., 2017, ApJ, 835, 174

Salim S., 2014, Serbian Astronomical Journal, 189, 1

Salomé P., Combes F., Revaz Y., Downes D., Edge A. C., Fabian A. C., 2011, A&A, 531, A85

Salomé Q., et al., 2023, MNRAS, 524, 3130

Salpeter E. E., 1955, ApJ, 121, 161

Salpeter E. E., 1964, ApJ, 140, 796

Salvestrini F., Gruppioni C., Pozzi F., Vignali C., Giannetti A., Paladino R., Hatziminaoglou E., 2020, A&A, 641, A151

Salvestrini F., et al., 2022, A&A, 663, A28

Sánchez-García M., García-Burillo S., Pereira-Santaella M., Colina L., Usero A., Querejeta M., Alonso-Herrero A., Fuente A., 2022, A&A, 660, A83

Sandage A., 1961, The Hubble Atlas of Galaxies

Sandage A., 2005, ARA&A, 43, 581

Sanders R. H., Huntley J. M., 1976, ApJ, 209, 53

Sanders D. B., Mazzarella J. M., Kim D. C., Surace J. A., Soifer B. T., 2003, AJ, 126, 1607

Santoro F., Oonk J. B. R., Morganti R., Oosterloo T. A., Tadhunter C., 2016, A&A, 590, A37

Sawicki M., 2012, PASP, 124, 1208

Schawinski K., et al., 2014, MNRAS, 440, 889

Schawinski K., Koss M., Berney S., Sartori L. F., 2015, MNRAS, 451, 2517

Scheuer P. A. G., 1974, MNRAS, 166, 513

Schiminovich D., et al., 2007, ApJS, 173, 315

Schisano E., et al., 2014, ApJ, 791, 27

Schmidt M., 1959, ApJ, 129, 243

Schmidt M., 1963a, ApJ, 137, 758

Schmidt M., 1963b, Nature, 197, 1040

Schmitt H. R., Ulvestad J. S., Antonucci R. R. J., Kinney A. L., 2001, ApJS, 132, 199

Schmitt H. R., Donley J. L., Antonucci R. R. J., Hutchings J. B., Kinney A. L., 2003, ApJS, 148, 327

Schneider N., et al., 2016, A&A, 587, A74

Schnorr-Müller A., et al., 2016, MNRAS, 462, 3570

Schöier F. L., van der Tak F. F. S., van Dishoeck E. F., Black J. H., 2005, A&A, 432, 369

Schruba A., et al., 2011, AJ, 142, 37

Schruba A., et al., 2017, ApJ, 835, 278

Scoville N. Z., Yun M. S., Clemens D. P., Sanders D. B., Waller W. H., 1987, ApJS, 63, 821

Scoville N., et al., 2007, ApJS, 172, 1

Scuseria G. E., Miller M. D., Jensen F., Geertsen J., 1991, J. Chem. Phys., 94, 6660

Sebastian B., Kharb P., O'Dea C. P., Gallimore J. F., Baum S. A., 2020, MNRAS, 499, 334

Seifried D., et al., 2017, MNRAS, 472, 4797

Sengupta D., et al., 2023, A&A, 676, A103

Sérsic J. L., 1963, Boletin de la Asociacion Argentina de Astronomia La Plata Argentina, 6, 41

Seyfert C. K., 1943, ApJ, 97, 28

Shakura N. I., Sunyaev R. A., 1973, A&A, 24, 337

Shankar F., Weinberg D. H., Miralda-Escudé J., 2009, ApJ, 690, 20

Shapiro S. L., 2005, ApJ, 620, 59

Shapiro S. L., Lightman A. P., Eardley D. M., 1976, ApJ, 204, 187

Sharda P., et al., 2022, MNRAS, 509, 2180

Shaw G., Ferland G. J., Abel N. P., Stancil P. C., van Hoof P. A. M., 2005, ApJ, 624, 794

Shields G. A., 1974, ApJ, 191, 309

Shields G. A., 1990, ARA&A, 28, 525

Shields G. A., 1999, PASP, 111, 661

Shimizu T. T., et al., 2019, MNRAS, 490, 5860

Shirley Y. L., 2015, PASP, 127, 299

Shu F. H., 1977, ApJ, 214, 488

Shull J. M., Beckwith S., 1982, ARA&A, 20, 163

Silk J., 2013, ApJ, 772, 112

Silk J., Rees M. J., 1998, A&A, 331, L1

Singh V., Shastri P., Risaliti G., 2011, A&A, 532, A84

Singha M., O'Dea C. P., Baum S. A., 2023, Galaxies, 11, 85

Slipher V. M., 1917, Lowell Observatory Bulletin, 3, 59

Smartt S. J., 2009, ARA&A, 47, 63

Smercina A., et al., 2022, ApJ, 929, 154

Smirnova-Pinchukova I., et al., 2022, A&A, 659, A125

Smith R. J., 2020, ARA&A, 58, 577

Sobolev V. V., 1960, Moving Envelopes of Stars, doi:10.4159/harvard.9780674864658.

Solomon P. M., Sage L. J., 1988, ApJ, 334, 613

Solomon P. M., Rivolo A. R., Barrett J., Yahil A., 1987, ApJ, 319, 730

Soltan A., 1982, MNRAS, 200, 115

Somerville R. S., Hopkins P. F., Cox T. J., Robertson B. E., Hernquist L., 2008, MNRAS, 391, 481

Spaans M., Meijerink R., 2008, ApJ, 678, L5

Speranza G., et al., 2022, A&A, 665, A55

Speranza G., et al., 2023, arXiv e-prints, p. arXiv:2311.10132

Spitzer L., 1978, Physical processes in the interstellar medium, doi:10.1002/9783527617722.

Stark D. P., 2016, ARA&A, 54, 761

Storchi-Bergmann T., Schnorr-Müller A., 2019, Nature Astronomy, 3, 48

Strateva I., et al., 2001, AJ, 122, 1861

Strauss M. A., et al., 2002, AJ, 124, 1810

Strömgren B., 1939, ApJ, 89, 526

Strong A. W., Moskalenko I. V., Ptuskin V. S., 2007, Annual Review of Nuclear and Particle Science, 57, 285

Strubbe L. E., Quataert E., 2009, MNRAS, 400, 2070

Stutzki J., Bensch F., Heithausen A., Ossenkopf V., Zielinsky M., 1998, A&A, 336, 697

Su Y.-C., et al., 2022, ApJ, 934, 173

Sun M., et al., 2015, ApJ, 802, 14

Sun J., et al., 2018, ApJ, 860, 172

Swartz W. E., Nisbet J. S., Green A. E. S., 1971, J. Geophys. Res., 76, 8425

Swings P., Rosenfeld L., 1937, ApJ, 86, 483

Tacconi L. J., Genzel R., Sternberg A., 2020, ARA&A, 58, 157

Tadhunter C., Morganti R., Rose M., Oonk J. B. R., Oosterloo T., 2014, Nature, 511, 440

Tarchi A., Castangia P., Columbano A., Panessa F., Braatz J. A., 2011, A&A, 532, A125

Tchekhovskoy A., Bromberg O., 2016, MNRAS, 461, L46

Temporin S., Ciroi S., Rafanelli P., Radovich M., Vennik J., Richter G. M., Birkle K., 2003, ApJS, 148, 353

Teng Y.-H., et al., 2023, ApJ, 950, 119

Terao K., Nagao T., Hashimoto T., Yanagisawa K., Matsuoka K., Toba Y., Ikeda H., Taniguchi Y., 2016, ApJ, 833, 190

Thomas D., Maraston C., Schawinski K., Sarzi M., Silk J., 2010, MNRAS, 404, 1775

Thompson T. A., Fabian A. C., Quataert E., Murray N., 2015, MNRAS, 449, 147

Thompson T. A., Quataert E., Zhang D., Weinberg D. H., 2016, MNRAS, 455, 1830

Thorp M. D., Ellison S. L., Pan H.-A., Lin L., Patton D. R., Bluck A. F. L., Walters D., Scudder J. M., 2022, MNRAS, 516, 1462

Tielens A. G. G. M., 2005, The Physics and Chemistry of the Interstellar Medium

Tielens A. G. G. M., 2008, ARA&A, 46, 289

Tielens A. G. G. M., Hollenbach D., 1985, ApJ, 291, 722

Tombesi F., Cappi M., Reeves J. N., Palumbo G. G. C., Yaqoob T., Braito V., Dadina M., 2010, A&A, 521, A57

Tombesi F., Cappi M., Reeves J. N., Palumbo G. G. C., Braito V., Dadina M., 2011, ApJ, 742, 44

Tombesi F., Cappi M., Reeves J. N., Nemmen R. S., Braito V., Gaspari M., Reynolds C. S., 2013, MNRAS, 430, 1102

Tonry J. L., 1984, ApJ, 283, L27

Tonry J. L., 1987, ApJ, 322, 632

Torres-Albà N., et al., 2021, ApJ, 922, 252

Treister E., Schawinski K., Urry C. M., Simmons B. D., 2012, ApJ, 758, L39

Tristram K. R. W., Burtscher L., Jaffe W., Meisenheimer K., Hönig S. F., Kishimoto M., Schartmann M., Weigelt G., 2014, A&A, 563, A82

Trussler J., Maiolino R., Maraston C., Peng Y., Thomas D., Goddard D., Lian J., 2020, MNRAS, 491, 5406

Tucker W., Kellogg E., Gursky H., Giacconi R., Tananbaun H., 1973, ApJ, 180, 715

Tully R. B., Fisher J. R., 1977, A&A, 54, 661

Ueda J., et al., 2014, ApJS, 214, 1

Umemoto T., et al., 2017, PASJ, 69, 78

Urry C. M., Padovani P., 1995, PASP, 107, 803

Utomo D., et al., 2018, ApJ, 861, L18

Uttley P., McHardy I. M., 2005, MNRAS, 363, 586

Valentino F., et al., 2020, A&A, 641, A155

Vallini L., Ferrara A., Pallottini A., Gallerani S., 2017, MNRAS, 467, 1300

Vallini L., Pallottini A., Ferrara A., Gallerani S., Sobacchi E., Behrens C., 2018, MNRAS, 473, 271

Vallini L., Tielens A. G. G. M., Pallottini A., Gallerani S., Gruppioni C., Carniani S., Pozzi F., Talia M., 2019, MNRAS, 490, 4502

Van Rossum G., Drake F. L., 2009, Python 3 Reference Manual. CreateSpace, Scotts Valley, CA

Vazquez-Semadeni E., 1994, ApJ, 423, 681

Veilleux S., 1991, ApJS, 75, 383

Veilleux S., Osterbrock D. E., 1987, ApJS, 63, 295

Veilleux S., Cecil G., Bland-Hawthorn J., 2005, ARA&A, 43, 769

Veilleux S., Bolatto A., Tombesi F., Meléndez M., Sturm E., González-Alfonso E., Fischer J., Rupke D. S. N., 2017, ApJ, 843, 18

Veilleux S., Maiolino R., Bolatto A. D., Aalto S., 2020, A&ARv, 28, 2

Venturi G., et al., 2021, A&A, 648, A17

Vignali C., Alexander D. M., Gilli R., Pozzi F., 2010, MNRAS, 404, 48

Villanueva V., et al., 2021, arXiv e-prints, p. arXiv:2109.14167

Virtanen P., et al., 2020, Nature Methods, 17, 261

Viti S., et al., 2014, A&A, 570, A28

Volonteri M., Lodato G., Natarajan P., 2008, MNRAS, 383, 1079

Wagner S. J., Witzel A., 1995, ARA&A, 33, 163

Wagner A. Y., Bicknell G. V., Umemura M., 2012, ApJ, 757, 136

Wagner A. Y., Umemura M., Bicknell G. V., 2013, ApJ, 763, L18

Walter F., et al., 2016, ApJ, 833, 67

Wang X., Loeb A., 2018, New Astron., 61, 95

Wang F., et al., 2021, ApJ, 907, L1

Waskom M. L., 2021, Journal of Open Source Software, 6, 3021

Weaver R., McCray R., Castor J., Shapiro P., Moore R., 1977, ApJ, 218, 377

Weedman D. W., 1970, ApJ, 159, 405

Wehrle A. E., Morris M., 1987, ApJ, 313, L43

Weinreb S., Barrett A. H., Meeks M. L., Henry J. C., 1963, Nature, 200, 829

Weiß A., Ivison R. J., Downes D., Walter F., Cirasuolo M., Menten K. M., 2009, ApJ, 705, L45

Westmoquette M. S., Clements D. L., Bendo G. J., Khan S. A., 2012, MNRAS, 424, 416

Wetzel A. R., Tinker J. L., Conroy C., van den Bosch F. C., 2013, MNRAS, 432, 336

Weymann R. J., Morris S. L., Foltz C. B., Hewett P. C., 1991, ApJ, 373, 23

Wilson R. W., Jefferts K. B., Penzias A. A., 1970, ApJ, 161, L43

Wilson A. S., Baldwin J. A., Ulvestad J. S., 1985, ApJ, 291, 627

Wilson A. S., Braatz J. A., Heckman T. M., Krolik J. H., Miley G. K., 1993, ApJ, 419, L61

Winkler P. F. J., White A. E., 1975, ApJ, 199, L139

Wolfe A. M., Gawiser E., Prochaska J. X., 2005, ARA&A, 43, 861

Wolfire M. G., Hollenbach D., McKee C. F., 2010, ApJ, 716, 1191

Wolfire M. G., Vallini L., Chevance M., 2022, ARA&A, 60, 247

Woltjer L., 1959, ApJ, 130, 38

Wong T., et al., 2019, ApJ, 885, 50

Woo J.-H., Son D., Bae H.-J., 2017, ApJ, 839, 120

Wright E. L., et al., 2010, AJ, 140, 1868

Wylezalek D., Flores A. M., Zakamska N. L., Greene J. E., Riffel R. A., 2020, MNRAS, 492, 4680

Xanthopoulos E., Thean A. H. C., Pedlar A., Richards A. M. S., 2010, MNRAS, 404, 1966

Xia X. Y., et al., 2012, ApJ, 750, 92

Xu C. K., et al., 2014, ApJ, 787, 48

Yang X., Mo H. J., van den Bosch F. C., Pasquali A., Li C., Barden M., 2007, ApJ, 671, 153

Yang J., et al., 2020, ApJ, 897, L14

Yang H. Y. K., Ruszkowski M., Zweibel E. G., 2022, Nature Astronomy, 6, 584

Yaqoob T., 2012, MNRAS, 423, 3360

Young J. S., et al., 1995, ApJS, 98, 219

Yu Q., Tremaine S., 2002, MNRAS, 335, 965

Yuan F., Narayan R., 2014, ARA&A, 52, 529

Zaragoza-Cardiel J., Beckman J., Font J., Rosado M., Camps-Fariña A., Borlaff A., 2017, MNRAS, 465, 3461

Zel'dovich Y. B., 1964, Soviet Physics Doklady, 9, 195

Zhao Y., et al., 2016, ApJ, 820, 118

Zhuang M.-Y., Ho L. C., 2020, ApJ, 896, 108

Zinn P. C., Middelberg E., Norris R. P., Dettmar R. J., 2013, ApJ, 774, 66

Zubovas K., King A., 2012, ApJ, 745, L34

da Cunha E., Charlot S., Elbaz D., 2008, MNRAS, 388, 1595

de Vaucouleurs G., 1959, Handbuch der Physik, 53, 275

de Vaucouleurs G., de Vaucouleurs A., Corwin J. R., 1976, Second reference catalogue of bright galaxies, 1976, 0

de Vaucouleurs G., de Vaucouleurs A., Corwin Herold G. J., Buta R. J., Paturel G., Fouque P., 1991, Third Reference Catalogue of Bright Galaxies

de los Reyes M. A. C., Kennicutt Robert C. J., 2019, ApJ, 872, 16

den Brok J. S., et al., 2021, MNRAS, 504, 3221

pandas development team T., 2020, pandas-dev/pandas: Pandas, doi:10.5281/zenodo.3509134, https://doi.org/10.5281/zenodo.3509134

van der Tak F. F. S., Black J. H., Schöier F. L., Jansen D. J., van Dishoeck E. F., 2007, A&A, 468, 627

van der Velden E., 2020, The Journal of Open Source Software, 5, 2004

van der Werf P. P., et al., 2010, A&A, 518, L42

<div align="right">*A*</div>

Appendix to Chapter 2

A.1   CO line ratios

In this section we show the CO luminosity ratios, both with denominators the CO(1–0) and the CO(6–5) luminosity. The CO(1–0) luminosities have been corrected to take into account only the emission up to $r = 250$ pc from the center of the galaxies (with Equation 2.1). Firstly we plot the luminosity ratios against the FUV flux G_0 and the X-ray flux F_X, fitting the points with a regression line, respectively as in Figures 2.3 and 2.4. The details can be found in Sections 2.5.1 and 2.5.2. Secondly, we plot the same points but with the Cloudy models at different gas densities superimposed, as in Figure 2.5, and as explained in detail in Section 2.5.3.

A.2   CO(6–5) atlas

In this section we present the rest (in addition to Figure 2.1) of the images of CO(6–5) emission for our sample galaxies. All the CO(6–5) data cubes are from the ALMA Archive, already calibrated, cleaned, and when available, primary-beam corrected. Using CASA 5.6 (McMullin et al., 2007), we produce the moment 0 map from the data cubes with the task immoments. We then plot the ALMA CO(6–5) contours over the optical image of the galaxy.
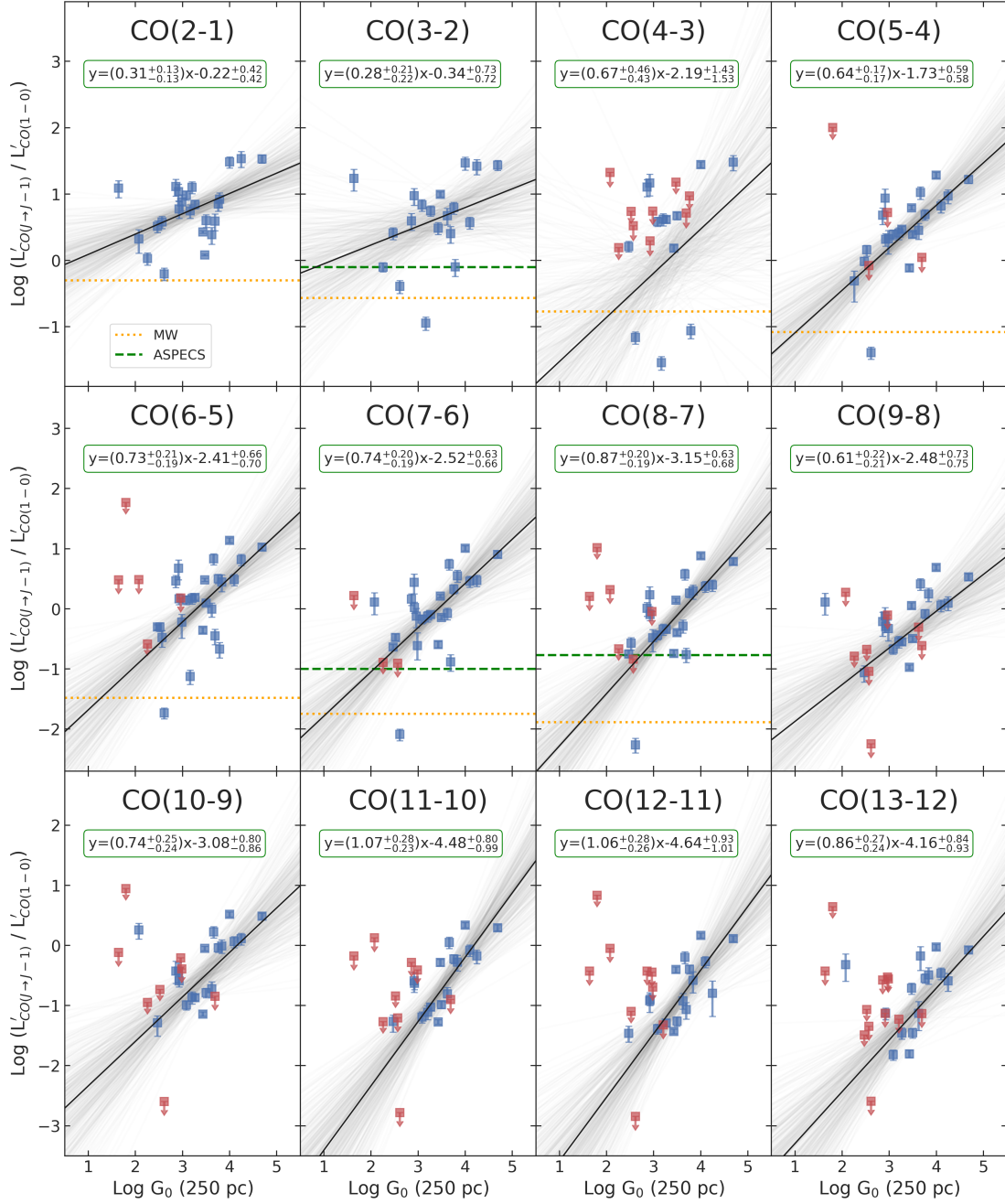
Figure A.1: CO line ratios, with respect to the CO(1–0) line, vs. G_0. The *x*-axis is the Habing field G_0 (for $r = 250$ pc). The *y*-axis is the luminosity ratio $L'_{CO(J \to J-1)}/L'_{CO(1 \to 0)}$ to the nuclear ($r = 250$ pc) fraction of CO(1–0). The luminosities L' are in units of K km s^{-1} pc^{-2}, and J is indicated on the top of each panel. Blue squares indicate 3σ detections in both lines; red squares with downward arrow indicate less than 3σ in the higher-*J* line (i.e. censored data). The lines are regression fits to the observed data: solid black line is the median Linmix regression, thin shaded green lines show fits drawn from the posterior distribution of Linmix regression. When available, the Milky Way (dotted orange line, data from Fixsen et al. 1999) and the ASPECS AGN (green dashed line, data from Boogaard et al. 2020) CO ratios are also shown.
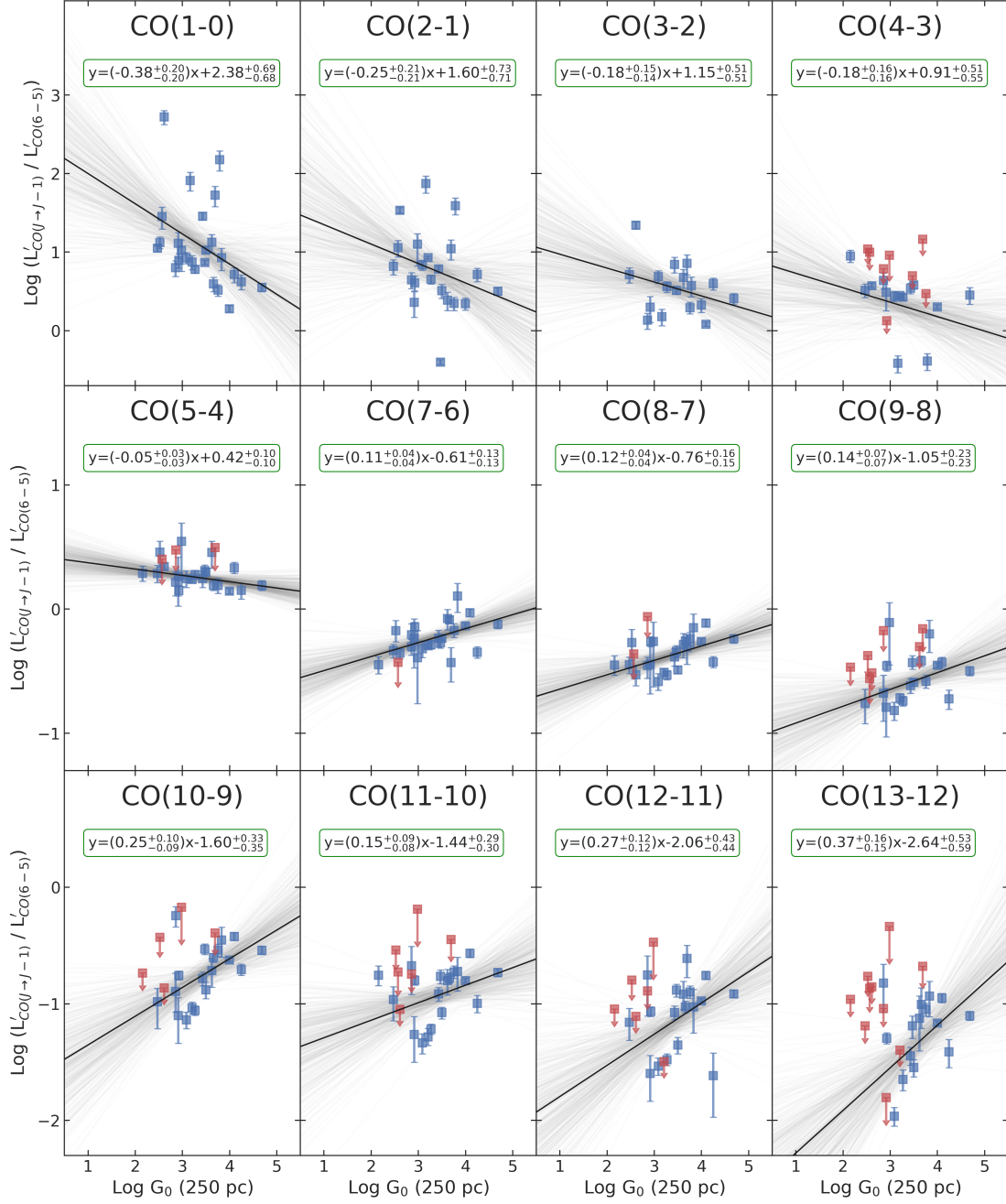
Figure A.2: CO line ratios, with respect to the CO(6–5) line, vs. G_0. The x-axis is the Habing field G_0 (for $r = 250$ pc). The y-axis is the luminosity ratio $L'_{\mathrm{CO}(J \to J-1)}/L'_{\mathrm{CO}(6 \to 5)}$ to the CO(6–5) line. Data points and lines are described in Figure A.1.
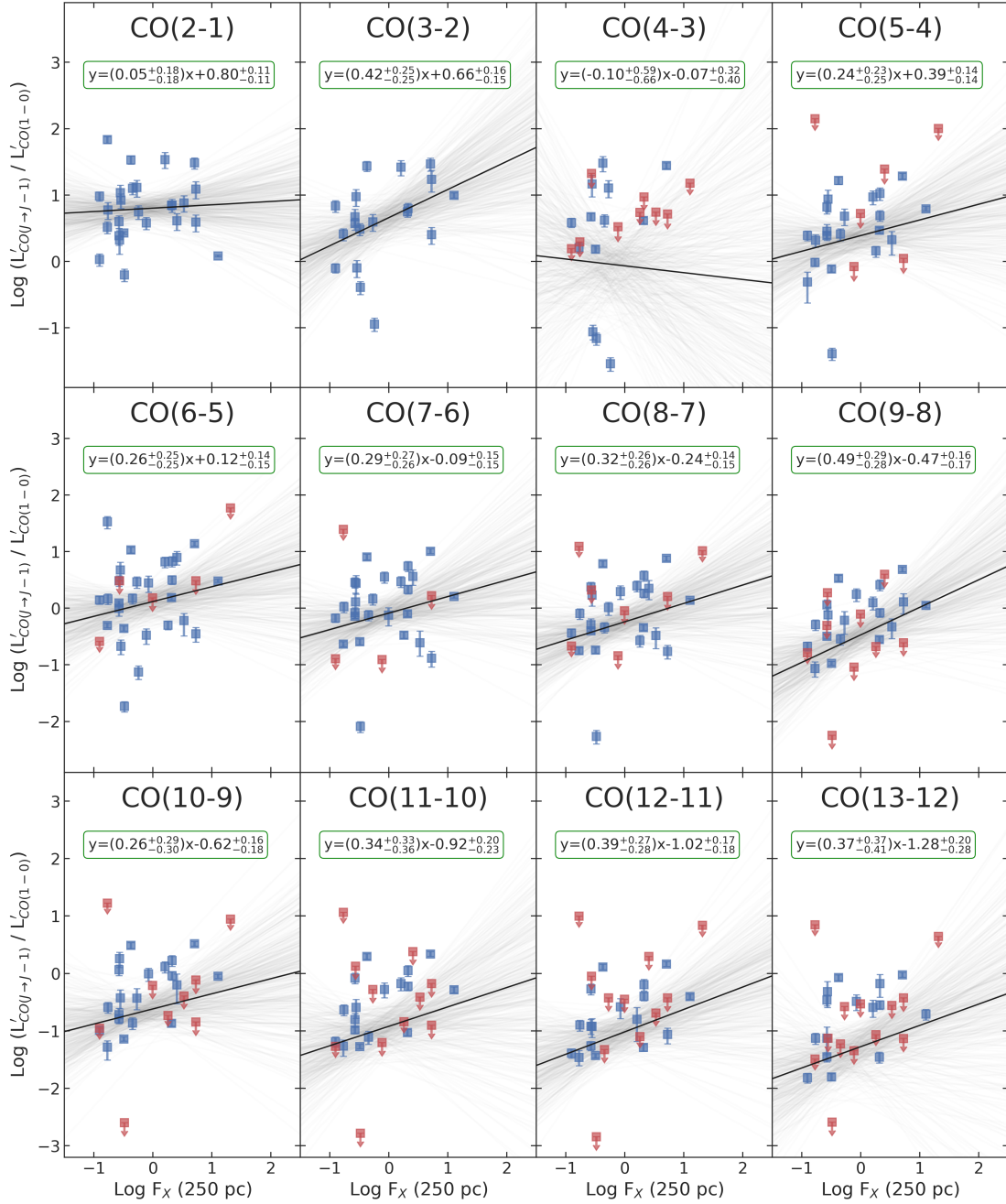
Figure A.3: CO line ratios, with respect to the CO(1–0) line, vs. F_X. The x-axis is F_X (for $r = 250$ pc), in units of erg s^{-1} cm^{-2}. The y-axis is the luminosity ratio $L'_{CO(J \to J-1)}/L'_{CO(1 \to 0)}$ to the nuclear ($r = 250$ pc) fraction of CO(1–0). Data points and lines are described in Figure A.1.
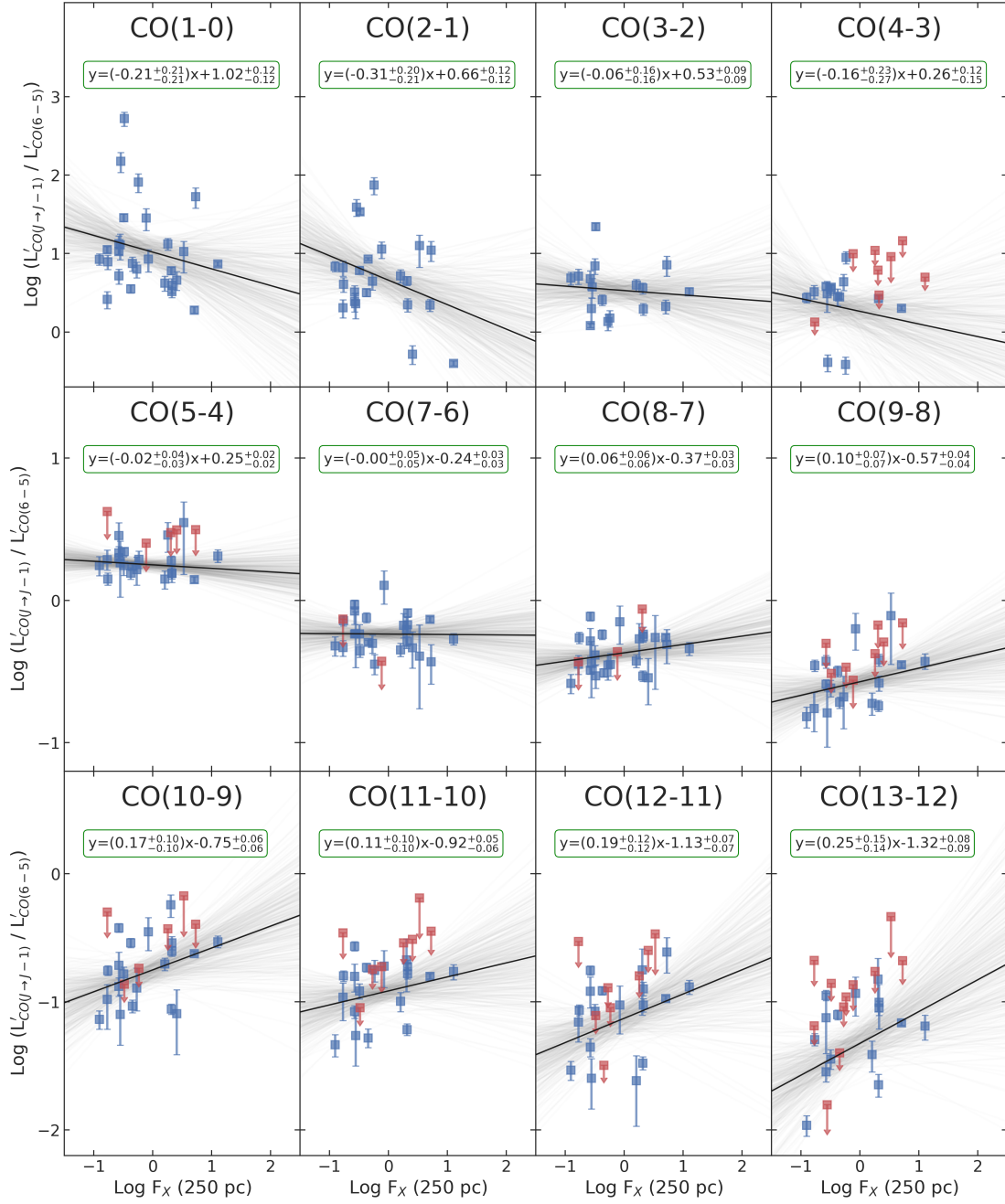
Figure A.4: CO line ratios, with respect to the CO(6–5) line, vs. F_X. The x-axis is F_X (for $r = 250$ pc), in units of erg s^{-1} cm^{-2}. The y-axis is the luminosity ratio $L'_{CO(J \to J-1)}/L'_{CO(6 \to 5)}$ to the CO(6–5) line. Data points and lines are described in Figure A.1.
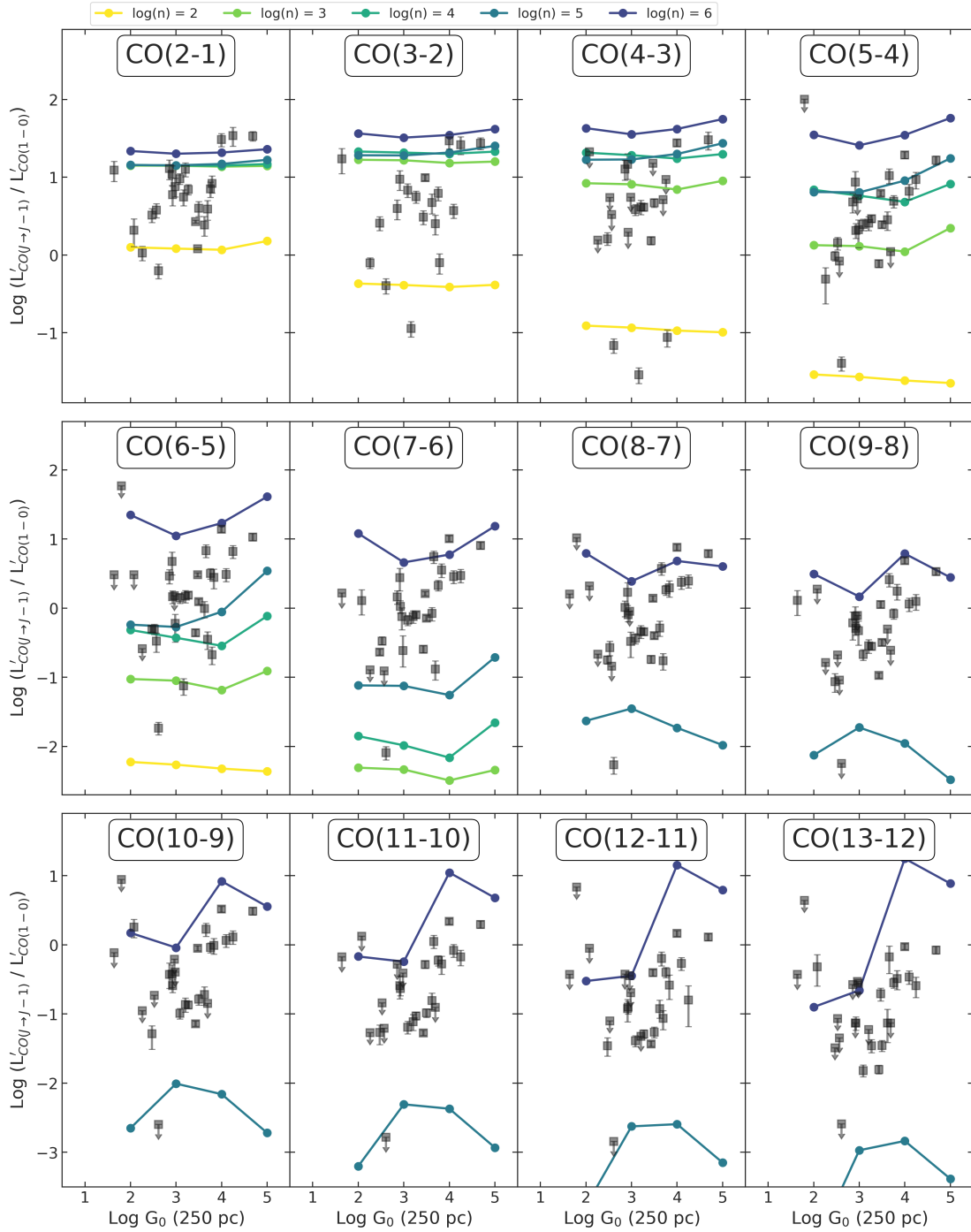
Figure A.5: CO line ratios, with respect to the CO(1–0) line, vs. G_0. The x-axis is the Habing field G_0 (for $r = 250$ pc). The y-axis is the luminosity ratio $L'_{\mathrm{CO}(J\to J-1)}/L'_{\mathrm{CO}(1\to 0)}$ to the nuclear ($r = 250$ pc) fraction of CO(1–0). The luminosities L' are in units of K km s^{-1} pc^{-2}, and J is indicated on the top of each panel. Squares with downward arrow indicate less than 3σ detections in the higher-J line (i.e. censored data). The colored overplotted lines are Cloudy numerical models at different gas densities, namely 10^2 (yellow), 10^3 (light green), 10^4 (dark green), 10^5 (blue) and 10^6 (purple) cm^{-3}.
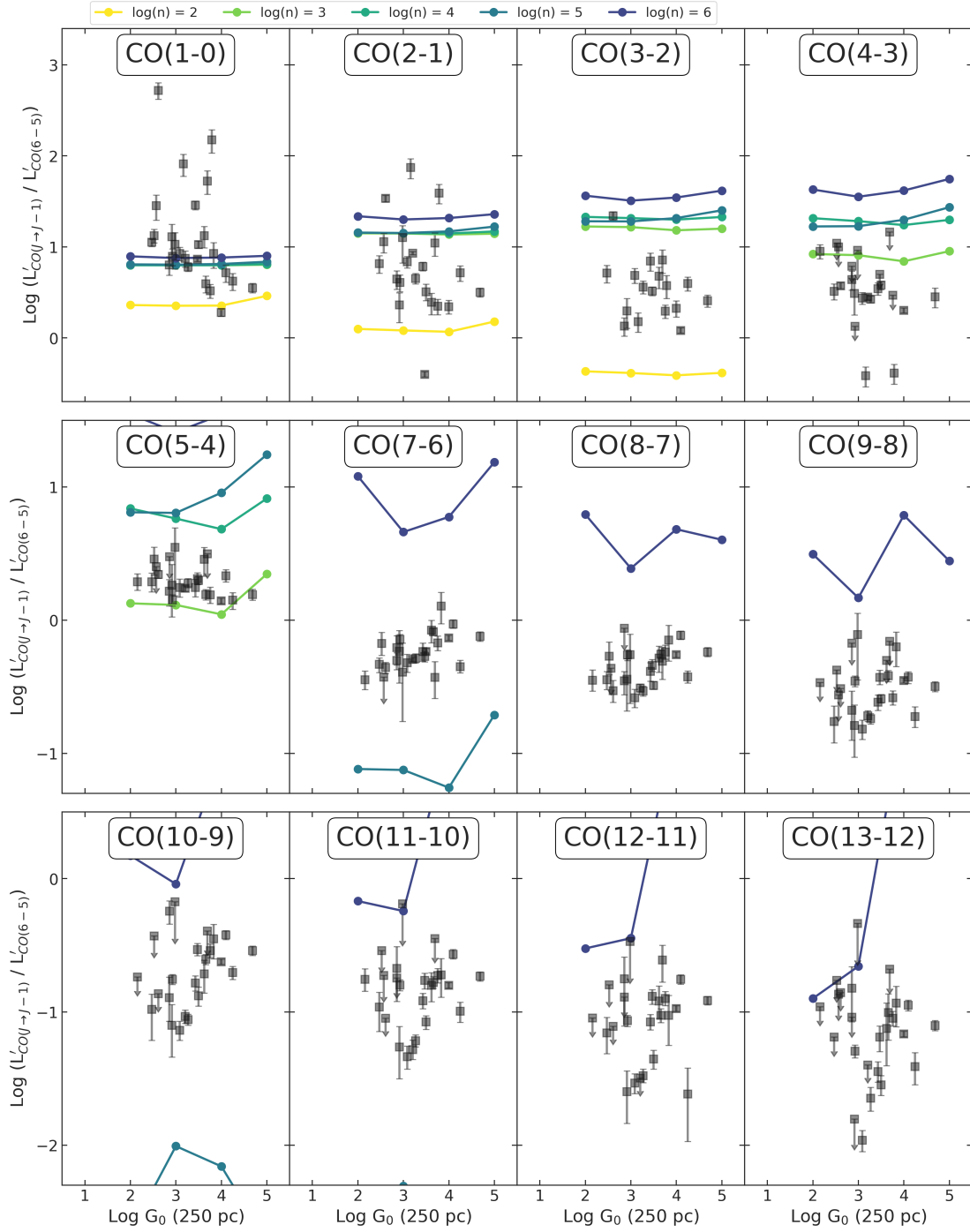
Figure A.6: CO line ratios, with respect to the CO(6–5) line, vs. G_0. The *x*-axis is the Habing field G_0 (for $r = 250$ pc). The *y*-axis is the luminosity ratio $L'_{CO(J\rightarrow J-1)}/L'_{CO(6\rightarrow 5)}$ to the CO(6–5) line. Data points and lines are described in Figure A.5.
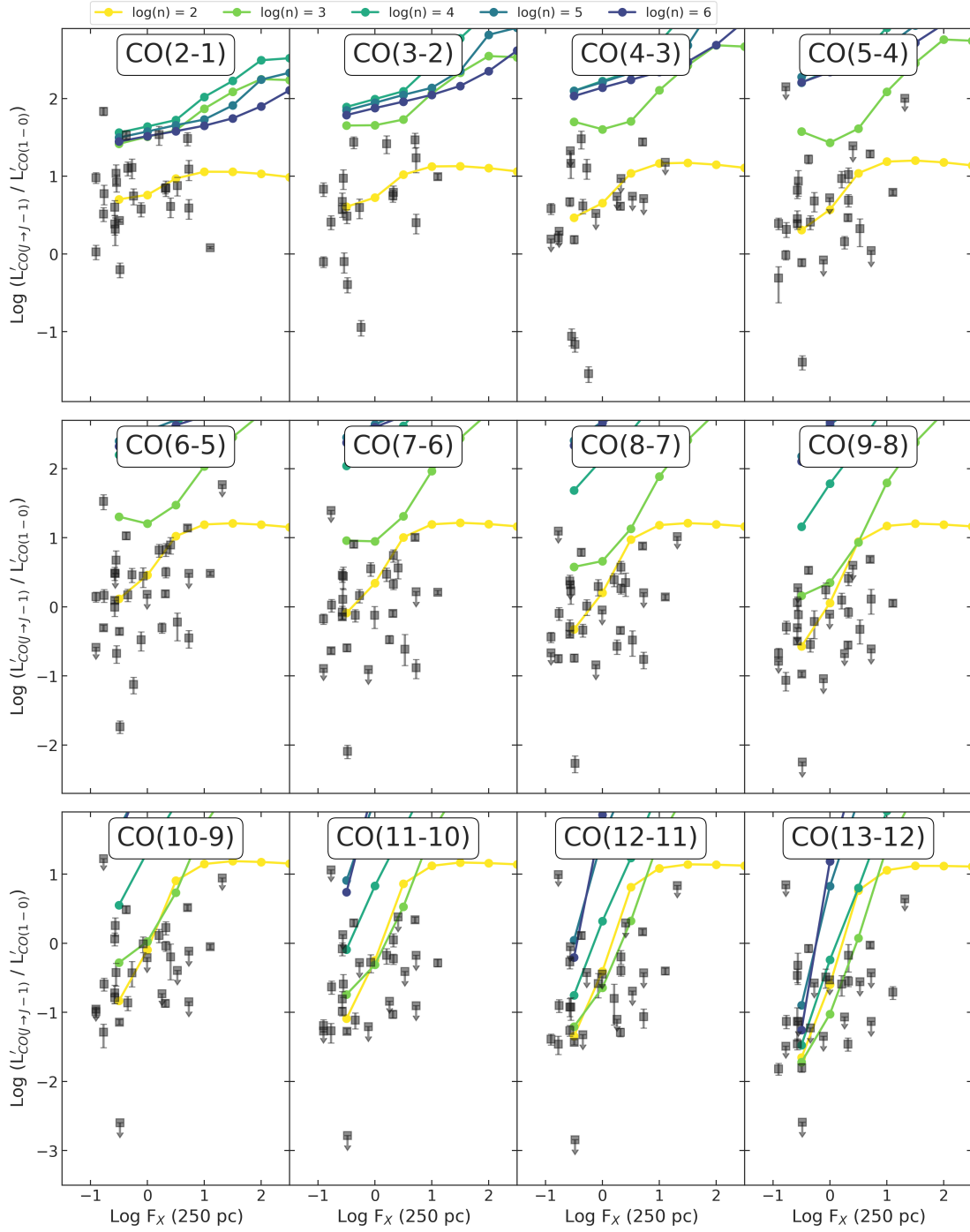
Figure A.7: CO line ratios, with respect to the CO(1–0) line, vs. F_X. The *x*-axis is F_X (for $r = 250$ pc), in units of erg s^{-1} cm^{-2}. The *y*-axis is the luminosity ratio $L'_{\mathrm{CO}(J\to J-1)}/L'_{\mathrm{CO}(1\to0)}$ to the nuclear ($r = 250$ pc) fraction of CO(1–0). Data points and lines are described in Figure A.5.
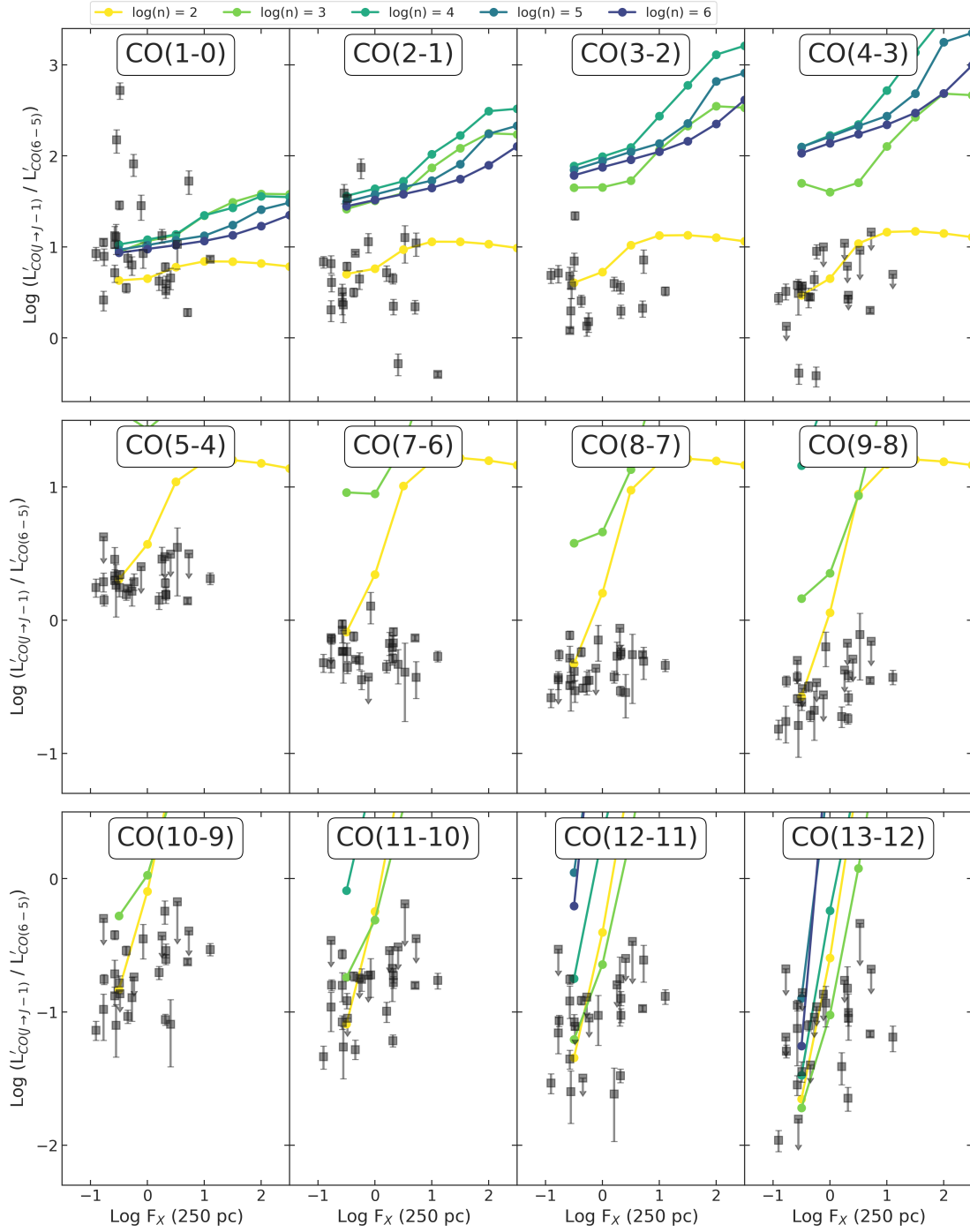
Figure A.8: CO line ratios, with respect to the CO(6–5) line, vs. F_X. The x-axis is F_X (for $r = 250$ pc), in units of erg s^{-1} cm^{-2}. The y-axis is the luminosity ratio $L'_{CO(J \to J-1)}/L'_{CO(6 \to 5)}$ to the CO(6–5) line. Data points and lines are described in Figure A.5.
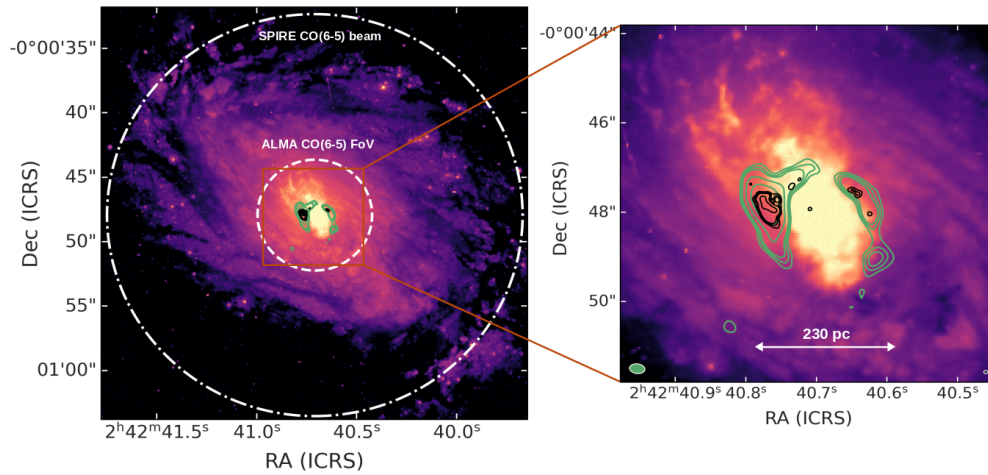
Figure A.9: *Left panel:* HST WFPC2 F606W image of NGC 1068 (from Malkan et al. 1998) with superimposed the contours of two ALMA CO(6–5) observations, in green at the resolution of 250 mas (project 2011.0.00083.S, PI: García-Burillo), in black of 90 mas (project 2013.1.00014.S, PI: Elitzur). Both the contours are at the respective $(3, 4, 5, 10, 20) \times \sigma$, where $\sigma = 6.2$ Jy beam^{-1} km s^{-1} for the green lines and $\sigma = 1.1$ Jy beam^{-1} km s^{-1} for the black lines. The inner white dashed circle indicates the FoV of both ALMA observations, with a radius of $4\farcs3$ (~340 pc), while the outer dash-dotted circle represents the *Herschel*/SPIRE-FTS beam FWHM for CO(6–5) observations, with a $15\farcs6$ radius. *Right panel:* zoom of the inner 670 pc. Restored ALMA beams of the 250 and 90 mas images are shown as ellipses with white edges, at the bottom left (with the green area) and right (with the black area), respectively. The 250 mas ALMA image has not been primary-beam corrected.
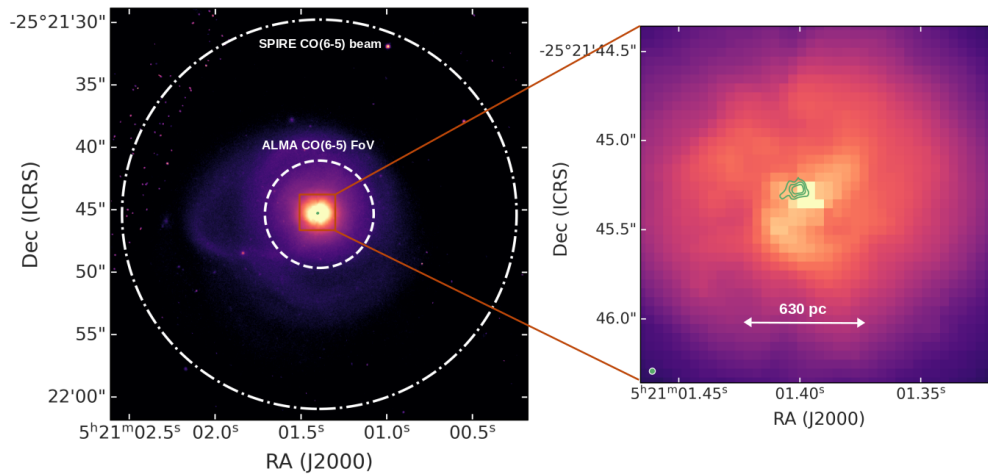
Figure A.10: *Left panel:* HST ACS F814W image of IRAS F05189–2524 (from Evans 2005), with superimposed, in green, the contours of ALMA CO(6–5) moment 0 at the resolution of 40 mas (project 2016.1.01223.S, PI: Baba). The contours are drawn at $(3, 4, 5, 10, 20) \times \sigma$, where $\sigma = 0.55$ Jy beam^{-1} km s^{-1}. The inner white dashed circle indicates the FoV of both ALMA observations, with a radius of $4\farcs3$ (~3.6 kpc), while the outer dash-dotted circle represents the *Herschel*/SPIRE-FTS beam FWHM for CO(6–5) observations, with a $15\farcs6$ radius. *Right panel:* zoom of the inner 1.7 kpc. The restored ALMA beam is shown as a green ellipse with white edges at the bottom left.
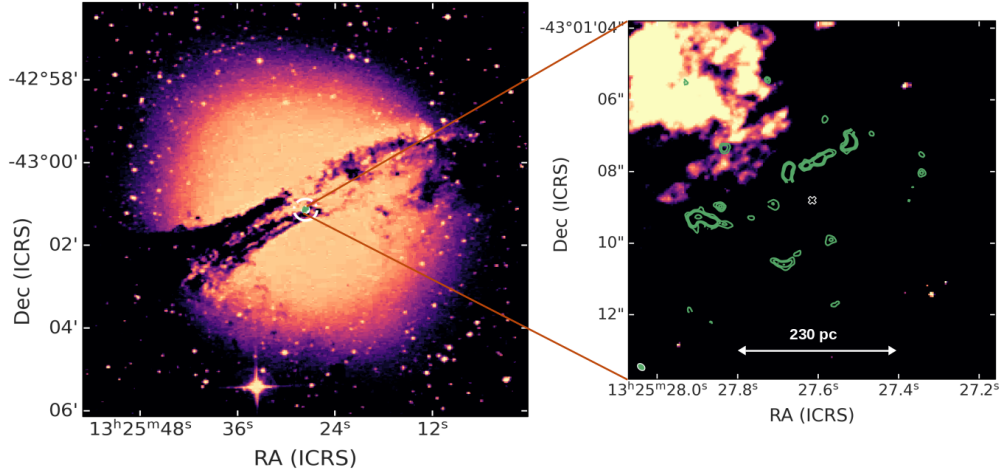
Figure A.11: *Left panel:* DSS-2 B-band image of NGC 5128. The inner white dashed circle indicates the FoV of both ALMA observations, with a radius of $4\rlap{.}''3$ ($\sim$160 pc), while the outer dash-dotted circle represents the *Herschel*/SPIRE-FTS beam FWHM for CO(6–5) observations, with a $15\rlap{.}''6$ radius. *Right panel:* zoom of the inner 380 pc, with HST WFPC2 F555W image of NGC 5128 (from Marconi et al. 2000) in the background, with superimposed, in green, the contours of ALMA CO(6–5) moment 0 at the resolution of 170 mas (project 2012.1.00225.S, PI: Espada). The contours are drawn at (3, 4, 5, 10, 20) $\times \sigma$, where $\sigma = 0.42$ Jy beam^{-1} km s^{-1}. The restored ALMA beam is shown as a green ellipse with white edges at the bottom left. A "X" marker, black with white edges, indicates the center of the galaxy.
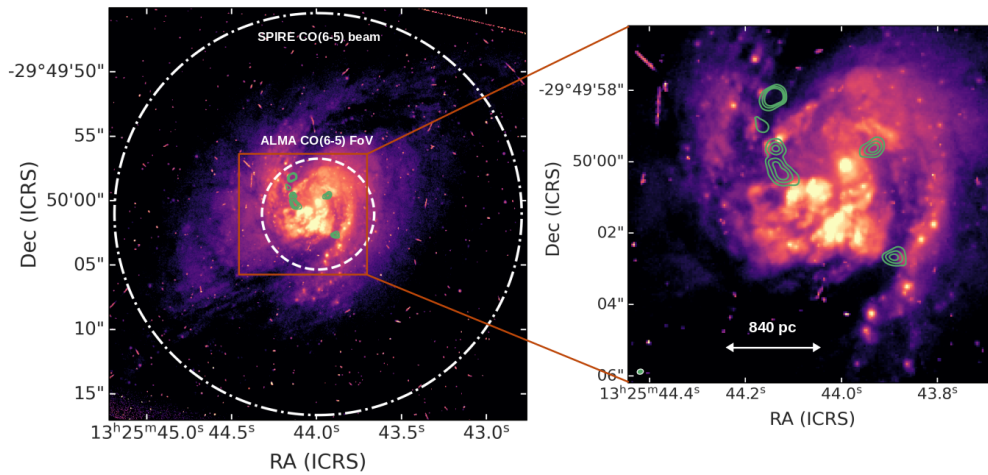
Figure A.12: *Left panel:* HST WFPC2 F606W image of NGC 5135 (from Malkan et al. 1998), with superimposed, in green, the contours of ALMA CO(6–5) moment 0 at the resolution of 170 mas (project 2013.1.00524.S, PI: Lu). The contours are drawn at (3, 4, 5, 10, 20) $\times \sigma$, where $\sigma = 1.2$ Jy beam^{-1} km s^{-1}. The inner white dashed circle indicates the FoV of both ALMA observations, with a radius of $4\rlap{.}''3$ ($\sim$1.2 kpc), while the outer dash-dotted circle represents the *Herschel*/SPIRE-FTS beam FWHM for CO(6–5) observations, with a $15\rlap{.}''6$ radius. *Right panel:* zoom of the inner 2.5 kpc. The restored ALMA beam is shown as a green ellipse with white edges at the bottom left.
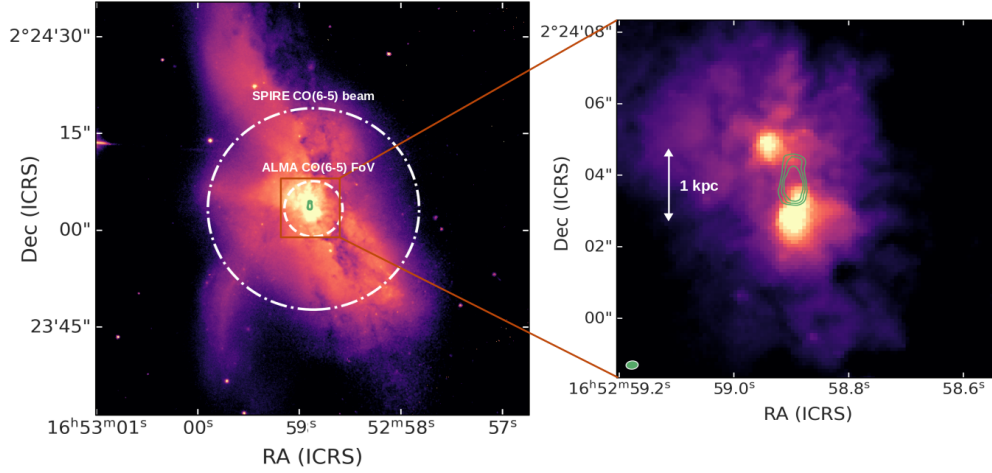
Figure A.13: *Left panel:* HST WFPC2 F814W image of NGC 6240 (from Gerssen et al. 2004), with superimposed, in green, the contours of ALMA CO(6–5) moment 0 at the resolution of 250 mas (project 2015.1.00658.S, PI: Rangwala). The contours are drawn at (3, 4, 5, 10, 20) $\times \sigma$, where $\sigma = 29$ Jy beam^{-1} km s^{-1}. The inner white dashed circle indicates the FoV of both ALMA observations, with a radius of 4$\farcs$3 ($\sim$2.1 kpc), while the outer dash-dotted circle represents the *Herschel*/SPIRE-FTS beam FWHM for CO(6–5) observations, with a 15$\farcs$6 radius. *Right panel:* zoom of the inner 4.5 kpc. The restored ALMA beam is shown as a green ellipse with white edges at the bottom left.
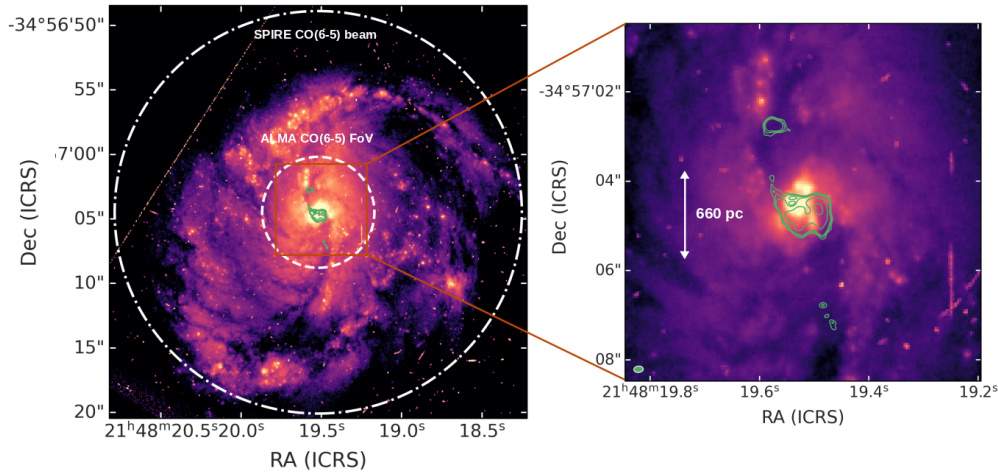
Figure A.14: *Left panel:* HST WFPC2 F606W image of NGC 7130 (from Malkan et al. 1998), with superimposed, in green, the contours of ALMA CO(6–5) moment 0 at the resolution of 180 mas (project 2013.1.00524.S, PI: Lu). The contours are drawn at (3, 4, 5, 10, 20) $\times \sigma$, where $\sigma = 1.5$ Jy beam^{-1} km s^{-1}. The inner white dashed circle indicates the FoV of both ALMA observations, with a radius of 4$\farcs$3 ($\sim$1.4 kpc), while the outer dash-dotted circle represents the *Herschel*/SPIRE-FTS beam FWHM for CO(6–5) observations, with a 15$\farcs$6 radius. *Right panel:* zoom of the inner 2.3 kpc. The restored ALMA beam is shown as a green ellipse with white edges at the bottom left. This ALMA image has not been primary-beam corrected.

Appendix to Chapter 3

B.1 Update of observed fluxes for our sample

Reviewing the data contained in Chapter 2, we have found a better source for one CO line luminosity in one galaxy. The $CO(2-1)$ of NGC 1275 was taken, in Chapter 2, from Salomé et al. (2011), which was converted to $303^{+8}_{-8} \times 10^2$ $L_\odot$. Since this flux was observed, in Salomé et al. (2011), from a very small nuclear region of NGC 1275, we wanted to improve the measurement by finding another observation with a larger beam. Lazareff et al. (1989) observed the $CO(2-1)$ emission with the IRAM-30m telescope, which has a full-width at half maximum (FWHM) of $10\farcs5$, finding a larger $CO(2-1)$ luminosity of $15^{+3}_{-3} \times 10^4$ $L_\odot$. Throughout this paper we use this value, since it is the one with the larger beam we can find for this galaxy; in this way the $CO(2-1)$ beam is almost equal to the projected r_{CO} of the galaxy: $r_{CO} = 10\farcs9$.

B.2 Radial profiles of galaxies

In Figure B.1 we show the radial profiles of the molecular mass $M_{mol}(r)$, the volume $V_{mol}(r)$, the incident fluxes $G_0(r)$ and $F_X(r)$, and the intrinsic column density $N_H(r)$. $M_{mol}(r)$ has been recalculated with the best-fit α_{CO}. The radial profiles all follow the Equations (3.5) − (3.9).

B.3 Observed and modelled CO SLEDs for the whole galaxy sample

Figures B.2 - B.24 show the "Baseline model", and "$N_{H, \text{X-ray}}$ model" for each galaxy of the sample with orange and brown lines, respectively. The observed CO SLED is plotted
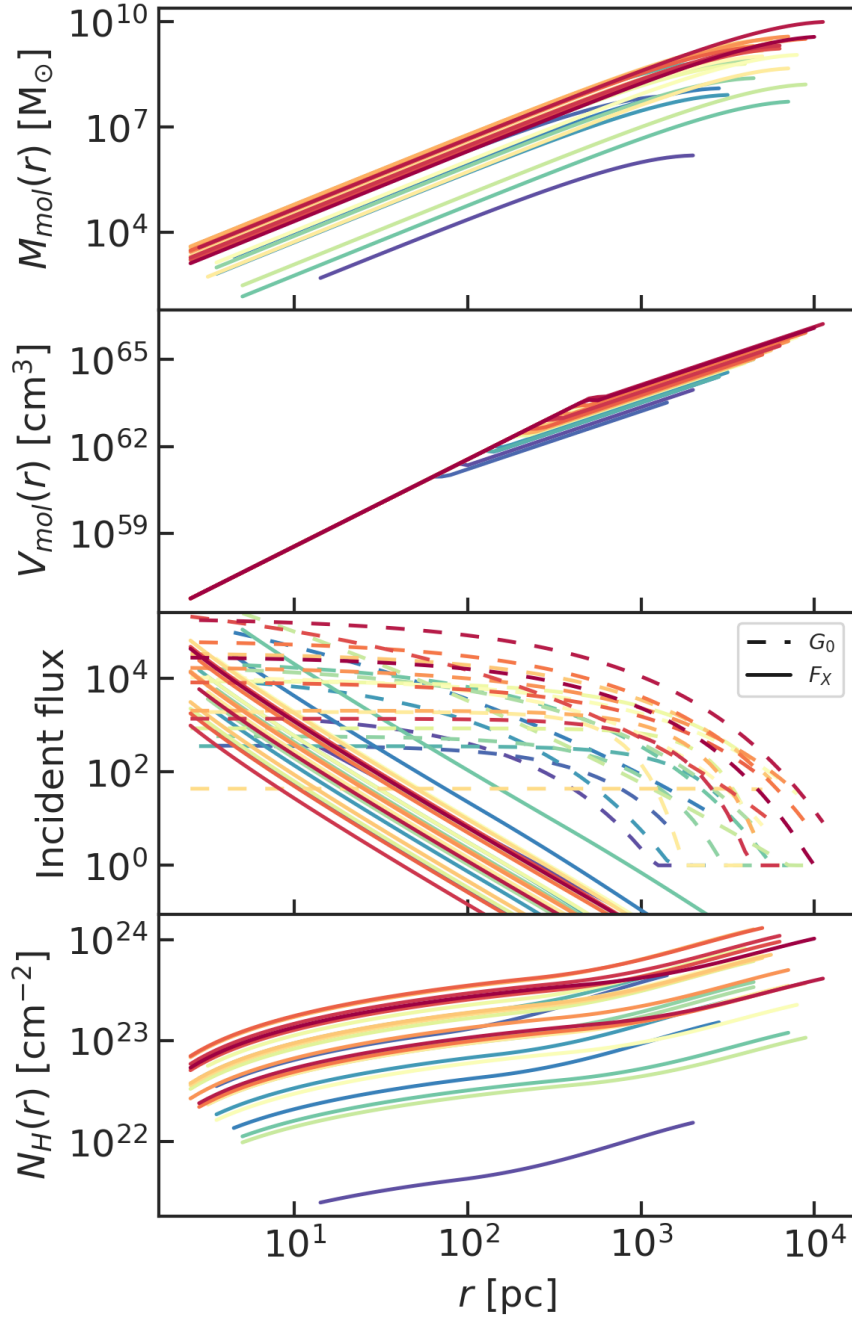
Figure B.1: Radial profiles of our sample of 24 galaxies, sorted by their total molecular mass when measured with a Milky Way α_{CO}. The four panels show, from top to bottom, the molecular mass $M_{mol}(r)$ (recalculated with the best-fit α_{CO}), the molecular volume $V_{mol}(r)$, the incident fluxes $G_0(r)$ and $F_X(r)$, and the "Baseline model" column density $N_H(r)$. $G_0(r)$ and $F_X(r)$ are in G_0 and erg s^{-1} cm^{-2} units and they are plotted with dashed and solid lines, respectively. Colors are the same as Figure 3.5.
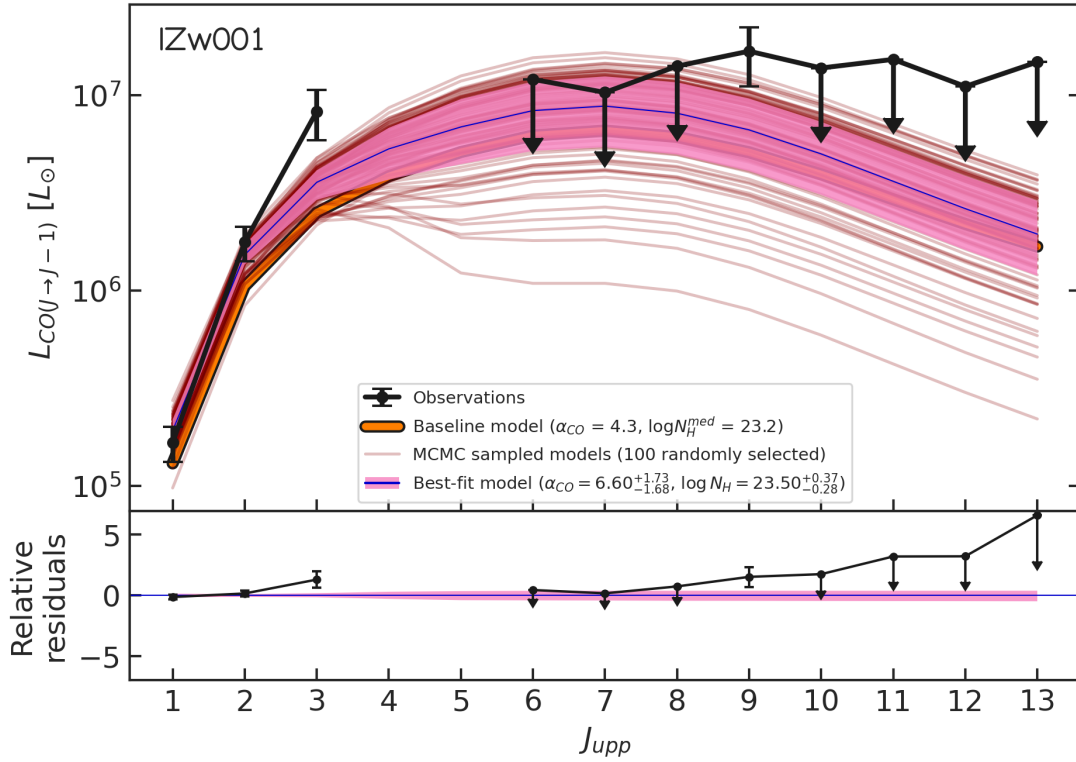
Figure B.2: I Zw 1 (UGC 545) CO SLEDs.

with a black line, with vertical bars representing measurement errors, and downward arrows indicating censored data points (i.e. upper limits). We randomly select, from the posterior distributions of the model parameters α_{CO} and $\log N_H$, 100 different modelled CO SLEDs, plotted in red. The blue lines and pink shadings, are the modelled CO SLEDs with the median and 1σ spread of the model parameters posterior distributions, respectively; we call "Best-fit model" the one with the median values of α_{CO} and $\log N_H$. For each galaxy, the bottom panels of Figures B.2 - B.24 show in black the relative residuals, calculated as the difference between observations and best fit model, divided by the latter; the best-fit model is the blue line (fixed at 0), with the 1σ spread in pink shading.
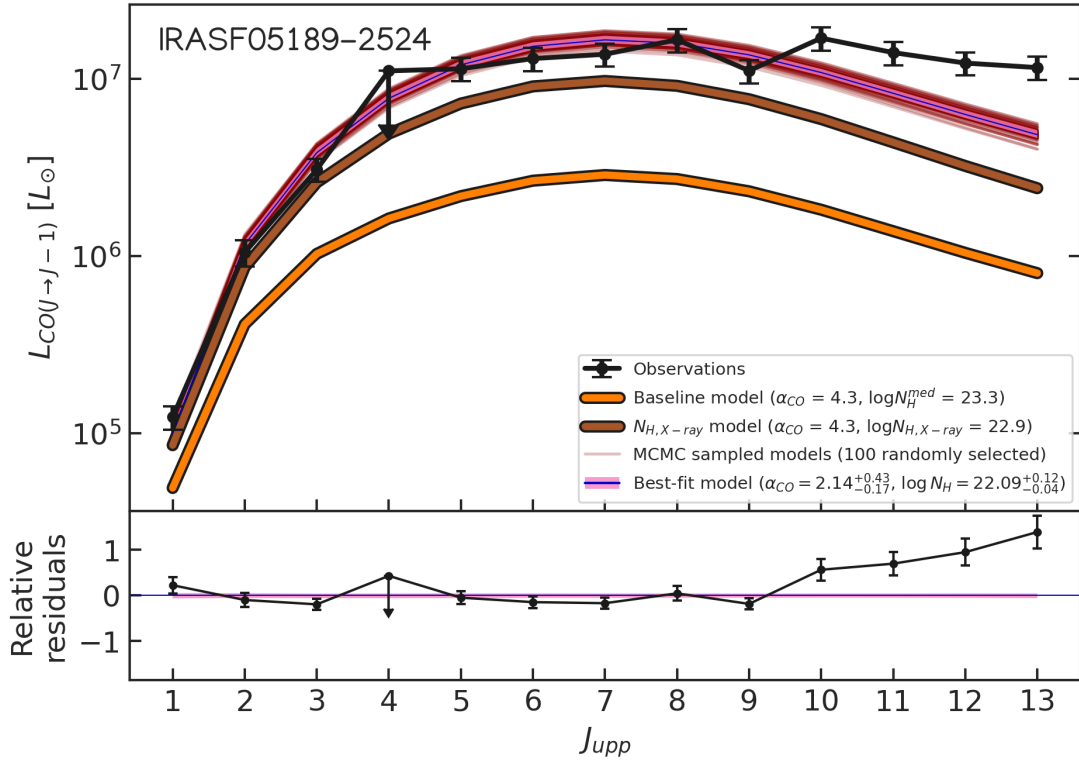
Figure B.3: IRAS F05189−2524 CO SLEDs.
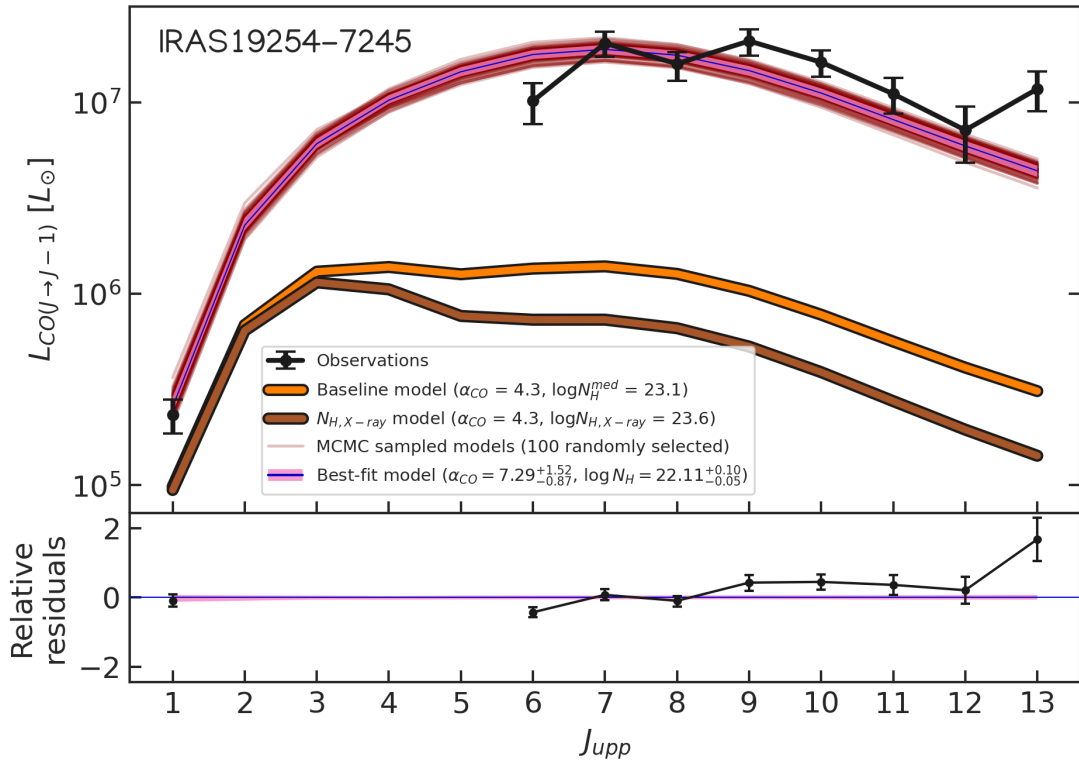
Figure B.4: IRAS 19254−7245 (Superantennae) CO SLEDs.
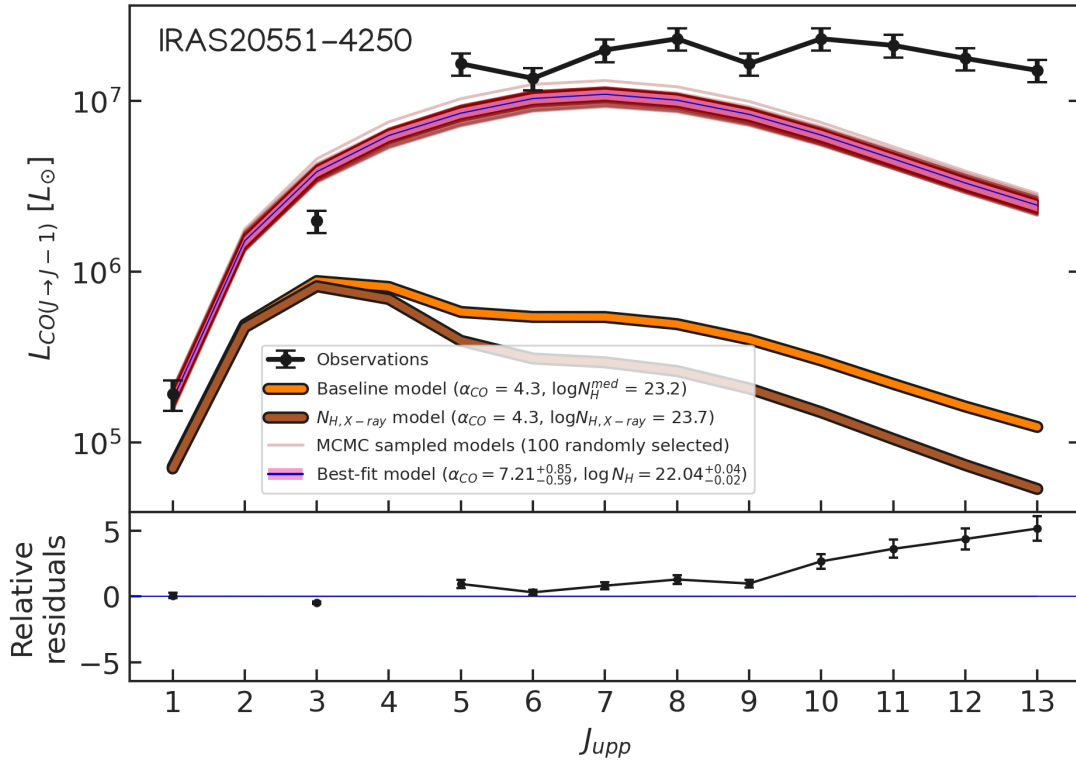
Figure B.5: IRAS 20551−4250 (ESO 286−IG019) CO SLEDs.
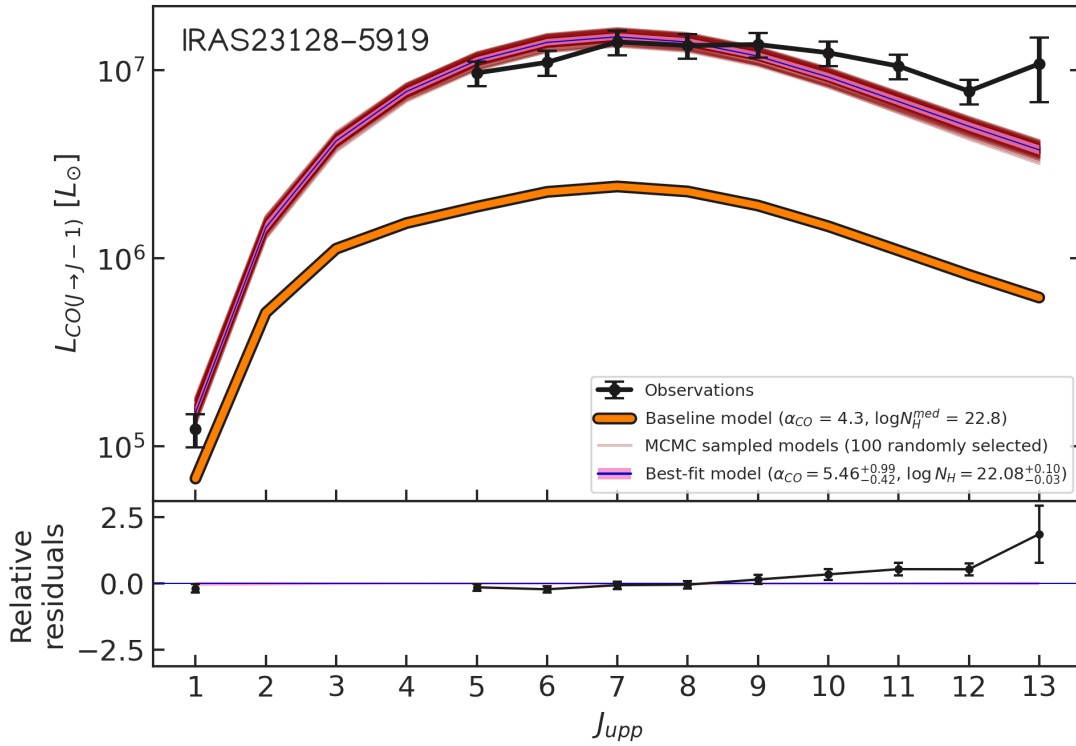
Figure B.6: IRAS 23128−5919 (ESO 148−IG002) CO SLEDs.
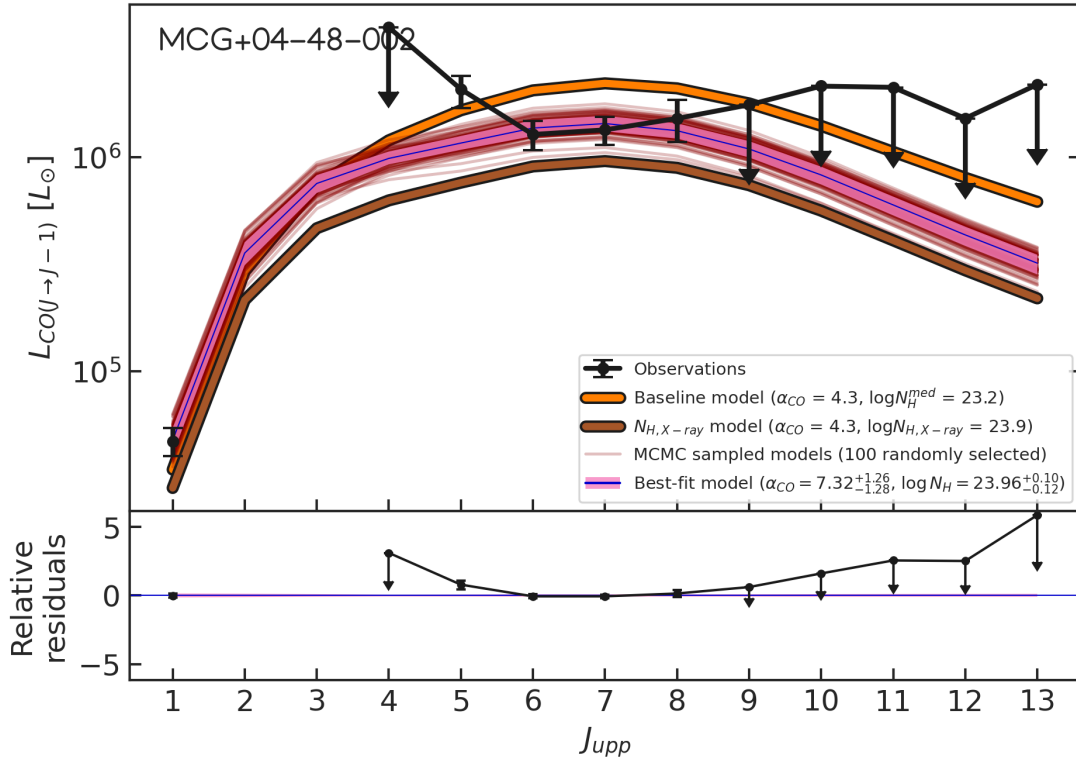
Figure B.7: MCG +04−48−002 CO SLEDs.
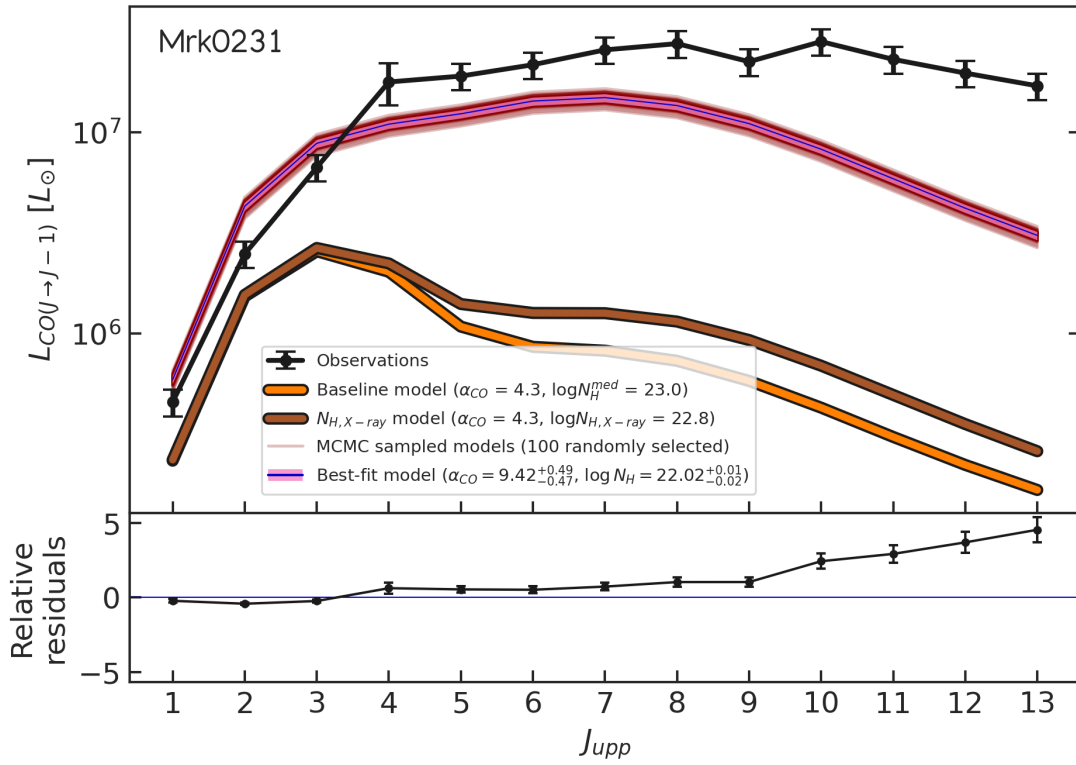
Figure B.8: Mrk 231 CO SLEDs.
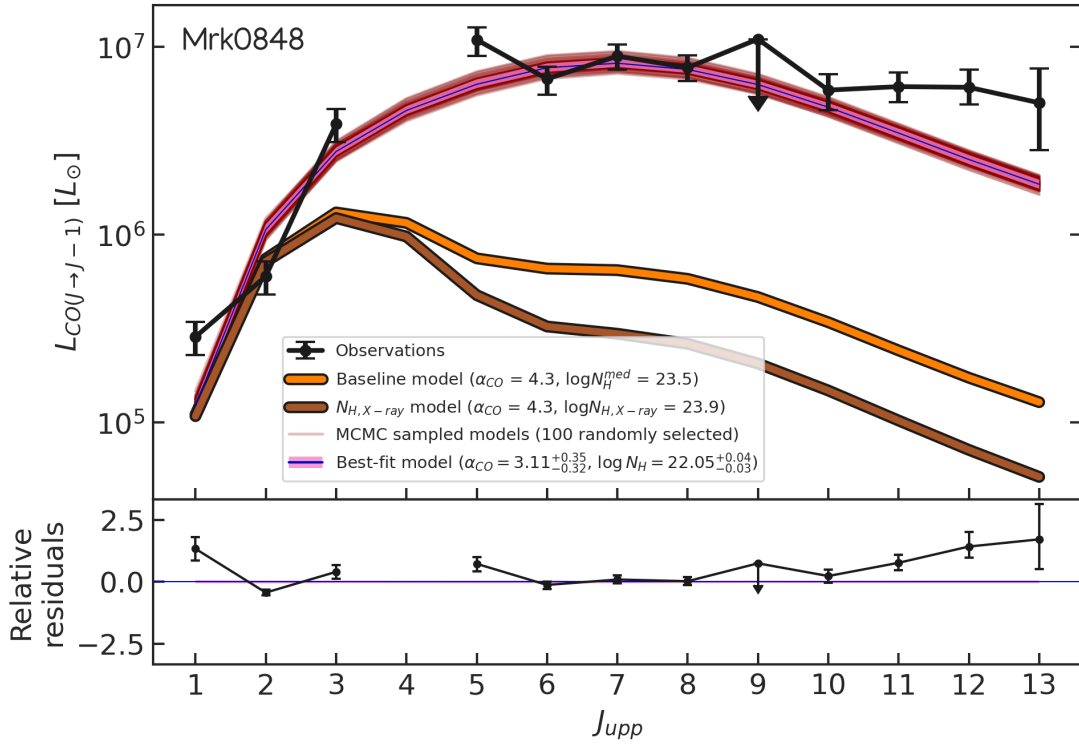
Figure B.9: Mrk 848 (VV 705) CO SLEDs.
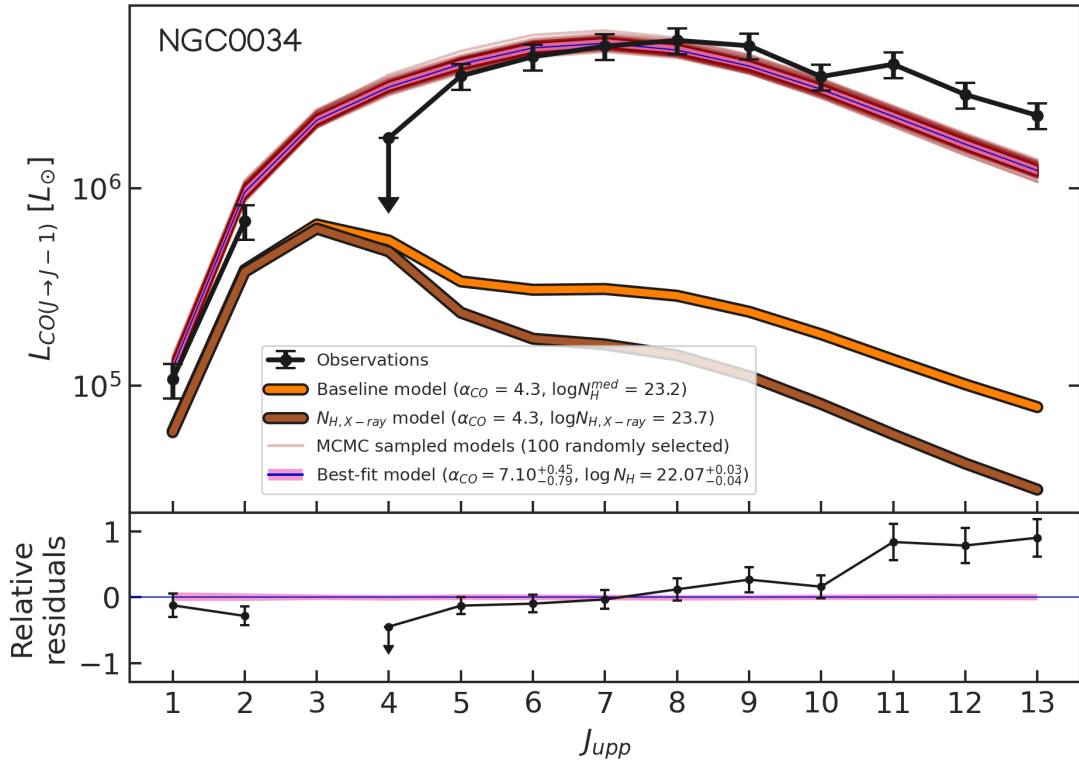
Figure B.10: NGC 34 (Mrk 938) CO SLEDs.
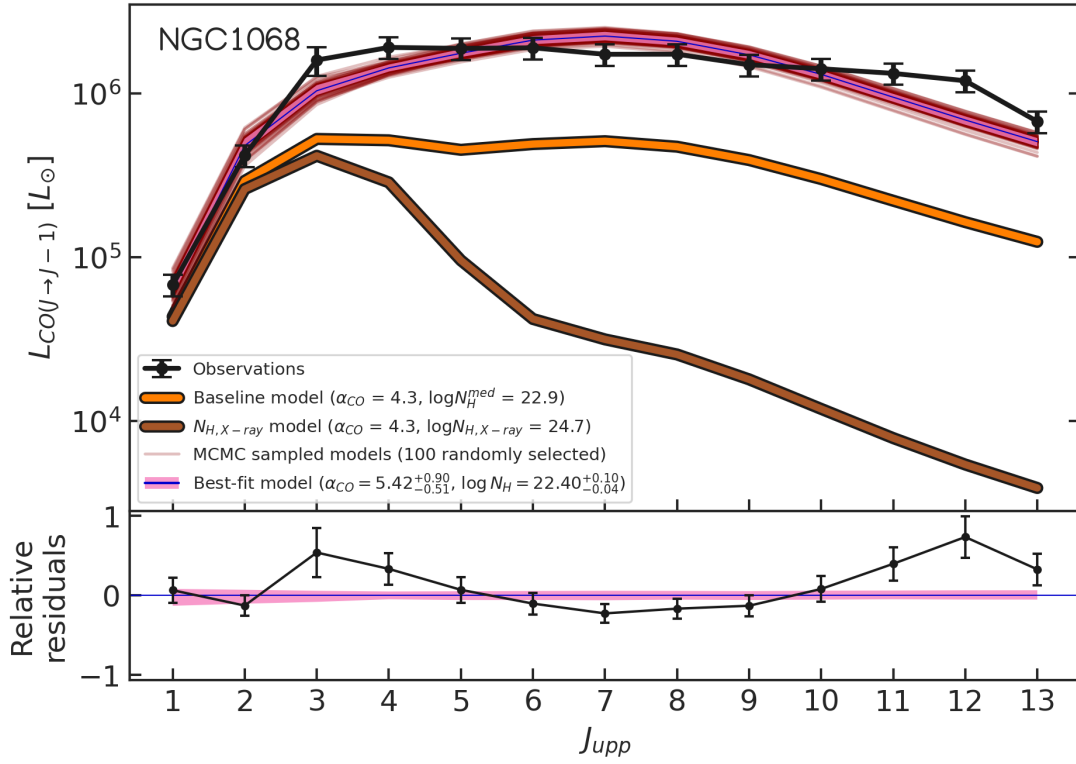
Figure B.11: NGC 1068 (M77) CO SLEDs.
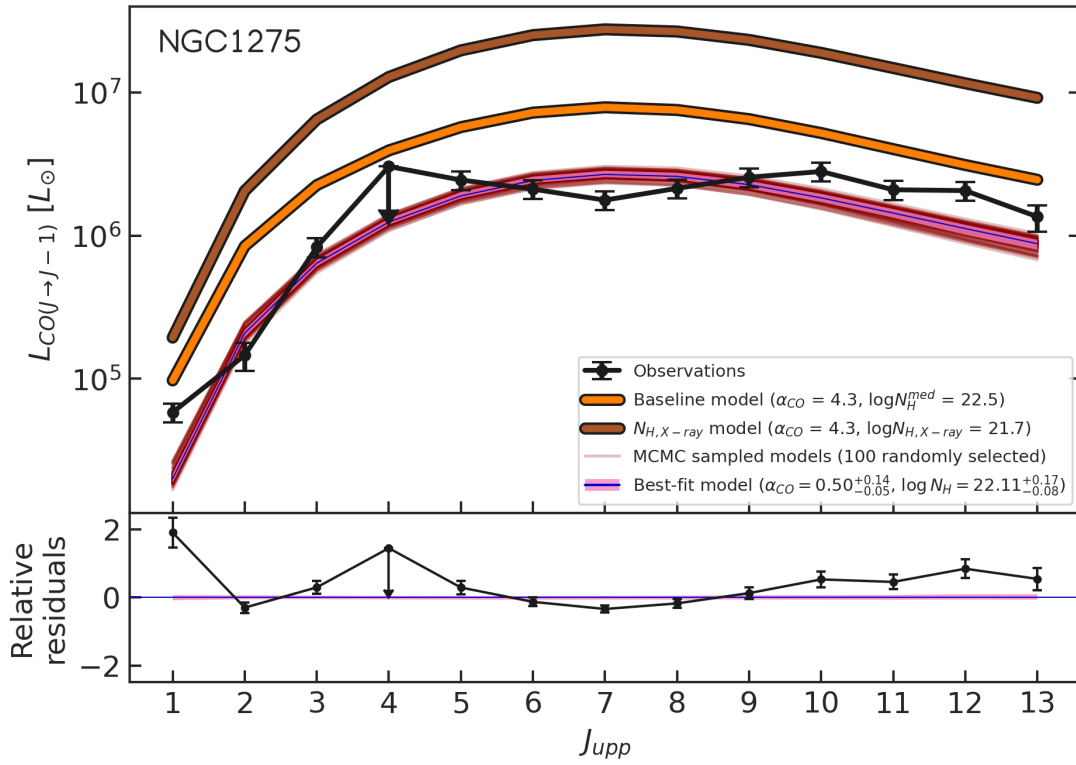
Figure B.12: NGC 1275 (3C84, Perseus A) CO SLEDs.
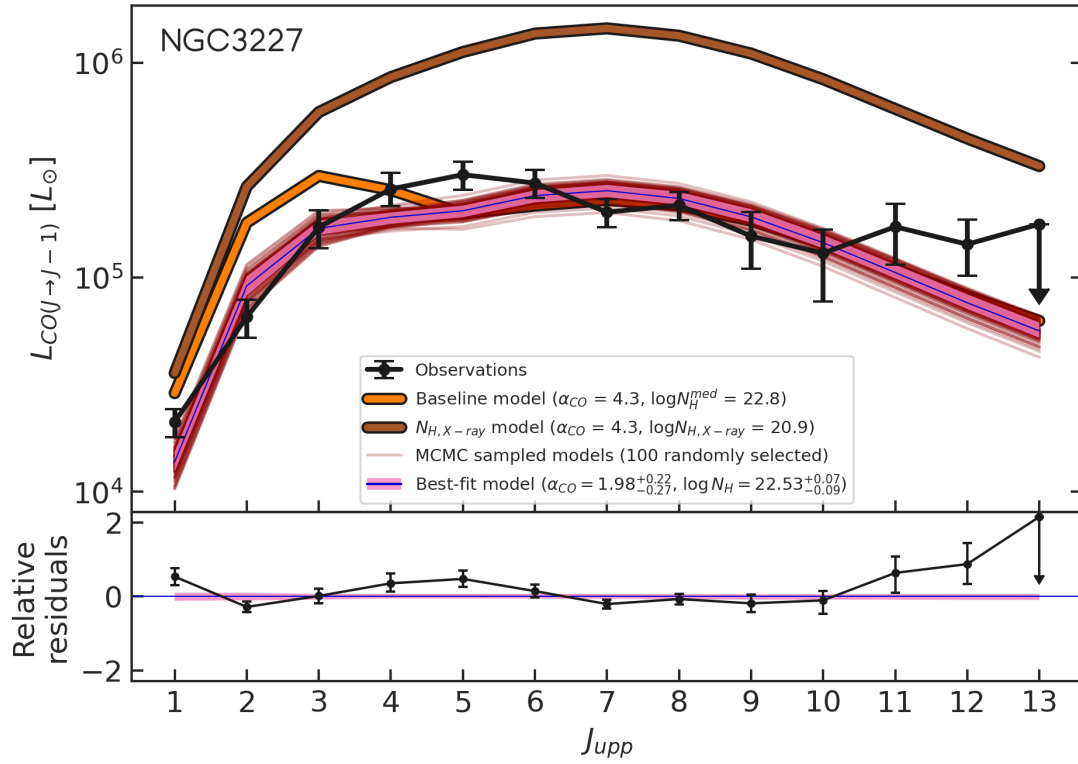
Figure B.13: NGC 3227 CO SLEDs.
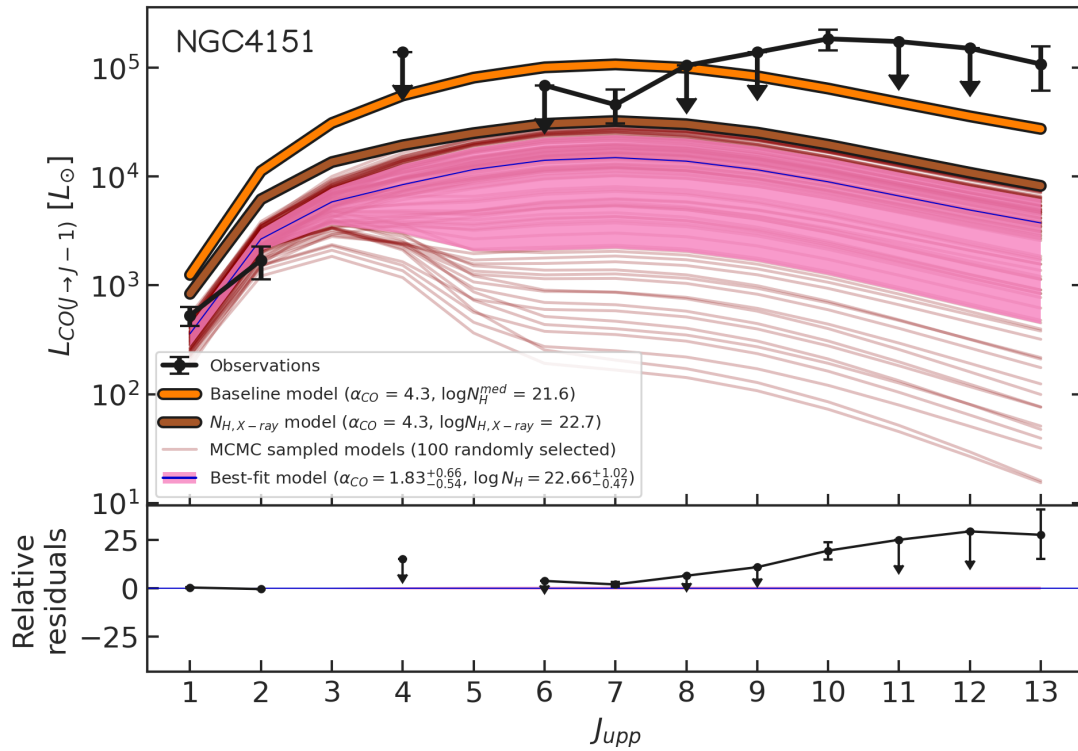
Figure B.14: NGC 4151 CO SLEDs.
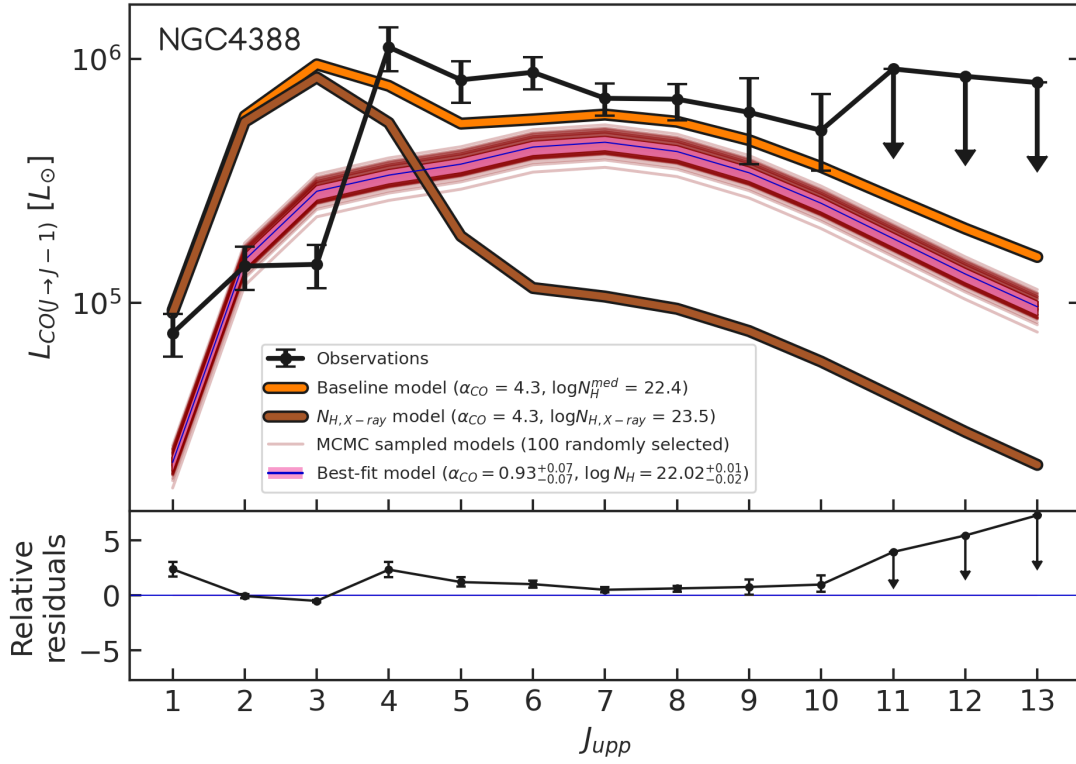
Figure B.15: NGC 4388 CO SLEDs.
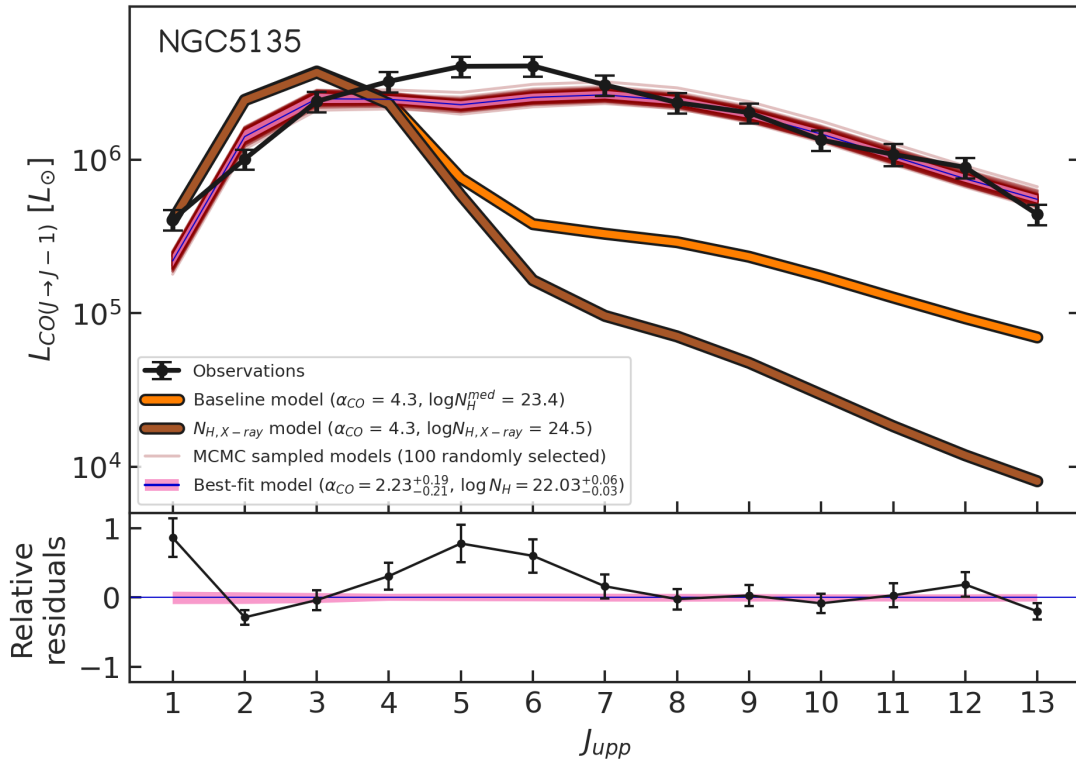
Figure B.16: NGC 5135 CO SLEDs.
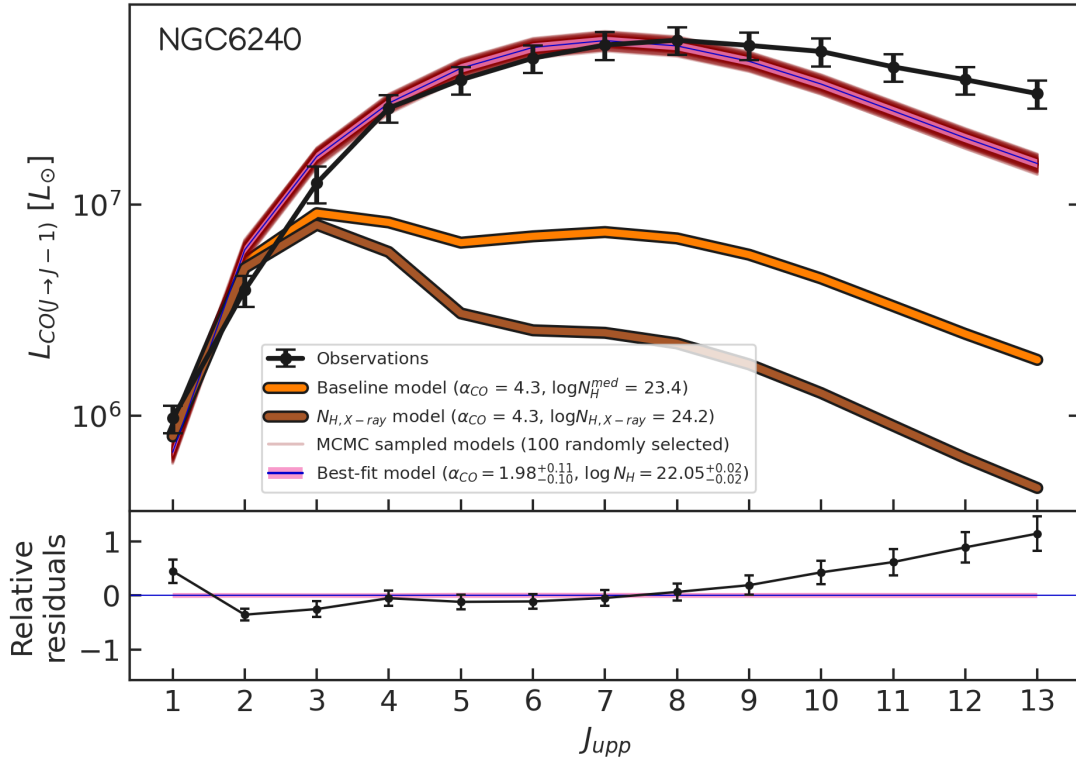
Figure B.17: NGC 6240 CO SLEDs.
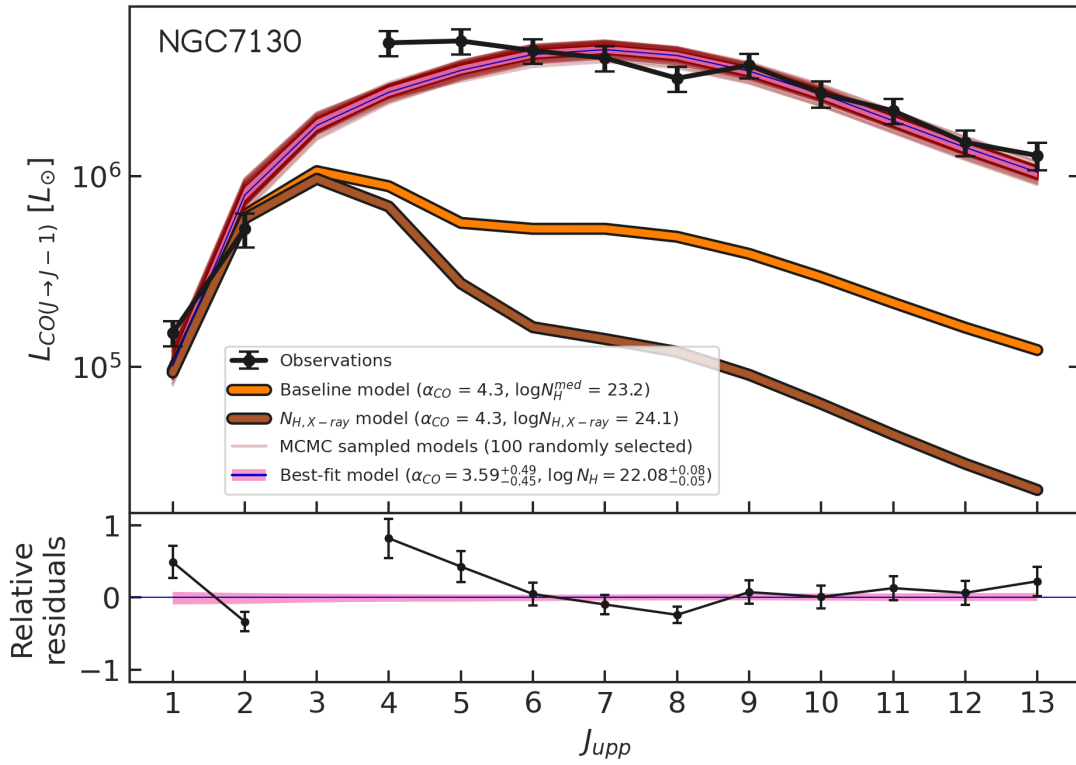
Figure B.18: NGC 7130 CO SLEDs.
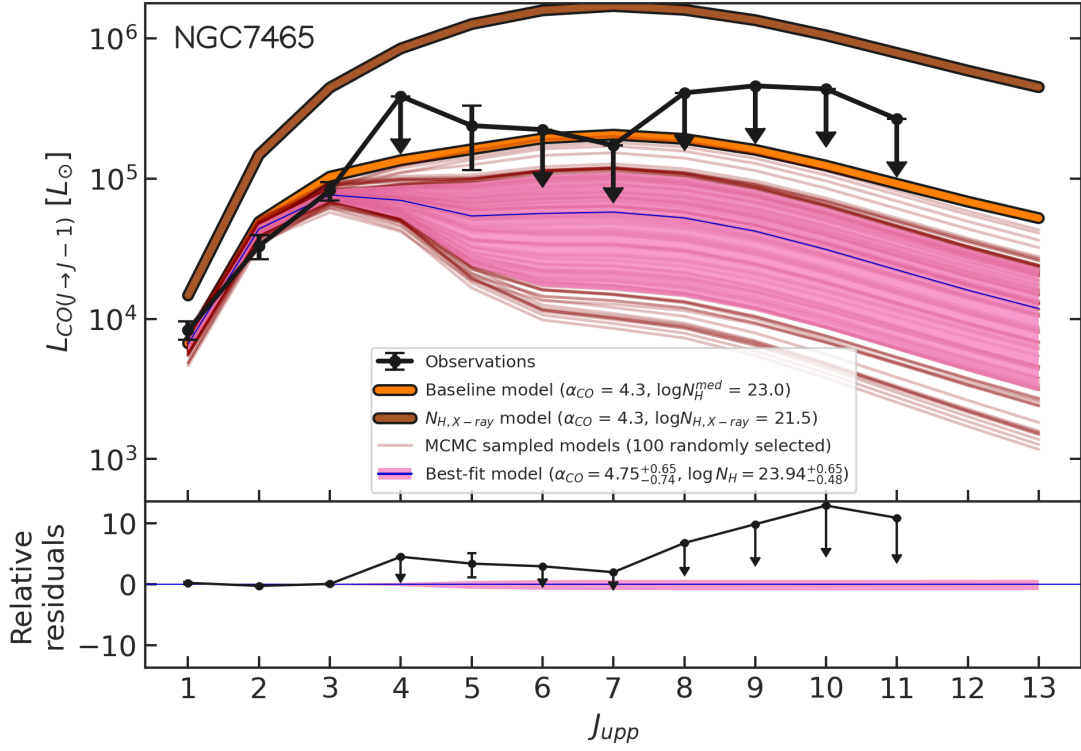
Figure B.19: NGC 7465 CO SLEDs.
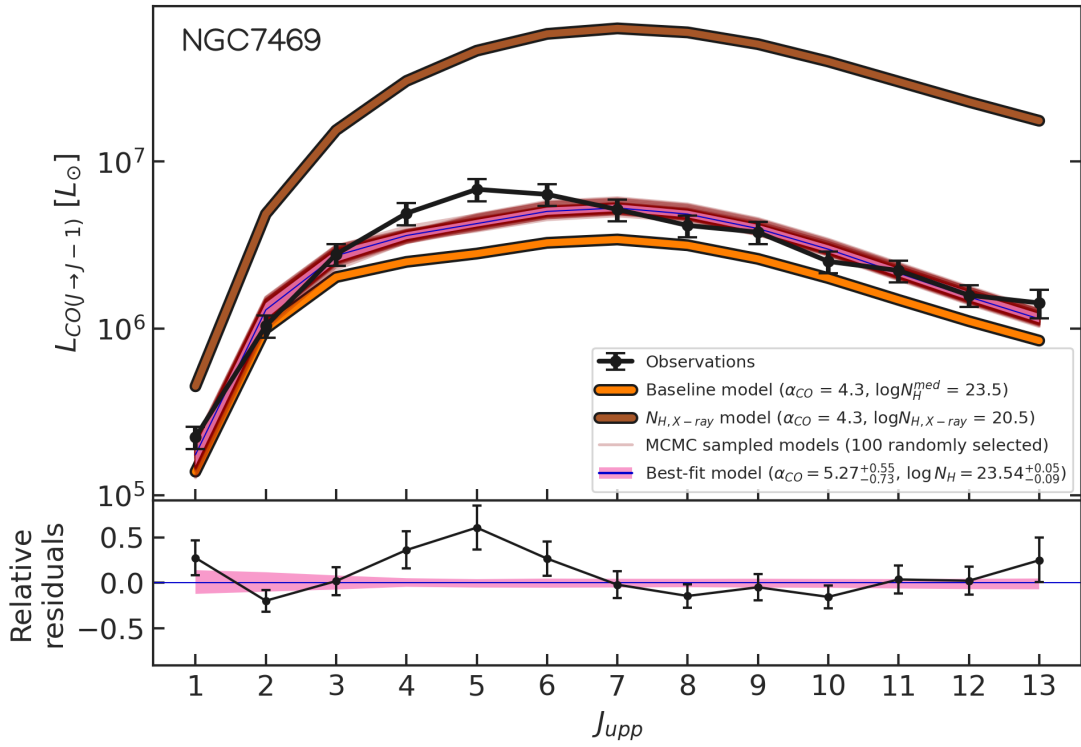
Figure B.20: NGC 7469 CO SLEDs.
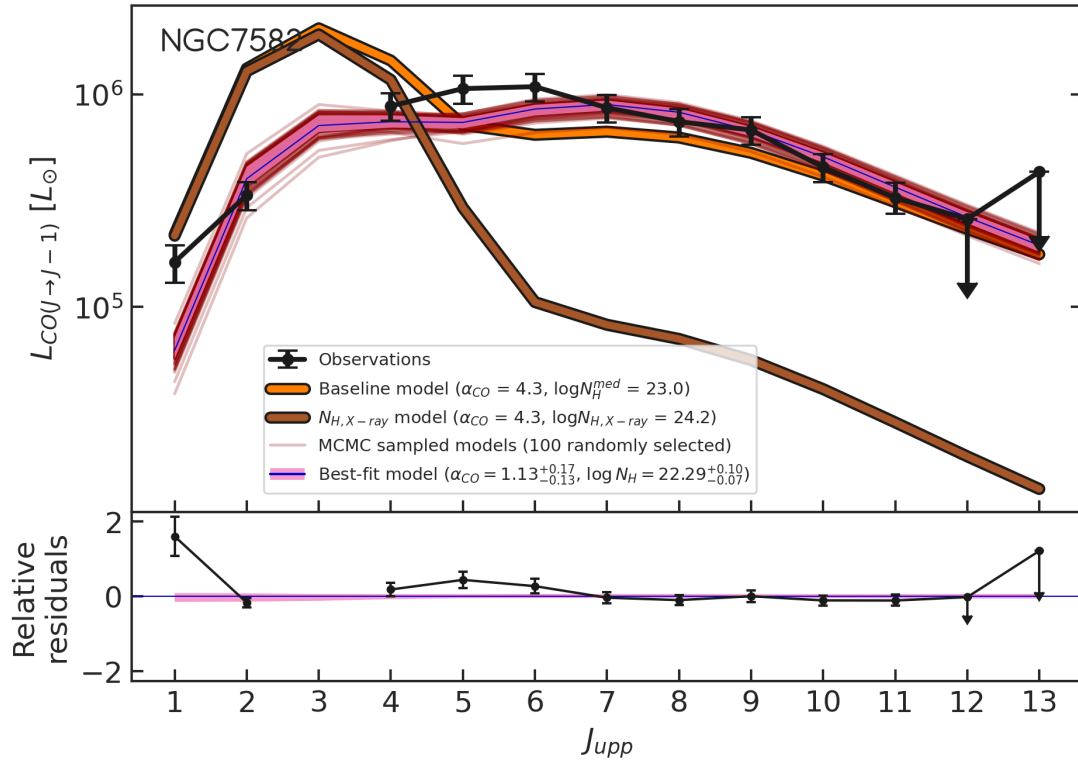
Figure B.21: NGC 7582 CO SLEDs.
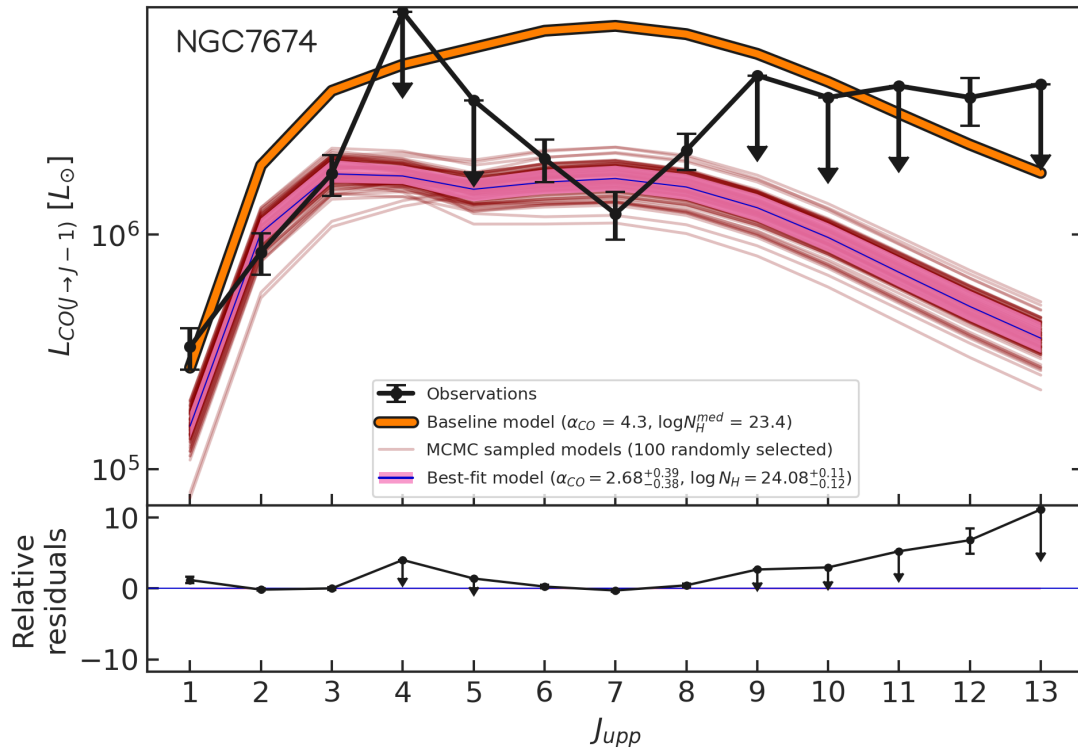
Figure B.22: NGC 7674 (Mrk 533) CO SLEDs.
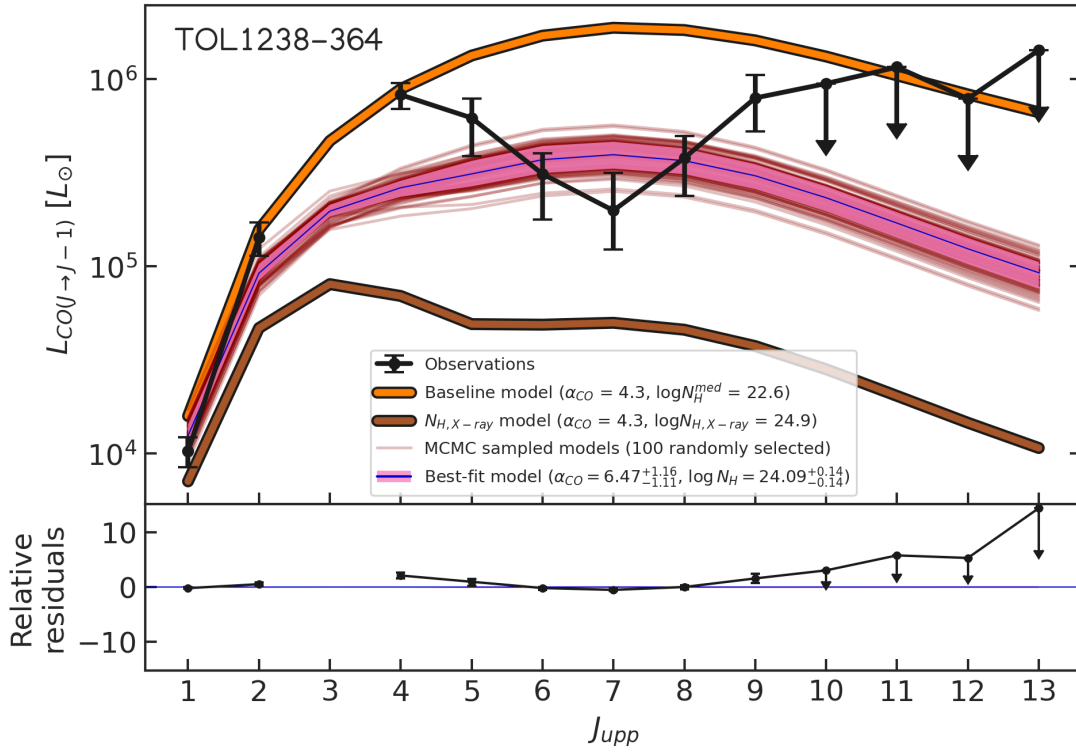
Figure B.23: TOL 1238-364 (IC 3639) CO SLEDs.
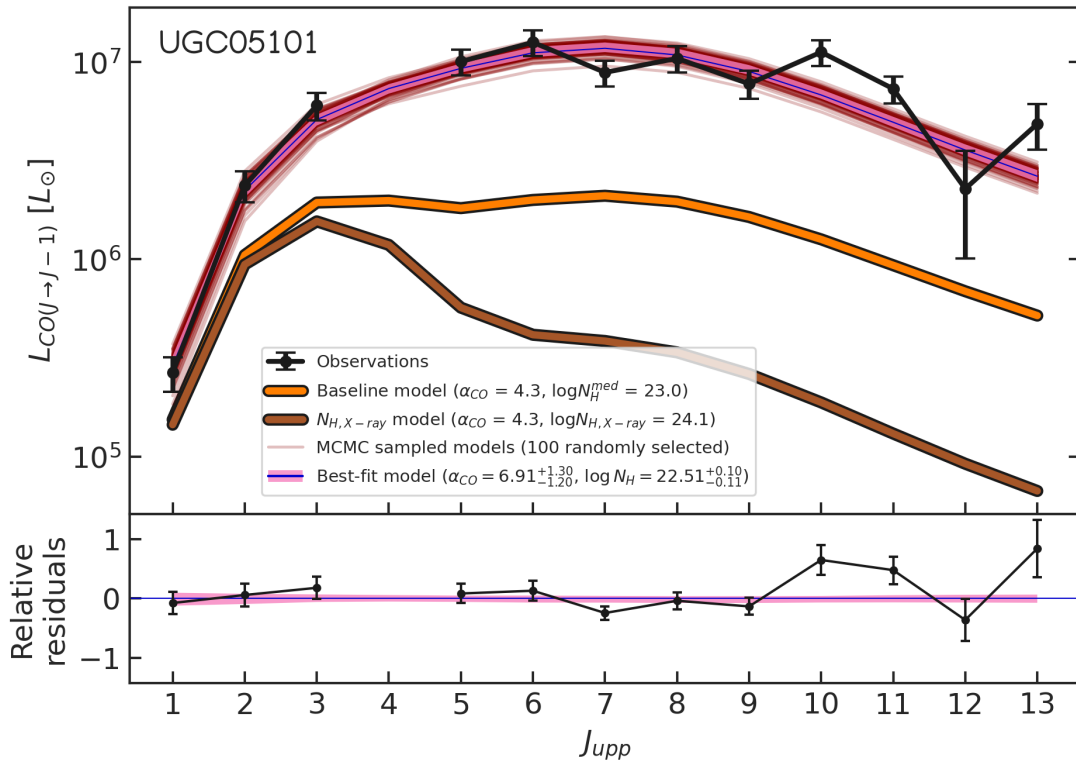
Figure B.24: UGC 5101 CO SLEDs.

C.1 Goodness of ALUCINE fit

See Figure C.1.

C.2 Gaussian decomposition of MEGARA lines

See Figures C.2, C.3, C.4, C.5, and C.6.

C.3 BPT diagrams of MEGARA lines

See Figures C.7, C.8 and C.9.
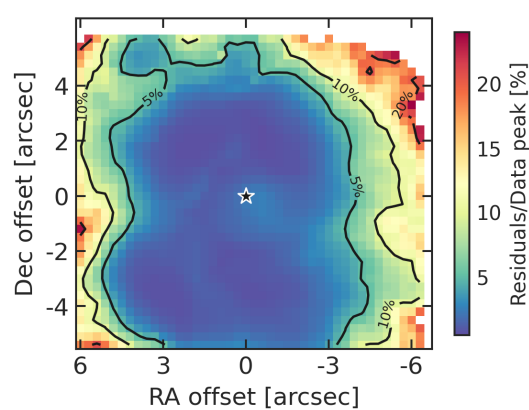
Figure C.1: Residuals of the [OIII] ALUCINE fit (defined as —observations - model—) divided by the observed peak flux, in every spaxel, in percentage.
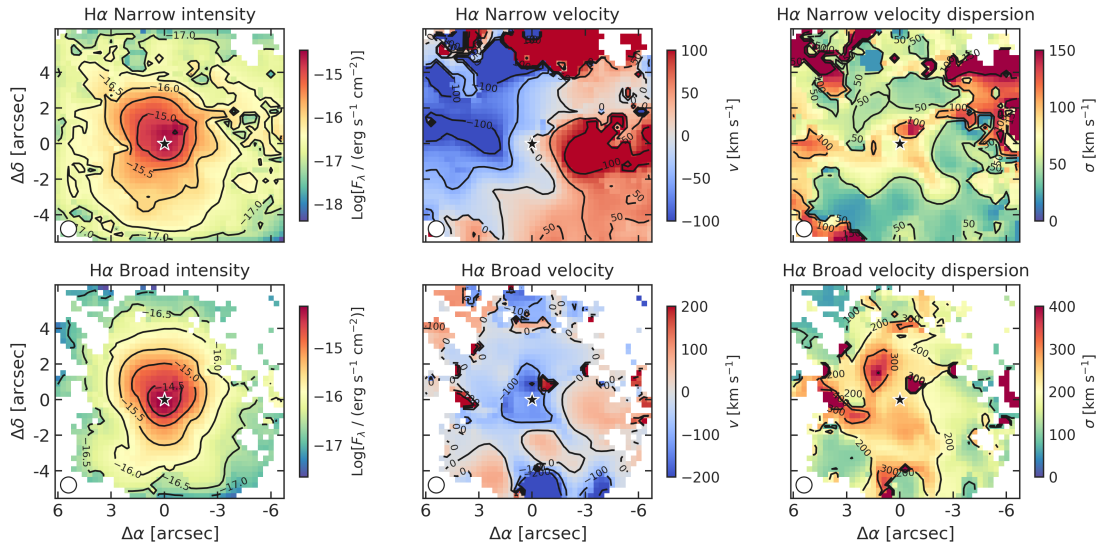
Figure C.2: Gaussian decomposition made by ALUCINE for the Hα line. Top and bottom panels are for narrow and broad component, respectively, while in the three columns, from left to right, are the intensity, velocity, and velocity dispersion maps. The AGN position is marked with a black star symbol, and distances are measured from it. The white circle in the bottom left is the MEGARA seeing conditions.
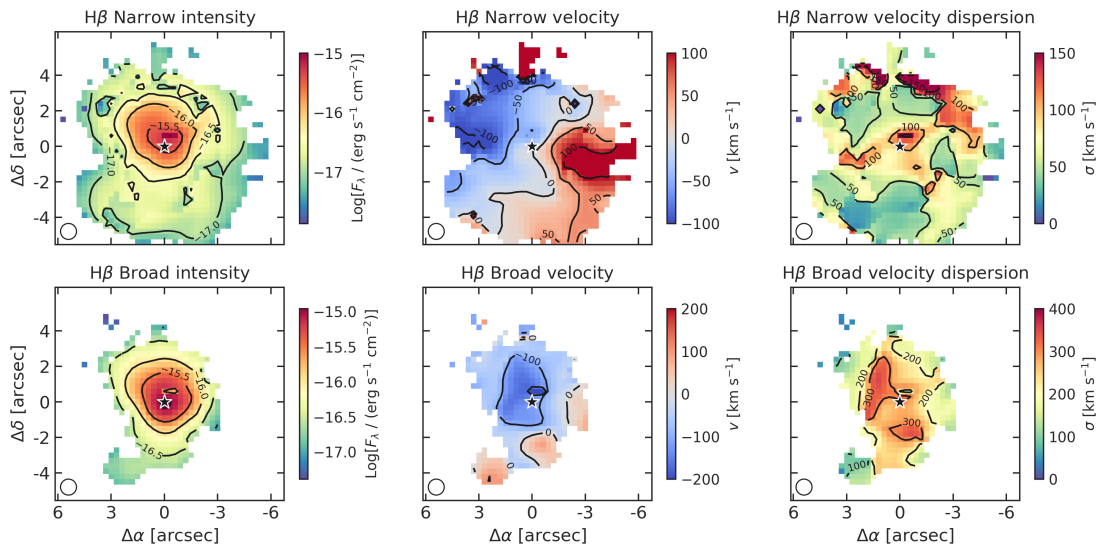
Figure C.3: Same as Figure C.2, but for the Hβ line.
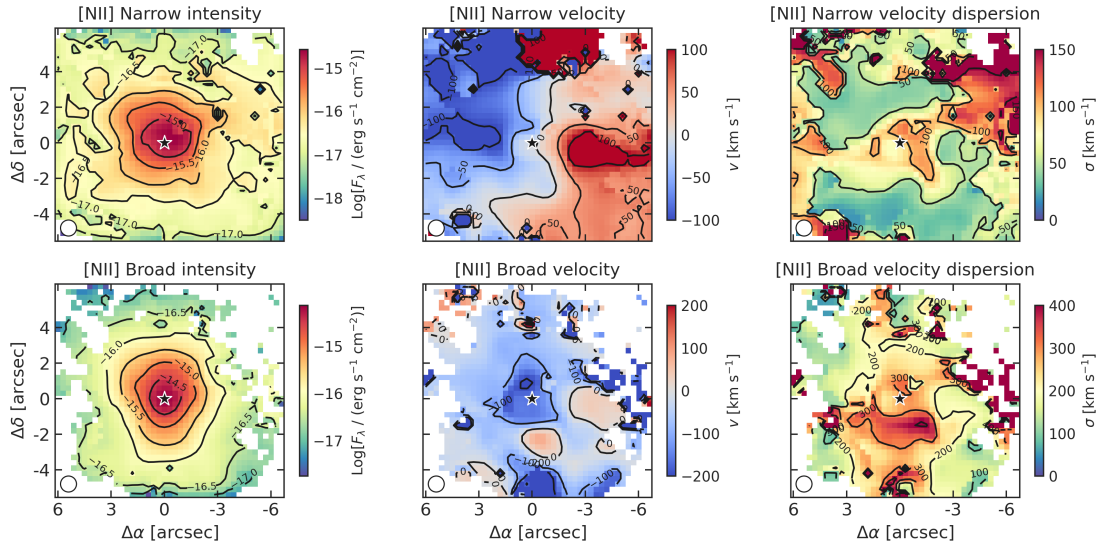
Figure C.4: Same as Figure C.2, but for the [NII]$\lambda\lambda6548, 6583$ doublet. The intensity maps show the sum of the two lines of the doublet, while the kinematics are assumed to be the same between the two lines. The [NII] emission is fitted together with the blended Hα line (Figure C.2) to properly separate their kinematics.
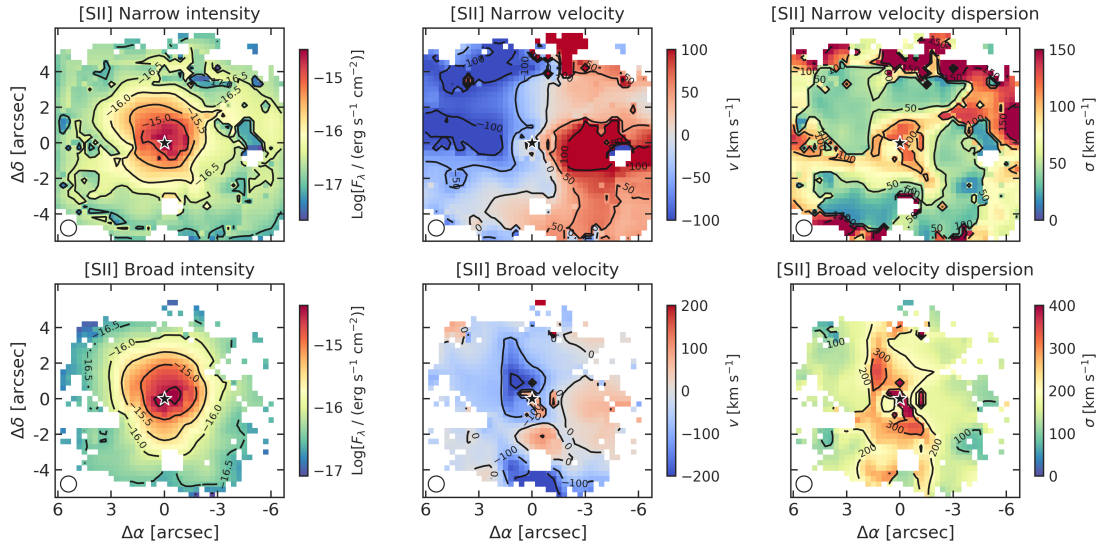
Figure C.5: Same as Figure C.2, but for the [SII]$\lambda\lambda6716, 6731$ doublet. The intensity maps show the sum of the two lines of the doublet, while the kinematics are assumed to be the same between the two lines.
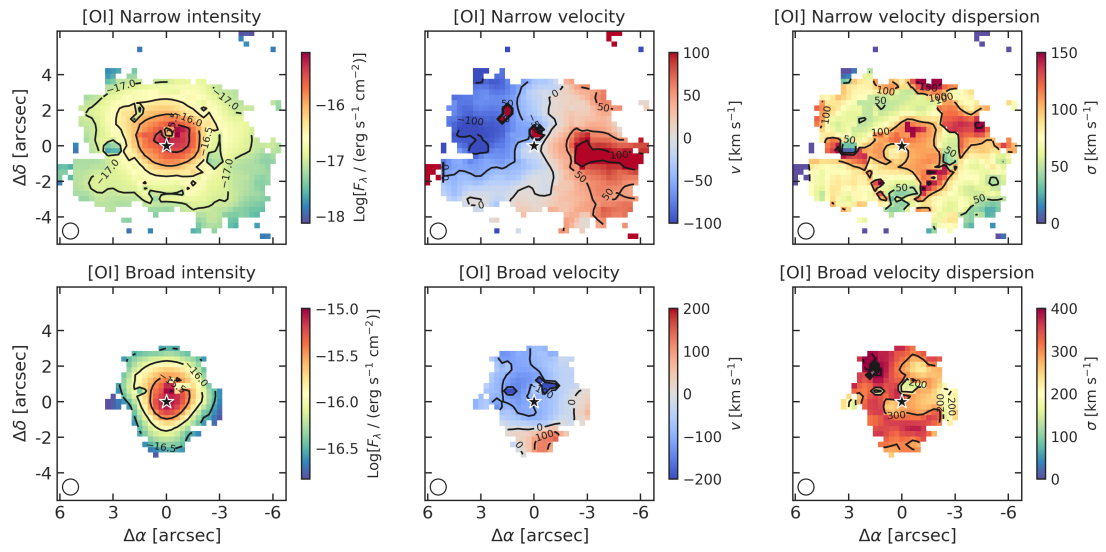
Figure C.6: Same as Figure C.2, but for the [OI]λ6300 line.

C.4 Mean velocities radial profiles of all MEGARA lines

See Figure C.10.
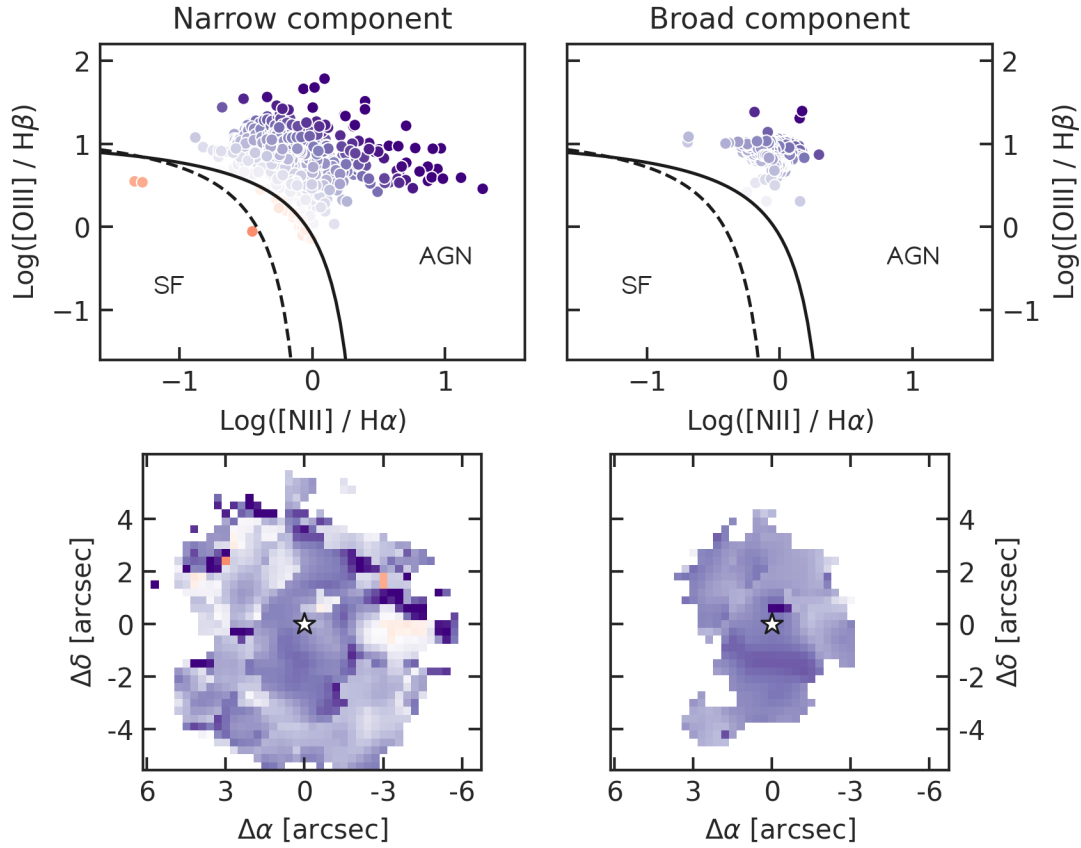
Figure C.7: Diagnostic Baldwin, Phillips, Telervich (BPT) diagram (Baldwin et al., 1981; Veilleux & Osterbrock, 1987) of [OIII]/Hβ vs. [NII]/Hα line ratios, for the narrow (*left panels*) and broad (*right panels*) components of the ionised gas. Solid and dashed black lines are empirical curves derived by Kewley et al. (2001) and Kauffmann et al. (2003), that separate different excitation mechanisms, marked on the plots as SF (star formation) and AGN. The spaxels are colored depending on their distance from the separation lines, and are plotted with the same colours in the spatially-resolved maps (bottom panels). The black star marks the AGN position.
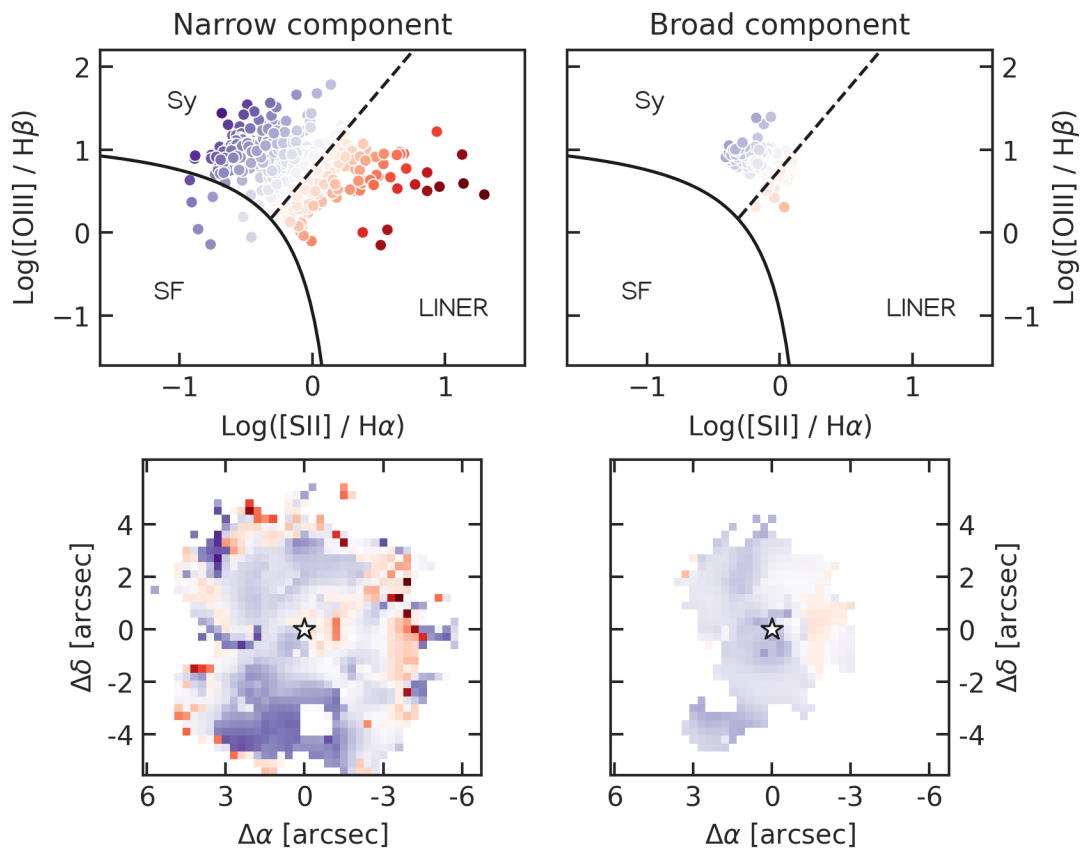
Figure C.8: Same as Figure C.7, but for the [OIII]/Hβ vs. [SII]/Hα. The different excitation mechanisms are marked on the plots as SF (star formation), Sy (Seyfert), and LINER (low-ionisation nuclear emission-line region).
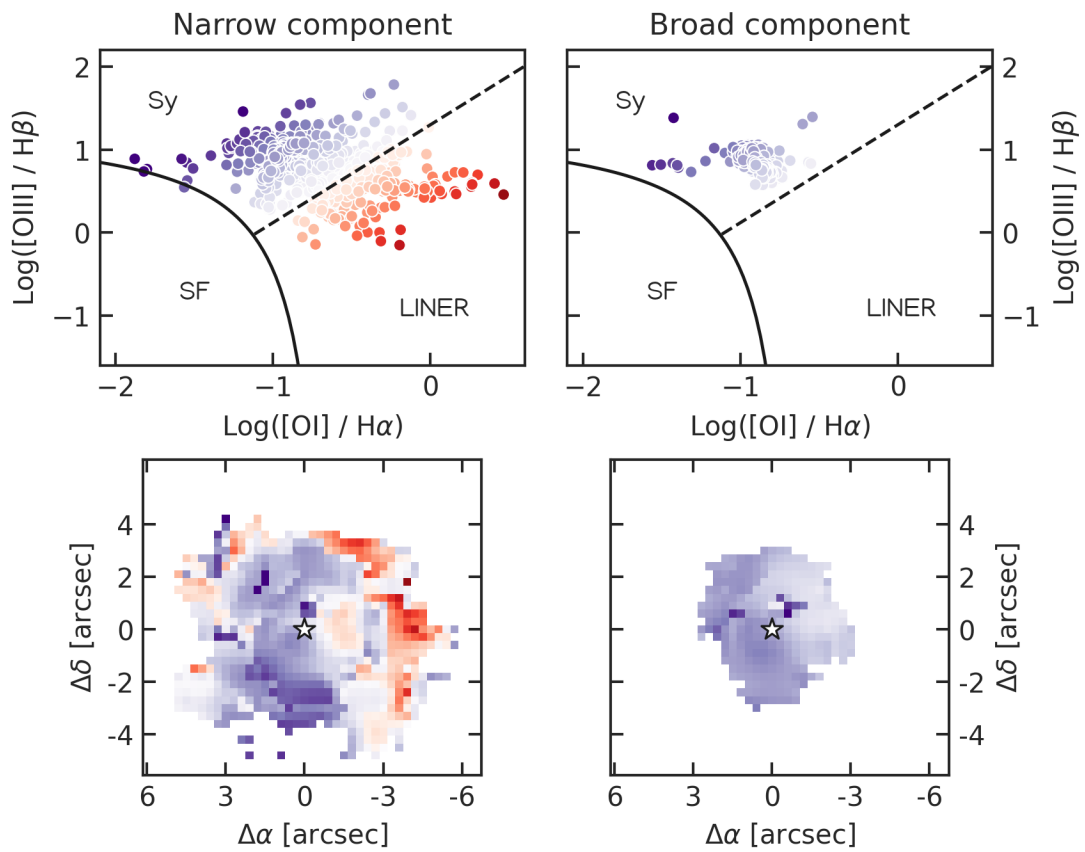
Figure C.9: Same as Figure C.7, but for the [OIII]/Hβ vs. [OI]/Hα. The different excitation mechanisms are marked on the plots as SF (star formation), Sy (Seyfert), and LINER (low-ionisation nuclear emission-line region).
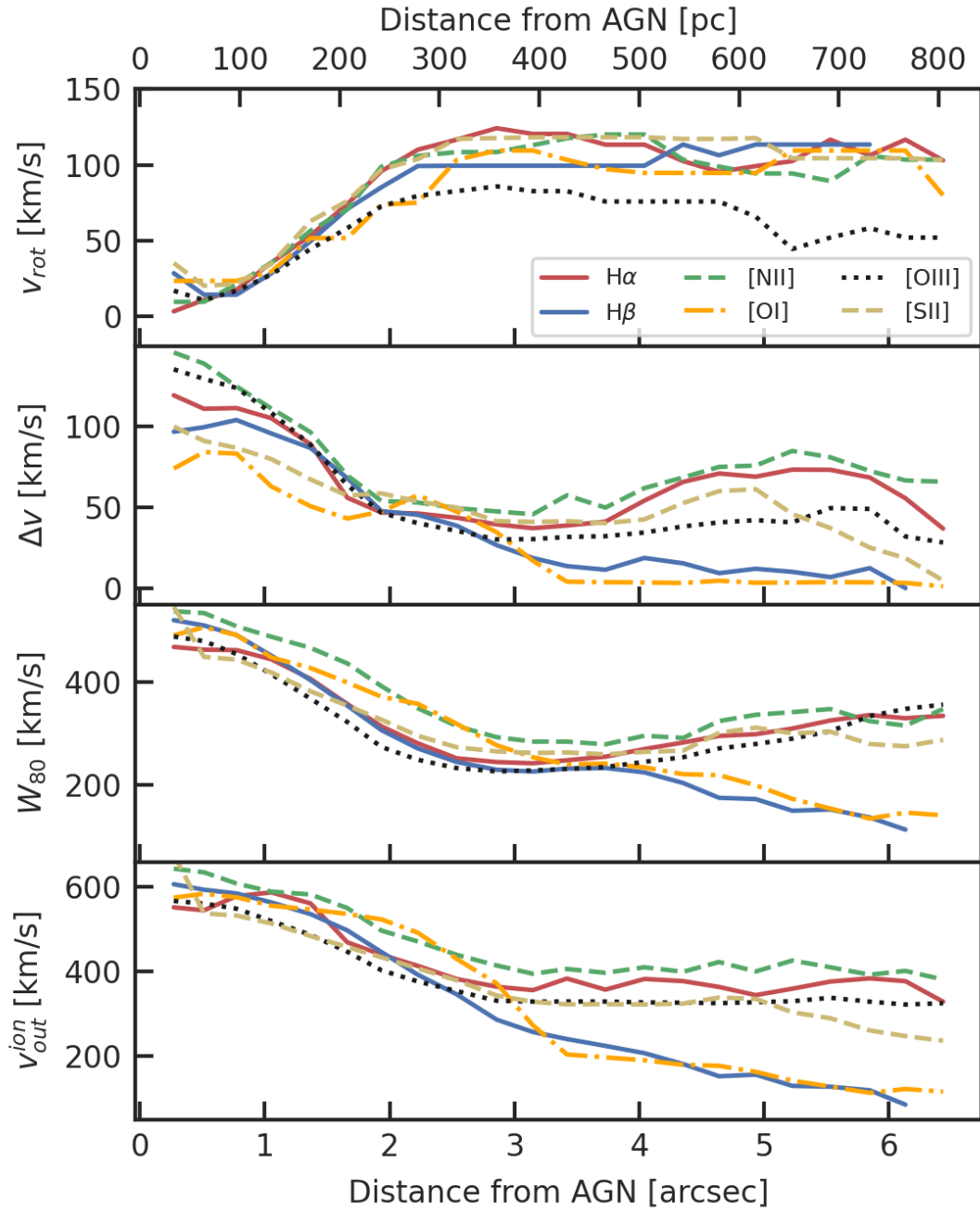
Figure C.10: Same as Figure 4.14, but for all the ionised gas emission lines.

Acknowledgements

This Thesis would not have been possible without the precious contribution and support of my supervisors. Francesca, you really taught me how to do science, with deep questions and a continuous exploration. Livia, you guided my confidence for the obtained results. Viviana, your addition helped me believing more in myself and our work. Your mentorship, marked by patience and love, is something I will always cherish.

I am truly thankful to Almudena and Santiago, who warmly welcomed me in Madrid. Getting to know you and collaborating with you on such fascinating observations has been an exciting experience.

Thanks for inspiration to the many professors and researchers I encountered during my studies, particularly Fabrizio Brighenti, Andrea Cimatti, Luca Ciotti, Daniele Dallacasa, Francesco Ferraro, Filippo Fraternali, Lauro Moscardini, Rosita Paladino, and Cristian Vignali. Beyond the lectures topics, I learned a lot from each of you.

A special thanks to all the people who organized the seminars, workshops, and meetings in which I participated. I grew up a lot within the small space and time of these events. I am especially grateful to Chiara Circosta, Carlotta Gruppioni, Isabella Lamperti, Annagrazia Puglisi, Eugenio Schisano, and Jonathan Tan.

Thanks for all the shared moments, both within and outside the institutional buildings, to my fellow Ph.D. comrades, and especially to Dhrubo and Blessing. You made Bologna seem as vast as the entire world (which is vast when you don't look to outer space).

Despite being away most of the time, I owe much to my office, as it was there that I met you, Giovanna. With you, I explored distant places and deep emotions. You are a significant part of this Thesis, thanks to your constant support and advice.

Thanks to my parents, Cristina and Massimo, who have always supported all my life choices. Special thanks to my brothers, Matteo and Davide, and my nephews, Jari and Liam. Wherever I am, thinking of all of you always helps me navigate through everything.

Finally, special thanks go to Bologna – its narrow streets, its polyculturalism, the incredible music and films I discovered there, and the amazing people who live there and and constantly transform the city. Special thanks go to Annalaura, Cristina, Eugenio, Francesco, Giovanni, Helena, Sonia, Susanna, and Xavi.

From when I applied for this Ph.D. position in the middle of the Nullarbor desert, exchanging emails with Francesca about my comeback, to this last day in the middle of the Atlantic Ocean, exchanging emails with Francesca, Livia, and Viviana about the Thesis submission, I have loved every moment of this scientific journey.

Colophon